

TECHNISCHE UNIVERSITÄT MÜNCHEN

Wacker-Lehrstuhl für Makromolekulare Chemie

Micro- and Nanostructured Polymer Grafts

Marin Steenackers

Vollständiger Abdruck der von der Fakultät für Chemie der Technischen
Universität München zur Erlangung des akademischen Grades eines

Doktors der Naturwissenschaften

genehmigten Dissertation.

Vorsitzender:

Univ.-Prof. Dr. K. Köhler

Prüfer der Dissertation:

1. Priv.-Doz. Dr. R. Jordan
2. Univ.-Prof. Dr. S. Weinkauff
3. Univ.-Prof. Dr. M. Stutzmann

Die Dissertation wurde am 25.06.2007 bei der Technischen Universität München eingereicht und durch die Fakultät für Chemie am 27.07.2007 angenommen.

Acknowledgments

First of all, I wish to express my very special thanks to *PD Dr. Rainer Jordan* for his excellent supervision and the possibility he offered me to work on this very exciting topic. I also want to thank him for the freedom he gave me during this work, his helpful advices and for the unforgettable conferences in Flic en Flac, San Francisco and Budapest.

I would also like to thank *Professor Oskar Nuyken* and *Professor Bernhard Rieger* for giving me the opportunity to work at the Wacker Lehrstuhl für Makromolekulare Chemie. I thank *Dr. Heidi Samarian* and *Dr. Carsten Troll* for the work done behind the stage.

My thanks also go to *Professor Sevil Weinkauff*, *Professor Martin Stutzmann* and *Professor Klaus Köhler* for accepting to be part of my jury and for examining this work.

I offer my warmest thanks to *Dr. Alexander Küller* and *Professor Michael Grunze* from the Universität Heidelberg, *Simon Lud* and *Dr. José Antonio Garrido* from the Walter Schottky Institut and *Dr. Rüdiger Berger* from the Max-Planck-Institut in Mainz for the exceptional collaborations and all the fruitful discussions.

I'm also very grateful to *Gerhard Richter* for his kind help with the German parts of this dissertation and to *Carola Gantner* for the magnificent layout.

My thanks also go to the interns *Francis Adigbli*, *Carlos 'de Tenerife'*, *Pierre Göppert*, *Näïma Hutter* and *Spyridon Korres* for their excellent participation in the different projects.

I take a particular pleasure in thanking *Robert Luxenhofer* (the Marindeutsch-Deutsch translator) and *Karin Lüdtke* for the wonderful time in Flic en Flac. A big thank also to my lab colleges *Barbara Gall*, *Stephan Huber*, *Gerhard Richter* and *Max Erhard* for the wonderful work atmosphere.

I also want to thank all the other MAKROS, *Timo Anselment*, *Dr. Erwin Bacher*, *Annette Bauer*, *Dr. Martin Bortenschlager*, *Helga Brebeck*, *Dr. Sonia Cesana*, *Andreas Feigl*, *Annalisa Giró*, *Dr. Andreas Junger*, *Dr. Steffen Jungermann*, *Dr. Daniel Käsmayr*, *Dr. Doris Kaufmann*, *Monika Kellner*, *Dr. Tomaz Koz*, *Dr. Martin Mayershofer*, *Julia Müller*, *Michael Reif*, *Dr. Benjamin Roßbach*, *Udo Schmidt*, *Martin Schneider*, *Dr. Jurgen Smeenk*, *Dr. Ralf Weberskirch*, *Dr. Alexander Wörndle*, *Ulrike Will*, *Ning Zhang* and all the freshly arrived

MAKROS for their constant helpfulness and for the outstanding atmosphere in Garching, Thurnau, Sudelfeld and Freiburg.

Finally, I would like to thank my family, my friends and especially Isabelle for their great support and much more...

Abbreviations and acronyms

AA	acrylic acid
AB	4'-amino-1,1'-biphenyl
AFM	atomic force microscopy
AIBN	N,N-azobisisobutyronitril
ATR-FTIR	attenuated total reflectance Fourier transform infrared
ATRP	atom transfer radical polymerization
BDE	bond dissociation energy
BP	benzophenone
BT	4-mercapto-1,1'-biphenyl
cABT	crosslinked 4'-amino-1,1'-biphenyl-4-thiol
cBT	crosslinked BT
cHBT	crosslinked HBT
cMBT	crosslinked MBT
CVD	chemical vapor deposition
DCM	dichloromethane
DP	degree of polymerization
DPN	dip pen nanolithography
DRIFT	diffusion reflectance Fourier transformed infrared
EBCD	electron beam induced carbon deposition
EBCDs	electron beam induced carbon deposits
EBCL	electron beam chemical lithography
Eq.	equation
ETFE	ethylene-co-tetrafluoroethylene
EUV	extreme ultraviolet
eV	electron volt
Fig.	figure
GA	glycidyl acrylate
GC	gas chromatography
GPC	gel permeations chromatography
HBT	hydroxy-1,1'-biphenyl-4-thiol
HEA	2-hydroxyethyl acrylate

HEMA	2-hydroxyethyl methacrylate
IR	infrared
MAA	methacrylic acid
MBT	4'-methyl-1,1'-biphenyl-4-thiol
mC	micro Coulomb
MEMS	microelectromechanical systems
NBD	4-nitrobiphenyldiazonium tetrafluoroborate
NBT	4'-nitro-1,1'-biphenyl-4-thiol
NCD	nanocrystalline diamond
NHPI	N-(hydroxymethyl)phthalimide
NMP	nitroxide-mediated polymerization
NMR	nuclear magnetic resonance
P2VP	poly(2-vinylpyridine)
P4VP	poly(4-vinylpyridine)
PAMS	poly((4-aminomethyl)styrene) grafts
PDMS	poly(dimethyl siloxane)
PE	polyethylene
PET	poly(ethylene terephthalate)
PMAA	poly(methacrylic acid)
PMMA	poly(methyl methacrylate)
PNS	poly(nitrostyrene)
PP	polypropylene
PS	polystyrene
PSSA	poly(styrenesulfonic acid)
PtBMA	poly(tert-butyl methacrylate)
PVBP	poly(4-vinylbenzyl)phthalimide grafts
PVBP	poly(4-vinylbenzyl)phthalimide
PVC	polyvinylchloride
RAFT	reversible addition-fragmentation chain transfer polymerization
RBITC	rhodamine B isothiocyanate
RDS	rate determining step
rms	root-mean-square
SAM	self-assembled monolayer

SEC	size-exclusion chromatography
SEM	scanning electron microscope
SIP	surface-initiated polymerization
SIPGP	self-initiated photografting and photopolymerization
SIPP	surface-initiated photopolymerization
SPM	scanning probe microscopy
St	styrene
STM	scanning tunneling microscopy
TFA	trifluoroacetic acid
UNCD	ultrananocrystalline diamond
UV	ultraviolet
XPS	X-ray photoelectron spectroscopy
μ CP	microcontact printing

Symbols

ϕ	liquid volume fraction in polymer
d	diameter
D	electron beam dosage
D'	onset corrected electron beam dosage
E	electric potential
h	polymer layer thickness
h_d	dry polymer layer thickness
h_s	swollen polymer layer thickness
I	initiator
I_A	XPS emission intensity of element A
k_d	dissociation rate constant
k_p	propagation rate constant
k_{te}	termination rate constant
k_{tr}	transfer rate constant
M	monomer

M_n	number average molecular weight
M_p	molar mass of one monomer unit in the polymer backbone
N	polymer chain length
N_{Av}	Avogadro constant
Q	degree of swelling, charge
R_g	radius of gyration
RH	relative humidity
R_p	propagation rate
R_{te}	termination rate
R_{tr}	transfer rate
S	surface area, stability factor of monolayers
t_p	polymerization time
u	absorbance coefficient
$w_{1/2}$	full width at half maximum height
θ	error
λ	wavelength
μ	scattering coefficient
ρ	bulk density
σ	grafting density
χ	Flory-Huggins interaction parameter

Table of contents

1	INTRODUCTION	1
2	BACKGROUND	3
2.1	POLYMER GRAFTS: GENERAL FEATURES AND SYNTHESIS	3
2.2	SURFACE-INITIATED POLYMERIZATION	5
2.2.1	<i>Surface-bonded initiator systems</i>	5
2.2.2	<i>Surface-initiated polymerization versus polymerization in solution: some general considerations</i>	7
2.2.3	<i>Free radical surface-initiated polymerization</i>	8
2.3	PHOTOGRAFTING	11
2.3.1	<i>Photoinitiators</i>	11
2.3.2	<i>Bulk surface photografting polymerization</i>	12
2.3.3	<i>Self-initiated photografting and photopolymerization</i>	14
2.4	SYNTHESIS OF MICRO AND NANOSTRUCTURED POLYMER GRAFTS	16
2.5	NANOPATTERNED SURFACE FUNCTIONALITIES	17
2.5.1	<i>Microcontact printing</i>	17
2.5.2	<i>Scanning probe microscopy based methods</i>	18
2.5.2.1	Dip-pen-nanolithography	18
2.5.2.2	Nanoshaving.....	19
2.5.2.3	SPM-tip induced transformations.....	20
2.5.3	<i>Photolithography</i>	20
2.5.4	<i>Electron beam lithography</i>	22
2.5.4.1	Electron beam resist lithography.....	22
2.5.4.2	Chemical lithography	23
2.5.4.3	Electron beam carbon deposition	28
2.6	STRUCTURAL PROPERTIES OF NANOPATTERNED POLYMER GRAFTS	29
3	PURPOSE AND OBJECTIVES	33
4	RESULTS AND DISCUSSION	34
4.1	3D MICRO- AND NANOSTRUCTURED POLYMER GRAFTS ON GOLD BY EBCL AND SIPP	34
4.1.1	<i>Ex situ kinetic studies</i>	35

4.1.2	<i>Influence of the electron dose on the polymer layer thickness</i>	39
4.1.2.1	Correlation between the polymer layer thickness and the amino surface concentration	42
4.1.3	<i>Influence of initial structure widths and electron beam dosage</i>	46
4.2	3D MICRO- AND NANOSTRUCTURED POLYMER GRAFTS ON GOLD BY EBCL AND SIPGP	52
4.2.1	<i>Surface-initiated photopolymerization (SIPP) versus self-initiated photografting and photopolymerization (SIPGP)</i>	52
4.2.2	<i>SIPGP on structured BT SAMs</i>	53
4.2.2.1	Influence of the electron dosage on the polymer thickness	57
4.2.3	<i>SIPGP on different ω-functionalized biphenylthiol SAMs</i>	60
4.2.4	<i>Comparison between cABT and cAMBT SAMs</i>	62
4.3	MODIFICATION OF DIAMOND SUBSTRATES	67
4.3.1	<i>Background</i>	67
4.3.1.1	Synthetic diamond.....	68
4.3.1.2	Chemical modification of diamond: State of the art	68
4.3.2	<i>Nitrobiphenyl SAMs on diamond</i>	69
4.3.2.1	Preparation of nitrobiphenyl SAMs	70
4.3.2.2	Characterization of NB monolayers on polished polycrystalline diamond by AFM	71
4.3.2.3	Characterization of NB monolayers on UNCD by XPS	73
4.3.2.4	Radiation induced conversion of NB monolayers on UNCD	76
4.3.2.5	Electrochemical characterization of NB monolayers on UNCD	76
4.3.3	<i>Microstructured polymer grafts on diamond by SIPGP</i>	80
4.3.3.1	Preparation of PS grafts on microstructured oxidized UNCD	81
4.3.3.2	Functionalization of PS grafts on oxidized UNCD.....	83
4.3.3.3	Nitration and sulfonation of PS grafts on oxidized UNCD.....	84
4.3.3.4	Preparation of poly((4-aminomethyl)styrene) grafts on oxidized UNCD ...	87
4.3.3.5	Functionalization of microstructured PAMS grafts on UNCD with a fluorescence dye	89
4.3.4	<i>SIPGP of styrene on glassy carbon and graphite</i>	91
4.4	3D MICRO- AND NANOSTRUCTURED POLYMER GRAFTS ON ISOLATORS, SEMICONDUCTORS AND CONDUCTORS BY SIPGP ON ELECTRON BEAM INDUCED CARBON DEPOSITS	95

4.4.1	<i>General approach</i>	95
4.4.2	<i>SIPGP on EBCDs on silica</i>	97
4.4.2.1	SIPGP of styrene on EBCDs on silica	97
4.4.2.2	Stability of the polymeric layer and EBCDs on silica	98
4.4.2.3	SIPGP on EBCDs on silica: <i>ex situ</i> kinetic studies	99
4.4.2.4	Influence of the electron dosage on the polymer layer thickness and preparation of three dimensional polymer architectures	100
4.4.3	<i>Micro- an nanostructured polymer grafts on various substrates</i>	104
4.4.3.1	Structured polymer grafts on isolators	104
4.4.3.2	Structured PS grafts on semiconductors and conductors	107
4.4.4	<i>Molecular architecture of polymer grafts prepared by SIPGP</i>	114
4.4.5	<i>Successive SIPGP</i>	116
4.4.6	<i>Functionalization of PS grafts on EBCDs</i>	119
4.4.6.1	Structured PAMS grafts on silica	119
4.4.6.2	Functionalization of structured PAMS grafts.....	121
4.4.6.3	Nitration and sulfonation of structured PS grafts.....	122
4.4.7	<i>Functionalization of P4VP grafts with gold</i>	126
5	CONCLUSION	131
6	GERMAN ABSTRACT	139
7	EXPERIMENTAL PART	147
7.1	CHARACTERIZATION TECHNIQUES.....	147
7.2	SOLVENTS, CHEMICALS AND SUBSTRATES	150
7.2.1	<i>Substrate pretreatment</i>	150
7.2.2	<i>Preparation of ω-functionalized biphenylthiol SAMs on gold</i>	153
7.2.3	<i>Micro- and nanostructuring of the substrates by electron beam lithography</i>	153
7.3	SYNTHESIS AND CHARACTERIZATION OF CHEMICAL COMPOUNDS	154
7.3.1	<i>Nitrobiphenyl SAMs on H-terminated diamond</i>	156
7.3.2	<i>Surface-initiated polymerization (SIPP and SIPGP)</i>	156
7.3.3	<i>Polymer analogue reactions</i>	157
8	REFERENCES	159

1 Introduction

Coating materials were already used in the Stone Age as is witnessed by prehistoric cave paintings from ca. 15 000 B.C. discovered in the south of France and in the north of Spain. *Although they do not correspond to our notion of modern coatings, they were based on the same principle: they contained a binding agent (lard) and a pigment (ochre).*¹ The invention of protective coatings is attributed to the Chinese, 7000 years ago.² They used lacquer, made from the resin of the tree *Rhus verniciflua* to protect wooden objects. Until the beginning of the 20th century, vegetable oils and tree resins remained the most important raw materials for the production of coatings. Today, coating materials are mainly produced in the chemical industry and the application range of coatings extends much beyond the simple decoration and protection aspects.

Thin organic coatings have received a growing scientific and commercial interest in the past decades. A substrate coated with a thin organic layer has different surface properties than the bare substrate, while the bulk mechanical, optical and electrical properties are retained. Adhesion is one of the key properties of coatings. A number of technologically important coating techniques such as spin coating, dip coating, evaporation and vapor deposition rely on physical interactions between the deposited molecules and the substrate. However, physical interactions are rather weak and the adhesion and long term stability of coatings can be improved significantly by attaching the coating molecules chemically to the substrate chemical.³

In some applications, substrates are modified by a single molecular layer of a few Ångströms thickness. A prominent example is the modification of an automobile windshield with hydrophobic silane self-assembled monolayers (SAMs) to reduce the adhesion of raindrops.⁴ For many other applications, where SAMs are too thin to fulfill the desired coating function, the substrates are coated with polymer films, covalently attached to the surface, so-called polymer grafts. Functional polymer grafts are applied in various *high-tech* areas such as microelectronics⁵ or modern medicine. Polymer grafts are of particular interest in biomedical research, because the grafted polymer chains can extend from the surface into the adjacent liquid phase. Due to the flexibility of the grafted chains, the liquid phase can penetrate the polymer layer and molecules can interact with binding partners within the layer. Compared to the direct immobilization of molecules on flat surfaces, this three dimensional arrangement of binding sites allows the modelization of systems which resemble more to real biological

environments.⁶ Hydrophilic polymer grafts have found various applications in commercial biomedical products such as contact lenses,⁷ biological adhesives and antithrombogenic coatings for catheters.⁸

Thin organic coatings have also played a predominant role in the preparation of micro- and nanostructured surfaces.⁴ In the last years, these surfaces have been the subject of intense research efforts. They have been applied in various fields such as molecular electronics,⁹ microelectronics, photonics,¹⁰ microelectromechanical systems (MEMS),¹¹ sensor technology¹² and biology.¹³ While various techniques have been developed for the preparation of structured SAMs,⁴ only a few studies have been devoted to micro- and nanostructured polymer grafts.⁶ New strategies need to be developed for the preparation and characterization of these new nanomaterials. Sensor technologies,¹⁴ combinatorial science,¹⁵ biomedicine,¹⁶ and nanofluidics¹⁷ are only a few examples of fundamental and applied research areas in which the preparation of structured polymer layers with control over chemical functionality, shape and feature dimension on the nanometer length scale may open new perspectives. This is a challenging and interdisciplinary project where chemistry, physics, and biology meet.

2 Background

2.1 Polymer grafts: general features and synthesis

A polymer graft is defined as a polymer chain, chemically attached to a surface. Polymer grafts can have different molecular architectures (linear, branched, crosslinked, etc.) as well as different chemical compositions (homopolymers, copolymers, etc.). The molecular conformations of grafted polymer chains are significantly different from those of free polymers in solution.¹⁸ The molecular conformations of macromolecules in solution are mainly influenced by the quality of the solvent, the chain stiffness and the degree of polymerization, DP. In good solvents, homopolymers adopt an expanded coil conformation. The favorable interactions between polymer and solvent molecules dominate the loss of entropy due to chain stretching and the radius of gyration of a polymer, which is a measure of the size of the macromolecule, is given by $R_g \sim DP^{3/5}$. In poor solvents, polymers adopt a collapsed coil conformation to minimize the contact between polymer and solvent molecules and the radius of gyration scales as $R_g \sim DP^{1/3}$.¹⁸

Grafting a polymer chain to a surface modifies dramatically the molecular conformation. *In addition to DP, the conformation of end-tethered polymer chains is governed by the number of polymer chains grafted per unit area of the substrate characterized by grafting density of chains on the surface, σ .*¹⁹ When the grafting density is low, individual tethered polymer chains remain isolated and the conformation of these chains is similar to that in the solution. The polymer chains do not overlap and the thickness of the grafted chains, h , is independent of σ . Under good solvent conditions, the polymer chain adopts a so-called mushroom conformation and the polymer layer thickness scales as $h \sim DP\sigma^0$. As the grafting density increases, polymer molecules overlap and the chains have to stretch away to the surface. Polymer grafts in this conformation are called polymer brushes.²⁰ The wet thickness of polymer brushes in good solvents scales as $h \sim DP\sigma^{1/3}$. It must be noted here that the mentioned scaling relations are only valid for neutral polymer chains and in the absence of special interactions between the substrate and the polymers. Due to the stretching of the polymer chains (perpendicularly to the surface), several new physical phenomena arise. A well known example is the ultralow friction between surfaces coated with polymer brushes.²¹

Another example is the so-called autophobic behavior of polymer brushes²² (chemically identical free polymer chains do not wet their own brushes).

When placed in the dry state, the surface-tethered polymers collapse, giving rise to the so-called collapsed chain conformations. The thickness of dry polymer grafts is given by

$$h_d = M_n \sigma / \rho N_{Av} \quad \text{Eq. 1}$$

where M_n , σ , ρ are respectively the number average molecular weight, grafting density and bulk density of the grafted polymer chains and N_{Av} the Avogadro constant.²³ This relationship is independent of the polymer architecture.

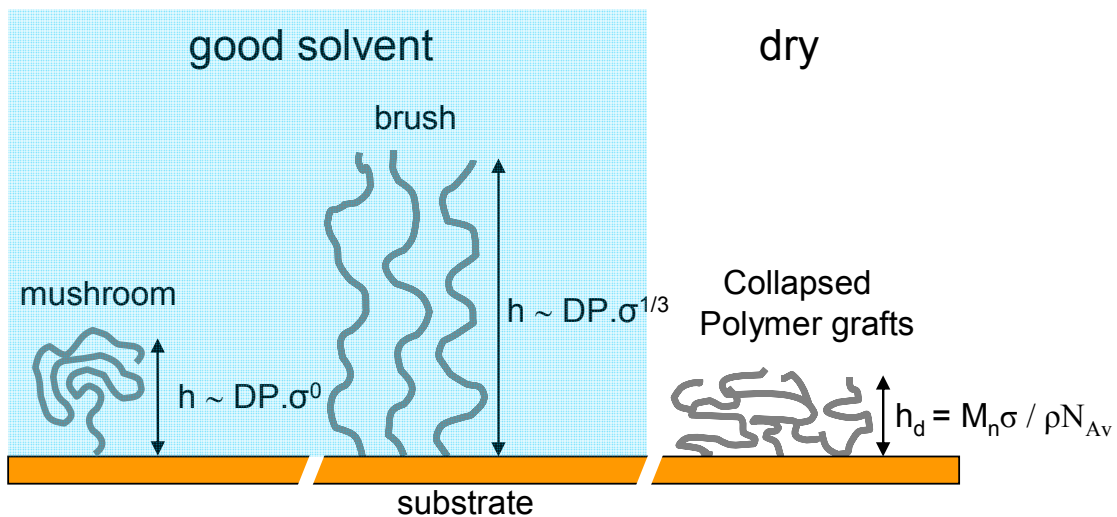


Figure 1. Schematic representation of grafted polymers in mushroom (left) and brush (middle) conformations in good solvents and in dry, collapsed state (right).

In general, polymer grafts can be prepared using two different approaches (Figure 2): the *grafting to* method and the surface-initiated polymerization (SIP, also called *grafting from* method). In the first method, polymer chains carry one or more “anchor” groups that react with the substrate. The *grafting to* method is experimentally simple, but has some limitations. It is difficult to achieve high grafting densities (number of grafted polymer chains per surface area) because of the screening of reactive surface sites by already adsorbed polymers. Films generated by this method are limited to thicknesses between 1 and 5 nm.²⁴

The SIP from initiators bond to surfaces is a powerful alternative to control the functionality, density and thickness of polymer grafts with almost molecular precision. Since the diffusing

species during the SIP are small monomer molecules (instead of macromolecules in the *grafting to* method) high surface density of the chains can be achieved.

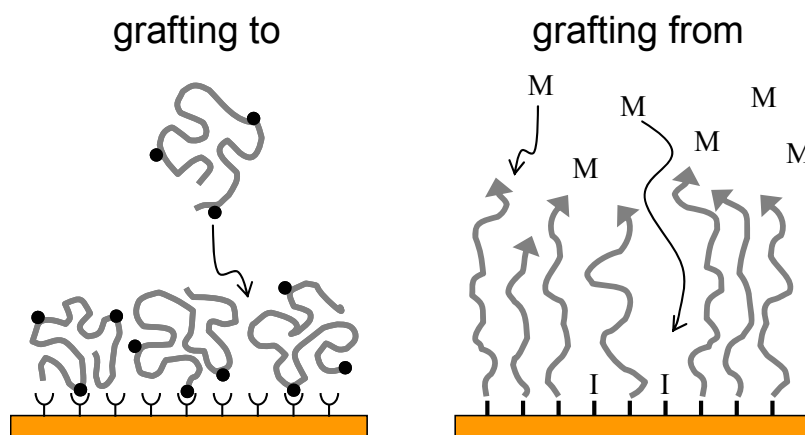


Figure 2. Schematic representation of the *grafting to* (left) and *grafting from* (right) approaches. M: monomer; I: Initiator.

2.2 Surface-initiated polymerization

SIP has recently attracted considerable attention within the polymer community and has been used for the preparation of dense polymer coatings on planar surfaces as well as on nanoparticles.²⁵ SIP has been demonstrated for all types of polymerization methods including free²⁶ and controlled²⁷ radical, living anionic,²⁸ living cationic²⁹ and ring opening metathesis³⁰ polymerization. Controlled radical polymerization techniques such as ATRP (atom transfer radical polymerization), NMP (nitroxide-mediated polymerization) and RAFT (reversible addition-fragmentation chain transfer polymerization) have become the most popular route, mostly because of their tolerance to a wide range of functional monomers and the possibility to form highly defined block copolymers.³¹

2.2.1 Surface-bonded initiator systems

Various strategies have been developed for the immobilization of initiators on substrates. Defined initiator systems can be prepared by the modification of the substrate with a SAMs of bifunctional molecules bearing a surface grafting function and an initiator function as its precursor.

SAMs can be formed on almost any surface, as long as the anchor group is correctly chosen.³² Various surface coupling strategies have been developed during the last decades. Silane and organosulfur compounds have been widely used to form SAMs on various substrates. Silane derivatives form SAMs on hydroxylated surfaces such as silicon oxide,³³ aluminum oxide,³⁴ glass,³⁵ mica,³⁶ zinc selenide,³⁵ germanium oxide,³⁵ gold³⁷ and oxidized diamond³⁸ surfaces. Organosulfur compounds coordinate strongly with gold,³² silver,³⁹ copper,⁴⁰ Platinum,⁴¹ mercury,⁴² iron,⁴³ GaAs⁴⁴ and InP⁴⁵ surfaces. More recently, strategies based on the electrochemical reduction of aryl diazonium salts⁴⁶ or on the photochemical grafting of terminal alkenes^{47,48} were developed for the formation of very stable SAMs on different carbon allotropes such as graphite, carbon nanotubes, glassy carbon, and diamond.

In general, a surface functionality R can be introduced on a substrate preparing a SAM of a bifunctional molecule bearing one surface adhesion function and the desired function R. However, to get predictable surface chemistry, the monolayer must be well-ordered and R may not bind competitively to the substrate. This limits the available surface chemistry using SAM approaches. This is for instance a major problem when carboxylic surface groups have to be introduced on oxidized substrates.³² However, many schemes have been developed to expand the range of available SAMs functionalities using protective groups, which are removed once the monolayer has been formed.^{49,50}

A broad variety of bifunctional molecules has been prepared for different substrate/polymerization type combination. Some examples are illustrated in Figure 3.

Also few SAM-free approaches have been investigated recently for the immobilization of initiators. Teare *et al.*⁵¹ reported on a single-step substrate-independent route to prepare ATRP initiator surfaces by the deposition of halogen-containing initiator films by pulsed plasma polymerization. Padeste *et al.*⁶ reported on the formation of peroxides on organic substrates using extreme ultraviolet irradiation of the sample, followed by a free radical polymerization of vinyl monomers.

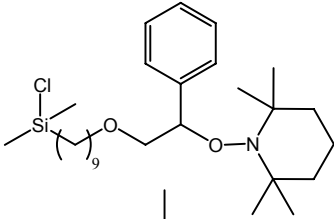
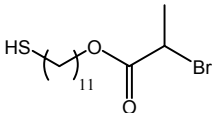
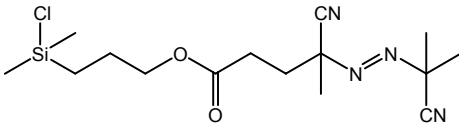
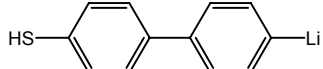
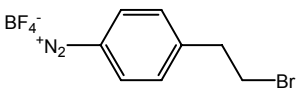
bifunctional molecule	polymerization type	substrate
	NMP	silicon oxide
	ATRP	gold
	free radical polymerization	silicon oxide
	anionic polymerization	gold
	ATRP	carbon nanotube

Figure 3. Structure of some known bifunctional molecules bearing a surface grafting function and an initiator function for the SIP.^{52,53,54,55,56}

2.2.2 Surface-initiated polymerization versus polymerization in solution: some general considerations

Polymerization reactions from surface-bonded initiators bring about new situations due to the tethering and crowding of growing polymer chains. Different important fundamental questions arise: what is the efficiency of surface-attached initiators compared to analogue initiators in solution? Is the kinetic of the SIP identical to the kinetic of analogue polymerization reactions in solution and does it depend on the surface morphology or grafting density? What is the molecular mass, the polydispersity and the molecular architecture of tethered polymer chains prepared by SIP? Etc.

The difficulty to answer some of these questions is mainly due to fact that standard techniques to analyze polymerization reactions in solution such as NMR, gas chromatography (GC) and size-exclusion chromatography (SEC) cannot be applied for the characterization of grafted polymer chains. This problem can sometimes be circumvented by using a linker between the substrate and the initiator which can be cleaved after the SIP reaction. The cleaved polymer chains can then be analyzed in solution. This approach has been used by e.g. Chaumont and coworkers.⁵⁷ They showed that polymer grafts prepared using NMP on planar surfaces had

similar molar masses and polydispersities as polymer chains formed in solution. However, it is noteworthy that large surface areas need to be coated to obtain enough material for one single analytical measurement: e.g., one square meter of 10 nm thick polystyrene (PS) grafts has a weight of approximately 10 mg, which is the minimum amount needed for one NMR and one GPC measurement. Sufficient polymer material can be obtained more easily by the SIP on nanoparticles or porous materials due to the high specific surface area to volume ratio (up to 900 m²/g). Another major advantage of this approach is that polymer chains, grafted on nanoparticles can be characterized directly using standard solution NMR and IR techniques.²⁴ Polymer grafts prepared with SIP on silica nanoparticles have been intensively studied.⁵⁸ A widely used procedure to recover the grafted polymer chains is the dissolution of the silica particles in HF solutions. These *degrafted* polymer chains were then compared with polymer chains prepared under analogue polymerization conditions in solution. Several research groups have observed a very good agreement between the molecular weight and polydispersity of polymers prepared in solution and by SIP.^{59,60,61} The same observation has been made for the SIP on particles having different diameters (ranging from 12 nm to 1,5 μm), suggesting that the curvature of the surface had negligible effect on the polymerization kinetics.⁶² Based on these results, it is now commonly assumed that the SIP, even on planar substrates, is similar to polymerization reactions in solution. However, it must be pointed out that the strong analogies between the kinetics of polymerization in solution and SIP have not been demonstrated for all types of polymerization. The mechanism and kinetics of SIP is still the subject of various studies.

2.2.3 Free radical surface-initiated polymerization

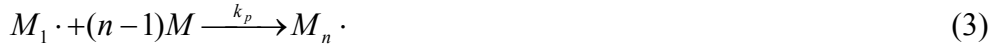
In general, the free radical polymerization can be described in four steps: initiation, propagation, transfer and termination. The initiation step involves two reactions. The first reaction is the production of free radicals by an initiator I. The usual case is the homolytic dissociation of I which results in a pair of radicals R·



with the dissociation rate constant, k_d . The second reaction of the initiation step is the addition of R· to the first monomer



with a monomer, M, and the rate constant for the initiation step, k_i . During the propagation reaction, $M_1 \cdot$ grows by the successive addition of a large numbers of monomer molecules

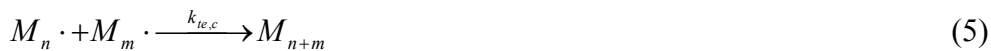


where k_p is the propagation rate constant. Due to the high reactivity of growing polymer chain ends, unavoidable side-reactions take place. The radical on a growing polymer chain can be transferred to another molecule X (monomer, solvent, polymer or any other compound) by e.g. hydrogen abstraction:



Chain transfer reactions do not terminate the overall polymerization reaction since $X \cdot$ usually reacts with a monomer and initiates a new chain propagation reaction.

Termination of the propagation reaction with the annihilation of the radical occurs with the combination of two radicals or with disproportionation:



where $k_{te,c}$ and $k_{te,d}$ are the rate constants for termination by radical coupling and disproportionation respectively. One can express also the termination step with



where the particular mode of termination is not specified. k_{te} is given by

$$k_{te} = k_{te,c} + k_{te,d} \quad \text{Eq. 2}$$

In the case of free radical polymerization, the propagation reaction is much faster than the initiation step, which is the rate determining step ($k_p \gg k_d$). In contrast, the propagation reaction is the rate determining step in the case of living polymerization.

If we assume that $X \cdot$ radicals (generated by transfer reactions) are able to initiate a new chain propagation reaction, the average degree of polymerization DP is given by

$$DP = \frac{R_p}{R_{te}} = \frac{k_p[M][M \cdot]}{2k_t[M \cdot]^2} = \frac{k_p[M]}{2k_t[M \cdot]} \quad \text{Eq. 3}$$

where R_p and R_{te} are the rate of propagation and termination respectively and $[M \cdot]$ is the total concentration of all chain radicals. In order to eliminate $[M \cdot]$ in Eq. 3, the *steady-state* assumption is made: the concentration of radicals increases initially, but almost

instantaneously reaches a constant (steady state) concentration (usually around 10^{-8} mol/L).⁶³

With the steady state assumption, DP is given by

$$\frac{1}{DP} = \frac{\sqrt{4fk_d k_{tr}[I]}}{k_p[M]} \quad \text{Eq. 4}$$

with f as the initiator efficiency.

We have applied here the same approach to express the degree of polymerization of grafted polymer chains created by the free radical SIP. However, some differences appear directly between the free radical SIP and polymerization in solution. First of all, the dissociation of a surface-bonded initiator molecule generates only one surface-bonded radical for the SIP while in the case of polymerization reactions in solution, the dissociation of one initiator molecule generates two suitable radicals. Furthermore, for polymerization reactions in solution, chain transfer reactions on monomer or solvent do not reduce the average degree of polymerization. In the case of SIP, chain transfer reactions between a propagating surface-bonded polymer chain and molecules in the liquid phase can be considered as a form of termination reaction because it reduces the total amount of surface-bonded reactive centers. The rate of all transfer reactions between a propagating surface-bonded polymer chain ($M_S\cdot$) and molecules in the liquid phase (X_i) is given by

$$R_{tr} = [M_S\cdot] \sum_{i=1}^x k_{tr,i}[X_i] \quad \text{Eq. 5}$$

It can be observed that the rate of transfer reactions is proportional to $[M_S\cdot]$ while the rate of termination reactions by the combination or disproportionation of two radicals is proportional to $[M_S\cdot]^2$.

The degree of polymerization of polymer grafts created by the free radical SIP is given by

$$\frac{1}{DP} = \frac{\sqrt{2fk_d k_{te}[I] + K_{tr}^2}}{k_p[M]} + \frac{K_{tr}}{2[M]k_p} \quad \text{Eq. 6}$$

where

$$K_{tr} = \sum_{i=1}^x k_{tr,i} [X_i] \quad \text{Eq. 7}$$

The first term in Eq. 6 is almost identical to Eq. 4, for the polymerization in solution. The factor 2 in Eq. 6 instead of the factor 4 in Eq. 4 is a consequence of the fact that the dissociation of a surface-bonded initiator gives only one suitable radical.

2.3 Photografting

2.3.1 Photoinitiators

When a molecule is irradiated with visible or UV-light, it can absorb a photon having an energy $E = h\nu$. The molecular orbital (MO) theory can be used to describe the different electronic states involved in the electronic transitions in a simplified one-electron picture (Figure 4).

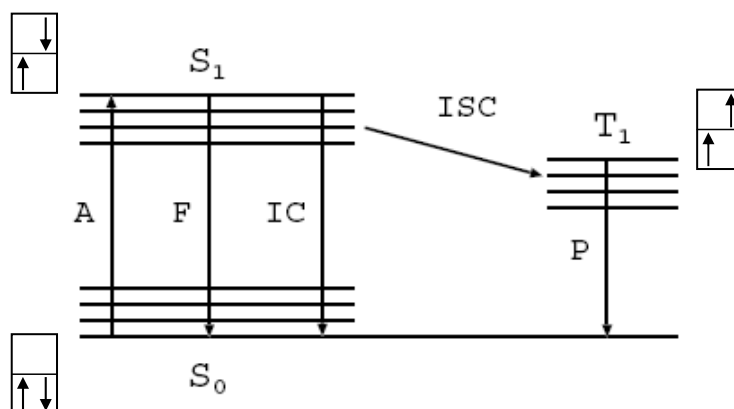


Figure 4. Energy-diagram (Jablonsky diagram): A = Absorption, F = Fluorescence, IC = Internal Conversion, ISC = Intersystem Crossing, P = Phosphorescence. S_0 = ground, singlet state, S_1 = lowest excited, singlet state, T_1 = lowest triplet state.⁶⁴

When a molecule absorbs energy, the π -electrons *jump* from the ground singlet state S_0 to an unoccupied excited singlet state S (S_1 is the lowest excited singlet state). The excited state S_1 can lose its energy by different processes:

1. Radiation by singlet-singlet emission (fluorescence, F) and triplet-singlet emission (phosphorescence, P).

2. Radiationless processes by transitions between states of the same spin (internal conversion, IC) and transitions between states of different spin (intersystem crossing, ISC).⁶⁵
3. Radiationless energy transfer by a chemical reaction. A photoinitiator is a compound which, upon absorption of light, undergoes a photoreaction and produces reactive species which are capable to initiate or to catalyze chemical reactions.⁶⁶

Various radical producing photoinitiators have been developed for radical polymerization reactions. In general, light absorption results in radical production by either of two pathways:

1. Excitation and subsequent decomposition into radicals



2. Excitation and subsequent H-abstraction of an H-donor (HD)



Widely used initiators of the first class are peroxides and azo-initiators. The second type initiators are also called photosensitizers. A photosensitizer is a chemical compound that readily undergoes photoexcitation and then transfers its energy to another molecule, also called quencher.⁶⁷ Benzophenone (BP) is the most utilized photosensitizer for the initiation of free radical polymerization reactions.

2.3.2 Bulk surface photografting polymerization

In the 1990s, Rånby and coworkers⁶⁸ developed a process called bulk surface photografting polymerization. This single-step process allows the formation of thick (2-5 μm) and dense polymer grafts directly onto ordinary crosslinked polymer substrates such as polyethylene (PE), poly(ethylene terephthalate) (PET), nylon, polypropylene (PP) and polyvinylchloride (PVC) without the previous immobilization of initiators on the substrate. The polymer grafts are formed by a simple and fast procedure: the substrate is placed in a solution of benzophenone in bulk monomer and irradiated with UV-light of a spectral distribution between 300 and 400 nm.⁶⁹

The authors present the following mechanism: when irradiating BP molecules with UV-light, they absorb energy and reach an excited singlet state $[\text{BP}]^{\text{S}}$. Through ISC, $[\text{BP}]^{\text{S}}$ is transformed into the more stable triplet state $[\text{BP}]^{\text{T}}$. The polymer substrate (P) acts here as H-donor and

$[\text{BP}]^{\text{T}}$ reacts to the diphenyl ketyl radical. The radical formed on the polymer substrate ($\text{P}\cdot$) can initiate the free radical polymerization of the monomer (Figure 5).

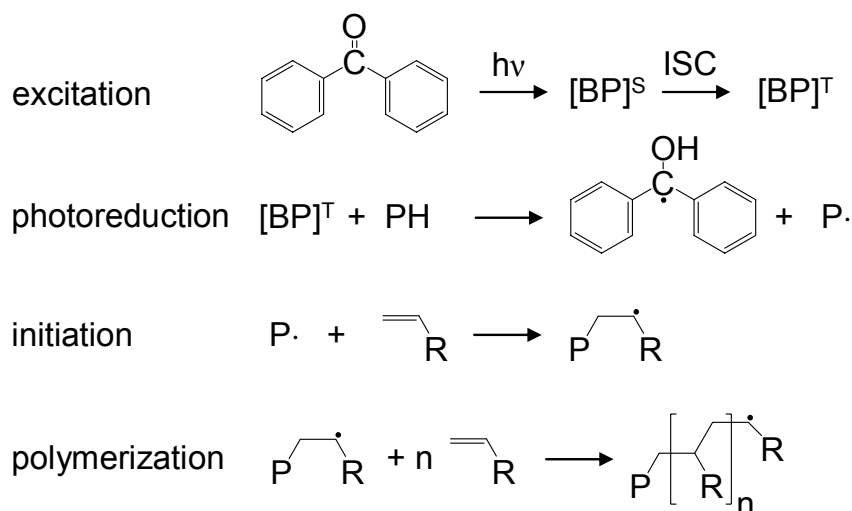


Figure 5. Principle of surface photografting polymerization. P represents the polymer substrate.

The diphenyl ketyl radical is relatively stable and does not initiate a radical chain polymerization in solution. However, $[\text{BP}]^{\text{T}}$ may also abstract hydrogen radicals from monomer molecules (M) in solution and the $\text{M}\cdot$ radicals, created by this mechanism, could initiate a free radical polymerization in solution. The grafting efficiency G_{E} of the process given by

$$G_{\text{E}} = \frac{W_{\text{G}}}{W_{\text{G}} + W_{\text{S}}} \quad \text{Eq. 8}$$

where W_{S} is the weight of polymer formed in solution and W_{G} the weight of grafted polymer. The authors demonstrated that G_{E} was determined by the difference between the required energy for hydrogen abstraction from surface functionalities and for hydrogen abstraction from molecules in the liquid phase.⁷⁰

The bulk surface photografting polymerization of acrylic acid on polyethylene substrates gave high grafting efficiencies (~80%). This was attributed to the difference between the bond dissociation energy (BDE) of C-H bonds in polyethylene substrates (95 kcal/mol) and the BDE of vinyl C-H bond (104 kcal/mol) in acrylic acid. The grafting efficiency decreased drastically when *H-donor additives* were added in the liquid phase (Figure 6). In this case, $[\text{BP}]^{\text{T}}$ abstracted preferentially hydrogen radicals from the *H-donor* in solution. This explains also why lower grafting efficiencies were found for the bulk surface photografting polymerization of monomers having easily abstractable hydrogen.

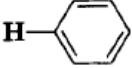
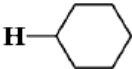
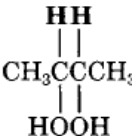
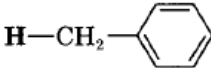
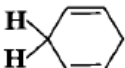
Additive	Chemical Structure	Bond Energy (kcal/mol)	Grafting Efficiency (%)
None	—	—	80
Benzene		111	82
Cyclohexane		94	79
2,3-Dihydroxyl <i>n</i> -butane		91	50
Toluene		86	20
1,4-Cyclohexadiene		73	0

Figure 6. The effect of H-donor additives on the grafting efficiency for the bulk surface photografting of acrylic acid on polyethylene substrates (5 wt % BP and 5 wt % additives).⁶⁸

2.3.3 Self-initiated photografting and photopolymerization

A few years later, the same group found that the concentration of BP during the bulk surface photografting polymerization of styrene on PE substrates had only a slight effect on the grafting efficiency.⁷¹ They found that almost the same grafting efficiency was obtained in the total absence of BP, i.e. polymer grafts were formed on the organic substrate, simply by immersing the substrate in bulk monomer and irradiating it with UV-light.

Based on a study of Li *et al.*,⁶⁷ the following mechanism was proposed: by absorbing a photon, styrene acts as a photosensitizer and reaches an excited singlet state which is transformed through ISC into the more stable triplet state. This triplet state is in equilibrium with a form containing two free radicals ($\cdot\text{St}\cdot$). In solution, $\cdot\text{St}\cdot$ can initiate a free radical polymerization. In the meantime, $\cdot\text{St}\cdot$ may also abstract a hydrogen atom from the PE substrate. The radical formed on the PE substrate initiates the free radical surface-initiated polymerization of styrene.

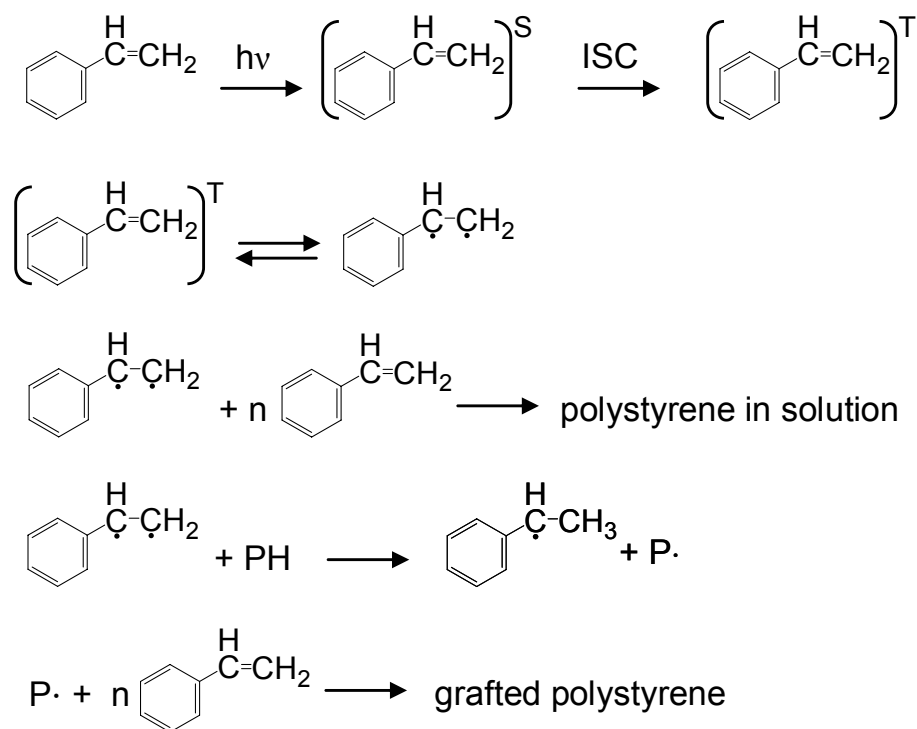


Figure 7. Principle of the self-initiated photografting and photopolymerization of styrene on a polymer substrate (P).

This mechanism is called *self-initiated photografting and photopolymerization* (SIPGP). Three years later, Brown *et al.*⁷² presented very similar results for the photografting of various acrylic monomers on high density polyethylene substrates. Fang and Liu calculated the excited states of acrylic acid.⁷³ According to their results, the T₃ triplet state of acrylic acid has a potential energy of 112.5 kcal·mol⁻¹ (T₁: 71.4 kcal·mol⁻¹; T₂: 86.9 kcal·mol⁻¹). Brown *et al.* argue that hydrogen radicals could be abstracted from the PE substrate, since the T₃-state potential energy of acrylic acid is higher than the C-H BDE in PE substrates (the BDE of primary, secondary and tertiary hydrogen atoms is 100, 96 and 93 kcal·mol⁻¹). *Similarly, the other acrylic monomers can also absorb UV-light and be excited to a state with enough energy to abstract hydrogen from the [...] surface and initiate the grafting reaction.*⁷²

Hollas *et al.*⁷⁴ determined the potential energy of the lowest two triplet states of styrene experimentally (T₁: 62.0 kcal·mol⁻¹; T₂: 91.8 kcal·mol⁻¹). Recently, Wan *et al.*⁷⁵ calculated that the third T₃ triplet state of styrene has a potential energy of 104 kcal·mol⁻¹.

The monomers that have already been grafted by SIPGP on PE substrates are listed in Figure 8.^{71,72}

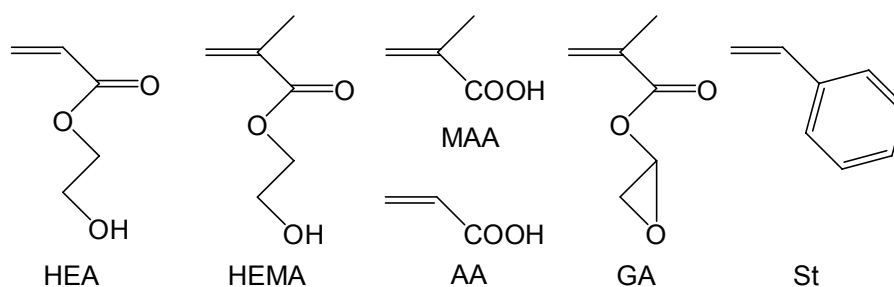


Figure 8. Monomers that have been grafted by SIPGP on PE substrates: 2-hydroxyethyl acrylate (HEA), 2-hydroxyethyl methacrylate (HEMA), methacrylic acid (MAA), acrylic acid (AA), glycidyl acrylate (GA) and styrene (St).^{71,72}

The SIPGP process cannot strictly be considered as surface-initiated polymerization since the initiation step, the photoactivation of a monomer molecule, is located in the liquid phase. Surprisingly, this straightforward approach for the preparation of thick polymer grafts has not attracted much attention in the polymer community.

2.4 Synthesis of micro and nanostructured polymer grafts

In principle, besides the ablation of unstructured polymer grafts, two different “bottom up” strategies can be followed for the preparation of structured polymer grafts:

1. *Grafting from* or *grafting to* on a pre-structured sample. An example of this approach is the SIP on patterned SAMs.
2. Spatially controlled *grafting from* or *grafting to* on a uniform sample. An example of this approach is the surface-initiated photopolymerization through a photomask on an unstructured SAM bearing photoinitiators (this is the only known example of microstructured polymer grafts prepared by the second strategy).²⁴

The first approach has different advantages, especially for the fabrication of structured polymer grafts on the micro- and nanometer scale. In principle, every *grafting from* or *grafting to* technique developed for the preparation of unstructured polymer grafts can be applied in the first approach. Thus, a broad variety of methods are already available for the preparation of patterned surface functionalities.

In the next chapter, different methods for the preparation of micro and nanostructured surfaces functionalities are summarized. In principle, all these methods can be applied for the preparation of surface-bonded two-dimensional initiator systems for SIP.

2.5 Nanopatterned surface functionalities

Well-defined nanopatterned surface functionalities are usually prepared by SAM preparation techniques.⁷⁶ In general, structured SAMs can be prepared by spatially controlled application of SAM molecules or by local modification/displacement of uniform SAMs. Highly-ordered nanostructured SAMs have been applied recently in fundamental studies on molecular electronics⁷⁷ and nanobiology.⁷⁸ However, also different *SAM-free techniques* allow the preparation of nanopatterned surfaces with the same lateral resolution and control in chemical functionality.

2.5.1 Microcontact printing

Microcontact printing (μ CP) was first developed by Whitesides and coworkers in 1993.⁷⁹ This technique, also called *soft lithography*, uses an elastomeric stamp (usually PDMS (polydimethyl siloxane)) to deposit SAM molecules onto the substrate. The stamp is first *inked* with a solution of functional molecules and pressed onto the surface (Figure 9).

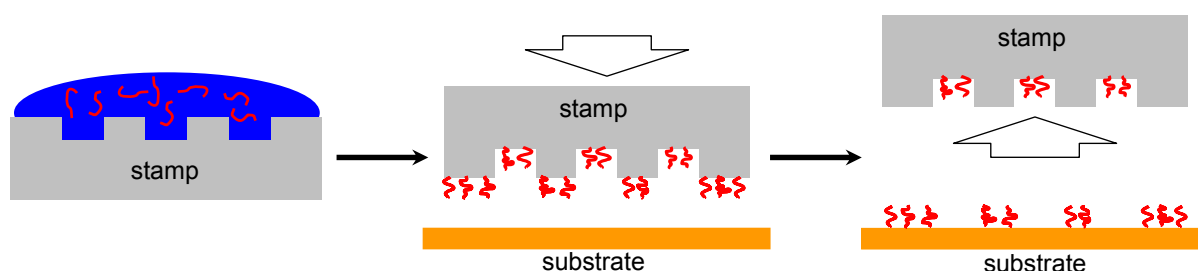


Figure 9. Schematic representation of μ CP.

The maximal resolution that could be achieved by microcontact printing was approximately 30 nm and the minimum feature size around 50 nm.^{80,81,82} Microcontact printing has been performed with a broad variety of *inks*: simple thiol⁷⁹ and silane derivatives,⁸³ proteins,⁸⁴ nanoparticles⁸⁵ and polymers.⁸⁶ While in theory, complex two-dimensional structures can be

fabricated, μ CP is commonly used to prepare relatively simple patterns, due to experimental difficulties and the facile preparation.⁴

Different studies reported on the preparation of microstructured polymer brushes by SIP on SAMs structured by μ CP.^{87,88,89} By repeating successive microcontact patterning and SIP steps, Zhou *et. al.*⁹⁰ created laterally distinctive multicomponent polymer brushes on gold, with a lateral resolution of 2 μ m.

2.5.2 Scanning probe microscopy based methods

*Scanning probe microscopy (SPM) covers several related technologies for imaging and measuring surfaces on a fine scale, down to the level of molecules and groups of atoms. These technologies share the concept of scanning an extremely sharp tip (3-50 nm radius of curvature) across the object surface. [...] Various interactions between the tip and the surface can be studied depending on the probe sensors used.*⁹¹ The two most common types of scanning probe techniques are atomic force microscopy (AFM) and scanning tunneling microscopy (STM). AFM measures the interaction force between the tip and surface while STM measures a weak electrical current flowing between the tip and a conductive sample. SPM can also be used as a powerful lithography tool to modify the local structures or chemical properties of surfaces with atomic resolution.⁹² Surface material can be locally applied, removed or modified.^{93,94,95} However, due to limited throughput of SPM based techniques, they have not been incorporated into industrial fabrication systems. A solution to this problem may be the use of several tips in parallel.⁹⁶

Recently, different studies reported on polymer grafts with lateral resolution of a few hundred nanometers by SIP on SAMs structured by STM or AFM tips.^{97,98,99,100}

2.5.2.1 Dip-pen-nanolithography

Dip-pen-nanolithography (DPN) was introduced in 1999 by Mirkin and coworkers.¹⁰¹ DPN uses an AFM tip as a *nib*, a solid-state substrate as *paper*, and molecules with a chemical affinity for the solid-state substrate as *ink*. Capillary transport of molecules from the AFM tip to the solid substrate is used in DPN to “write” patterns consisting of a relatively small collection of molecules in sub-micrometer dimensions. DPN is very comparable to μ CP, however, if DPN is analogue to writing with a pen, μ CP is a printing press. DPN allows a

better resolution (~ 15 nm) than μ CP and minimum feature size below 50 nm can be obtained (Figure 10).¹⁰²

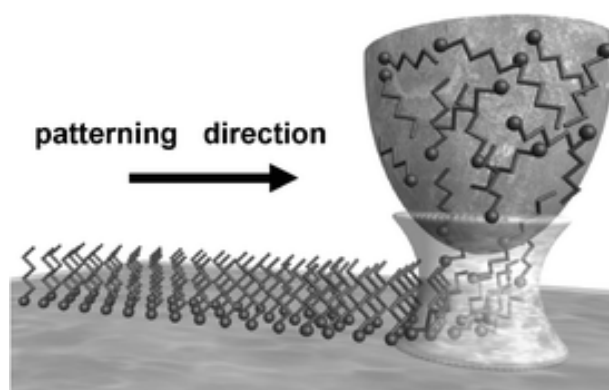


Figure 10. Schematic representation of DPN. A water meniscus is formed between the AFM tip and the substrate.¹⁰³

2.5.2.2 Nanoshaving

In nanoshaving, the AFM tip is used to etch the molecules out of a uniform SAM. A properly applied force mechanically removes the monolayer without deforming the underlying substrate. This concept was first introduced by Xu *et al.* in 1997.¹⁰⁴ The same concept can be used with an STM tip: upon elevating the applied voltage, organothiolate SAMs are desorbing from gold surfaces.¹⁰⁵

Nanoshaving in the presence of a second SAM-forming compound is called nanografting (Figure 11).¹⁰⁶ Nanoshaving can also be applied to remove thin (~ 2 nm) native oxide layers on silicon wafers.¹⁰⁷

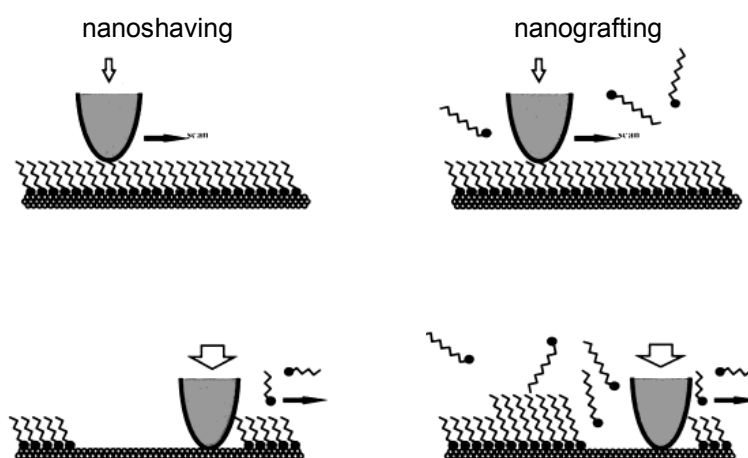


Figure 11. Schematic representation of nanoshaving (left) and nanografting (right).¹⁰⁸

2.5.2.3 SPM-tip induced transformations

Different strategies have been developed for the chemical modification of SAMs by SPM tips. A monolayer can be electrochemically altered by the electrical current flowing between the STM tip and the sample. Fréchet and coworkers¹⁰⁹ prepared SAMs bearing a protected thiol group. The protective group was then locally cleaved under the influence of the STM tip induced electric field. The same approach has been used for the preparation of nanostructured surface-bonded alcohol¹¹⁰ and carboxylic acid groups.¹¹¹

Direct electrochemical anodic oxidation of bare substrates is also possible for some materials.^{112,113} Further chemical functionalization of the oxidized surface areas can for instance be performed with silane compounds.¹¹⁴

AFM tips have also been used for the chemical modification of SAMs. The AFM tip is first functionalized with a catalyst that induces a chemical modification of the SAM molecules upon contact with the tip. This technique has been used for the local hydrolysis of azides¹¹⁵ and ethers,¹¹⁶ Suzuki coupling reaction,¹¹⁷ addition to terminal alkenes¹¹⁵ and reduction of imines.¹¹⁸

2.5.3 Photolithography

Radiation lithography is nowadays the most common technique for the fabrication of micro- and nanostructured surfaces. Different forms of radiation, including UV-VIS light, x-rays, extreme ultraviolet (EUV), electron and ion-beams, can be used.

Photoresist photolithography is a well-established process for the fabrication of silicon chips and microdevices.¹¹⁹ Photoresist materials are usually based on polymers. A polymeric photoresist solution is spin-coated onto the wafer surface and illuminated through a mask with (UV) light (Figure 12). Due to photochemical reactions, the irradiation induces an enhancement (positive resist) or a decrease (negative resist) of the solubility of the spin coated material in the photoresist developer (solvent used to dissolve the more soluble part). After development of the exposed film, a pattern is obtained. The structured photoresist is used as a mask in a subsequent etching or deposition process. Photoresist materials have been developed for almost any etching, deposition or grafting process. The remaining photoresist film can be removed easily at the end of the structuring process, since the adhesion between the spin

coated film and the substrate is rather weak. This process is repeated tenths of times in the fabrication of integrated circuits.¹²⁰

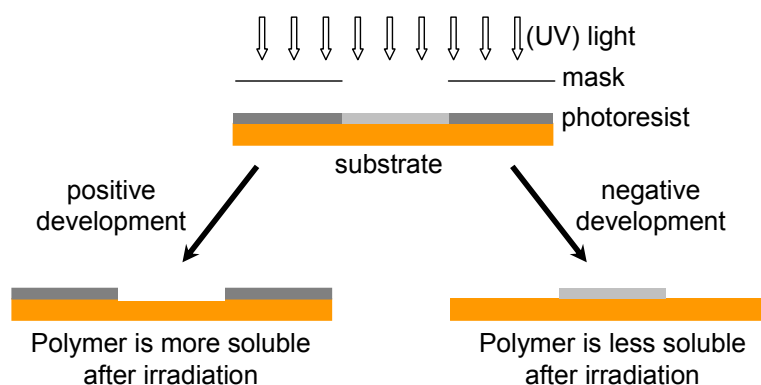


Figure 12. Schematic representation of positive and negative photoresist.

There are plenty of possible strategies to create structured functional surfaces with photolithography. Also various resist-free techniques have been developed for the modification of SAMs^{121,122,123} or uncoated materials directly with UV-light.⁶ However, photolithography has one major drawback: the limited resolution due to the diffraction limit of light. Photolithography uses a projection camera to form a demagnified image of a mask pattern. The size of the smallest features that can be printed by such an optical system, i.e. the resolution (r), is given by the relation:

$$r = k \cdot \lambda / NA \quad \text{Eq. 9}$$

where k is a constant, λ is the wavelength and NA is the numerical aperture of the optical projection system. *Over the years, the wavelength used in production has shifted from the visible into the deep UV region to be able to provide higher resolution. Currently lasers operating at 193 nm wavelength are used in production. The technology at this wavelength is expected to enable fabrication down to the 45 nm resolution node.*¹²⁰ To further reduce the minimum feature size, new radiation lithography strategies are developed based on electromagnetic radiation with very short wavelength such as EUV ($\lambda = 13.4$ nm) and X-rays ($\lambda = 10 - 0.01$ nm) or on focused ion and electron beams.¹²⁴

2.5.4 Electron beam lithography

Electron beam lithography (EBL) has been developed a few years after the invention of the scanning electron microscope (SEM) in 1955.¹²⁵ EBL was one of the first processes used in the fabrication of integrated circuits, in 1957.¹²⁶ While larger surface areas can be structured using an electron flood gun in combination with a stencil mask, much smaller and more complex structures can be fabricated by *direct writing* with a focused electron beam. EBL is thus not restricted to any length scale. Already in the seventies, important improvements in electron optics allowed sub-10 nm resolution.¹²⁷ Nowadays, EBL is widely exploited to produce structures in the sub-100 nm range.^{128,129,130} Compared to photolithography, the lateral resolution achieved by EBL is higher because the electron beam can be focused to a diameter of approximately 1 nm. Except for scanning probe microscopy based lithography methods, the resolution of EBL has been unsurpassed by any other form of lithography.¹³¹

While EBL has found wide usage in research, it has not yet become a standard technique for mass production in the chip industry. The main reason for this is speed. E.g. to pattern a single layer of semiconductor containing 60 devices, it would take an EBL system approximately two hours, compared with less than two minutes for an optical system.¹³² Up to now, EBL is mainly used in the industry for rapid prototyping of integrated circuits, in specific small productions and for the production of exposure masks used for conventional photolithography.^{132,133}

2.5.4.1 Electron beam resist lithography

Today, EBL is almost exclusively used in resist approaches. The process steps are identical as those for conventional photoresist. Spin coated poly(methyl methacrylate) (PMMA) is usually used as the positive resist film. With today's electron optics, electron beam widths can routinely be achieved to a few nm. The resolution limit is not determined by the beam size but by the size of the resist molecules and by secondary processes like forward scattering, backscattering, secondary electrons traveling in the resist material and proximity effects.¹³⁴ For most resist materials, it is difficult to go below 25 nm lines and spaces.¹³⁵ The forward scattering can be decreased by using higher energy electrons or thinner resist layers, but the generation of secondary electrons is inevitable. Some studies report on sub-10 nm structures achieved with spin coated PMMA^{136,137} or inorganic resists¹³⁸ exposed at very high energy electron beams of 100 keV. For high resolution EBL with PMMA resist, the development step

is critical and requires an increase of the exposure dose. Although very high resolution can be achieved using inorganic resists, they require high electron doses and high electron beam energies.¹³⁹

Recently, Zauscher and coworkers reported on nanostructured polymer grafts prepared by an EBL resist approach.^{140,141,142} In a first step, gold nanostructures (height: 40 nm, width: down to 210 nm) were fabricated by thermal evaporation of gold on a silicon surface, coated with a structured PMMA resist layer. The resist layer was then removed (lift-off) from the substrate and the gold nanopatterns were *amplified* by surface-initiated ATRP of N-isopropylacrylamide from a thiol bonded initiator (Figure 13).

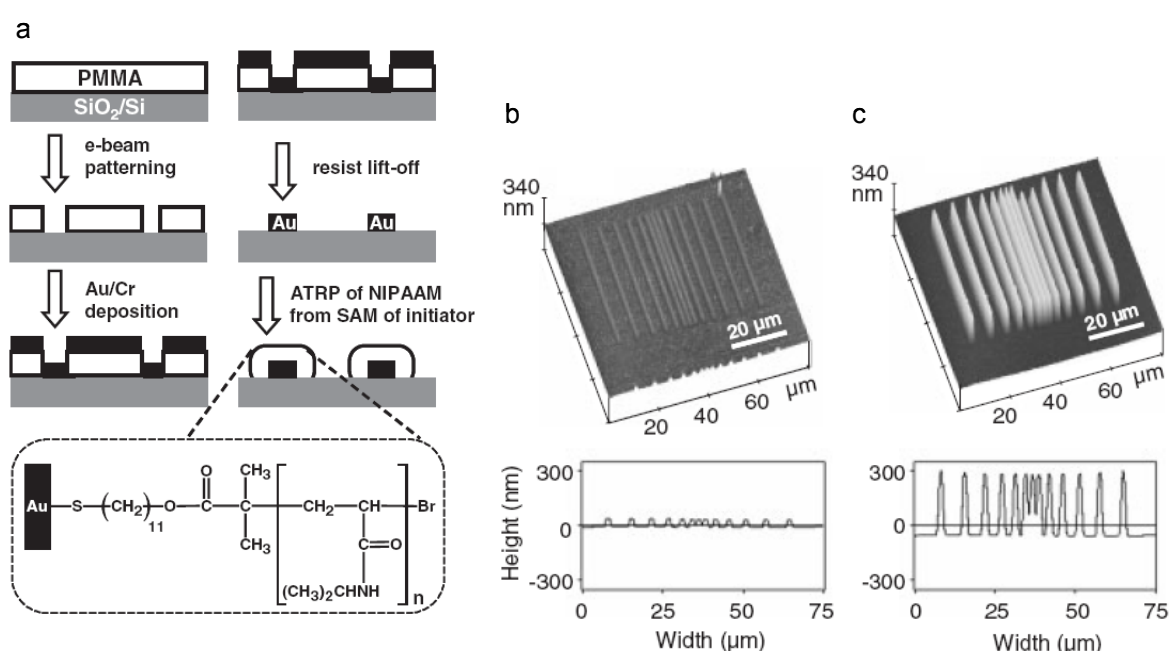


Figure 13. (a) Approach used by Zauscher and coworkers for the preparation of nanostructured poly(N-isopropylacrylamide) brushes. (b) AFM height image and cross section analysis of gold line pattern created by lift-off EBL. (c) Same substrate after surface-initiated ATRP from thiol bonded initiator on the gold patterns.¹⁴⁰

2.5.4.2 Chemical lithography

An ideal electron beam resist material should be thin and composed of small subunits to avoid forward scattering of the primary beam and permitting high resolution patterning. Furthermore, a very thin resist layer allows the use of low primary beam energies. These

criteria are fulfilled by SAMs. The smallest structures that have been generated by EBL on SAMs were approximately 5 to 6 nm.¹³⁹

*The reactions of aliphatic SAMs with low energy electrons have been investigated in great detail. In brief, electrons induce the cleavage of C-H bonds in aliphatic SAMs, which leads to orientational and conformational disorder of the chains, the desorption of material, and the formation of C=C double bonds in the fragments remaining on the surface (Figure 14).*¹⁴³

These reactions lower the layer stability of the irradiated regions and aliphatic SAMs are used as positive tone resists.

Grunze and coworkers^{144,145,146} investigated the electron beam induced damage in well-ordered aromatic biphenylthiol (BT) SAMs. The electron irradiation induced a C-H cleavage which is then followed by crosslinking between neighboring phenyl units (Figure 14). During this process, the crosslinked molecules maintain their orientation and only little material desorbs. Hence, the electrons generate a well-ordered and crosslinked monolayer.¹⁴³ The crosslinking reaction enhances the layer stability and aromatic SAMs can be used as positive tone resist.¹⁴⁴ Very recently, the preparation of freestanding nanosheets of the crosslinked biphenyl SAMs was demonstrated.¹⁴⁶

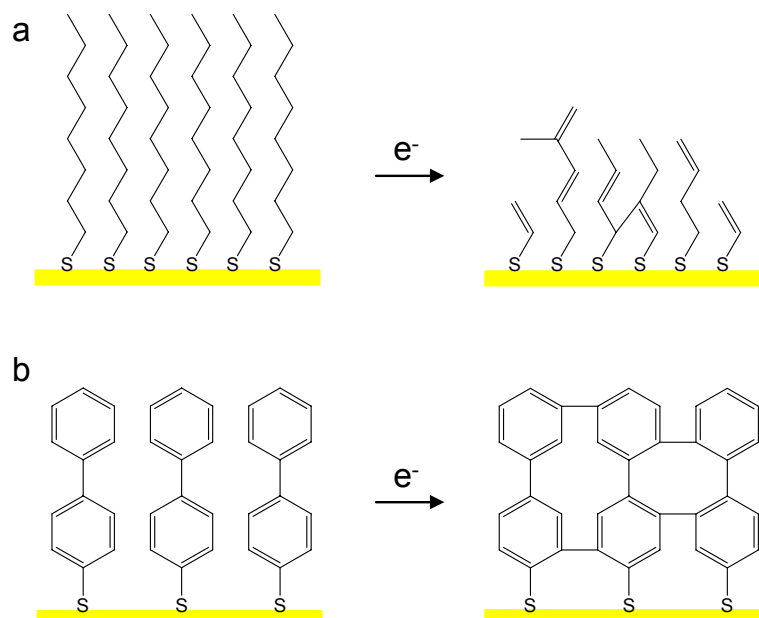


Figure 14. Electron beam induced modification of aliphatic (a) and BT (b) SAMs.

The electron beam induced reactions in different ω -functionalized biphenylthiol (methyl- (MBT), hydroxy- (HBT) and nitrobiphenylthiol (NBT)) SAMs was investigated (Figure 15). Cyganik *et al.*¹⁴⁷ demonstrated that the methyl group of MBT SAMs remains unaffected during the electron beam induced crosslinking reaction while Korniaikov *et al.*¹⁴⁸ showed that

the irradiation of HBT SAMs causes a partial OH abstraction. In NBT SAMs, the electron beam irradiation induces besides the crosslinking reaction of the biphenyl moieties, a simultaneous conversion of the nitro to the amino group, resulting in crosslinked 4'-amino-1,1'-biphenyl-4-thiol (cABT) SAMs.^{149,150} The electron beam induced conversion of one chemical function in another (here nitro to amine) is called electron beam chemical (nano)lithography (EBCL).

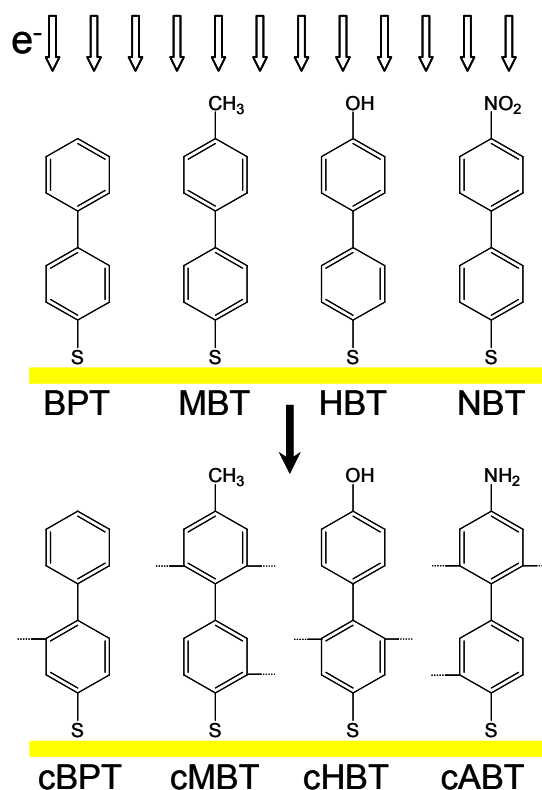


Figure 15. Electron beam irradiation of 4-mercapto-1,1'-biphenyl (BT), 4'-methyl-1,1'-biphenyl-4-thiol (MBT), 4'-hydroxy-1,1'-biphenyl-4-thiol (HBT) and 4'-nitro-1,1'-biphenyl-4-thiol (NBT) SAMs results into respectively crosslinked cBT, cMBT, cHBT and cABT (4'-amino-1,1'-biphenyl-4-thiol) SAMs.

Schmelmer *et al.*¹⁵¹ reported on the preparation of nanostructured polystyrene (PS) brushes with sub-50 nm resolution by a combination of the EBCL of NBT SAMs on gold and amplification of the primary structure by SIP of styrene (Figure 16).

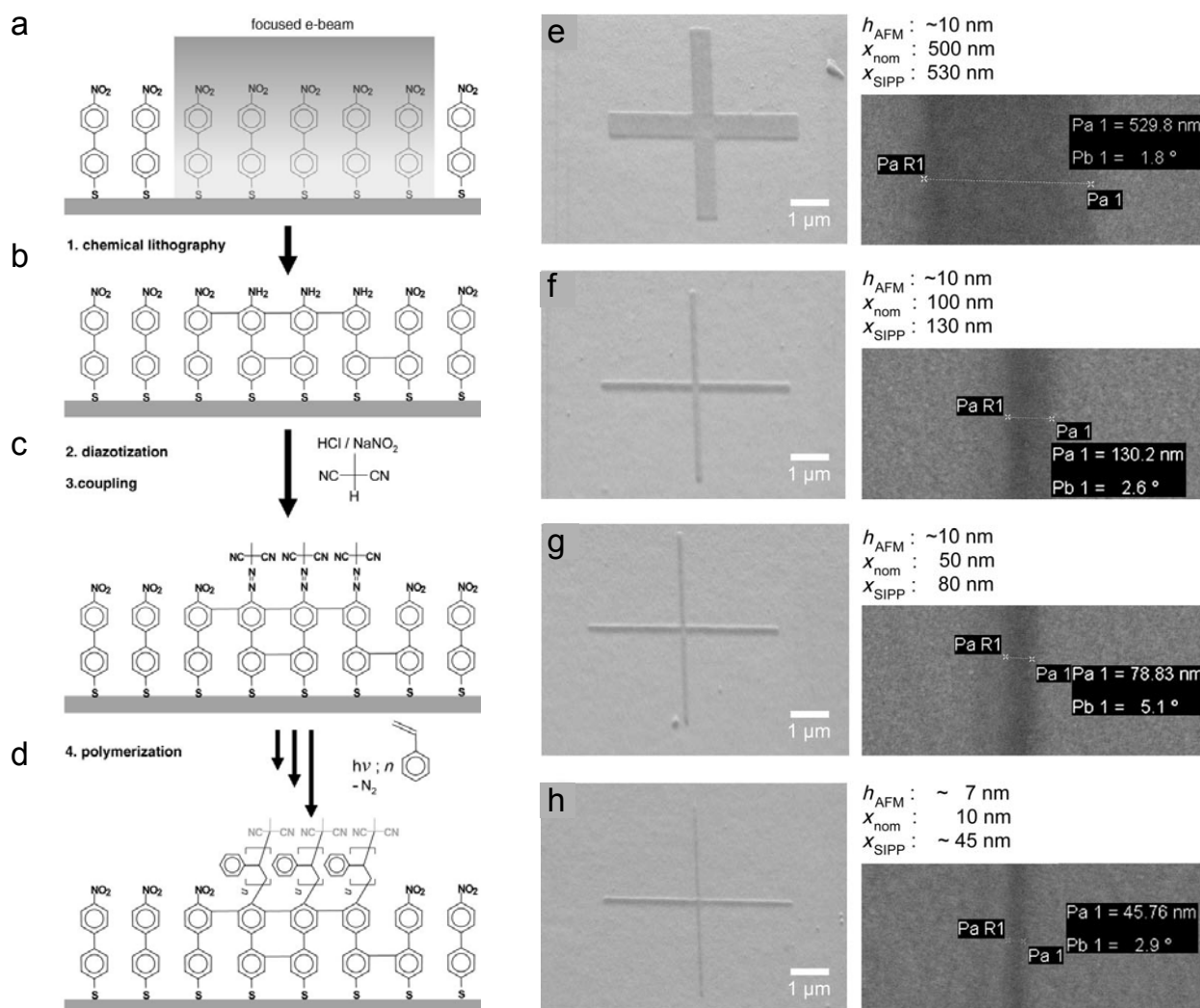


Figure 16. Left: reaction scheme. (a) Electron beam irradiation of NBT SAMs on gold with a focused electron beam. (b) Electron beam induced conversion of NBT in cABT (c) Diazotization and coupling with malonodinitrile gives a SAM that bears an asymmetric azo-initiator (cAMBT) (d) Thermal or photochemical SIP of styrene.

Right: SEM images of nanostructured PS grafts: individual crosses with initial (EBCL) line width (x_{nom}) of (e) 500, (f) 100, (g) 50, and (h) 10 nm and SEM analysis of the line width of the resulting structures created by surface-initiated photopolymerization (x_{SIPP}) along with the height of the PS structures determined by AFM (h_{AFM}).¹⁵¹

The terminal amino group of cABT was first diazotized and treated with methylmalonodinitrile to give a surface-bonded crosslinked monolayer bearing an azo-initiator. (4'-azomethylmalonodinitrile-1,1'-biphenyl-4-thiol, cAMBT). Phenyl diazenylalkylmalonodinitriles and their derivatives are suitable initiators for the radical polymerization of a broad variety of vinyl compounds in solution,¹⁵² as well as for SIP.¹⁵³ Azo-initiators, such as N,N-azobisisobutyronitril (AIBN), are commonly used for the initiation of the free radical

polymerization. By thermal or photochemical activation, AIBN decomposes into one nitrogen molecule and two 2-cyanoprop-2-yl radicals (Figure 17).

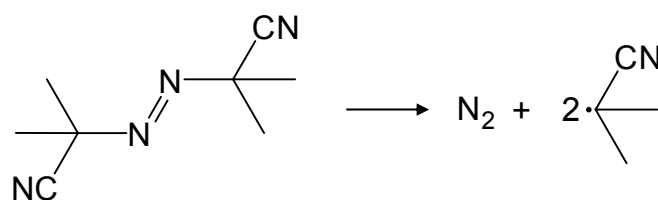


Figure 17. Decomposition of AIBN.

*In contrast to commonly used symmetric azo initiators, thermal or photoinitiated decomposition yields a highly reactive [...] phenyl radical and a free, stable malonodinitrile radical, which is not capable of initiating radical polymerization owing to its resonance stabilization (Figure 18). In other words, by the decomposition of the surface-bonded, asymmetric phenylazoalkyl initiator, the polymerization is only initiated at the surface and not by a cleaved free radical in solution, as is the case with dialkylazo initiators.*¹⁵⁴

The effect of the polymerization conditions on the increase of the polymer layer thickness as a function of the reaction time was investigated.¹⁵⁵ It was reported that the surface-initiated photopolymerization (SIPP) of styrene at room temperature leads to denser, more homogeneous and significantly thicker polymer grafts as compared to the thermally initiated SIP. Preliminary results demonstrated that the SIPP with UV-light of a spectral distribution between 300 and 400 nm ($\lambda_{\text{max}} = 350$ nm) leads to much thicker polymer brushes.

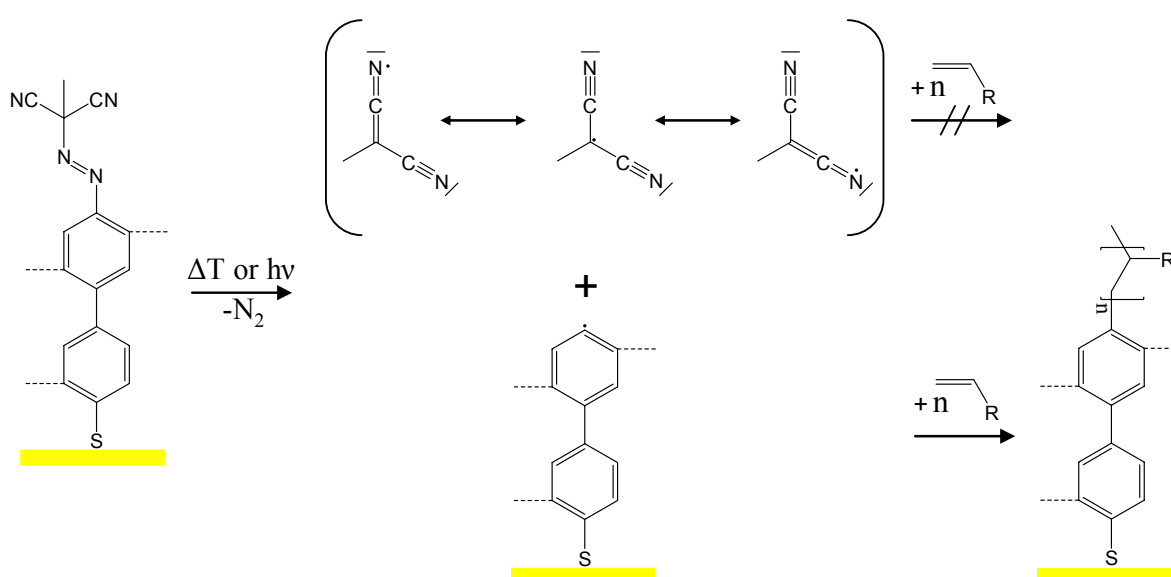


Figure 18. Decomposition of the surface-bonded azomethylmalonodinitrile initiator.

One major advantage of the EBCL approach for the preparation of structured polymer grafts (besides the unmatched resolution), compared to other SAM approaches, is that the electron beam induced crosslinking of the biphenyls enhances the stability of the monolayer due to the multiple adhesion sites of the entire layer. This allows the polymerization at elevated temperatures or with intense UV-light.¹⁵⁶

2.5.4.3 Electron beam carbon deposition

SAM techniques for the preparation of nanostructured surface functionalities have several drawbacks. First of all, new bifunctional molecules have to be prepared for every new substrate/surface functionality combination. Furthermore, the relative low thermal and chemical stability of commonly used SAMs systems does not allow polymerization or further functionalization of the grafted polymer chains under more demanding reaction conditions. Silane monolayers are prone to hydrolysis¹⁵⁷ and thiol bonded SAMs desorb or rearrange at elevated temperatures.¹⁵⁸

A well known resist free, single-step and direct-writing technique for the formation of stable surfaces coatings with a lateral resolution down to a few nanometers, is the electron beam induced deposition (EBD)¹⁵⁹. The EBD process uses an electron beam to decompose gaseous precursor molecules (e.g. metalorganic compounds) at low pressure (typically 10^{-6} Pa) and induces the formation of deposited structures on the radiated surface areas.

Highly crosslinked hydrocarbon deposits can be formed without the introduction of precursor molecules using a conventional scanning electron microscope (SEM) or an electron flood gun on various substrates. Residual hydrocarbon molecules present in the vacuum chamber, originated from the pump oil, are responsible the formation of these electron beam induced carbon deposits (EBCDs) (Figure 19). The growth rate of EBCDs is strongly dependent on the vapor pressure in the chamber, the exposure time (electron beam dosage), and the substrate. In order to accelerate the growth rate, different organic precursor molecules were deliberately introduced into the irradiation chamber.

It was found that the EBCD composition was completely independent of the organic precursor molecule.¹⁶⁰ EBCD has a composition close to $C_9H_2O_1$ with 90% sp^2 and 10 % sp^3 carbon and contains diverse functionalities including ketones, alcohol, aromatic C-H and aliphatic C-H groups.¹⁶¹ Recently, it has been demonstrated that EBCDs with a thickness of around one nanometer can block completely and selectively a wide range of chemical and electrochemical reactions, even when it is exposed to extreme reaction conditions. Due to the

high chemical inertness of EBCDs, it has been applied as negative resist material in various etching processes¹³¹ and as mask for electrodeposition.¹⁶²

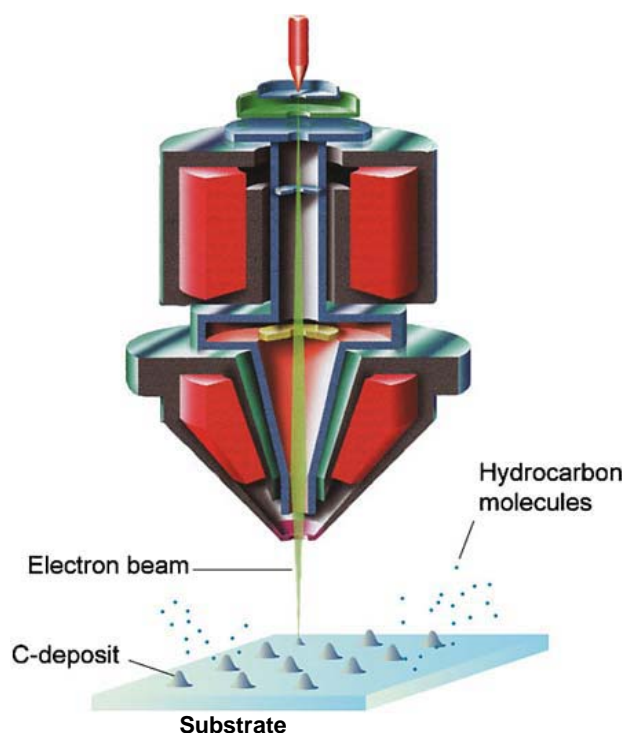


Figure 19. Principle of EBCD. The electron beam cracks the residual hydrocarbon molecules leading to the formation of a highly crosslinked carbonaceous deposit at the point of impact of the beam.¹³¹

2.6 Structural properties of nanopatterned polymer grafts

The influence of the polymer chain length (N) and the grafting density (σ) on the thickness of unstructured polymer grafts in the brush regime has been the subject of various experimental as well as theoretical studies.¹⁹ As discussed in chapter 2.1, the wet thickness of polymer brushes in good solvents scales as $h \sim N\sigma^{1/3}$ while the thickness of dry polymer brushes scales as $h_d \sim N\sigma$.

The first theoretical study about the structural properties of nanopatterned polymer grafts has been performed very recently by computer-simulation in the research group of Linse.¹⁶³ They found that the thickness of nanostructured polymer grafts in good solvents depends not only on the polymer length and grafting density, but also on the feature width (Δ). This is due to the fact that the length of the grafted macromolecules is already comparable to the dimension of the lateral structures (e.g. polystyrene with $DP = 2000$, which are very easily obtained by controlled or free radical polymerization, have a end-to-end length of approximately 500 nm)

and that polymer chains at the edges of the structures can extend to polymer free surface regions. This allows a conformational relaxation of the stretched chains and a decrease of the polymer layer thickness (Figure 20).

The model system used for this theoretical study was composed of a planar surface on which polymers were grafted onto a stripe with width Δ .

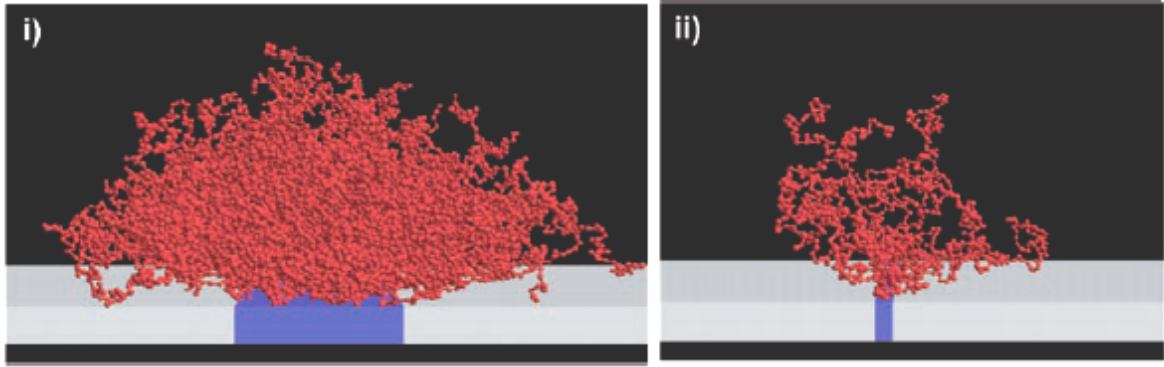


Figure 20. Images obtained by computer simulations of nanopatterned polymer grafts in good solvent. The polymer chain length is identical in the two structures. The feature width is ten times smaller in image (ii) than in image (i).¹⁶⁴

It was found that the maximum height of nanostructured polymer grafts in good solvents is given by

$$h(\Delta, N, \sigma) = N\sigma^{1/3}\bar{h}(\Delta/N) \quad \text{Eq. 10}$$

It is noteworthy that the term $N\sigma^{1/3}$ is identical to the scaling behavior of unstructured polymer grafts in the brush regime in good solvents. The influence of Δ appears as $\bar{h}(\Delta/N)$, where $\bar{h}(\Delta/N)$ is a universal function of its argument Δ/N with the limit 0 for $\Delta/N = 0$ and a finite value of order one for $\Delta/N \rightarrow \infty$.

The possibility of the chains to extend to polymer free surface regions results also in a widening of the structures. It was found that the excess width (w_{ex}) of the structures in good solvent can be expressed by following relation:

$$w_{\text{ex}}(\Delta, N, \sigma) = N\sigma^{1/2}\Psi(\Delta/N) \quad \text{Eq. 11}$$

where $\Psi(\Delta/N)$ is a universal function with a finite maximum value for $\Delta/N \rightarrow \infty$.

These theoretical studies were partially corroborated by recent experimental findings in the research group of Zauscher.¹⁶⁴ The nanopatterned polymer grafts were prepared by amplification of gold nanopatterns by surface-initiated ATRP from a thiol initiator, as described in chapter 2.5.4.1. In Figure 21, the polymer structure height in air and in aqueous solution is plotted as a function of the pattern feature width. Figure 21 shows that h is influenced by the pattern feature size for diameters up to 3 μm . This long-range phenomenon underlines the highly cooperative effect within dense polymer grafts.

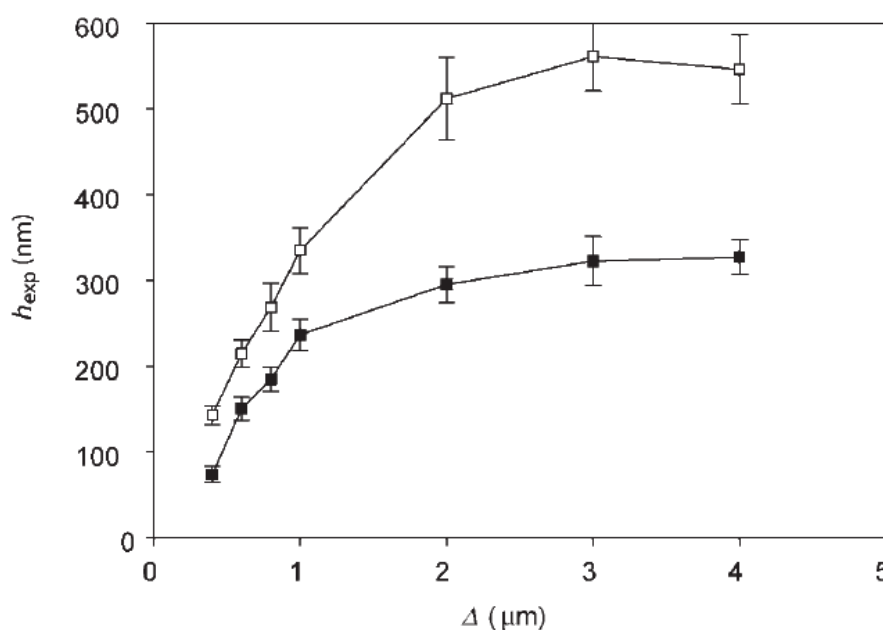


Figure 21. Brush height in air (h_{exp} , solid squares) and in aqueous solution (h_{exp} , open squares) at 25°C as a function of pattern feature width (Δ).¹⁶⁴

However, the experimental data obtained by AFM measurements of these polymer structures cannot be compared with the theoretical data obtained by computer simulations due to the following reasons: first of all, the SIP was not performed on a flat substrate (as in the theoretical model) but on gold features that were raised above the background by approximately 40 nm which results in additional lateral growth of polymer grafts.¹⁶⁴ In this perspective, the SIP on flat nanostructured surfaces prepared by EBCL (chapter 2.5.4.2) has a major advantage to study the structural properties of nanopatterned polymer grafts. The second experimental limitation is inherent to the AFM measurement itself. The necessary contact between the AFM tip and the polymer grafts distorts the polymer chains and thus the measured object.¹⁶⁵ Furthermore, the shape of the AFM tip plays an important role for the interpretation of the measurements results.¹⁶⁶

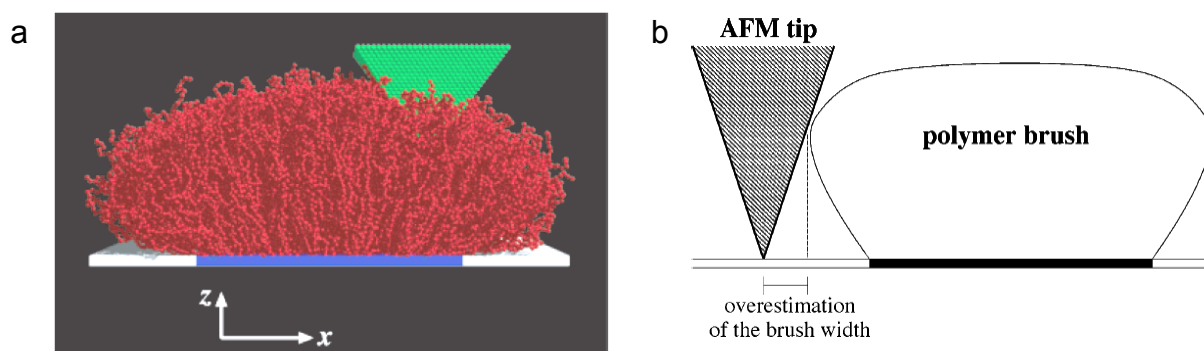


Figure 22. (a) Schematic representation of a pyramid representing the AFM tip (green) penetrating into nanopatterned polymer brushes (red). The polymer chains are grafted onto the blue region. (b) Schematic representation of the steric effect of the AFM tip resulting in a structure width overestimation.¹⁶⁷

The interaction between nanopatterned polymer brushes and a rigid pyramidal body representing an AFM tip has been investigated recently by Patra and Linse using molecular dynamics simulations.¹⁶⁷ This study showed that the thickness of the polymer structures measured by AFM is smaller than the effective structure height due to the penetration of the AFM tip into the polymer brush structure (Figure 22a). However this effect is almost eliminated when the polymer grafts are measured in the dry state.¹⁶⁸ Furthermore, the structure width is systematically overestimated due to the steric effect of the AFM tip (Figure 22b).

3 Purpose and objectives

The preparation of chemical and thermal stable, nanopatterned polymer layers, covalently attached to flat surfaces, has attracted considerable scientific and industrial attention. These new nanomaterials may find applications in various modern technologies. However, until now, only very few strategies have been developed for the synthesis of these materials.

Nanostructured polymer grafts with an unmatched lateral resolution have recently been prepared in the research groups of Jordan¹⁴⁶ and Zauscher¹⁴¹ by the combination of the electron beam lithography (EBL) and surface-initiated polymerization (SIP). The 2D locus of a grafting point for the SIP process is controlled during the EBL step. The main advantages of this approach are the following:

1. EBL is not restricted to any length (from sub-10 nm resolution with focused electron beams up to the macroscopic scale with electron flood guns).
2. Various SIP techniques have already been developed for the preparation of well defined and dense polymer grafts.

The first motivation of this work was to provide answers to different fundamental questions related to this two-step approach: What are the kinetics of SIP on nanostructured surfaces? What is the influence of the lateral feature size on the resulting polymer structure? What is the influence of the electron beam dosage or energy on the resulting polymer grafts? What is the molecular architecture of the grafted polymer chains? How do nanostructured polymer grafts behave in various environments? Etc.

The second purpose of this work consists in the development of new EBL/SIP-based strategies for the preparation of micro- and nanostructured polymer grafts with well a defined dimension, (three dimensional) architecture and (bio)-chemical functionality on various substrates.

4 Results and discussion

4.1 3D micro- and nanostructured polymer grafts on gold by EBCL and SIPP

Jordan and coworkers¹⁵¹ developed a four-step process for the preparation of micro- and nanostructured polymer grafts on gold (chapter 2.5.4.2):

1. Modification of a gold substrate with a NBT SAM.
2. Structuring of the NBT SAM by EBCL.
3. Modification of the amino group to an azo-initiator.
4. Surface-initiated photopolymerization (SIPP) by submerging the substrate in monomer and irradiating it with UV-light ($\lambda_{\text{max}} = 350 \text{ nm}$).

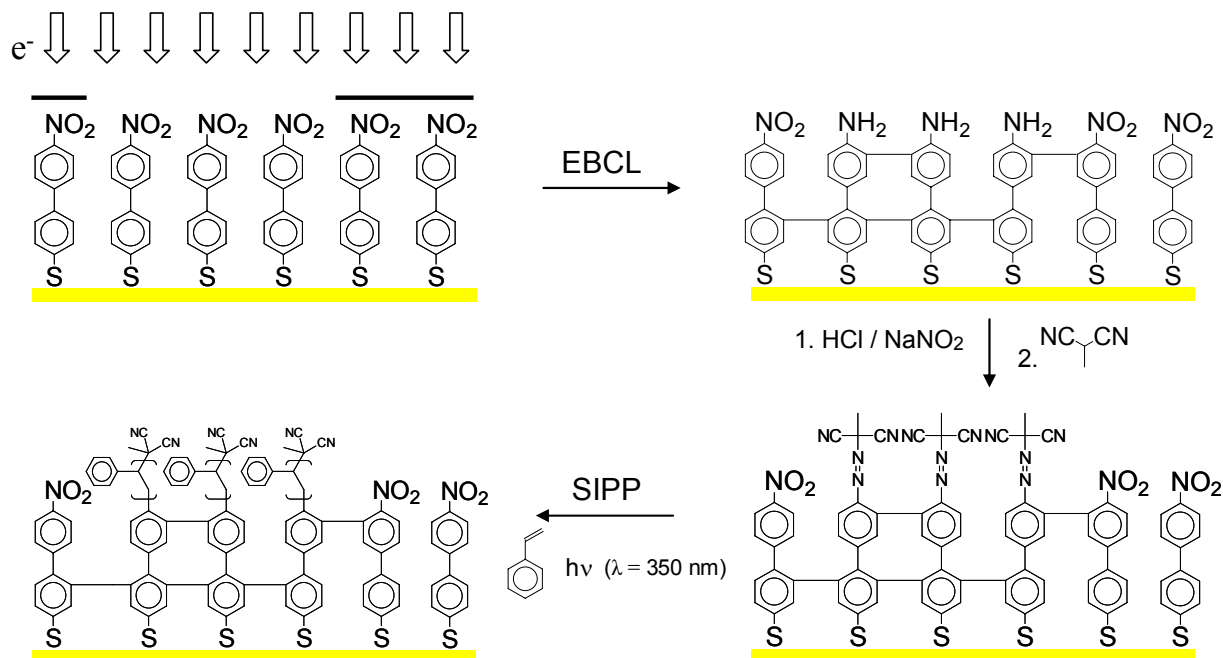


Figure 23. Preparation of structured polymer grafts by EBCL, diazotization and coupling of the amino group with malonodinitrile (resulting in cAMBT SAMs) and SIPP.

Preliminary results have demonstrated the potential of this approach for the preparation of nanostructured polymer grafts. In this work, the influence of different parameters on the

polymer layer morphology and topography was studied. This work has been performed in close collaboration with the research group of Prof. Dr. Michael Grunze at Universität Heidelberg.¹⁶⁹

4.1.1 *Ex situ* kinetic studies

The *ex situ* kinetic studies of the SIPP of styrene were performed on structured cAMBT SAMs. The samples were structured by EBCL using a flood gun in combination with a stencil mask with circular openings of 1 μm radius. Individual samples were used for each polymerization time (t_p). *Ex situ* study means that the substrates were taken out of the monomer after the SIPP step, intensively washed by Soxhlet extraction (to ensure that only chemically grafted PS remained on the surface), dried, and measured with AFM under ambient conditions.

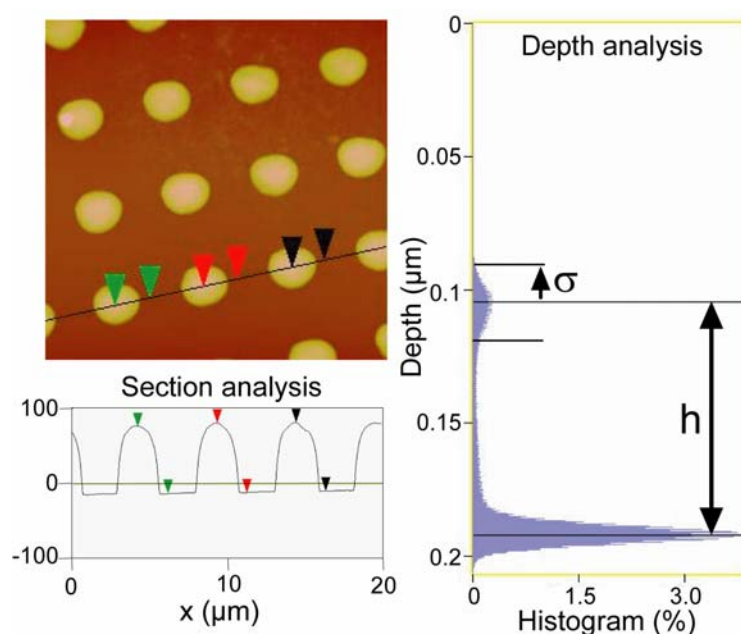


Figure 24. AFM scan ($20 \times 20 \mu\text{m}^2$), section analysis and depth analysis of patterned PS grafts (t_p : 10h). The depth analysis of the scan gives an average height (h) and error (θ) of the polymer layer thickness.

Figure 24 shows an AFM scan of a typical polymer structure obtained by this approach. Well defined polymer structures were selectively formed on the surface areas that were previously irradiated during the EBCL step.

The average height of the structures was obtained using the depth analysis routine of the software (see Figure 24). Two distinct populations of the height distribution were found (one for the bare substrate level and one for the polymer structure plateaus). The difference between the maximum of both distributions was taken as the average height of the polymer structures. The error, σ , was taken from the distribution originating from the polymer features. By this, the structure quality (height distribution of the structures) as well as surface roughness of the polymer features are taken into account.

In Figure 25, the height of the dry polymer structures (h_d) and error (σ) are plotted as a function of the irradiation time. Figure 25 reveals an almost linear relationship between h_d and the irradiation time up to ~ 200 nm after 20 h irradiation. Longer irradiation times did not result in a further increase of the layer thickness. Under these irradiation conditions, it was observed that the bulk monomer phase became highly viscous. This indicates significant polymer content in the monomer phase due to the self-initiated polymerization of styrene in solution under UV-irradiation (chapter 2.3.3).

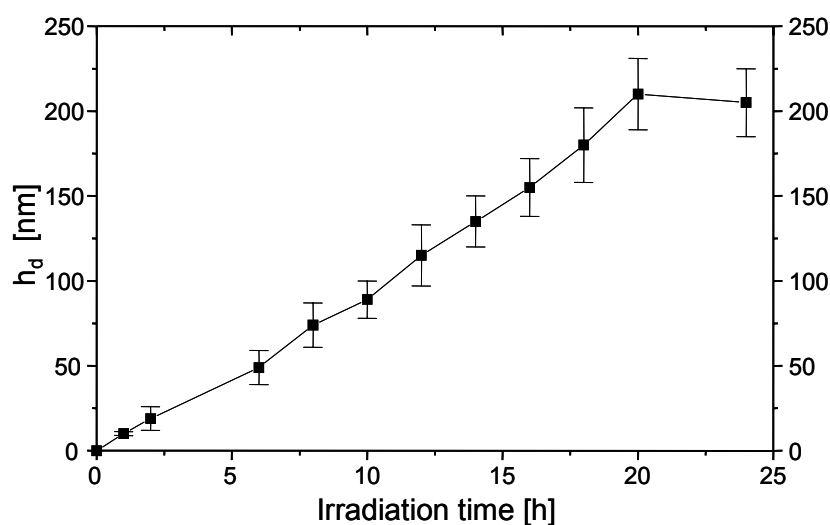


Figure 25. Dry polymer layer thickness, h_d , as a function of the irradiation time as measured by AFM on structured polymer grafts (1 μm radius, 4 μm spacing, EBCL at 50 eV; electron dosage: 60 mC/cm^2).

The limited film growth can be explained by:

1. The limited mass transport of the remaining monomer due to the viscosity increase.
2. Chain transfer reactions between a propagating surface-bonded polymer chain and molecules in the liquid phase (this kind of transfer reactions reduces the amount of surface-bonded reactive centers, see chapter 2.2.3).

The increase of the viscosity of the monomer phase avoids the possibility to perform experiments with an irradiation time over 30 h due to the solidification of the reaction mixture.

In contrast to the findings of Dyer *et al.*,^{170,171} observing a four-stage growth for the SIPP of styrene on unstructured AIBN-type initiators (Figure 26), no significant deviation from this linear thickness increase between 0 and 20 h could be observed. Our findings are similar to the findings of R uhe *et al.*¹⁷² also observing a linear layer thickness increase with the polymerization time. However, it is noteworthy that the experimental set-ups (light source, reaction vessels, irradiation geometry, etc.) as well as the initiator systems and the UV intensity (Dyer *et al.*: 1.6 mW/cm²; R uhe *et al.*: 30 mW/cm²; here: 9.2 mW/cm²) are different and may influence not only the growth rate but also the growth characteristics.

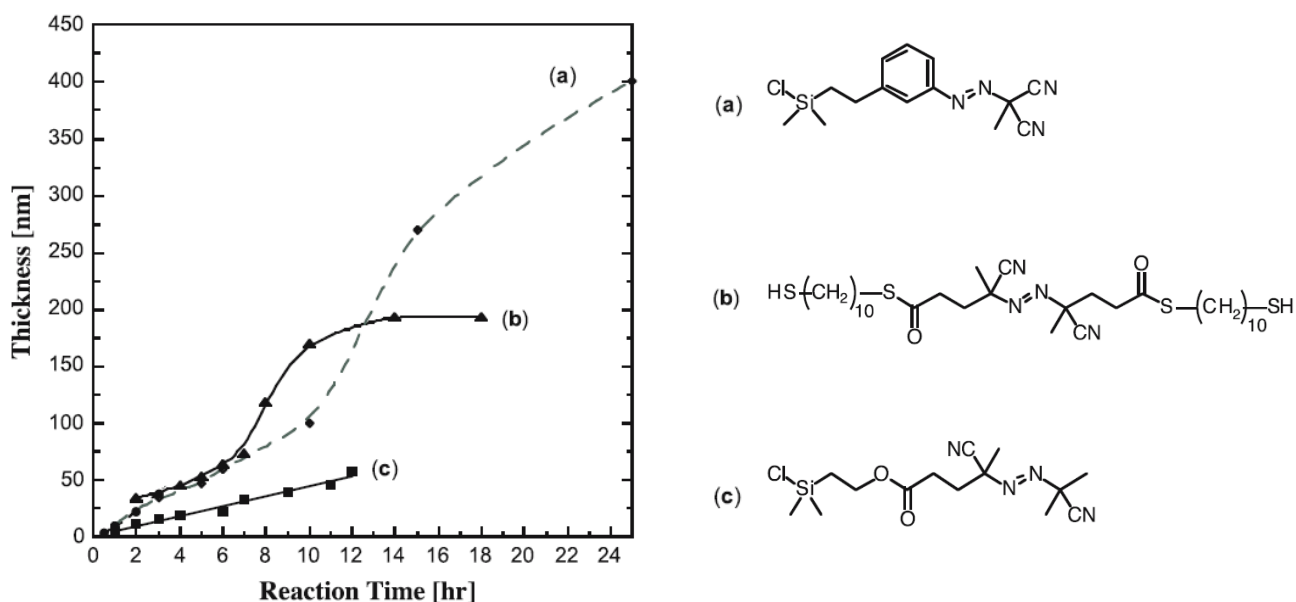


Figure 26. Growth (measured by ellipsometry) of PS grafts from various unstructured photoinitiating SAMs on gold (b) or silicon (a and c) substrates.¹⁷³

Besides the polymerization of styrene, this system can in principle be used for the SIPP of every vinyl monomer, which can be polymerized by free radical polymerization. E.g. methyl methacrylate (MMA) and acrylic acid (AA) were successfully tested. However, it was found that the thickness growth rate is specific for each monomer: after 3.5 h of irradiation, SIPP of MMA resulted in a polymer layer thickness of 120 nm (and 92 nm after 3 h) and after only 10 min AA gave a graft thickness of 290 nm.

In Table 1, the growth rates (k_g), expressed in $\text{mol}\cdot\text{cm}^{-2}\cdot\text{s}^{-1}$, for the different monomers are compared to the rate constant for the propagation reaction (k_p) for the free radical polymerization in solution, known from literature.¹⁷⁴ k_g is given by:

$$k_g = -\frac{dn_M}{dt} \cdot \frac{1}{S} \quad \text{Eq. 12}$$

where n_M is the monomer amount in solution (in mol) and S the surface area. k_g can be calculated from the measured thickness growth rate (dh_d/dt) using Eq. 1 and Eq. 12:

$$k_g = -\frac{dn_M}{dt} \cdot \frac{1}{S} = \frac{dh_d}{dt} \cdot \frac{\rho}{M_p} \quad \text{Eq. 13}$$

where M_p is the molar mass of one monomer unit and ρ the bulk density of the polymer (M_p is equal to the molar mass of the free monomer in the case of vinyl polymerization). The dh_d/dt -value for styrene was calculated by a linear fit of the data points presented in Figure 25. Since a systematic kinetic study was not performed for MMA and AA, the dh_d/dt -values were calculated from only 2 data points for MMA and 1 data point for AA. It can be observed in Table 1 that the k_g values correlate roughly with k_p .

monomer	dh_d/dt [$\text{nm}\cdot\text{h}^{-1}$]	ρ [$\text{g}\cdot\text{cm}^{-3}$] ¹⁷⁴	k_g [$\text{mol}\cdot\text{cm}^{-2}\cdot\text{h}^{-1}$]	k_p [$\text{mol}\cdot\text{l}^{-1}\cdot\text{s}^{-1}$]
Styrene	9.8	1.05	0.099	44
MMA	33.8	1.19	0.40	143
AA	1740	1.15	28	6600

Table 1. Comparison between k_g for the SIPP and k_p for the free radical polymerization in solution at room temperature from literature¹⁷⁴ for styrene, MMA and AA.

The knowledge of the dh_d/dt -values allows to control the structure thickness by varying the polymerization time.

It should be noted here that in contrast to surface-initiated living polymerization, the increase of polymer layer thickness by a longer polymerization time does not mean that the length of the grafted polymer chains increase in the case of free radical SIP. In (surface-initiated) free radical polymerization, the initiation in the rate determining step (RDS) and the propagation step is extremely fast (see chapter 2.2.3), e.g. a PS chain of more than 1000 monomer units is

obtained at room temperature in less than one second.¹⁷⁴ The increase of polymer layer thickness is thus attributed to an increase of the grafting density (and a linear polymer layer thickness increase means a linear grafting density increase). In the case of living polymerization, the propagation step is the RDS (a linear polymer layer thickness increase means here a linear increase of the average molecular weight of the grafted polymer chains). In this light, the here reported good control of the layer thickness by a free radical polymerization technique becomes even more surprising.

4.1.2 Influence of the electron dose on the polymer layer thickness

In some experiments deviations in the morphology of individual polymer structures were noticeable, i.e. that the polymer layer thickness varies to some extent within a single pattern feature. Instead of the regular dots (Figure 27a), *soft-boiled egg* shapes (Figure 27b) were observed.

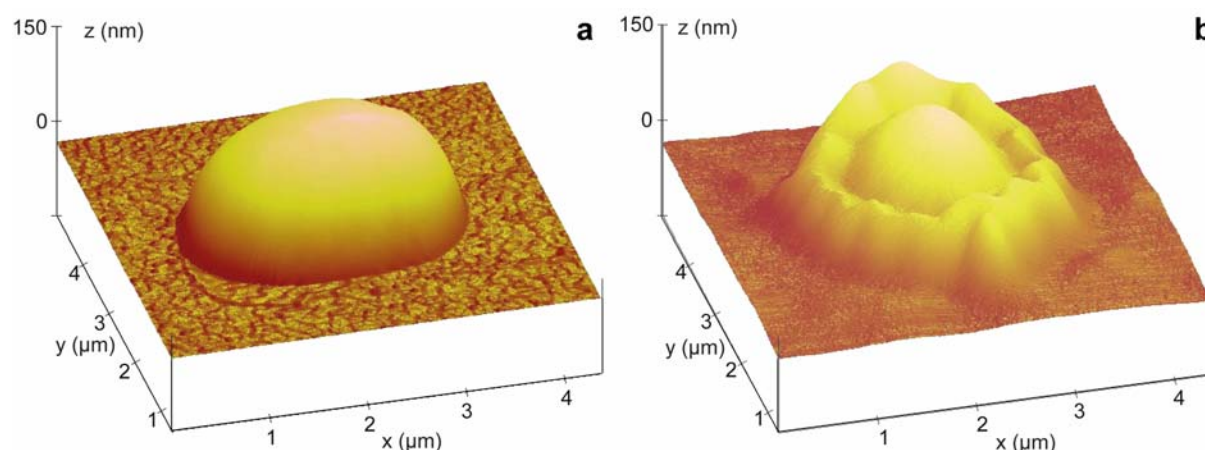


Figure 27. AFM scans of polymer dots. (EBCL: 1 μm radius, 50 eV, 60 mC/cm^2 ; SIPP of styrene). (a) Structure obtained after homogeneous electron irradiation of an NBT SAM. (b) PS dot with a *soft-boiled egg* shape caused by inhomogeneous electron irradiation.

Closer inspection revealed that these complex polymer structures only appeared where the stencil mask, used during the EBCL process, was not in direct contact with the sample surface (Figure 28). This resulted in inhomogeneous electron irradiation of the NBT SAM. The existence of such interference has been previously demonstrated by X-ray absorption spectromicroscopy.¹⁷⁵

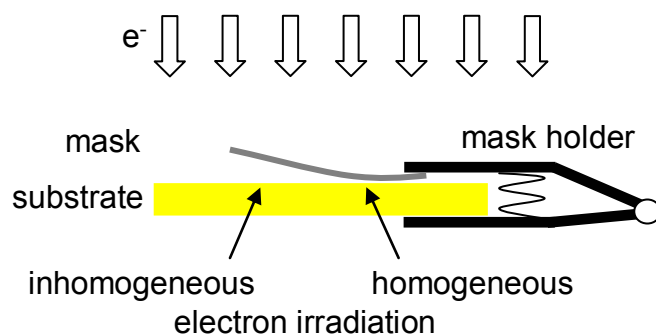


Figure 28. Schematic representation of the experimental setup used during EBCL process. Due to the experimental setup, a considerable gap between the flexible stencil mask and the substrate can arise.

This observation was the first indication of a direct dependence between the polymer layer thickness and the locally applied electron dosage.

The influence of the electron dosage during the EBCL step on the thickness of the resulting polymer grafts was studied on a *gradient surface* on which the electron dose was continuously increased within a defined area instead of irradiation of a large number of individual areas with different irradiation doses. Apart from being faster, this approach guarantees that all further reaction parameters remain constant.

The preparation of a $10 \times 50 \mu\text{m}^2$ gradient structure was performed by Dr. Küller in the lab of Prof. Grunze using a focused electron beam of a scanning electron microscope (SEM) coupled to a pattern generator (direct e-beam writing). The pattern generator allows the creation of almost any imaginable two dimensional structure. Furthermore, the applied electron dosage can be controlled with in each structure. For a $10 \times 50 \mu\text{m}^2$ gradient, a writefield of 100 parallel $10 \times 0.5 \mu\text{m}^2$ lines was created. The lines were *written* with linearly increasing electron dosage from 0 to 115 mC/cm^2 .

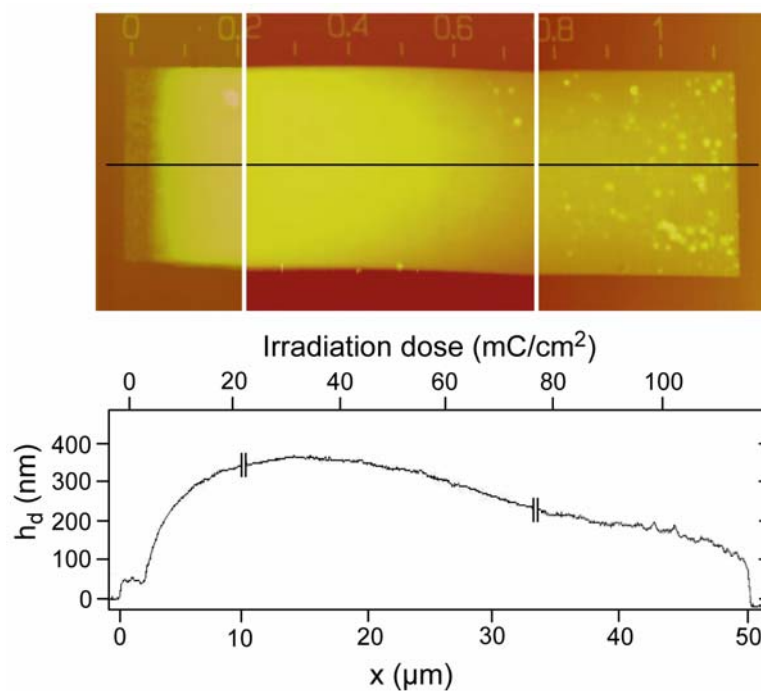


Figure 29. AFM image and height profile of a PS gradient structure. The image was recorded by 3 individual scans for better resolution. The electron dosage increases linearly from 0 to 115 mC/cm² going from left to right, as indicated by the written scale bar visible at the top of the AFM image ($t_p = 16.5\text{h}$).

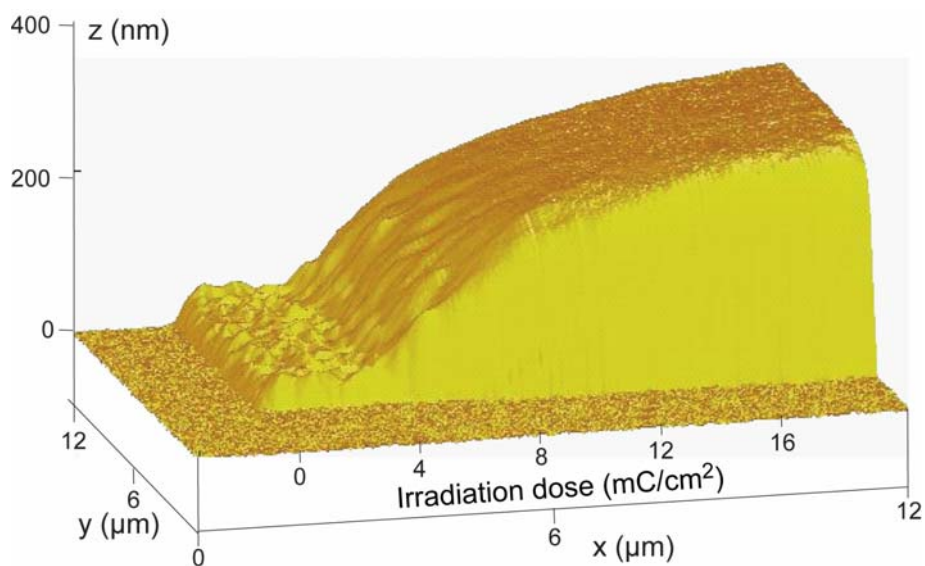


Figure 30. Three dimensional representation of the AFM height image of the gradient shown in Figure 29 for a dose range of 0 - 20 mC/cm².

Figure 29 shows an AFM image of the polymer structure after the SIPP of styrene ($t_p = 16.5\text{h}$) and the corresponding height profile along the gradient direction. Figure 30 shows a detailed

view of the same structure at the onset of the gradient prepared with electron doses from 0 to 20 mC/cm².

Obviously, the height of the polymer grafts can be directly controlled by the applied electron dosage for the conversion of NBT to cABT within the EBCL step. As outlined in Figure 23, the consecutive conversion by diazotization of surface-bonded amino group and coupling of methylmalonodinitril into the azo-initiator (cAMBT) is only possible for the reduced cABT and only there the SIPP can occur. In the polymer brush regime, the dry brush layer thickness, h_d , scales not only with the degree of polymerization but also with the grafting density (Eq. 1). Since the reaction conditions were the same for the entire gradient, the increase of the polymer layer height can be attributed to the continuous increase of the grafting density. EBCL thus provides a direct tool to control not only the 2D locus of a grafting point for the SIP process but by the variation of the locally applied electron dosage, the grafting density can be directly controlled and thus adds a third dimension in the morphology control of structured polymer grafts.

4.1.2.1 Correlation between the polymer layer thickness and the amino surface concentration

Based on the results presented in the previous section, it can be assumed that there is a direct relation between the thickness of the polymer structures and the amino surface concentration created during the EBCL process. In order to control this hypothesis, the height profile in Figure 29 was compared with the available literature about EBCL. In 2000, Grunze and coworkers¹⁷⁶ studied the nitro to amino conversion as a function of the applied electron dosage by *ex situ* XPS (Figure 31) measurements. Figure 29 shows that the height of the polymer gradient is not a linear function of the locally applied electron dose but follows, after an onset between 0 and 5 mC/cm², an exponential function. The onset, which is clearly visible in Figure 30, was caused by the fact that the electron irradiation dwelltime had to be optimized for high doses (up to 115 mC/cm²). Low electron doses (< 5 mC/cm²) could therefore not be controlled accurately if a maximum final dose of 115 mC/cm² was applied within the same irradiation process.

The exponential dependence agrees with the exponential nitro to amino conversion observed by Grunze and coworkers. Moreover, they observed a full nitro-to-amino conversion at about ~ 35 mC/cm². This coincides nicely with the dose corresponding to the maximum height of the polymer layer of $h_d = 380$ nm in the gradient (Figure 30).

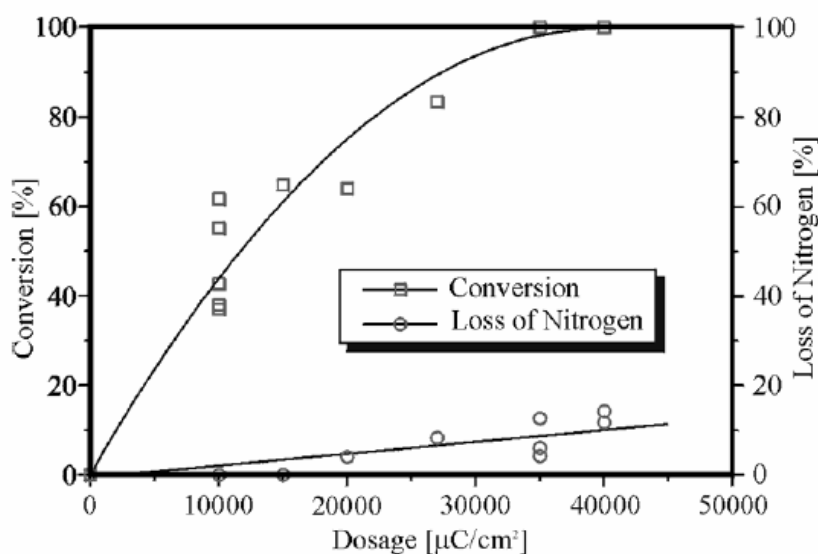


Figure 31. *Ex situ* XPS analysis of the N1s spectra of the NBT SAMs exposed to 50 eV electrons. Conversion of nitro to amino groups (top; amount of NH₂ versus total present amount of nitrogen) and loss of nitrogen relative to the amount of sulfur (bottom) with increasing electron dosage.¹⁷⁶

A similar thickness dependency has also been reported by the same research group, in earlier experiments on chemical coupling of small organic molecules to the cABT amino groups, created by EBCL with different electron doses.¹⁵⁰ Also here, the thickest structures were observed on the NBT areas irradiated with a dosage between 30 to 50 mC/cm² and primary electron energies of 2.5 keV. The height increase as a function of the electron dosage, $h(D)$, could be fitted exponentially by

$$h(D) = h_0[1 - \exp(-D/D_0)] \quad \text{Eq. 14}$$

with h_0 as the maximum measured height, D the applied electron dose, and D_0 as a measure for the process efficiency. However, the data in reference 176 (Figure 31) shows a relatively large scattering because of the experimental difficulties accompanied with an *ex situ* method (e.g. because of surface contamination) and the direct correlation between the amino surface concentration and polymer layer thickness cannot be concluded based on these data.

In order to investigate this process with more reliable and detailed data, the electron induced conversion of NBT to cABT was studied again in the research group of Prof. Grunze but this time with *in situ* XPS measurements. This means that the electron beam conversion and the XPS measurements were performed in the same vacuum chamber, which considerably reduces possible contaminations. Unfortunately, the experimental setup did not allow the

irradiation with 3 keV electrons (which were used in the SEM pattern generator setup), but with 10 eV electrons. The dose was varied between 0 and 350 mC/cm². Similar to the previous results,¹⁷⁶ the N1s spectra of the irradiated NBT SAMs exhibited the characteristic emission related to the nitro group and irradiation-induced amino group. The respective intensities as well as the total intensity of the N1s signal are presented as function of the irradiation dose in Figure 32a.

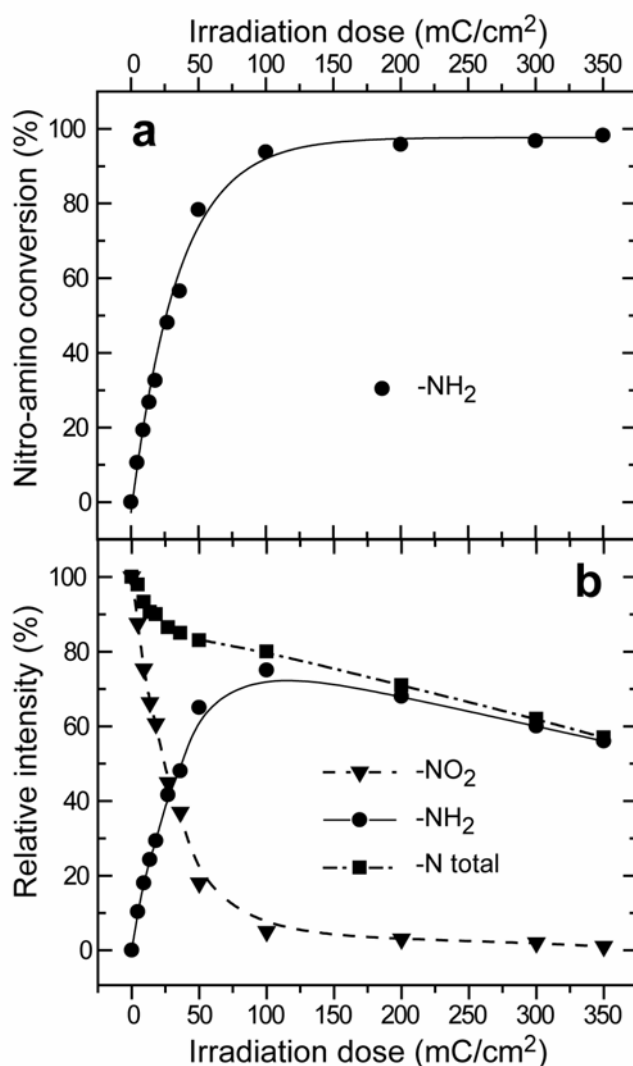


Figure 32. Results of the analysis of the N1s XPS spectra of the NBT SAMs exposed to 10 eV electrons. (a) The intensities of the N1s emissions related to the nitro and amino groups as well as to the total N1s intensity as functions of irradiation dose. (b) The extent of the nitro and amino group derived from the above intensities and the Au4f XPS spectra were used as reference.

Figure 32a clearly shows that the electron dose dependent conversion of the nitro group of the NBT monolayer to the amino group of the resulting cABT SAM follows an exponential function. This corroborates the hypothesis that the polymer layer thickness is directly dependent on the amino group surface concentration.

However, comparing these *in situ* results with previously reported data reveals more about the dependence of the nitro to amino conversion on the electron energy of the used irradiation. While the complete NBT to cABT conversion is achieved at an electron dosage of ~ 35 mC/cm² at energies of 50 eV (Figure 31), an irradiation dosage of ~ 120 mC/cm² is needed for the same conversion at electron energy of 10 eV (Figure 32). This can be explained by the fact that not only the primary, but also secondary electrons with energies of 5-10 eV contribute to the conversion. Primary electrons with a higher kinetic energy create a larger amount of secondary electrons and are therefore more efficient for the conversion than electrons of 10 eV energy, which create only a small number of secondary electrons.

By comparing the XPS N1s signal with the Au4f signal, it was observed that along with the nitro to amino conversion, the total nitrogen content decreased with increasing electron dose. This observation is not in contradiction with existing literature: although aromatic SAMs are stable under electron irradiation (chapter 2.5.4.2), it was already observed that terminal functions of biphenyl and terphenyl SAMs are decomposed and desorb from the monolayer at high electron doses. This was recently reported for thiol functionalized terphenyl SAMs¹⁷⁷ and was also previously observed for NBT films.¹⁷⁶ This is attributed to the irradiation induced desorption of the 4'-function and was found to be about 11 % of the total nitrogen content at full nitro conversion (Figure 31).

Also in this *in situ* study, a slow but steady decrease of the total nitrogen content was observed and at a dosage of 350 mC/cm², the loss of the surface functionality was about 20%. (Figure 32b).

The decrease of the total nitrogen content means that above 30-35 mC/cm², the surface density of initiators for the SIP decreases and results in a lower polymer grafting density.

Indeed, the section analysis in Figure 29 shows a slow and nearly linear decrease of h_d from 380 nm at 30 mC/cm² to 110 nm at 115 mC/cm².

These results support the hypothesis that the polymer layer thickness is directly dependent on the amino group surface concentration which controls the grafting density. However, it must be noted that the possibility that the kinetics of SIPP varies with the grafting density cannot be excluded without measuring the molar masses of the grafted brushes. This issue has already been pointed out by Genzer *et al.*¹⁷⁸ for the polymerization of acryl amide by ATRP on initiator gradient substrates. However, the presented data indicated that the degree of polymerization of the grafted polymers was not significantly influenced by the local initiator concentration.

In contrast to this, another study¹⁷⁹ reported for the surface-initiated ATRP of HEMA on flat substrates that the polymerization rate decreased at higher initiator density. The authors suggest an increase of the bimolecular termination reactions due to the high local radical concentration at the surface. However, as mentioned here above, free radical and controlled radical SIP cannot be compared directly.

4.1.3 Influence of initial structure widths and electron beam dosage

It has been shown by Zauscher and coworkers¹⁶⁴ that the thickness of structured polymer grafts is not only influenced by the polymer grafting density and the degree of polymerization, but also by the initial structure size (chapter 2.6). In this perspective, it can be argued that the size and shape of a gradient structure, such as in Figure 29, may influence the dependency between the polymer layer thickness and the electron beam dosage.

For a more quantitative study of the effect of the electron beam dosage as well as the structure size on the resulting polymer topography, an array of isolated structures was created varying the irradiation dosage from 5 to 100 mC/cm² as well as the feature diameter from 50 to 1000 nm. This approach has two major advantages compared to the gradient structure in Figure 29:

1. Proximity effects that appear in densely patterned regions are minimized: when an electron beam is incident on a material, the electrons are not destroyed but are scattered both elastically (with angle changes but without energy loss) and inelastically (with energy loss). The elastically scattered electrons generally have sufficient energy to travel a large distance. Back-scattered electrons often cause features written by electron beam lithography to be wider in densely patterned areas.¹⁸⁰

2. The local polymer layer thickness in a continuous gradient pattern is always influenced by the polymer grafting density in the vicinity. The study of isolated patterns gives a more precise relationship between the patterning parameters and the resulting polymer topography.

Figure 33 shows an overview of the resulting polymer structures. For better resolution, the height and width of the individual dots were determined by detailed AFM scans, such as shown in Figure 33b. In Figure 34, the maximum dry height of the polymer dots is plotted as functions of the electron dosage for structures with different diameters.

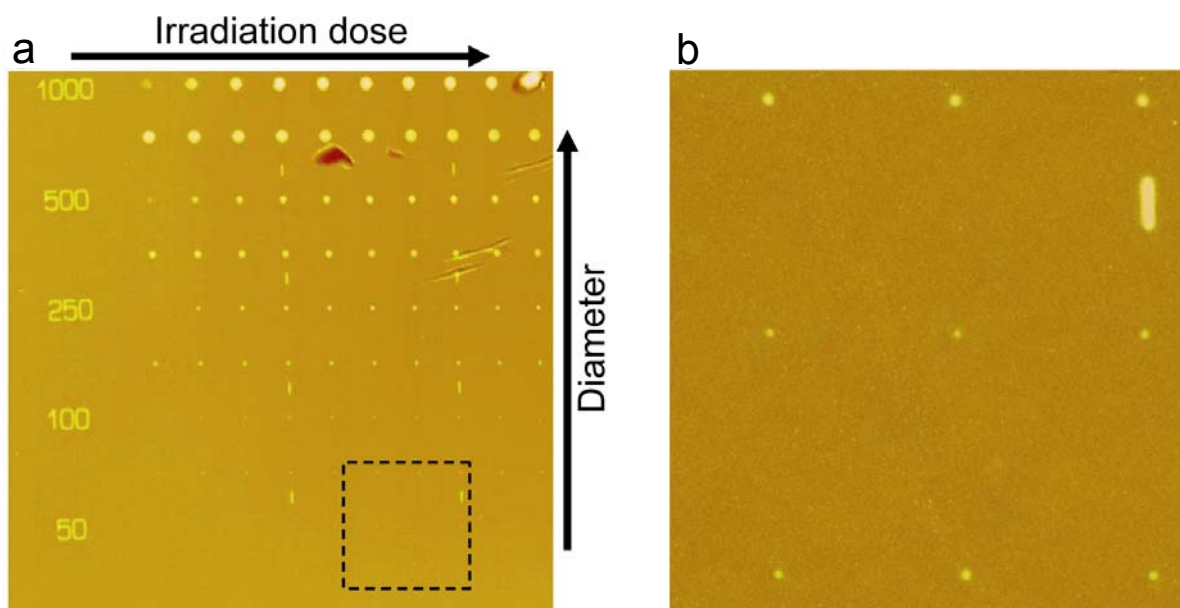


Figure 33. (a) AFM image ($50 \times 50 \mu\text{m}^2$) of an array of structured PS grafts by the SIPP of styrene ($t_p = 16.5\text{h}$) on dots with a diameter of 1000, 500, 250, 100 and 50 nm and an electron irradiation dose of 5 to 100 mC/cm^2 . The visible stripes were intentionally created for orientation within the array. (b) A detailed second AFM scan of $12 \times 12 \mu\text{m}^2$ area indicated in (a).

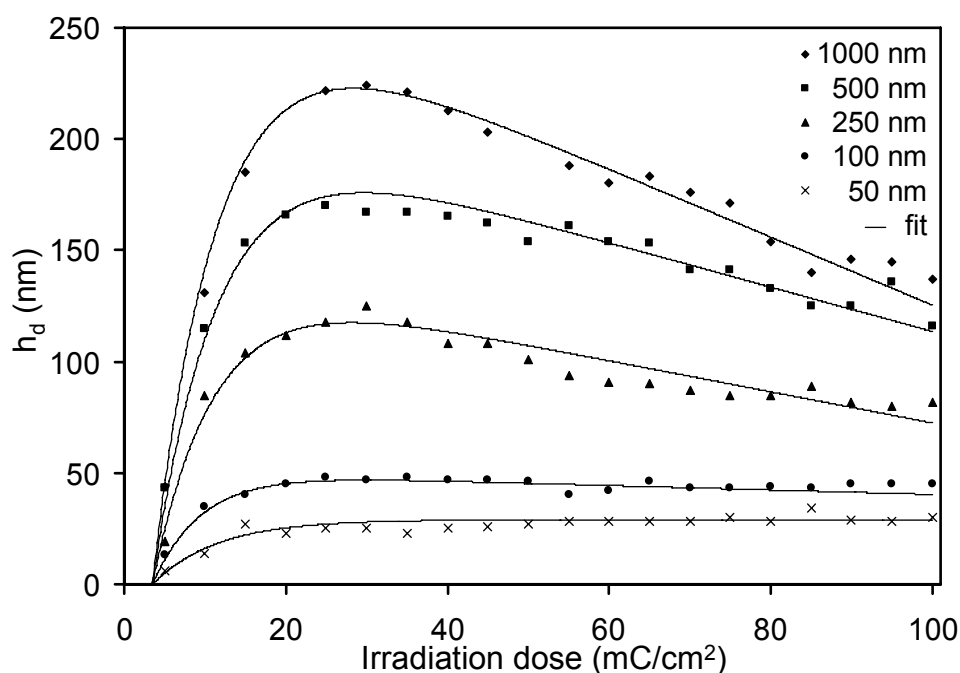


Figure 34. Maximum dry height (h_d) of the polymer dots in air as a function of the electron dosage for dots with diameters of 50, 100, 250, 500 and 1000 nm. The fit function is $h_d(D) = h_{d0}[1 - \exp(-D/D_0)] - D \cdot S$. Used values: see Table 2.

At first view, Figure 34 shows qualitatively, the same dependence between the polymer layer thickness and the electron dosage as the gradient structure in Figure 29 (exponential thickness increase between a dosage of 0 and 30 mC/cm² and a linear thickness decrease above 30 mC/cm²). The polymer layer thicknesses in Figure 34 can be fitted using the function

$$h_d(D) = h_{d0}[1 - \exp(-D'/D_0)] - D' \cdot S \quad \text{Eq. 15}$$

where h_{d0} is the structure height at maximum NBT to cABT conversion and D' the onset corrected dosage. The fit function is a combination of an exponential term ($h_{d0}[1 - \exp(-D'/D_0)]$), which describes the electron radiation induced conversion of the nitro to amino group (Eq. 12) and a linear term ($-D' \cdot S$), which describes the radiation induced damage of the monolayer. D_0 is the efficiency factor of the process: it describes not only the efficiency of the exponential NBT to cABT conversion but also the effect of the NBT to cABT conversion on the polymer layer thickness increase. S is the stability factor of the monolayer. The values used in the fit function for different feature diameters are listed in Table 2.

d (nm)	D' (mC/cm ²)	h_{d0} (nm)	D_0 (mC/cm ²)	S (cm ² /mC)
1000	D-3.5	273	8	1.53
500	D-3.5	210	8	1
250	D-3.5	140	7.5	0.7
100	D-3.5	50	6	0.1
50	D-3.5	29	8	0

Table 2. Values used for the fit functions (Eq. 15) in Figure 34.

In all fit functions, the same onset corrected dosage could be used. Furthermore, the efficiency factor is very similar for the different feature diameters. This indicates that the effect of the NBT to cABT conversion was identical on the relative polymer layer thickness for all structure sizes. This means that the influence of the grafting density on the structure height is independent of the structure size. This behavior is in agreement with the theoretical study performed by Parta and Linse, discussed in chapter 2.6. They found that the influence of the grafting density on the polymer layer thickness is independent of the structure width (Eq. 10). However, Figure 34 also shows that the thickness decrease between 30 and 100 mC/cm², described by the stability factor S in Table 2, depends on the structure diameter (e.g., for dots with a diameter of 1000 nm, h_d decreases by 39 % between 30 and 100 mC/cm² and only by

4.3 % for dots with a diameter of 100 nm). This can have two distinct causes: the radiation induced damage of the monolayer is faster for larger structures (e.g. due to proximity effects) or the decrease of the grafting density (due to the radiation induced damage) on the polymer structure height is more pronounced for larger structures. However, no experimental evidences support either of these two hypotheses.

The good correlation between the polymer layer thickness and the surface amino group concentration was demonstrated by Michael Zharnikov in a unified plot of the normalized polymer layer thickness and normalized amino group surface concentration (Figure 35). This demonstrates that the EBCL controls the local initiator density and in consequence, the grafting density and the height of the resulting polymer grafts. The correlation is good for structures with a diameter of 250, 500 or 1000nm (because of the normalization, the data scattering of the height values increases for layer thicknesses below 30 nm).

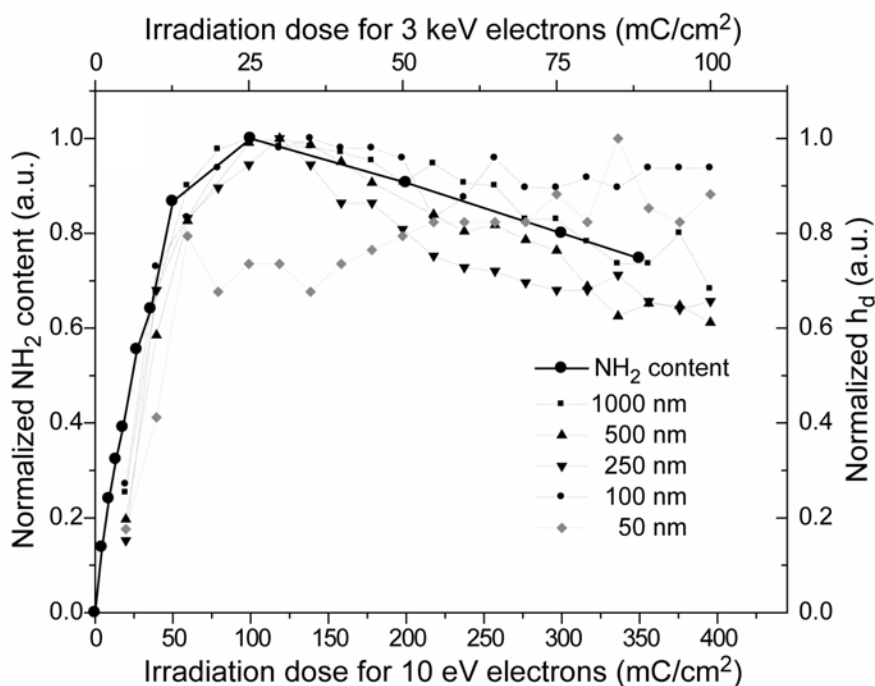


Figure 35. Unified plot of the normalized h_d and normalized amino group content vs. the irradiation dose for all structures.

Figure 34 also shows that for polymer dots created under identical conditions, the dry polymer layer thickness is strongly influenced by the lateral feature size. This effect is illustrated in Figure 36.

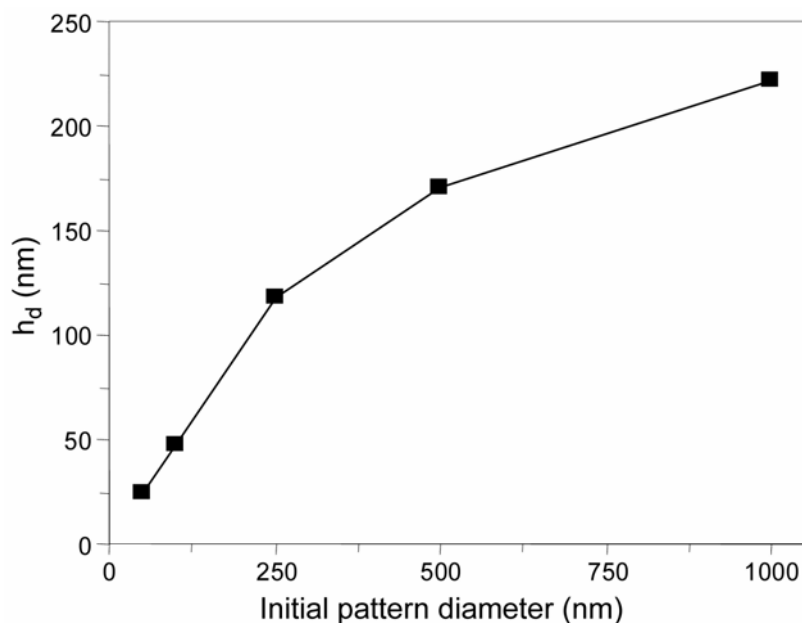


Figure 36. Maximum height of the polymer dots in air as a function of the initial pattern size (dot diameter). (dose = 25 mC/cm²; t_p = 16h).

This behavior is in agreement with recent work done in the research group of Zauscher and is due to the fact that polymer chains at the edges of the structures can extend to polymer free surface regions, as discussed in chapter 2.6 (see Figure 21). This leads to less chain crowding and, thus, less chain stretching in small structures.

The possibility of the grafts to extend to polymer free surface regions results also in a widening of the structures. In Table 3, the width at half maximum height ($w_{1/2}$) of the dot structures created under identical conditions (measured by AFM) are compared to the original feature diameter (d).

d [nm]	$w_{1/2}$ [nm]	$w_{1/2} - d$ [nm]
1000	1099	99
500	600	100
250	337	87
100	209	109
50	156	106

Table 3. Lateral dimensions of nanopatterned PS grafts compared to the original feature diameter created by EBCL (d = diameter of the pattern created by EBCL, $w_{1/2}$ = width at half maximum height of the polymeric structures).

The values in Table 3 show that the lateral broadening of the structures is with about 100 nm nearly independent of the pattern diameter. This result is in contradiction with computer simulations performed by Parta and Linse (Eq. 11 in chapter 2.6). However, the broadening of structured polymer grafts was never measured before and cannot be compared with available experimental data from literature. This effect could for instance not be measured accurately by Zauscher and coworkers due to the fact that they performed SIP on nanostructured gold *islands* (see chapter 2.5.4.1) on gold features that are raised above the background by approximately 40 nm which resulted in additional lateral growth of polymer grafts.

Finally, it must be pointed out that a common idea in the SIP scientific community is that well defined polymer layers can only be achieved by living SIP.³¹ In this chapter, it was clearly demonstrated that also a free radical polymerization technique allows an excellent control over the polymer layer morphology.

4.2 3D micro- and nanostructured polymer grafts on gold by EBCL and SIPGP

During control experiments, it was found that the third step of this four-step procedure (modification of the amino group to an azo-initiator) was not required: structured PS grafts with similar thicknesses were created by submerging an unmodified structured NBT SAM in styrene and irradiating it with UV-light. PS grafts were selectively formed on the previously crosslinked SAM regions. This unexpected result was the starting point for the development of an initiator-free approach for the preparation of structured polymer grafts, presented in the next chapters.

4.2.1 Surface-initiated photopolymerization (SIPP) versus self-initiated photografting and photopolymerization (SIPGP)

In chapter 2.3.3, the self-initiated photografting and photopolymerization (SIPGP) of styrene and various acrylic monomers was discussed. SIPGP allows the preparation of polymer grafts onto organic substrates, simply by submerging the substrate in bulk monomer and irradiating with UV-light. The monomer acts as a photosensitizer and reaches a biradical ($\cdot M \cdot$), which can initiate a free radical polymerization in solution. In the meantime, $\cdot M \cdot$ may also abstract a hydrogen atom from a surface functionality on the organic substrate. The radical formed on the organic substrate initiates the free radical SIP of the monomer (Figure 7).

The only example of SIPGP on SAMs was performed by Dyer and coworkers.¹⁷⁰ They reported on the formation of approximately 200 nm thick PS grafts as well as 675 nm thick PMMA grafts on thiol SAMs on gold containing tertiary amines. The SAMs were immersed in a monomer solution in the absence of photoinitiator and irradiated by UV-light. The authors suggest that the photoactivated monomer activates the amino group by electron transfer or hydrogen abstraction. Because no polymer grafts were observed under analogue reaction conditions on octanethiolate SAMs, the authors postulate that the presence of the tertiary amino groups was necessary for the SIPGP. However, Rånby and coworkers demonstrated that the SIPGP can also be performed on polyethylene substrates that contain only alkanes.

A multitude of studies reported on the surface-initiated photopolymerization (SIPP) of styrene and acrylic monomers on SAMs bearing a photoinitiator.^{154,173,181,182,183,184,185,186,187} However, from the data presented in these studies, it is not possible to discern whether the polymer grafts were formed by the proposed mechanism or by the SIPGP of the monomer or by a combination of the two mechanism. In chapter 4.1.1, it was mentioned that Dyer and coworkers observed a nonlinear growth for the SIPP of styrene on unstructured AIBN-type initiators (Figure 26). Based on this behavior, a four-stage growth model was proposed. However, the possibility that the nonlinear growth behavior is resulting from a combination of the SIPGP of styrene and the SIPP initiated by the AIBN-type SAMs was not taken into consideration.

In previous chapters, the SIPP of styrene on structured cAMBT SAMs was discussed. It cannot be excluded that the SIPGP of styrene was at least partially involved in the formation of the polymer structures. The difficulty to investigate the mechanisms during SIP has already been pointed out in chapter 2.2.2.

In this part of the work, it was investigated if highly defined structured polymer grafts could be prepared by the SIPGP of styrene and acrylic monomers, directly onto biphenylthiol SAMs on gold, structured by EBCL. This renders the SAM-modification step for the preparation of a surface-bonded initiator unnecessary. Furthermore, the comparison of polymer grafts prepared by SIPP and SIPGP using analogue systems and under identical UV-irradiation conditions may give more insight into the processes involved during the SIPP of vinyl monomers.

4.2.2 SIPGP on structured BT SAMs

The following three-step procedure was used in a first set of experiments in order to investigate the possibility to prepare structured polymer grafts by SIPGP:

1. Modification of a gold substrate with a biphenylthiol (BT) SAM.
2. Structuring of the BT SAM by EBCL (Figure 14).
3. SIPGP by submerging the substrate in freshly distilled and degassed styrene, MMA or tert-butyl methacrylate (tBMA) and irradiation with UV-light at $\lambda_{\max} = 350$ nm (the same UV source was used as for the SIPP experiments in chapter 4.1),

After the SIPGP, the substrate was taken out of the monomer, intensively washed by ultrasonification in various solvents (to ensure that only chemically grafted PS remained on

the surface), dried, and measured with AFM under ambient conditions. The AFM measurements revealed that well defined polymer grafts were selectively formed on the previously irradiated BT SAM regions (Figure 41). At this stage of our research, one question arises: Why are polymer grafts exclusively formed on the previously crosslinked SAM regions?

The electron beam induced lateral crosslinking reaction of BT SAMs enhances the stability of the monolayer due to the multiple adhesion sites of the entire layer. It is well known that thiol SAMs on gold can photooxidize by exposure to UV-light.¹⁸⁸ However, the stability of thiol SAMs on gold under UV-irradiation depends on many parameters such as light wavelength, SAM packing, morphology or functionality.^{188,189} It was presumed that not crosslinked BT molecules desorbed from the surface during the polymerization process due to intensive UV-irradiation. In order to control this hypothesis, a structured BT SAM was submerged in toluene and irradiated with UV-light over a period of 30 minutes. AFM measurements showed that crosslinked areas were $10 \pm 2 \text{ \AA}$ higher than their surroundings.

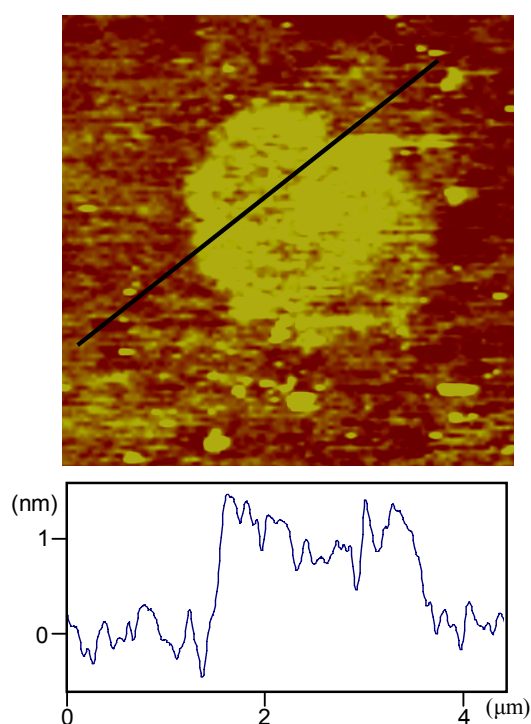


Figure 37. AFM measurement of a structured crosslinked BT SAM (EBCL: $1 \mu\text{m}$ radius; 50 eV; 60 mC/cm^2). The sample was submerged in toluene and irradiated with UV-light over a period of 30 minutes.

This value is in good agreement with the theoretical height of a BT SAM. This indicates that during the SIPGP, polymer grafts are formed on the crosslinked SAM regions while not

crosslinked SAM molecules desorb from the surface (Figure 38) (since the same UV source was used in chapter 4.1, it is very probable in this perspective, that the non-crosslinked NBT SAM molecules in Figure 23, also desorbed from the surface during the SIPP).

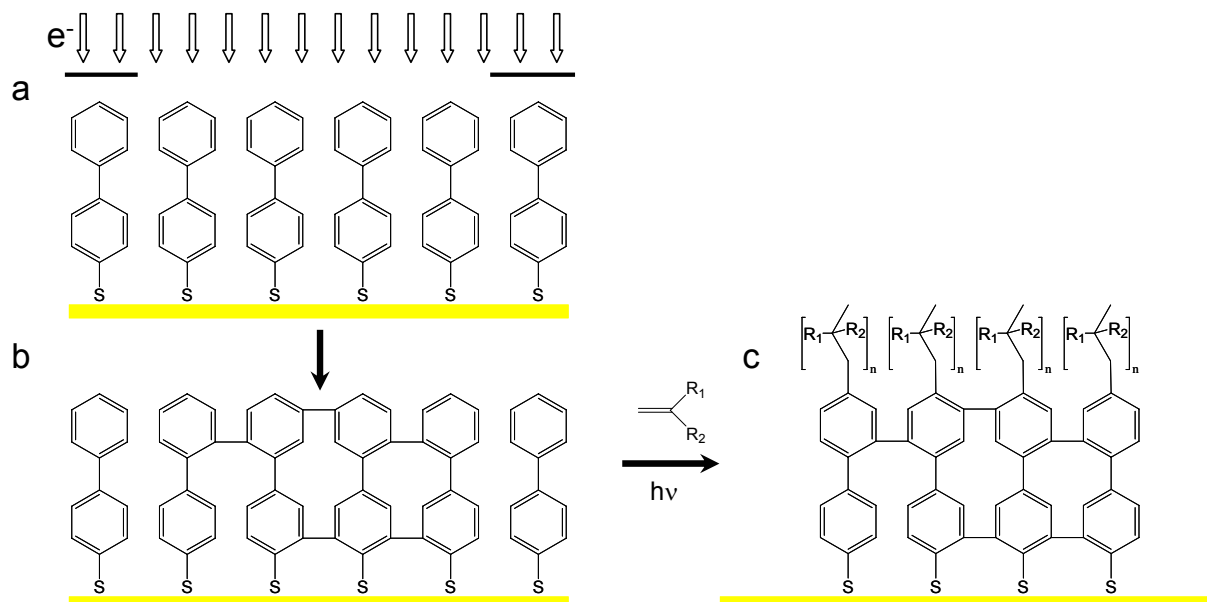


Figure 38. Reaction scheme. (a) Electron beam irradiation of BT SAMs on gold. (b) Crosslinking of the biphenyl mesogen. (c) SIPGP by exposure to a vinyl monomer and UV-irradiation results in patterned polymer grafts.

The SIPGP mechanism has been described in chapter 2.3.3: the monomer absorbs a photon and acts as a photosensitizer to activate a surface functionality (here benzyl) by hydrogen abstraction. The radical formed on the SAM initiates the free radical SIP of the monomer. In a control experiment, a clean gold substrate (without SAM) was irradiated with an electron beam and successively immersed in monomer and irradiated with UV-light. No polymer grafts were observed.

As mentioned above, all presented SIPGP experiments (also in next chapters) were performed at room temperature using a UV-light of a spectral distribution between 300 and 400 nm ($\lambda_{\text{max}} = 350$) from Rayonet. A few SIPGP experiments with styrene and acrylic monomers (MMA and tBMA) were also performed using another available Rayonet UV-lamp (with the same irradiation geometry) of a spectral distribution between 360 and 260 nm ($\lambda_{\text{max}} = 300$) (Figure 39).

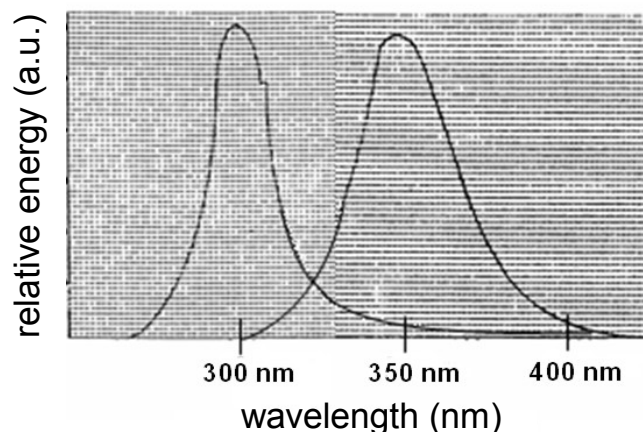


Figure 39. Emission spectra of two different Rayonet UV-lamps ($\lambda_{\text{max}} = 300 \text{ nm}$ and $\lambda_{\text{max}} = 350 \text{ nm}$).

A systematic study to investigate the influence of the applied light wavelength was not performed. However, it was observed that thick polymer grafts were only formed using the 350 nm light source. It has already been reported by Schmelmer *et al.*¹⁵⁵ that thick PS grafts could not be prepared by SIPP on cAMBT SAMs using the 300 nm light source. This is probably due to the absorption by PS of wavelengths smaller than 280 nm, which causes a significant photochemical decomposition of PS grafts by disproportionation and crosslinking.¹⁹⁰

At first view, this is a surprising result since styrene and acrylic monomers do almost not absorb UV-light between 300 and 400 nm (Figure 40). It can be argued that the absorption of monomer molecules close to the substrate is shifted to higher wavelengths due to interactions between the double bond and surface functionalities. However, in all performed experiments, the monomer phase became highly viscous which indicates that polymerization occurred also in the solution due to the self-initiated photopolymerization. This was observed in the presence as well as in the absence of substrates in the monomer phase.

It is a well known phenomenon that radiation induced processes can be performed with high quantum yields at wavelengths where the photosensitizer has a low absorbance. The quantum yield of a radiation-induced process is the number of times that a defined event (usually a chemical reaction step) occurs per photon absorbed by the system. Thus, the quantum yield is a measure of the efficiency with which absorbed light produces some effect.¹⁹⁰ For the self-initiated photopolymerization of styrene in solution, the quantum yield at wavelengths between 300 and 400 nm is only slightly lower than at 250 nm.¹⁹¹

This indicates that the SIPGP can be performed with a small overlapping of the emission spectrum of the UV-lamp and the absorption spectrum of the monomer. It must not lose sight of the fact that in all SIPGP experiments, relatively long UV irradiation times were needed

(e.g. around 16 h for styrene) which is probably due to this low emission/absorbance-overlap. However, this low emission/absorbance-overlap has also one major advantage: a photon which is completely absorbed by the monomer cannot pass through the liquid phase to reach the substrate surface.

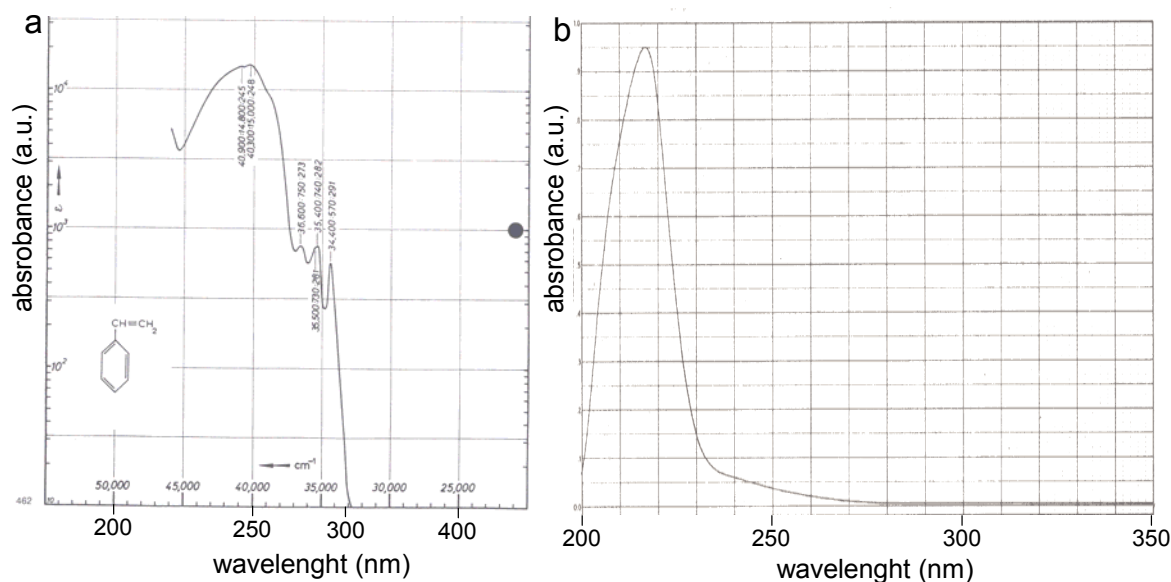


Figure 40. UV-VIS absorbance spectra of styrene (a) and tBMA (MMA and acrylic acid have the same absorbance characteristics between 200 and 350 nm) (b).¹⁹²

4.2.2.1 Influence of the electron dosage on the polymer thickness

In order to study the influence of the electron dosage during the EBCL step on the thickness of the resulting polymer grafts, three gradient structures were prepared on which the electron dose was continuously increased within an area of $10 \times 50 \mu\text{m}^2$. This was done as described in previous chapter (every gradient consisting of 100 parallel $10 \times 0.5 \mu\text{m}^2$ lines with linearly increasing electron dosage). In this experiment, a different electron beam writing strategy was used by Alexander Küller, which allowed a much better control of the locally applied electron beam dosage, even at low doses. The electron beam dosage increased linearly from 0 to 11, 0 to 37.5 and 0 to 110 mC/cm^2 . This was done in order to study in the same experiment the influence of the electron beam dosage at high as well as at very low electron doses. In other words, the 0 to 11 and 0 to 37.5 mC/cm^2 gradients give a more detailed, or *elongated* view of the 0 to 110 mC/cm^2 gradient.

The substrate was successively immersed in bulk styrene and irradiated for 16 h with UV-light. The AFM image of the resulting polymer structures and the corresponding height profiles are displayed in Figure 41.

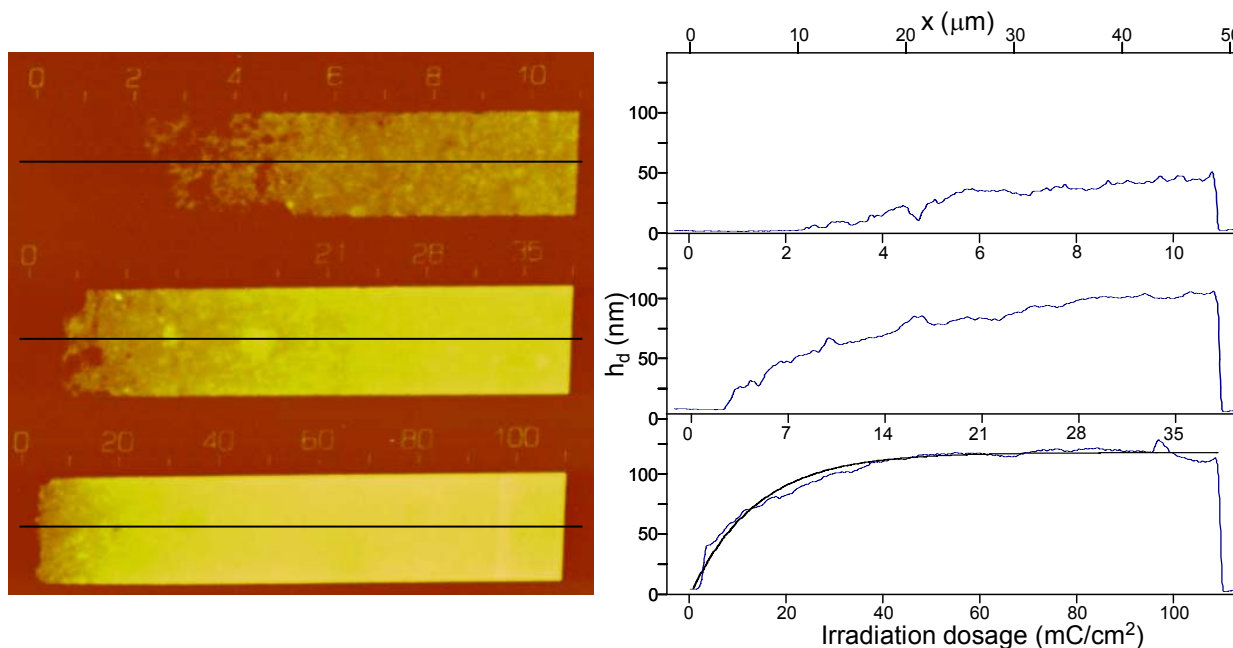


Figure 41. AFM image ($52 \mu\text{m}^2$) and height profile of three PS gradients on a BT monolayer on the same substrate. The electron beam dosage increases linearly from 0 to 11, 0 to 37.5 and 0 to 110 mC/cm^2 . ($t_p = 16 \text{ h}$). In the height profile of the 0 to 110 mC/cm^2 gradient, an exponential fit function is plotted in grey (see text for details).

As apparent from Figure 41, the height of the polymer layer is determined by the applied electron dosage. Furthermore, the dependence of the electron beam dosage on the polymer layer thickness is identical in the three gradients (e.g. the average polymer layer thickness at 8 mC/cm^2 is 38.5 nm in the first gradient, 37.5 nm in the second and 38.4 nm in the third gradient structure).

Since the reaction conditions were identical for all structures, the increase of the polymer layer thickness can be attributed to the increase of the grafting density (exactly as for the SIPP on cAMBT, chapter 4.1.2), assuming that the surface density does not influence the kinetics of the SIPGP.

As outlined in Figure 38, the SIPGP can only occur on crosslinked BT molecules. If the BT SAM is not fully crosslinked, non-crosslinked BT molecules desorb from the surface during the SIPGP. This lowers the surface density of potential grafting sites.

The absence of polymer grafts at electron beam doses under 2 mC/cm^2 , as observed in Figure 41, is attributed to the insufficient crosslinking of biphenyl mesogen at very low electron beam dosage resulting in the total desorption of the SAM during the SIPGP step.

Between 2 and 5 mC/cm^2 , PS grafts cover the surface only partially. This can be observed very clearly in the 0 to 11 mC/cm^2 gradient in Figure 41. Here, only some crosslinked *islands* remained attached to the gold surface.

At higher electron beam doses, a thicker and more homogenous PS layer is formed. The polymer layer thickness increases with the electron beam dosage to approximately 50 mC/cm^2 and reaches a value of approximately 105 nm . The maximum polymer layer thickness is attributed to the full crosslinking of the BT monolayer and thus the maximum grafting density of the polymer grafts. Above 50 mC/cm^2 , the polymer layer thickness remains constant. This denotes an unaltered structure of the crosslinked BT monolayer at areas irradiated with high electron beam doses.

It was found that the experimental dry polymer layer thickness can be fitted exponentially as a function of the irradiation dosage D :

$$h_d(D) = h_{d0}[1 - \exp(-D'/D_0)] \quad \text{Eq. 16}$$

where h_{d0} is the maximum polymer layer thickness. D_0 describes the efficiency of the process. Eq. 16 is similar to Eq. 13, used in the previous chapter. However, no stability factor is needed because the crosslinked BT SAM remains unaltered at high electron doses, while the electron irradiation of NBT SAMs induced the desorption of the 4'-functionality. D' is the onset corrected dosage. The onset is caused by the absence of polymer grafts at very low electron beam doses as discussed above. The used values for the fit function in Figure 41 were h_{d0} : 112 nm , D' : $D - 1.5 \text{ mC/cm}^2$ and D_0 : 13.5 mC/cm^2 . The good agreement between the experimental data and the fit function demonstrate that the polymer layer thickness increase is exponential.

The comparison of the polymer grafts created by the SIPP of styrene on cAMBT SAMs in the previous chapter and the SIPGP on cBT SAMs under identical UV irradiation conditions shows that polymer structures with comparable thicknesses can be created without surface-bonded initiators. This shows in general that during the SIPP of styrene and acrylic monomers on surface-bonded initiators, the surface-attached radicals are not only formed by the photoactivation of the initiator groups, but also by the abstraction of hydrogen atoms of surface functionalities by photo-activated monomers. In the following part, different

structured ω -functionalized biphenylthiols SAMs were prepared on gold, in order to study the influence of the surface functionality on the formation of the polymer grafts by SIPGP.

4.2.3 SIPGP on different ω -functionalized biphenylthiol SAMs

Four types of ω -functionalized biphenylthiol SAMs (BT, methyl- (MBT), hydroxy- (HBT) and nitrobiphenylthiol (NBT)) were prepared on gold. The SAMs were structured by irradiation with an electron flood gun through a stencil mask with circular openings of 1 μm radius. The different experiments were performed with identical irradiation parameters (electron energy: 50 eV, electron dosage: 60 mC/cm^2). The electron beam irradiation of ω -functionalized biphenylthiols SAMs causes the lateral crosslinking reaction of the biphenyl mesogen: BT, MBT, HBT and NBT SAMs are converted into crosslinked cBT,¹⁴⁴ cMBT,¹⁴⁷ cHBT,¹⁴⁸ and cABT¹⁴⁴ SAMs (see chapter 2.5.4.2).

In order to obtain reliable data on the influence of the surface functionality on the formation of the polymer grafts, poly(methyl methacrylate) (PMMA) grafts were prepared on the various crosslinked SAMs under identical reaction conditions. The different substrates were submerged in the same reaction vessel during the SIPGP. In all experiments, polymer grafts were selectively formed on the previously crosslinked SAM regions. This indicates that exactly as in the case of BT SAMs, not crosslinked MBT, HBT and NBT molecules desorb during the UV irradiation. Polymer grafts are selectively formed on the remaining crosslinked SAMs by hydrogen abstraction of the surface functionality (phenyl, methyl, alcohol or amino group) by photoactivated monomers.

SAM	surface functionality	h_d (nm)
cBT	phenyl	65 ± 8
cMBT	arom. methyl	82 ± 11
cHBT	arom. alcohol	70 ± 10
cABT	arom. amine	85 ± 11

Table 4. Dry PMMA layer thickness (h_d) created on different types of monolayers. The thickness and error was measured as outlined in Figure 24.

In Table 4, the thicknesses of structured PMMA grafts formed on the different structured SAMs are summarized. Surprisingly, no direct correlation between the PMMA layer thickness

and the surface functionality can be made which makes an interpretation of the influence of the surface group difficult. Furthermore, the different ω -functionalized biphenylthiol SAMs do not have exactly the same behavior when irradiated with an electron beam. The methyl group of MBT SAMs for instance, remains unaffected during the electron beam induced crosslinking reaction while the irradiation of HBT SAMs causes a partial OH abstraction.^{147,148} In other words, the surface concentration of the 4'-function is not identical for the different crosslinked ω -functionalized biphenylthiol SAMs. This further complicates the comparison of the reactivity of the different 4'-functions for the SIPGP process.

However, hydrogen radical abstraction can only be performed if the potential energy of the photoactivated monomer is higher than the R-H dissociation energy.⁷² The potential energy of a photoactivated monomer molecule cannot be higher than the photon energy of the applied UV-light (this is not valid for laser lights, where multiphoton absorption can be observed due to the very high photon density and photon flux).¹⁹³ In other words, hydrogen radicals can obviously not be abstracted from a surface group, if the R-H bond dissociation energy is higher than the photon energy of the applied UV-light. The SIPGP experiments were performed with UV-light of a spectral distribution between 300 and 400 nm (corresponding to photons with energies between 71.5 kcal·mol⁻¹ and 95.3 kcal·mol⁻¹).

molecule	BDE (kcal·mol ⁻¹)	reference
C ₆ H ₅ -H	111	68
C ₆ H ₆ CH ₂ -H	86	68
C ₆ H ₆ NH-H	89.3	194
C ₆ H ₆ O-H	87.3	195

Table 5. Experimental R-H bond dissociation energies (BDE).

Since no experimental or theoretical values of the R-H bond dissociation energies (BDEs) in the 4'-function of crosslinked biphenylthiol SAMs are available, we compare here the R-H BDEs in benzene, toluene, aniline and phenol (Table 5). However, these values are probably higher than the R-H BDEs of the corresponding ω -functionalized crosslinked biphenyl SAMs. These SAMs are conjugated systems, which allow the delocalization of electrons across the entire crosslinked monolayer. This may have a significant influence on the hydrogen dissociation energy as well as on the reactivity of the radicals formed on the surface after hydrogen abstraction. Theoretical studies demonstrated that the N-H and O-H BDEs are for instance, approximately 2 kcal·mol⁻¹ lower in 4-aminobiphenyl and 4-hydroxybiphenyl

molecules than in respectively aniline and phenol, due to electron delocalization in a second aromatic ring.^{196,197} Stein *et al.*¹⁹⁸ calculated that the C-H bonds of methyl groups, directly bonded to conjugated polycyclic aromatic hydrocarbons have a BDE of only 63 kcal·mol⁻¹, which is 23 kcal·mol⁻¹ lower than in toluene.

However, Aihara and coworkers calculated that the aromatic C-H bond dissociation energy is almost identical in conjugated polycyclic aromatic hydrocarbons as compared to benzene.¹⁹⁹ In this perspective, it is very surprising that polymer grafts were also formed on cBT SAMs with UV-light of a spectral distribution between 300 and 400 nm. Furthermore, it will be shown in chapter 4.3.3 that under identical polymerization conditions, no polymer grafts were formed on H-terminated diamond, which has a theoretical C-H bond dissociation energy of 96 kcal·mol⁻¹. One possible explanation is the contamination of the biphenyl SAMs during the electron beam irradiation, with the formation of a thin layer of electron beam induced carbon deposition (EBCD), due to the decomposition of residual hydrocarbon molecules (chapter 2.5.4.3). It will be shown in chapter 4.4 that polymer grafts can be formed on EBCDs under identical SIPGP conditions. However, for still unclear reasons, stable EBCD layers are not formed on every substrate. EBCD layers are for instance formed on bare silica substrates but not on bare gold. However, the research group of Prof. Grunze has a long experience with electron beam induced processes, and electron beam carbon contamination was never observed on crosslinked biphenyl SAMs.

Another possibility for the formation of polymer grafts on cBT SAMs is the presence of specific interactions between the conjugated SAM and absorbed vinyl monomers. These interactions may result in a reduction of the activation energy for the hydrogen abstraction. However, until now no experimental data confirmed this hypothesis.

4.2.4 Comparison between cABT and cAMBT SAMs

All previous experiments have shown qualitatively that the SIPGP plays probably an important role during the surface-initiated photopolymerization on SAMs bearing azo initiators. However, the importance of this effect cannot be quantified by comparing the here described SIPGP experiments and the SIPP experiments on cAMBT SAMs in chapter 4.1 since too many parameters were varied between the two sets of experiments (UV irradiation time, surface functionality, monomer, electron beam lithography parameters, etc.)

Thus, the photografting of styrene on cABT SAMs (prepared with exactly the same EBCL parameters as in chapter 4.1) is investigated and compared with the photografting of styrene on cAMBT SAMs, as presented in chapter 4.1, under identical polymerization conditions. Here, two very similar systems are compared. Only one parameter (the modification of the amino group into an azo initiator) is changed between the two sets of experiments (Figure 42).

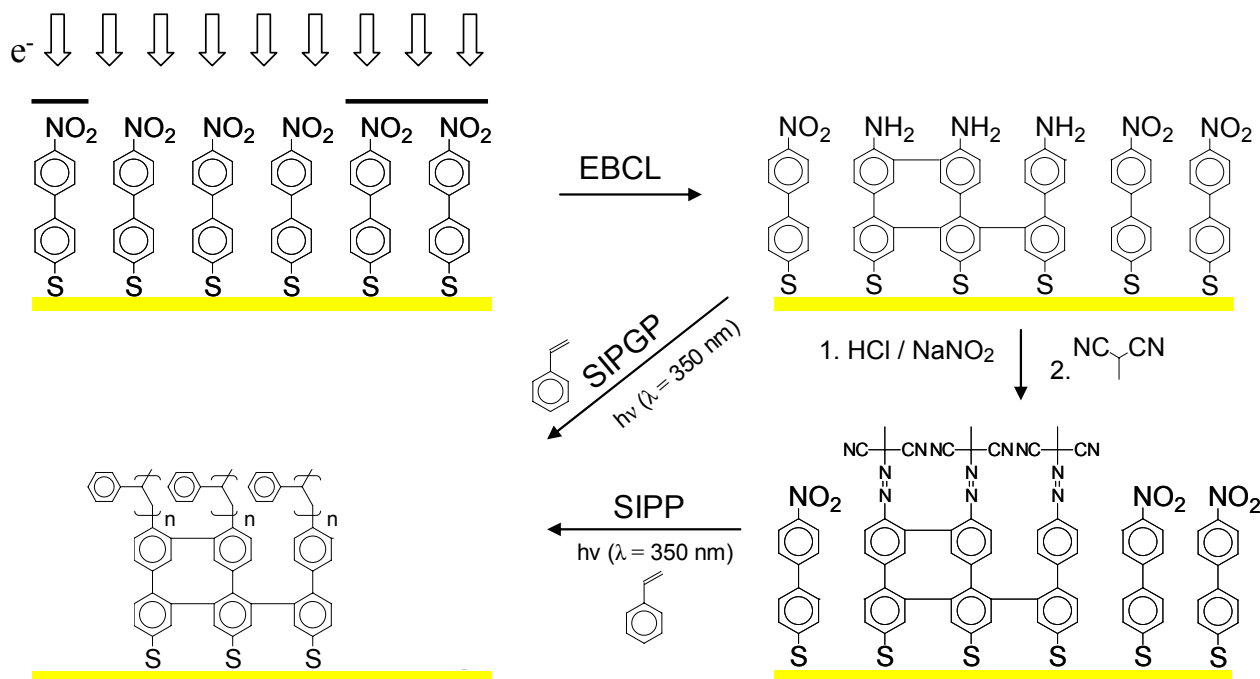


Figure 42. Preparation of structured polymer grafts by SIPGP on cABT SAMs or SIPP on cAMBT SAMs.

In Figure 43, the dry polymer layer thickness of PS grafts is plotted as function of the UV irradiation time for the photografting of styrene on structured cABT and cAMBT SAMs. Under identical reaction conditions, approximately three times thicker polymer structures were formed on cAMBT as compared to cABT. The average growth rate is 9.8 nm/h for cAMBT SAMs and 3.8 nm/h for cABT SAMs. The significantly faster thickness increase of the polymer structures on cAMBT, indicates that the surface-bonded asymmetric azo-compound accelerates the formation of the polymer structures.

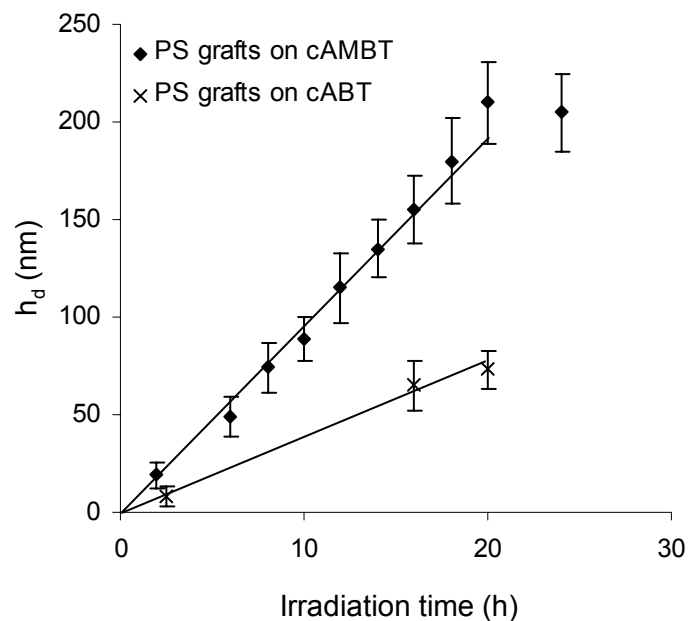


Figure 43. Polymer layer thickness as a function of the irradiation time ($\lambda_{\max} = 350$ nm) on structured cABT and cAMBT (EBCL: $1 \mu\text{m}$ radius; 50 eV; 60 mC/cm²).

The influence of the electron dosage during the EBCL step on the resulting h_d was also studied on cABT SAMs on gold. A gradient structure, on which the electron dose was linearly increased from 0 to 115 mC/cm² within an area of $10 \times 50 \mu\text{m}^2$ was prepared. The gradient parameters were identical to the experiments presented for the cAMBT system in Figure 29.

Figure 44 shows the resulting polymer structure. The polymer layer thickness increases with the locally applied electron dosage to approx. 35 mC/cm² and reaches a maximum of $h_d = 440$ nm. This can be attributed to the fact that at low electron beam dose, the crosslinking reaction of the biphenyl mesogen (as well as the conversion of the nitro to amino group) is not complete. This lowers the number of possible grafting sites due to the desorption of non-crosslinked SAM molecules during the UV irradiation, analogue to the BT SAMs (chapter 4.2.2).

Between 35 and 115 mC/cm², the polymer layer thickness decreases with increasing electron beam dosage. For the SIPP on cAMBT SAMs, it was argued that the decrease of the amino surface concentration at high electron beam doses (due to the partial desorption of the 4'-function) results in a decrease of the azo-initiator surface concentration and thus in a decrease of the final polymer grafting density.

In order to interpret the polymer layer thickness decrease above 40 mC/cm² in the case of the SIPGP on cABT SAMs, the surface function created after the desorption of the 4'-amino group has to be determined. This has not been investigated for cABT SAMs before. However,

unpublished results from the research group of Prof. Grunze, indicate that the alcohol function in cHBT SAMs is replaced by a proton (liberated during electron beam induced biphenyl crosslinking reaction).¹⁴⁸ In this perspective it is likely that the electron irradiation induced desorption of the amino group converts the cABT SAMs into cBT SAMs. This explains the polymer layer thickness decrease above 40 mC/cm², since significantly thicker polymer grafts are formed by the SIPGP on cABT than on cBT SAMs under identical reaction conditions (Table 4).

At first view, the electron beam dosage versus polymer layer thickness dependency is very similar for cABT and cAMBT SAMs (the height profile of PS grafts on cABT and cAMBT gradients are directly compared in Figure 44).

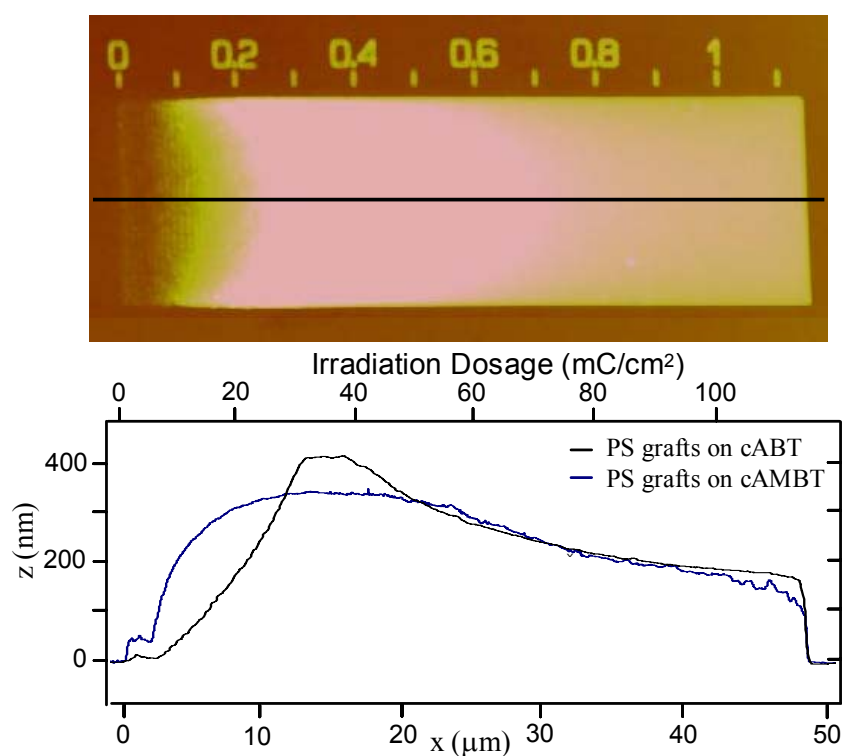


Figure 44. AFM scan ($55 \times 22.5 \mu\text{m}^2$) and height profile of PS grafts on an cABT electron beam dosage gradient. The electron beam dose increases linearly from 0 till 115 mC/cm² from the left to the right. (EBCL at 3 keV). In comparison, the height profile of PS grafts on an identical cABT electron beam dosage gradient (same geometry, electron beam dosage and onset) and successively converted to cAMBT is plotted (Figure 29). The polymerization on cABT and cAMBT SAMs was performed under identical reaction conditions ($t_p = 16\text{h}$).

Although the two height profiles show a similar trend, closer inspection reveals several differences. At low e-beam dosage (between 0 and 27 mC/cm²), significantly thicker polymer grafts were formed on cAMBT SAMs. This is in agreement with the kinetic study presented

in Figure 43 (the electron beam doses cannot be directly compared between these two sets of experiments since different electrons energies were used).

Very surprisingly, significant thicker polymer grafts were formed on cABT SAMs than on cAMBT SAMs between 30 and 50 mC/cm², corresponding to the electron beam doses where the highest amino surface concentration is reached during the EBCL step. This can be explained by the higher termination rate due to the coupling of two radicals at high azo-initiator concentration. However, no further experimental data could confirm this hypothesis. However, this result is similar to the findings of Dyer *et al.*¹⁷⁰ who observed faster polymer film growth rates on homogeneous dimethylamino-terminated SAMs than on SAMs bearing AIBN type initiators.

Summarizing this chapter, it can be stated that the SIPGP on structured (ω -functionalized) biphenylthiols SAMs on gold was found to be a straightforward three-step approach which allows the preparation of defined polymer grafts, without the need of a surface bonded initiator function. The thickness of the polymer grafts can be controlled by either the UV irradiation time or the locally applied electron dosage. This process allows the preparation of complex 3D polymer architectures on the micro- and nanometer scale.

In the following chapters different approaches for the preparation of structured SAMs and polymer grafts on various substrates are presented.

4.3 Modification of diamond substrates

4.3.1 Background

The work presented in this part is an ongoing collaboration with the diamond research group of Dr. José Antonio Garrido, at the Walter Schottky Institute of the TU München. This research group investigates the potential of synthetic diamond as semiconductor material to be used as biosensors or implants.

Diamond is well known for its exceptional hardness, thermal conductivity and high index of refraction. Diamond has also unique surface properties. The chemical inertness of diamond makes it suitable for most biological environments.²⁰⁰ Furthermore, diamond has excellent electrochemical properties.²⁰¹ The electric potential that can be applied to a diamond-based electrode without the hydrolysis of water is very large. This allows the study of redox reactions in aqueous media with a higher degree of sensitivity as compared to other electrode materials.

In this part of the work, we studied different strategies for the preparation of (structured) SAMs and polymer grafts on synthetic diamond. The aim of this work is to couple biological systems (enzyme, cells, etc.) to synthetic diamond in order to use this material as e.g. amperometric biosensors. *Enzyme-based electrochemical biosensors have been around for many years, involving many different types of enzymes, immobilization chemistries and substrates. Indeed, glucose sensors (used by millions who suffer from diabetes) work using this principle, and the covalent immobilization of glucose oxidase or similar enzymes on relatively inexpensive materials already forms the basis for commercial devices.*²⁰² The sensing principle of an amperometric glucose sensor is very simple: when a glucose molecule is oxidized into gluconolactone by glucose oxidase, two electrons are liberated. If the glucose oxidase is chemically attached to an electrode, the two liberated electrons will create an electric current. The glucose concentration in solution can then be determined by measuring the electric current.

Before the presentation of the different coupling strategies that have been investigated during this project, the existing methods for the preparation as well as for the functionalization of diamond surfaces are briefly reviewed.

4.3.1.1 Synthetic diamond

There are two main methods to produce synthetic diamond. The oldest method, *high pressure high temperature synthesis*, is still the most widely used process because of its relative low cost. It uses large presses that can weigh a couple of hundred tons to produce a pressure of 5 GPa at 1.500 °C, reproducing the natural conditions for the creation of diamond inside the earth.²⁰³ However, this method only allows the fabrication of small, single diamond crystals, which are not suitable as electrode material. The alternative method is using chemical vapor deposition (CVD) at elevated temperatures for the fabrication of thin diamond films on various substrates. A gas source, usually methane and hydrogen, is introduced into a chamber at low pressure and converted into sp² graphite and sp³ diamond in a microwave plasma.

The thin diamond films prepared by CVD are also called polycrystalline diamond. These films consist of sp³ diamond crystals with an average grain size of a few nanometers (ultrananocrystalline diamond, UNCD) to several hundred nanometers (nanocrystalline diamond, NCD) which are surrounded by non-diamond sp² carbon. The diamond grain size, and thus the morphology of the diamond films, can be controlled by the gas composition. It was found that the film morphology can be significantly modified by adding argon to the plasma.²⁰⁴ Argon was found to have an important effect on the plasma chemistry and enhance the diamond growth rate.²⁰⁵ The sp² carbon content is higher in films with smaller grain sizes, and reaches 10% in UNCD,²⁰⁶ whereas NCD has a much lower sp² carbon content.

Pure diamond is an excellent electrical isolator and thus unsuitable as electrode material.²⁰⁷ However, very conductive n-doped (conduction occurs through electrons and not through holes like in p-doped materials) diamond films can be prepared through the addition of nitrogen gas to the microwave plasma.²⁰⁸ Diamond films with a conductivity up to the metallic regime (250 Ω⁻¹ cm⁻¹) at room temperature can be obtained.²⁰⁹

4.3.1.2 Chemical modification of diamond: State of the art

In spite of the chemical stability of diamond, different strategies are known to functionalize diamond surfaces. A first type of functionalization is the direct modification of the diamond surface (often under drastic reaction conditions). Fluorine and chlorine terminated diamond surfaces have been prepared by reaction with elemental fluorine²¹⁰ and chlorine.^{211,212} Amino groups were introduced by amination of H-terminated diamond surfaces in an ammonia

plasma²¹³ or by UV irradiation of the substrate in ammonia gas.²¹⁴ Diamond can be oxidized using various conditions such as anodic polarization,²¹⁵ oxygen plasma treatment²¹⁶ or UV irradiation of the substrate in air.²¹⁷ Oxidized diamond surfaces have hydroxyl, carbonyl and ether surface groups.

A second functionalization method is the modification of diamond with bifunctional organic molecules, bearing one grafting function and one desired surface functionality. This approach allows a better control over the desired surface chemistry. Different studies report on the functionalization of oxidized diamond surfaces by reacting silane derivatives with the hydroxyl surface function.^{215,217,218} Although silane monolayers on oxidized surfaces are still widely used in the field of biomedical application, their poor stability in saline solutions at 37°C renders them inappropriate for long-term biomedical applications.^{157,219} Recently, different methods for the attachment of organic molecules on H-terminated diamond have been developed. Hamers and coworkers²⁰⁹ reported on the photochemical functionalization of polycrystalline diamond surfaces with terminal alkenes. Using this approach, Garrido and coworkers demonstrated that proteins can be covalently immobilized on UNCD surfaces and retain their functionality.²¹⁶

Carlisle and coworkers^{220,221} reported on the electrochemically induced grafting of aryl diazonium derivatives on UNCD films (Figure 45). However, one major drawback of this approach is the uncontrolled formation of multilayers due to the transfer of electrons through the growing film.^{222,223,224}

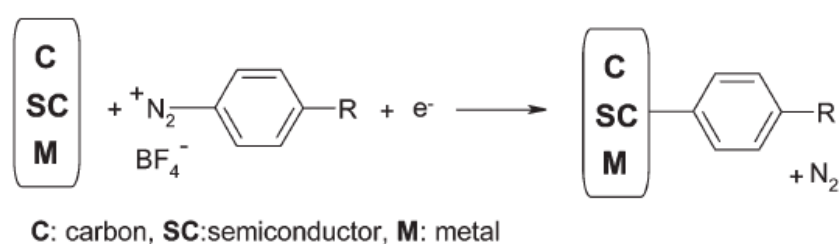


Figure 45. Electrochemical grafting of aryl diazonium salts on carbon (graphite, glassy carbon or diamond), semiconductors or metals.²²⁵

4.3.2 Nitrophenyl SAMs on diamond

Recently, it has been reported that aryl diazonium salts react spontaneously onto various substrates (H-terminated silicon,^{226,227} GaAs,²²⁷ Au,²²⁸ Pd,²²⁷ Cu²²⁹ and Fe²³⁰). The proposed

mechanism of the grafting reaction involves a spontaneous electron transfer between the substrate and the diazonium compound and might be otherwise similar to the electrografting reaction route.²²⁵ The major advantage of this single-step approach is its simplicity: the substrate is submerged in a solution of the aryl diazonium compound and no electrochemical equipment is needed.²³¹ However, the modification of diamond surfaces by this approach has not been reported.

In this chapter, the spontaneous grafting of 4'-nitro-1,1-biphenyl-4-diazonium tetrafluoroborate (NBD) on H-terminated UNCD was investigated (Figure 46). This choice was motivated by different reasons. First, the biphenyl moiety proved to be an excellent mesogen for the preparation of highly ordered and densely packed SAMs.¹⁵⁶ Furthermore, the biphenyl mesogen is conjugated and enables an *electrical contact* between the diamond substrate and the surface functionality. This is crucial for further functionalizations of the surface coating for amperometric biosensor applications. Moreover, as already mentioned in previous chapters, nitrobiphenyl (NB) SAMs on gold can be structured on the nanometer scale by the electron beam chemical lithography (EBCL). The grafting of NBD molecules may thus potentially expand the EBCL process to diamond surfaces.

4.3.2.1 Preparation of nitrobiphenyl SAMs

NBD (white crystals) was synthesized by the diazotation of the commercially available 4-amino-4'-nitrobiphenyl (red-orange crystals) with sodium nitrite.²³² The UNCD samples were first treated with an oxygen plasma, in order to remove all impurities. The samples were successively hydrogenated in a hydrogen plasma to obtain H-terminated diamond.

The NB SAMs were prepared by submerging freshly hydrogenated diamond substrates into a degassed and saturated NBD solution in acetonitrile and stirred for three days at room temperature (Figure 46). During the reaction, a gradual color change of the originally clear and colorless reaction solution to a bright yellow and finally to a deep orange color was observed, indicating the decomposition of NBD molecules in solution. The substrates were successively cleaned by sonification for several minutes in different solvents in order to remove physisorbed material.

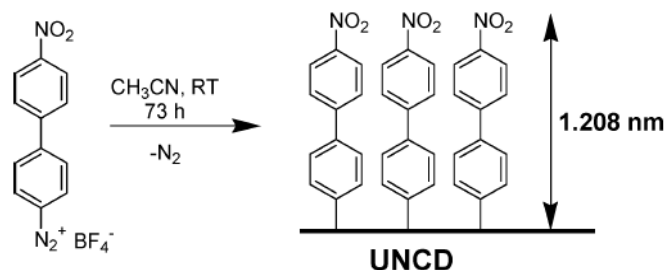


Figure 46. Grafting of NBD molecules on diamond by immersing the substrate, three days at room temperature, in a NBD solution in acetonitrile.

4.3.2.2 Characterization of NB monolayers on polished polycrystalline diamond by AFM

In order to verify the formation of a monolayer of NB on the diamond surface, the modified polycrystalline diamond substrate was subjected to a scratch experiment as described by McCreery *et al.*²²³ At high depletion forces a small section of the surface was *scanned* in full contact mode to remove grafted molecules but leave the hard diamond substrate intact. The determination of the layer thickness by this method is more accurate on flat substrates. For this reason, the scratch experiments were performed on polished polycrystalline substrates instead of unpolished UNCD substrates (UNCD substrates have a roughness of around 10 nm rms (root-mean-square) while polished polycrystalline substrates of only 0.12 nm rms).

Imaging of the intentional applied defect (Figure 47) and analysis of the height difference between the scratched and intact surface gave a difference of $\Delta d = 0.9 \pm 0.4$ nm (section analysis of individual scan lines). However, the average layer thickness can be determined much more accurately by a so-called localized depth analysis, in which the average height difference of two areas (inside and outside of the trench) is determined. The localized depth analysis gave an average height difference of 1.2 ± 0.2 nm (compared to the 0.9 nm in the section analysis in Figure 47). Taking into account the uncertainty of the measurement (e.g. tip-induced deformation of the monolayer) and variation of Δd due to the surface roughness of the substrate, the experimental thickness values of the modification is in excellent agreement with the theoretical height of a SAM of NB with a theoretical molecular length of 1.22 nm.

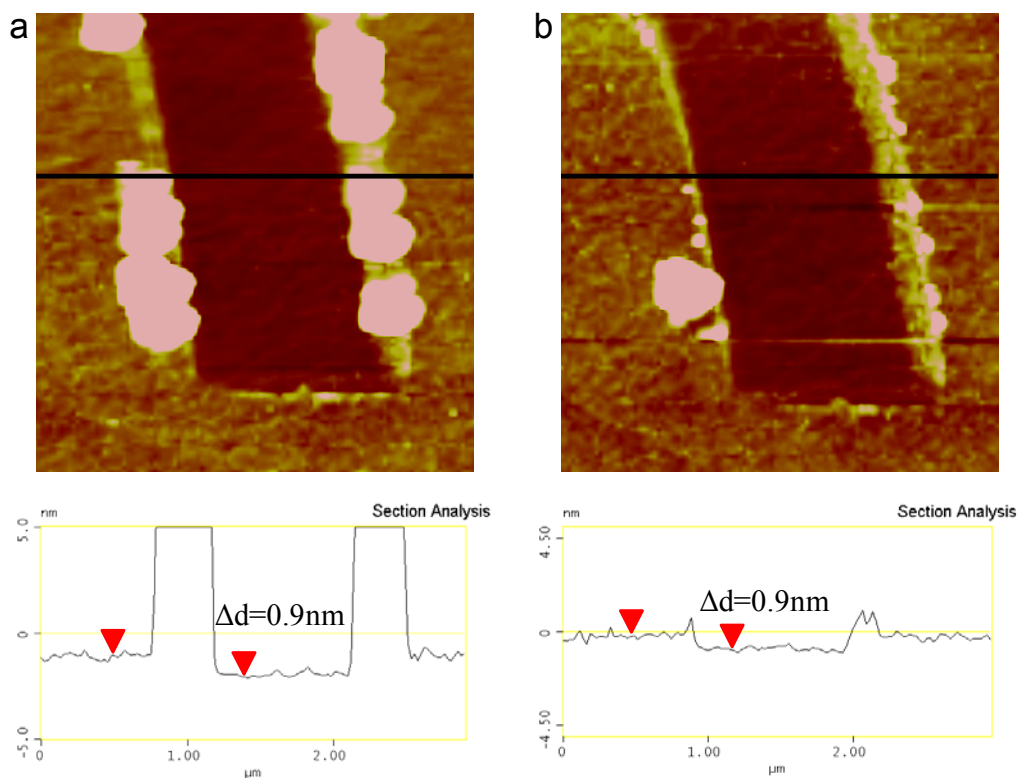


Figure 47. First (a) and second (b) AFM scan in tapping mode and section analysis of the same trench, fabricated in full contact mode by intentional remove of the NB SAM from the polished polycrystalline substrate using a depletion setpoint of 15 V. Visible is the removed material at the rim.

Moreover, investigation of several areas of the modified polycrystalline diamond showed a homogeneous topography and no indications of the formation of multilayers as reported for the electrochemical induced modification of carbon surfaces.²²²⁻²²⁴ From AFM inspection only, the formation of a homogenous ultrathin film with a thickness corresponding to the molecular dimension of NB can be stated.

Figure 47a shows also very clearly the organic material that has been removed by the AFM tip at the rim of the trench. Figure 47b shows that almost all free organic material has been removed during the first AFM tapping mode scan (the second AFM scan was performed immediately after the first scan).

The synthesis of NBD, the preparation of the SAMs as well as the characterization of the SAMs by AFM has been performed in our research group. Further characterizations of the NB SAMs by XPS and electrochemical studies were performed by Simon Lud, from the group of Dr. Garrido at the Walter Schottky Institute.

4.3.2.3 Characterization of NB monolayers on UNCD by XPS

For closer analysis, extensive XPS measurements were performed on UNCD substrates. The XPS overview spectra (not shown) of a native hydrogenated as well as a functionalized surface contain carbon, nitrogen, and oxygen core level peaks. The latter two appear with higher intensity in the NB-modified diamond sample, which indicates the presence of a nitro group containing molecule at the surface. Figure 48a shows two N1s spectra of UNCD samples before and after the grafting reaction of NB. In the N1s region, the neutral amino group as well as nitrogen bonded to carbon exhibits a binding energy peak at 400 eV, while the nitro sites appear around 406 eV. These assignments are in agreement with earlier reports.¹⁷⁶ The reason for the presence of an N1s amino peak will be discussed in next section.

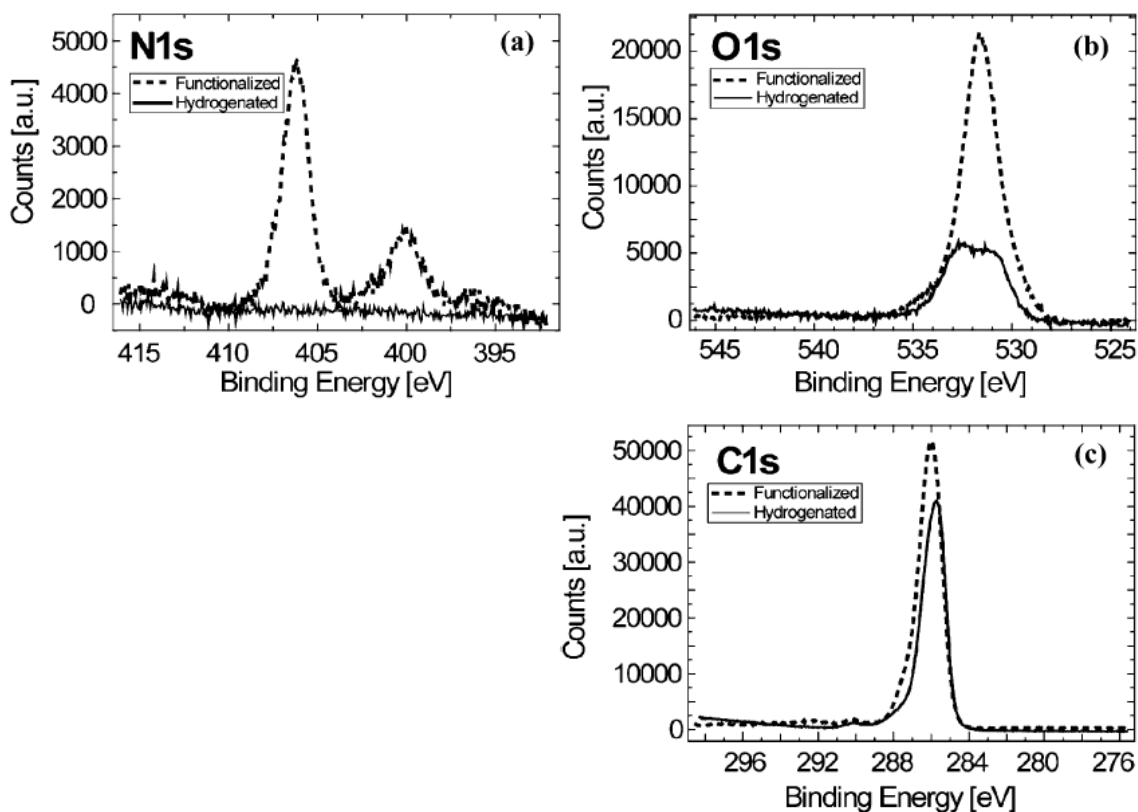


Figure 48. N1s (a), O1s (b) and C1s (c) XPS spectra of a NB-functionalized diamond surface as compared to a reference sample of hydrogenated UNCD.²³¹

XPS allows not only a qualitative study of the chemical surface functionalities (by the electron binding energy). The surface atom ratios can be quantitatively determined by the calculation of the peak areas and taking into account the sensitivity factors for the different

elements.²³³ The peak areas are usually calculated by a Voigt fit (80% Gaussian and 20 % Lorentzian) of the data points and integration of the fit function.

For the calculation of the expected N/C ratio of a dense monolayer on a diamond substrate, the inelastic mean free paths for electrons with the corresponding kinetic energy are a key parameter. For surface coverage quantification, we assume that the overall emission intensity I_A of a given XPS peak for element A follows a Lambert-Beer law for the escaping electrons:

$$I_A = \int_0^{\infty} I_{ML} e^{-ux} dx = \frac{I_{ML}}{\mu} \quad \text{Eq. 17}$$

where u is the absorbance coefficient, μ the scattering coefficient (inverse of the electron mean free path) and I_{ML} represents the intensity of a monolayer (approx. 0.28 nm in ultrananocrystalline diamond).²³⁴ The integration is along an axis parallel to the surface normal. In essence, this law states that the emission intensity is lower for atoms located deeper into the material due to the inelastic scattering of electrons.

For a densely packed NB monolayer, an N/C ratio of 0.14 is expected (evaluated from 4'-nitro-4-aminobiphenyl crystals).²³⁵ Table 6 shows the N/C and O/C atomic ratios calculated from the XPS spectra as described above. The measured N/C ratio of 0.11 corresponds to a packing density of the molecules in the monolayer of approximately 70 % with respect to the bulk crystal or to $4.6 \times 10^{-10} \text{ mol}\cdot\text{cm}^{-2}$ for the surface grafting density.

	chemical shift	binding energy (eV)	ratio to C1s substrate peak	packing density* (%)
nitrogen N1s	N-H, N•	399.9	0.11	70
	N-O	406.1		
oxygen O1s	O-N	531.7	0.25	80
	C-O, C=O	286.9		
carbon C1s	C-O, C=O	286.9	0.19	-
	C-C	286.0		

Table 6. XPS atom ratios of nitrogen, oxygen, and carbon together with the derived surface coverage of the 4-nitro-biphenyl layer.²³¹

(*) Calculated packing density of the NB monolayer with respect to the bulk crystal of 4'-nitro-4-aminobiphenyl.

Figure 49 shows the high resolution C1s XPS spectra before and after the grafting reaction of NB. The C1s spectrum of the hydrogenated sample was deconvoluted into four peaks at

different binding energies. From this fit it is possible to determine the relative percentages of carbon in various binding states: C=O, C-O, sp^2 , and sp^3 .

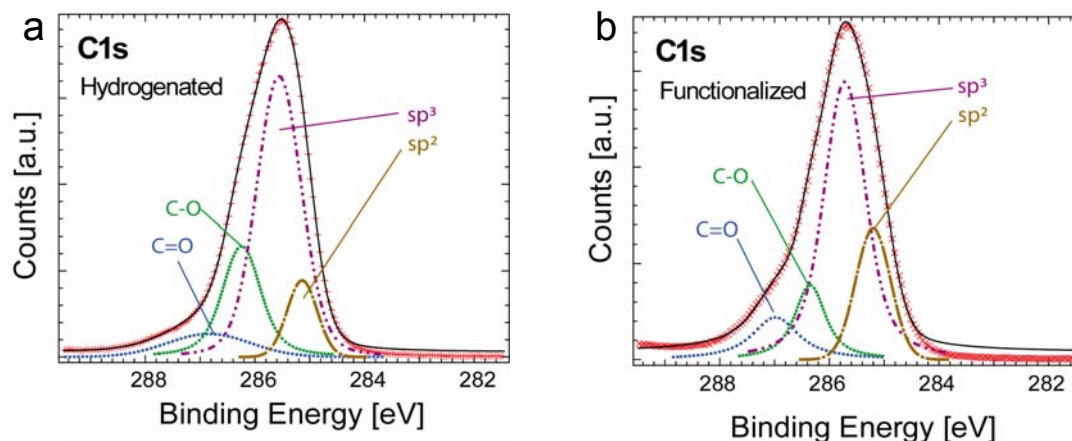


Figure 49. High resolution C1s spectra of a hydrogenated sample (a) and a functionalized sample (b).²³¹

The dominant peak of the C1s band at 285.6 ± 0.1 eV corresponds to the sp^3 hybridized carbon bonds, the peak located at slightly lower binding energy (285.1 ± 0.1 eV) can be assigned to the sp^2 hybridized carbon. The component around 286.2 ± 0.1 eV can be assigned to the C-O group,²³⁶ and the peak at the highest binding energy of 286.8 ± 0.1 eV originates from C=O.²³⁷ The sp^2/sp^3 ratio of the hydrogenated UNCD is in the order of 11 %, which is in good agreement with values for ultrananocrystalline diamond reported elsewhere (Table 7).²³⁸ The carbon-oxygen emission peak indicates a contribution from grain boundaries impurities. The deconvolution of the C1s emission peak is in very good agreement with results reported by Popov *et al.*²³⁹

Peak	C-C sp^2	C-C sp^3	C-O	C=O
Hydrogenated				
binding energy (eV)	285.1	285.6	286.2	286.8
composition	0.07	0.63	0.18	0.12
NB-Functionalized				
binding energy (eV)	285.2	285.7	286.3	287.0
composition	0.18	0.57	0.14	0.11

Table 7. C1s spectra deconvolution of the C1s region of a hydrogenated and the NB-functionalized UNCD surface.²³¹

4.3.2.4 Radiation induced conversion of NB monolayers on UNCD

During the XPS measurements, it was observed that prolonged irradiation with X-rays significantly changes the peak intensities in the N1s region (Figure 50). The N1s nitro peak at 406 eV decreases while the N1s amino peak increases from 20 % to 80 % with longer irradiation times. Furthermore, it was observed that the total amount of nitrogen correlated signals decreases. The total nitrogen loss is about 10 % after 12 h of X-ray irradiation.

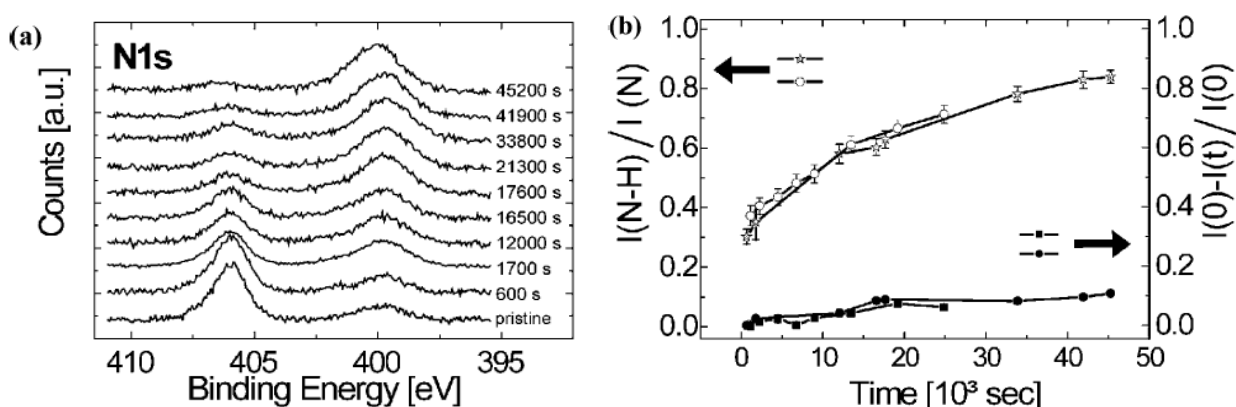


Figure 50. (a) Subsequently recorded N1s emission spectra of a NB-modified UNCD substrate for increasing X-ray irradiation time. (b) Dependence of the nitrogen peak area vs. the irradiation time of two individual samples. The left y-axis displays the fraction of nitrogen in the N1s amino peak; the right axis shows the total loss of nitrogen.²³¹

The irradiation-induced chemical reduction of the nitro group to amino group is analogue to the electron irradiation-induced NBT to cABT conversion (chapter 4.1.2) (primary and secondary electrons generate by X-rays can also induce the conversion).²⁴⁰

The X-ray induced chemical conversion indicates that the electron beam chemical lithography (EBCL) can potentially be applied to NB SAMs on diamond. The electron beam induced conversion of the nitro to amino group will be the subject of future research.

4.3.2.5 Electrochemical characterization of NB monolayers on UNCD

An independent quantitative analysis of the NB SAM on diamond was carried out by electrochemical methods. Here, the terminal nitro group is known to be a suitable electroactive group.^{241,242} First, the presence of NB monolayer on UNCD by cyclic voltammetry was studied under aprotic conditions. Figure 51 shows the cyclic voltammogram

recorded by sweeping the potential from -2.0 V to +0.75 V versus Ag/AgCl in an acetonitrile solution of 100 mM tetrabutylammonium tetrafluoroborate.

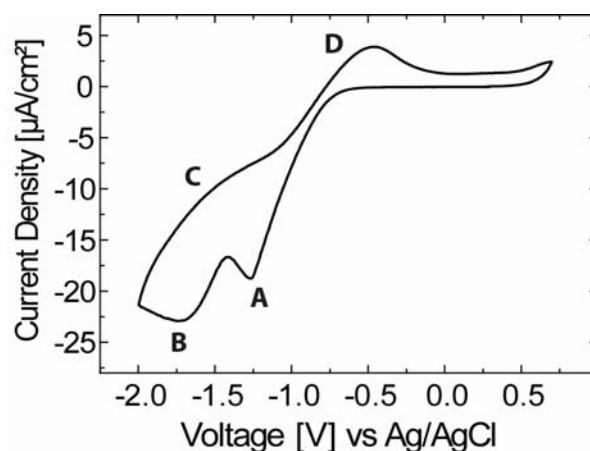


Figure 51. Cyclic voltammogram (recorded at a scan rate of 0.1 V s^{-1}) of a functionalized and doped UNCD electrode exposed to 0.1 M tetrabutylammonium tetrafluoroborate solved in CH_3CN at room temperature. Two reducing (A,B) and two oxidative (C,D) waves are distinguishable.²³¹

Under aprotic conditions, the nitro group shows a reversibly reduction to the radical anion, $\cdot\text{NO}_2$, involving a one-electron-transfer reaction.²⁴¹ The cathodic peak (B) located at -1.63 V is assigned to the reduction process of the NO_2 group. A large broadening of the corresponding nitro radical anion oxidation peak is clearly observed (C).

The total charge, Q , for the reduction of the nitro group can be used for the calculation of the grafting density of the NB monolayer if the exact electrode area (S) is known:

$$\sigma = \frac{Q}{n \cdot F \cdot S} = \frac{\int I dt}{n \cdot F \cdot S} \quad \text{Eq. 18}$$

F is the Faraday constant and n the number of electrons involved in the reduction of one nitro group ($n = 1$). A grafting density of $\sigma = 4.5 \times 10^{-10} \text{ mol}\cdot\text{cm}^{-2}$ was calculated, which is in excellent agreement with the XPS analysis ($\sigma = 4.6 \times 10^{-10} \text{ mol}\cdot\text{cm}^{-2}$). The appearance of the first cathodic peak (A) at $E = -1.26 \text{ V}$ can be attributed to a partial reduction of residual nitro to amino group as described later. This parasitic reaction can be explained by traces of water present in the electrolyte, since the experiment was carried out with a standard Ag/AgCl reference electrode. The created NB radicals in the monolayer react with protons from the small amount of water in the otherwise aprotic solvent.

The reductive conversion of the nitro group of the NB monolayer to the corresponding amino-terminated SAM can thus also be achieved by electrochemistry, which allows e.g. an in situ conversion of the SAM and immediate coupling of compounds additionally added to the electrolyte. The reduction of the nitro group occurs via an irreversible six-electron step process (Figure 52).²⁴³

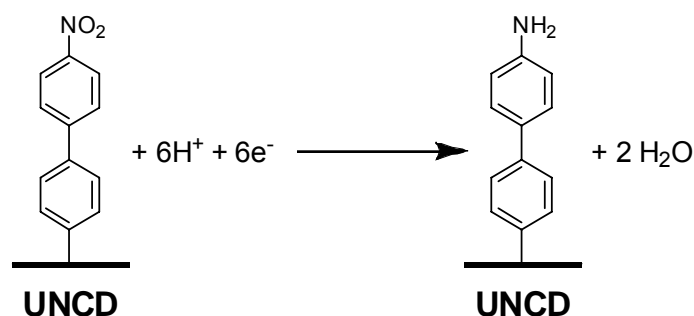


Figure 52. Electrochemical reduction of NB SAMs to 4'-amino-1,1'-biphenyl (AB) SAMs.²³¹

The electrochemical nitro to amino conversion was studied by cyclic voltammetry in a protic electrolyte. Figure 53a shows a strong cathodic peak (1) in the first scan, at a potential of -1.08 V versus Ag/AgCl, which can be assigned to the reduction of the NB nitro group. In subsequent cycles (2,3), no current peaks are observed. This indicates an irreversible electrochemical conversion of the NB nitro group to a surface bonded amino group. The nitro to amino conversion was confirmed by XPS (Figure 53b).

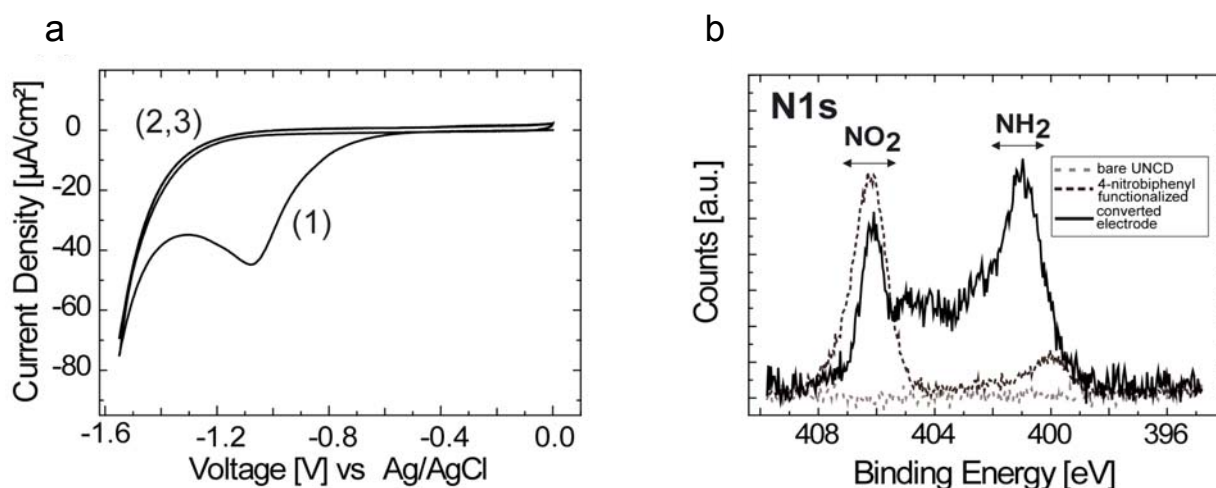


Figure 53. (a) Cyclic voltammogram of an NB-functionalized UNCD electrode recorded in 100 mM NaCl aqueous electrolyte solution. (b) N1s XPS spectra of the NB-functionalized UNCD electrode before and after the electrochemical reduction.²³¹

For the voltammogram in Figure 53a, the integrated charge is approx. 300 μC . Inserting this value into Eq. 18, a grafting density of $\sigma = 5 \times 10^{-10} \text{ mol}\cdot\text{cm}^{-2}$ was calculated, which is consistent to the above discussed results in an aprotic electrolyte as well with the XPS analysis.

Finally, cyclic voltammetry has been used in order to demonstrate that the NB molecules are chemically attached to the diamond substrates. Figure 54 shows different voltammograms of an electrochemically reduced NB monolayer on an UNCD electrode in protic electrolyte. An oxidation peak and a broad reduction peak can be observed.

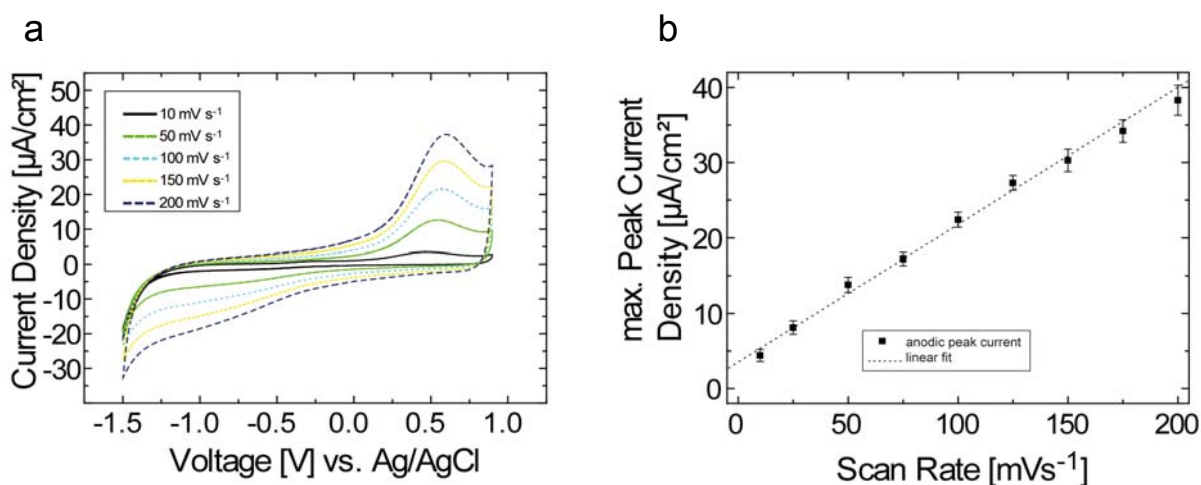


Figure 54. (a) Cyclic voltammograms of a reduced, NB-functionalized UNCD diamond electrode in a 100 mM NaCl aqueous solution at various scan rates (10 to 200 $\text{mV}\cdot\text{s}^{-1}$). (b) Plot of the maximum anodic peak current density versus the scan rate.²³¹

Increasing the scan rate causes the peak current to increase. Figure 54 shows that the height of the anodic peak is proportional to the potential scan rate up to 200 $\text{mV}\cdot\text{s}^{-1}$, indicating the presence of the surface-grafted redox group, namely the NO_2 group of the NB SAM. The observed reversible couple is assigned to the hydroxyaminobiphenyl/nitrosobiphenyl interconversion.²⁴⁴ The reduction route can be divided in a first, irreversible followed by a second reversible step (Figure 55). First, the nitro group is not completely reduced and ends up in an electro-active intermediate state. This can clearly be observed in Figure 53a. Assuming a two-electron process, the integrated charge (20 μC) from the cyclic voltammogrammetry represents a surface coverage of approx. $1.0 \times 10^{-10} \text{ mol}\cdot\text{cm}^{-2}$. This indicates that up to 20 % of the nitro group transform into a hydroxyamino during the reduction reaction. The nitroso groups or hydroxyl amino can not be further converted into an amino group and could explain the presence of nitrogen with a chemical shift corresponding to an N-O bond in the N1s XPS spectra of the converted electrode (Figure 54).

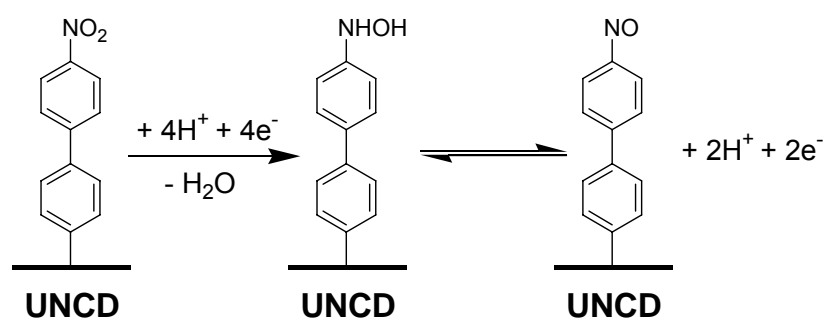


Figure 55. Reversible redox reaction between the hydroxyamino and nitroso function.²³¹

In conclusion, it can be stated that the spontaneous grafting of NBD molecules on diamond, results in stable, homogeneous and dense NB monolayers. The nitro group can be reduced with X-rays or electrochemically. Very recently, Gerhard Richter showed that after the reduction of the nitro group, the surface-bonded amino functionality can be further functionalized and that besides NBD molecules, different aryl diazonium salts containing various chemical functionalities can be grafted onto diamond substrates by this approach.²⁴⁵

4.3.3 Microstructured polymer grafts on diamond by SIPGP

It has been pointed out in the introduction that polymer grafts are of particular interest for biomedical applications. The liquid phase can penetrate into the polymer layer and molecules can interact with binding partners which are immobilized within the layer and that *this three-dimensional arrangement of binding sites allows designing model systems which much more resemble the biological environments compared to the direct immobilization on flat surfaces.*⁶ Furthermore, grafted polymer chains can have multiple binding sites for the coupling of e.g. enzymes (in contrast to most SAM systems, where each grafted SAM molecule has only one potential binding site). This may drastically increase the sensitivity of biosensors based on polymer coatings.

Until now, only three studies reported on polymer coatings covalently attached to diamond: Li *et al.*²⁴⁶ reported on the functionalization of oxidized nanodiamond particles via ATRP, Matrab *et al.*²²⁰ reported on ATRP of styrene and MMA initiated by electro-grafted aryl diazonium salt on H-terminated UNCD and Actis *et al.*²¹⁸ reported on the electropolymerization of pyrrole on oxidized diamond electrodes modified by silane monolayers bearing a pyrrolyl unit.

In chapter 4.2, it was shown that defined polymer grafts can be synthesized directly onto organic surfaces containing diverse functional groups by the self-initiated photografting and photopolymerization (SIPGP) of styrene and acrylic monomers. In this perspective, it has been investigated if the SIPGP can be applied for the preparation of dense, homogeneous and chemically stable polymer grafts directly onto UNCD substrates.

4.3.3.1 Preparation of PS grafts on microstructured oxidized UNCD

The SIPGP of styrene was performed in a first experiment, on a structured oxidized UNCD substrate. The structured oxidized UNCD substrate was prepared in the research group of Garrido as follow (Figure 56): a freshly H-terminated UNCD sample was patterned (20 μm wide parallel stripes) using a conventional spin-coated photoresist layer. The substrate was successively exposed to an oxygen plasma to form hydroxyl surface functionalities on diamond surfaces.²¹⁹ The photo resist layer was removed by ultrasound in different solvents. The patterned substrate was then submerged in styrene and irradiated with UV-light ($\lambda_{\text{max}} = 350 \text{ nm}$) for 16 h. To ensure that only chemically grafted polymer remained on the surface, the substrate was intensively cleaned in different solvents (toluene, ethyl acetate and ethanol, under ultrasonification for 5 minutes each).

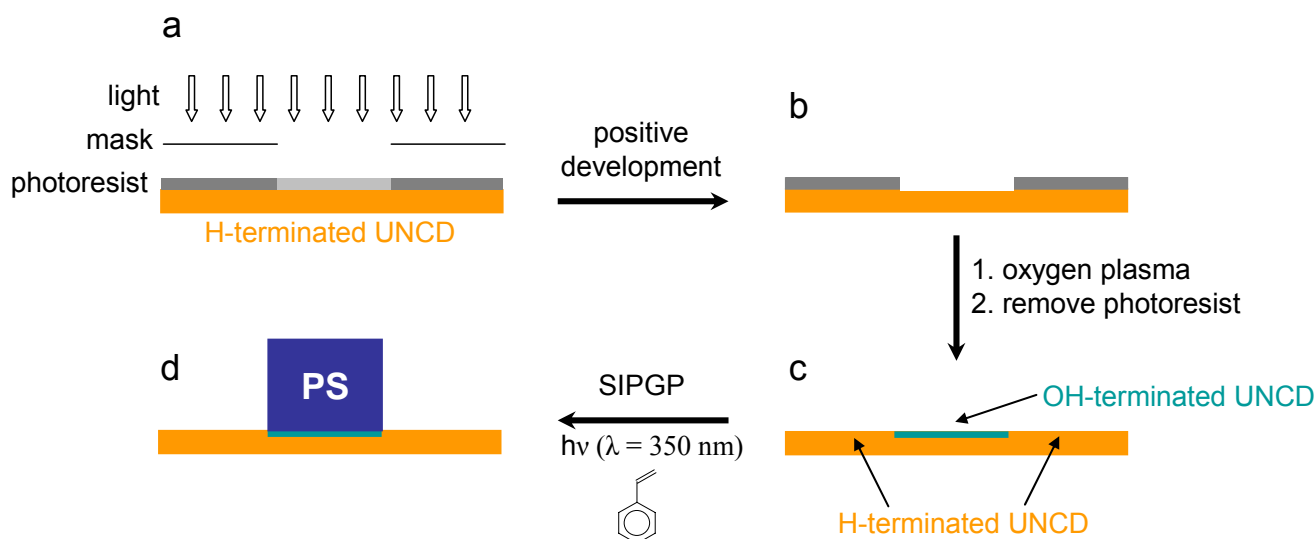


Figure 56. Preparation of structured PS grafts on UNCD. (a) An H-terminated UNCD sample is structured by a spin-coated photoresist material. (b) The substrate is exposed to an oxygen plasma after the positive development of the photoresist layer (c). (d) PS grafts are selectively formed on the oxidized UNCD surface regions by the SIPGP of styrene.

The AFM measurement of the sample revealed that PS grafts were selectively formed onto the previously oxidized surface regions (Figure 57). It is noteworthy that the observed structure roughness in Figure 57 is due to the roughness of bare UNCD substrates. Data analysis of the AFM scan revealed that the surface roughness on PS coated regions was, with an rms of 6.0 nm, lower than on unfunctionalized UNCD regions (rms 9.6 nm).

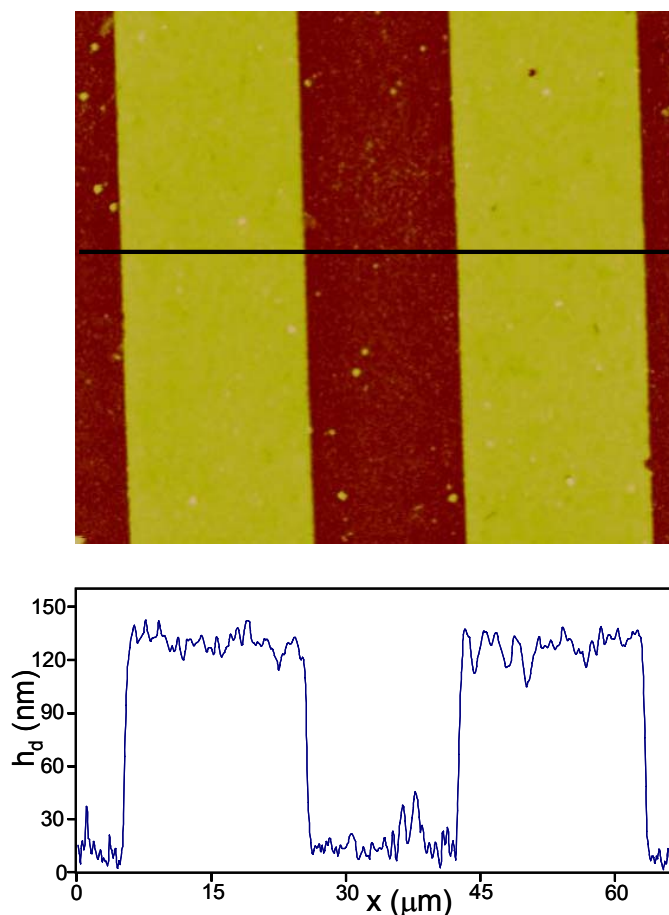


Figure 57. AFM scan ($70 \mu\text{m}^2$) and section analysis of patterned PS grafts on UNCD.

The apparent absence of polymer grafts on H-terminated UNCD surface regions is at first sight very surprising. In the SIPGP mechanism, the photoactivated monomer abstracts a hydrogen radical of a surface functionality and the radical formed on the surface-initiates the free radical SIP. According to this mechanism, the absence of polymer grafts on H-terminated diamond can have two reasons: photoactivated monomer molecules are not able to abstract hydrogen radicals or the radicals formed on the substrate are not able to initiate the free radical SIP. No experimental data confirmed either of these two hypotheses. However, the difference in reactivity between the H- and OH-terminated diamond surface regions can be explained by the energy, required for hydrogen radical abstraction. Karin Larsson calculated

the theoretical C-H bond dissociation energies (BDEs) on H-terminated (100) diamond surfaces and the O-H bonding energy on OH-terminated (100) diamond surface, based on the density functional theory. Using the same model as in reference 247, she calculated an O-H and C-H BDE of respectively 17 kcal·mol⁻¹ and 95.9 kcal·mol⁻¹. This indicates that the reactivity difference between hydrogenated and oxidized diamond substrates is determined by the energy needed to abstract one hydrogen radical from the substrate. This reactivity difference allows the formation of structured polymer grafts on diamond by this straightforward procedure.

The lateral resolution of this method is determined by the lateral resolution of the oxidation step. Conventional photolithography cannot be applied for the preparation of nanostructured polymer grafts. However, it has been mentioned in chapter 2.5.2.3, that various substrates can be locally oxidized by anodic oxidation, using a scanning tunneling microscopy (STM) tip. The SIPGP on diamond substrates structured by STM induced oxidation may be an interesting approach for the preparation of nanostructured polymer grafts on diamond. Furthermore, the hydroxyl surface concentration can be controlled during the STM oxidation step which may have a direct influence on the resulting polymer layer thickness.

However, for the preparation of diamond based (bio)-sensors, we were more interested to investigate different strategies for the preparation of polymer grafts bearing various organic functionalities to be used in further functionalization steps than to develop advanced structuring methods.

4.3.3.2 Functionalization of PS grafts on oxidized UNCD

In general, the preparation of polymer grafts with a desired chemical function can be achieved by the SIP of a monomer bearing this functionality. However, it is often easier to perform first the SIP of a simple monomer followed by a polymer analogue functionalization of grafted chains. This second approach was not only chosen for its simplicity, but also because only a very limited number of monomers can be grafted directly onto organic surfaces by SIPGP. This approach requires a high chemical and/or thermal stability of the linker between the surface and the polymer chains during the polymer analogue functionalization steps and this is a major limitation for commonly used thiol or silane based systems. In this case, the polymer grafts are linked via a stable ether bond, directly onto the diamond substrate.

In this section, different synthetic routes were investigated for the functionalization of PS grafts, under quite drastic reaction conditions. The explored functionalization reactions were

based on synthetic routes developed for solid phase organic synthesis on polymer resins. Crosslinked PS resins and their derivatives are widely used for solid phase organic synthesis and many strategies were developed for the functionalization of these resins.²⁴⁸ The use of synthetic routes developed for the organic phase synthesis on polymer resins presents several advantages, because synthetic transformations of polymer grafts and resins have to comply with the same requirements:

1. Homogeneous reaction conditions. The use of insoluble compounds during the modification of polymer grafts (e.g. K_2CO_3 as base in organic solvents) is problematic because the insoluble powder may scratch the thin and soft polymeric layer.
2. Chemical stability of the polymer (e.g. the use of strong bases or strong acids cannot be applied during the functionalization of polyester based resins). In the case of polymer grafts, also the chemical stability of the substrate is a prerequisite.
3. A sufficient swelling of the polymer layer is needed to ensure a sufficient mass transport of the binding partners within the layer. For this reason, the choice of the applied solvents is important. The functionalization of polymer resins with another solvent, in otherwise identical reaction conditions, can increase the reaction yield from less than one percent to nearly hundred percent.²⁴⁸

4.3.3.3 Nitration and sulfonation of PS grafts on oxidized UNCD

In a first set of experiments, PS grafts created by the SIPGP of styrene on oxidized UNCD were functionalized under drastic reaction conditions: the nitration by fuming nitric acid and the sulfonation by a sulfuric acid/acetic anhydride mixture (acetylsulfuric acid) at 60°C in 1,2-dichloroethane (DCE) (Figure 58).²⁴⁹ The substrates were intensively rinsed with different solvents after the functionalization reactions.

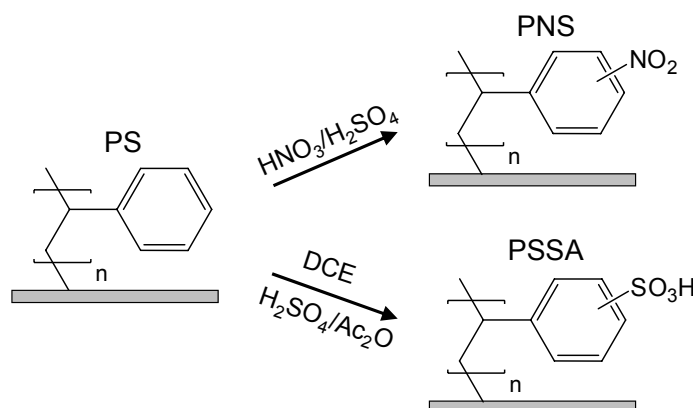


Figure 58. Nitration and sulfonation of PS grafts.

The conversion of PS grafts to poly(nitrostyrene) (PNS) and poly(styrenesulfonic acid) (PSSA) was investigated on unstructured oxidized UNCD substrates by diffusion reflectance Fourier transform infrared (DRIFT) spectroscopy and XPS.

The chemical composition of the polymer grafts was determined by DRIFT (Figure 59). The DRIFT spectrum of PS shows the characteristic stretching vibrational modes of aromatic groups ($\nu(\text{CH})$ at around 3030 cm^{-1} and $\nu(\text{CC})$ between 1430 and 1610 cm^{-1}) and the methylene groups of the polymer backbone with a maximum at 2923 cm^{-1} . After nitration of the PS layer, two strong absorption bands at 1350 cm^{-1} and 1531 cm^{-1} appear, characteristic for the symmetric ($\nu_s(\text{NO}_2)$) and asymmetric ($\nu_{as}(\text{NO}_2)$) vibration modes of aromatic nitro groups.²⁵⁰

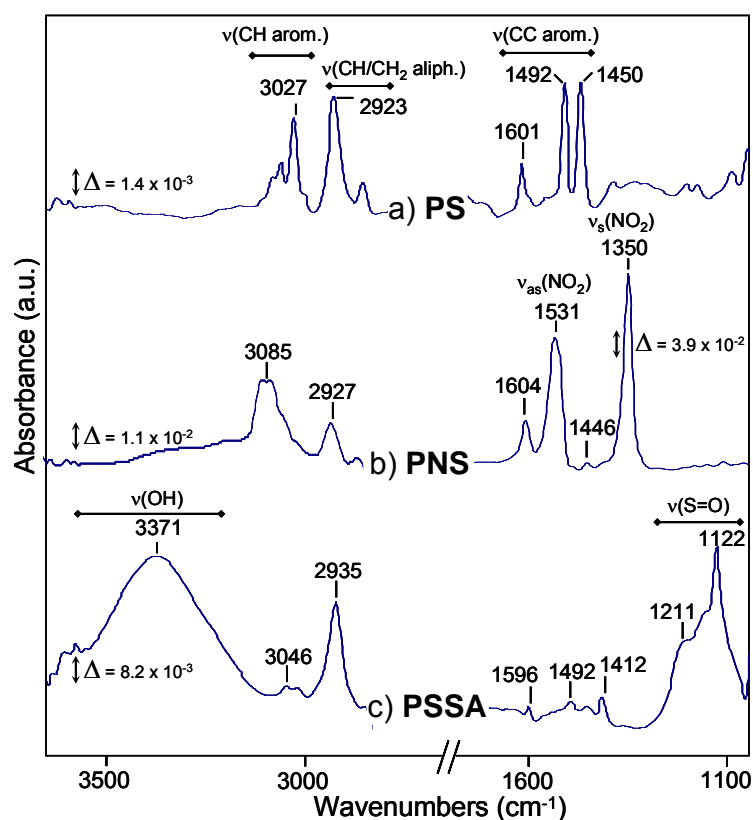


Figure 59. DRIFT spectra of PS, PNS and PSSA grafts on unstructured UNCD.

After sulfonation of the PS grafts, the spectrum shows one broad absorption band centered at 3371 cm^{-1} , characteristic for the sulfonic acid $\nu(\text{OH})$ stretching mode and two intense bands between 1100 and 1250 cm^{-1} corresponding to the $\nu(\text{S}=\text{O})$ stretching modes of aromatic sulfonic acid.^{250,251}

From these DRIFT measurements, it can be stated that PS was successful converted into PNS and PSSA. Furthermore, the intensive $\nu(\text{NO}_2)$ and $\nu(\text{S}=\text{O})$ bands indicates a high substitution rate through the entire polymeric layer.²⁵² A more quantitative analysis of the nitration and sulfonation substitution rates was performed by XPS measurements.

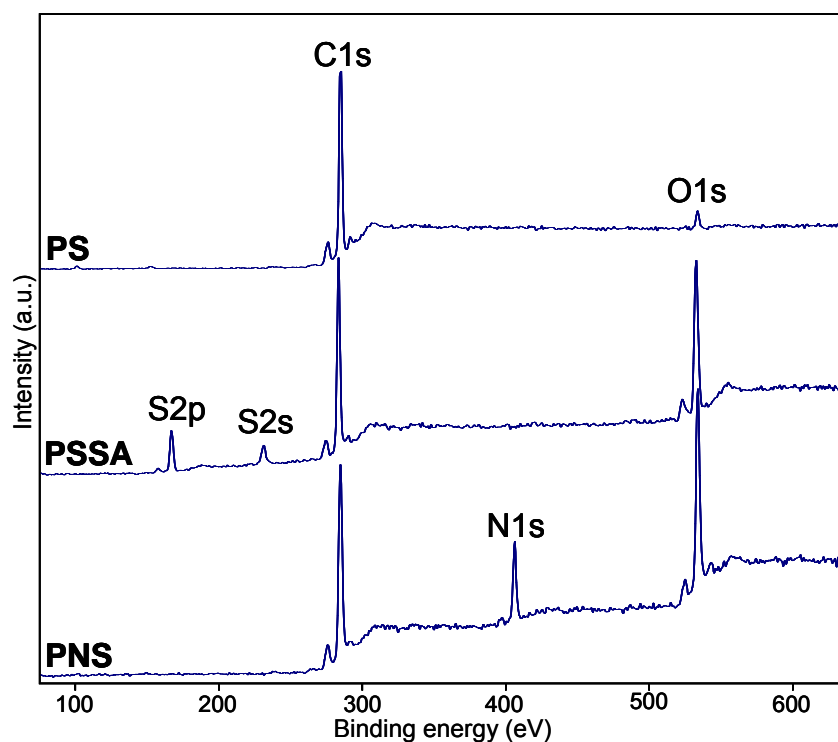


Figure 60. XPS survey scans of PS, PSSA and PNS grafts onto oxidized UNCD.

Figure 60 shows the survey scans of PS, PSSA and PNS grafts. The C1s and O1s peaks are centered at 285 and 533 eV, respectively. The N1s peak present in the PNS spectrum is centered at 406 eV indicates the presence of nitro groups.¹⁷⁶ The S2p and S2s centered at 168 and 232 eV can be attributed to the aromatic sulfonic acid group in PSSA.²⁵³

The relative atomic surface composition was determined by calculating the XPS peak areas with a Voigt fit function, taking into account the sensitivity factors for the different elements (Table 8).

Polymer	C	O	N	S
PS	8	0.46	–	–
PSSA	8	4.33	–	0.98*
PNS	8	3.58	2.66	–

Table 8. Relative atomic surface composition of the polymer grafts determined by XPS. (*) Average of the S content from the S2p (0.88) and S2s peak (1.08).

The S/C ratio of approximately 1/8 in PSSA grafts indicates an average of one sulfonic acid group per aromatic ring. As apparent from Table 8, the surface atom composition of PS and PSSA grafts have a slightly higher oxygen content than expected. The oxygen contamination might be caused by the presence of strongly absorbed water or organic solvent, used during the substrate cleaning process.

The N/C ratio for the PNS grafts of 2.66/8 indicates an average of 2.66 nitro groups per aromatic ring while the O/C ratio of 3.58/8 indicated a substitution ratio of only 1.89. The introduction of approx. two nitro groups on each aromatic ring under these reaction conditions ($\text{HNO}_3/\text{H}_2\text{SO}_4$ 2/5 mixture at 60°C) is in agreement with earlier reports: while the first substitution occurs in the para position, the second is located in ortho position.²⁵⁴

It is important to note that XPS measurements do not give the atomic composition of the entire polymeric layer but only from the upper few nanometers. It has been shown in chapter 4.3.2.3 that the emission intensity in XPS measurements is lower for functionalities located deeper in the material, due to inelastic scattering of electrons. Reorganization within the polymeric layer may influence the measured composition (e.g., the measured S/C ratio in PSSA grafts may be higher than the average S/C ratio in the entire polymer layer due to the interaction between sulfonic acid groups and air humidity).

The homogeneity of the polymer layer after the nitration and the sulfonation step was verified by AFM measurements. The bare oxidized UNCD samples used in these experiments had a roughness of rms = 16.5 nm. After the SIPGP of styrene (t_p : 16h), a roughness of 9.2 nm was measured. A roughness of respectively 5.1 and 5.5 nm (rms) was measured after the nitration and sulfonation reactions.

From these results, it can be concluded that PS grafts created by the SIPGP on oxidized diamond substrates are chemically stable in the presence of strong acids such as sulfuric acids, and strong oxidative agents such as fuming nitric acid. These first results show the major advantage of this approach, in which polymer grafts are directly and covalently attached to the substrate via thermal and chemical stable links. This allows the further functionalization of the polymer grafts without constraints with respect to the reaction conditions.

4.3.3.4 Preparation of poly((4-aminomethyl)styrene) grafts on oxidized UNCD

In this section, the modification of PS grafts to poly((4-aminomethyl)styrene) grafts (PAMS) was studied. Aminomethyl derivatives of crosslinked PS resins are widely used for solid

phase organic synthesis and many synthetic routes were developed for further functionalization of these resins.²⁴⁸ The conversion of the PS to the PAMS grafts was performed following the synthetic route developed by Merrifield and coworkers²⁵⁵ for the functionalization of crosslinked PS resins (Figure 61).

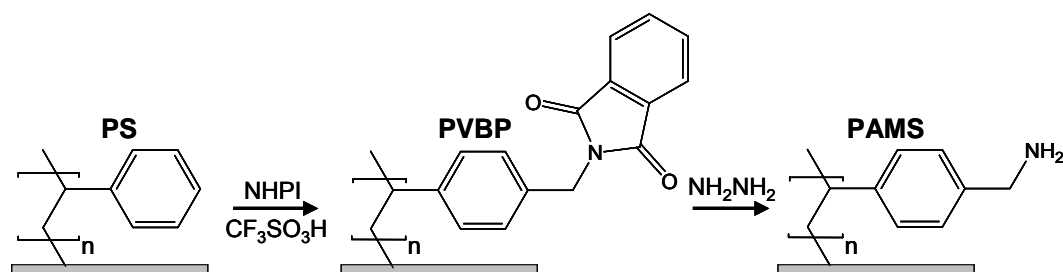


Figure 61. Synthetic route to PAMS grafts.

In a first step, the PS grafts are amidoalkylated by the Tscherniac-Einhorn reaction with N-(hydroxymethyl)phthalimide (NHPI) resulting in poly(4-vinylbenzyl)phthalimide grafts (PVBP). The reaction takes place at room temperature and is catalyzed by trifluoromethanesulfonic acid (CF₃SO₃H). In a second step, the phthalimide group was hydrazinolysed in refluxing ethanol over night (5 volume% hydrazine dihydrate). The surface was cleaned by sonification in different solvents after each reaction step.

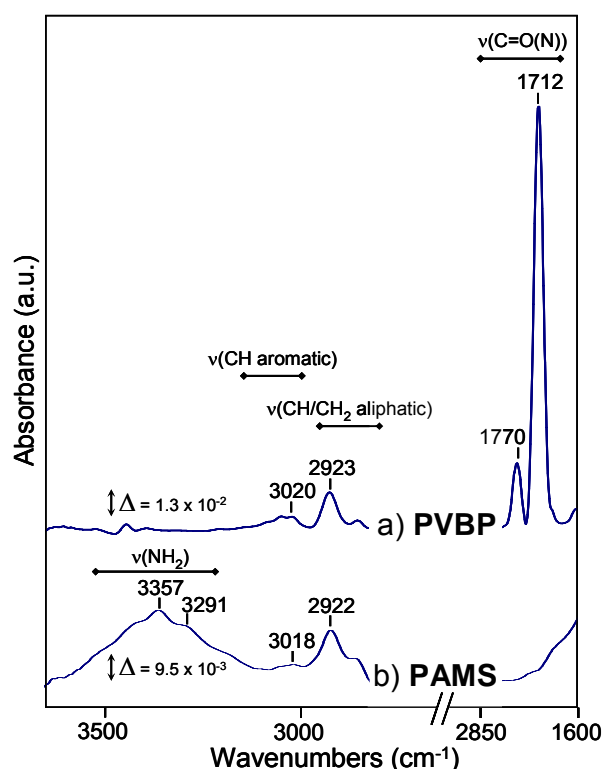


Figure 62. DRIFT spectra of PVBP and PAMS grafts on UNCD.

The successive reaction steps were followed by DRIFT spectroscopy (Figure 62). The two strong absorption bands at 1712 and 1770 cm^{-1} are characteristic for the phthalimide carbonyl stretching vibrational modes $\nu(\text{C}=\text{O}(\text{N}))$.²⁵⁶ The hydrazinolysis of the poly(4-vinylbenzyl)phthalimide (PVBP) grafts was confirmed by the absence of absorption bands at 1712 and 1770 cm^{-1} . The broad absorption band centered at 3357 cm^{-1} and the shoulder at 3291 cm^{-1} are characteristic for the asymmetric and symmetric amino stretching modes and the spacing of 66 cm^{-1} between the symmetric and asymmetric absorption bands in the IR spectrum is in agreement with earlier reports.²⁵⁰ The successful hydrazinolysis reaction in refluxing ethanol shows that the polymer grafts are also stable under reducing reaction conditions.

4.3.3.5 Functionalization of microstructured PAMS grafts on UNCD with a fluorescence dye

In this section, the reactivity and accessibility of the aminomethyl group in PAMS grafts was investigated. In order to demonstrate that the aminomethyl group can be functionalized even with relatively big organic molecules, PAMS grafts created on microstructured oxidized UNCD surfaces were labeled with rhodamine B isothiocyanate (RBITC) (Figure 63).

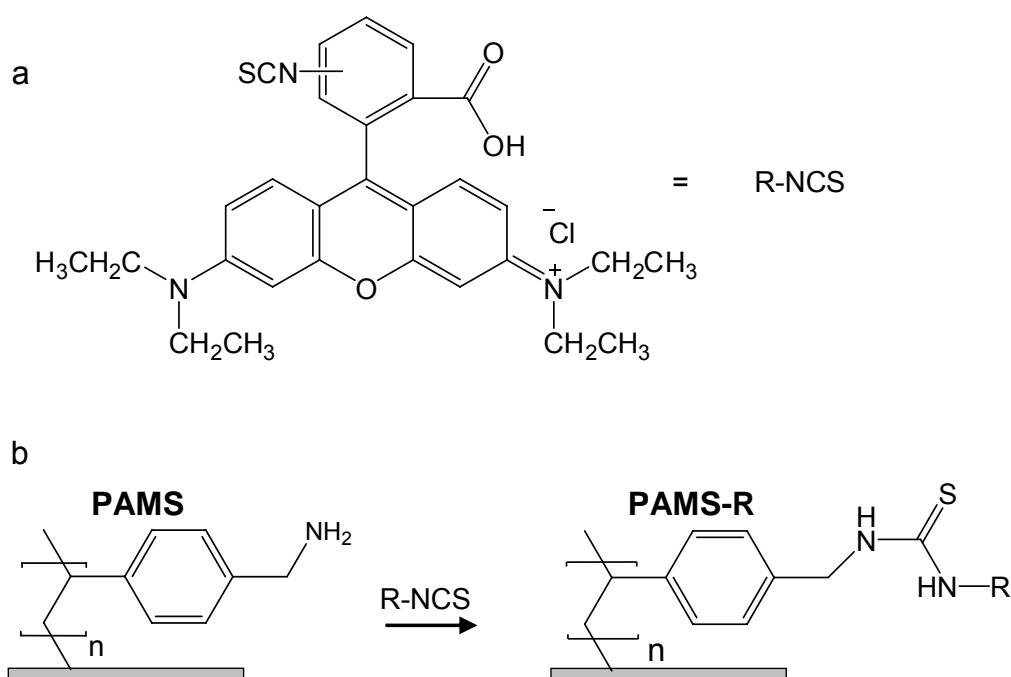


Figure 63. (a) Rhodamine B isothiocyanate. (b) Functionalization of PAMS grafts with Rhodamine B isothiocyanate.

Under absence of light, the substrate was immersed in a 10mM RBITC solution in ethanol for 3 days at room temperature. After intensive cleaning with ultrasound in ethanol in order to remove all physisorbed material, a strong fluorescence signal was detected on the oxidized UNCD surface areas (Figure 64) which shows that RBITC is covalently bonded to the PAMS grafts.

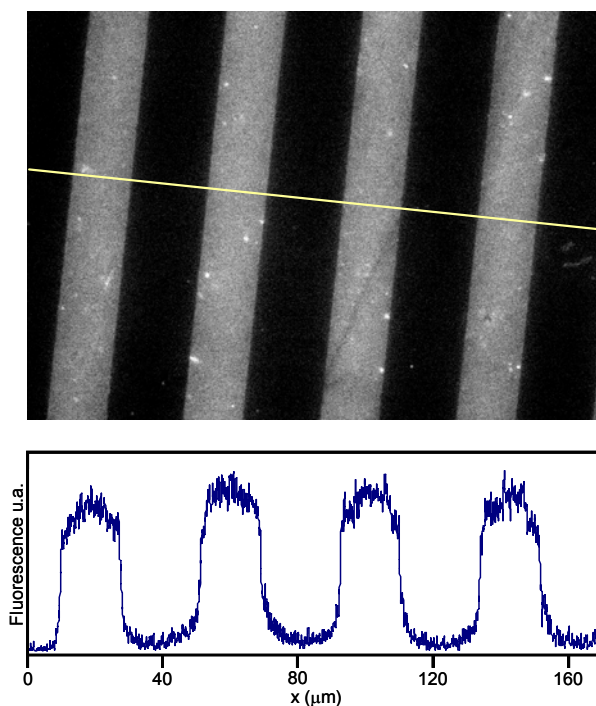


Figure 64. Fluorescence image and section analysis of a patterned oxidized UNCD surface, functionalized with PAMS grafts and labeled with RBITC. The bright regions correspond to the oxidized surface areas. The cross section was obtained by a pixel analysis of the 256 bit black and white fluorescence image.

The AFM image in Figure 57 shows that polymer grafts were created onto the oxidized UNCD regions. However, the height difference between the oxidized and non-oxidized regions does not unambiguously prove the absence of a thin polymer layer on the H-terminated UNCD regions. In order to control the presence of polymer grafts on the non-oxidized UNCD regions of microstructured substrates, the fluorescence signal of the dark regions in Figure 64 and the fluorescence signal of an unfunctionalized H-terminated UNCD sample were compared (Figure 65). Figure 65 shows that a reference sample of an unfunctionalized H-terminated UNCD sample, has approximately the same fluorescence intensity than the dark regions on the structured sample. This is a strong indication of the absence of polymer grafts on H-terminated UNCD regions since rhodamine B molecules can be detected at very low

surface concentration (less than one monolayer) by fluorescence measurements.²⁵⁷ Thus, PS grafts were selectively formed on the oxidized UNCD surface regions during the SIPGP step.

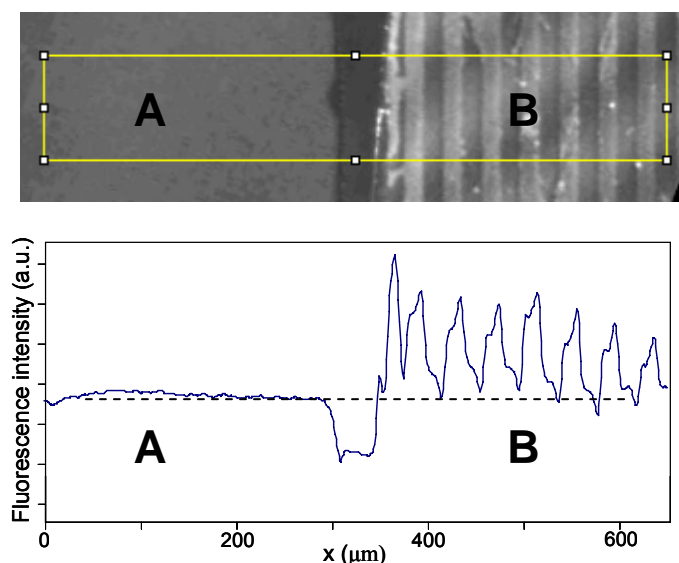


Figure 65. Fluorescence image and average section analysis of an unfunctionalized H-terminated UNCD sample as reference (A) and a patterned oxidized UNCD surface, functionalized with PAMS grafts and labeled with RBITC (B).

As conclusion, it can be stated that the SIPGP allows the preparation of polymer grafts directly and selectively onto oxidized UNCD substrates. The successful functionalization of PS grafts following the different synthetic routes, demonstrates that the polymer grafts are chemically stable under acidic (sulfuric acid), reducing (hydrazine) or oxidative (fuming nitric acid) reaction conditions. Further functionalizations of the aminomethyl group in PAMS grafts with enzymes for biosensor applications is currently under investigation in the research group of Garrido.

4.3.4 SIPGP of styrene on glassy carbon and graphite

One major advantage of the SIPGP is that this process can be performed using various surface functionalities. The only requirement is the presence of surface functionalities from which hydrogen radicals can be abstracted by a photoactivated monomer, and that the successively formed surface-bonded radicals can initiate a free radical polymerization. This allows the formation of polymer grafts on relatively undefined organic surfaces.

Advantage has been taken of this characteristic for the preparation of unstructured polymer grafts directly onto graphite and glassy carbon. Glassy carbon, also called vitreous carbon, is a non-graphitizing carbon which combines glassy and ceramic properties with those of graphite. The most important properties are high temperature resistance, extreme resistance to chemical attack and impermeability to gases and liquids. Glassy carbon electrodes are widely used. Glassy carbon is prepared by a series of heat treatments at temperatures up to 3000°C of organic precursors, such as polymeric resins. Glassy carbon is chemically almost identical to graphite (100 % sp^2 hybridized carbon), however, the properties which make glassy carbon so valuable are poorly understood, since its detailed atomic structure is not known. A recent study has shown that glassy carbon contains a high proportion of fullerene-related structures (Figure 66).²⁵⁸

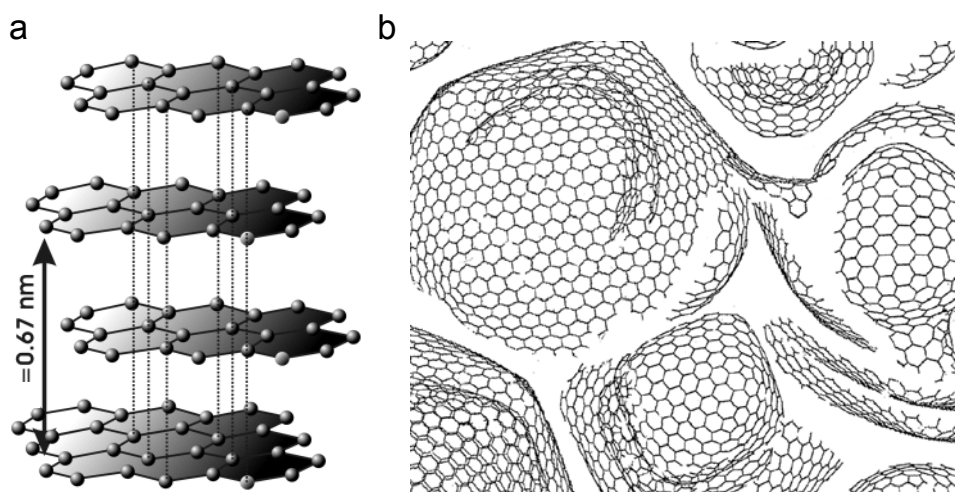


Figure 66. (a) Crystal structure of graphite.²⁵⁹ (b) Model for the structure of glassy carbon.²⁵⁸

A bare glassy carbon substrate was placed in bulk styrene and irradiated with UV-light ($t_p = 16h$). The substrate was successively cleaned by sonification in toluene, ethyl acetate and ethanol (each solvent 5 minutes) and dried. DRIFT measurements (Figure 67) showed the presence of PS grafts after the SIPGP of styrene on glassy carbon ($t_p: 16h$).

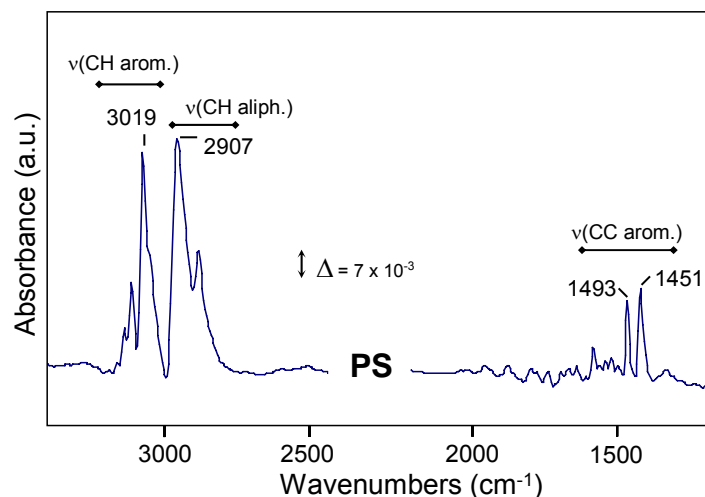


Figure 67. DRIFT spectra of PS on glassy carbon.

Since the surface composition of glassy carbon substrates is until now unknown, an exact mechanism for the SIPGP can not be presented here. At first sight, the reactivity difference between hydrogenated diamond and glassy carbon toward SIPGP may be surprising. However, it is likely that the BDEs for hydrogen abstraction on glassy carbon are significantly lower than on H-terminated diamond due to the stabilization of the surface bonded radicals by electron delocalization throughout the entire conjugated sp^2 hybridized carbon structures.

Preliminary results showed that PS grafts on glassy carbon have the same chemical stability as the PS grafts created on oxidized UNCD and that also other vinyl monomers can be polymerized. The preparation of chemically stable (unstructured) polymer grafts directly onto glassy carbon may have interesting electrochemical application.

Glassy carbon substrates may be used as cheap *test* electrode material for the study of the chemical functionalization of polymer grafts on diamond. Due to the high cost of UNCD substrates, new (bio)-responsive polymer grafts may first be developed and tested on glassy carbon substrates.

PS grafts were prepared under identical reaction conditions on graphite substrates. It was observed that when a bare graphite substrate was cleaned by ultrasonification, the solvent became turbid (Figure 68a).

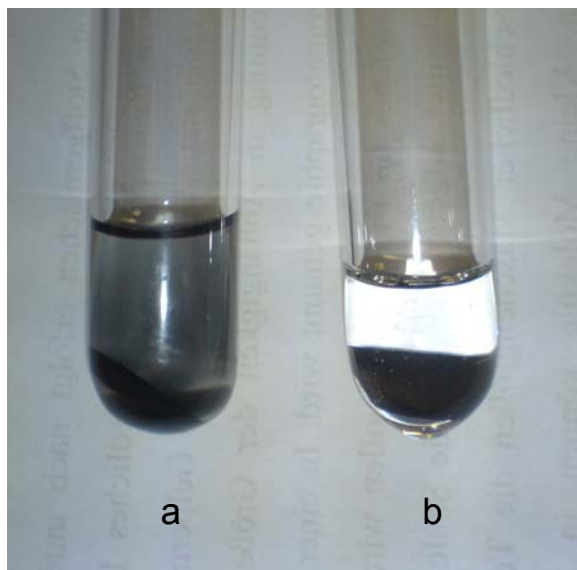


Figure 68. (a) Photograph of a bare graphite sample immersed in toluene after ultrasound treatment. (b) Photograph of a graphite sample coated with PS (SIPGP of styrene, $t_p = 16\text{h}$) immersed in toluene after the same ultrasound treatment.

This is caused by the detachment of weakly bonded graphite layers. However, when a graphite sample, coated with PS grafts (SIPGP t_p : 16h), was cleaned by identical ultrasound treatment, the solvent remained transparent (Figure 68b). This indicates that the PS layer stabilizes the entire graphite substrate. The preparation of protective coatings on different substrates by the SIPGP of styrene is currently under investigation by Ning Zhang.

4.4 3D micro- and nanostructured polymer grafts on isolators, semiconductors and conductors by SIPGP on electron beam induced carbon deposits

4.4.1 General approach

The different advantages of the SIPGP have already been pointed out in the previous chapters. The SIPGP can be performed on various organic substrates bearing *abstractable* hydrogen radicals. The possibility to form polymer grafts on oxidized UNCD or glassy carbon have shown that defined surface functionalities are not required. Furthermore, polymer grafts prepared by SIPGP are chemically very stable. This is due to the fact that the polymer grafts are directly linked via stable C-O-C, C-NH-C or C-C bonds to the substrate. SIPGP also allows the formation of defined three dimensional structured polymer grafts such as gradients, as shown in chapter 4.2. The key step in this approach is the fact that the locus as well as the thickness of the polymer grafts can be controlled during the EBCL step.

In chapter 2.5.4.3 the electron beam induced carbon deposition (EBCD) technique has been presented. This substrate independent technique allows the formation of stable, crosslinked hydrocarbon deposits with a lateral resolution comparable to that of EBCL. The structured carbon deposits are created directly onto a substrate, simply by irradiating the substrate with an electron beam in a vacuum chamber, without the introduction of additional precursor molecules. The decomposition of residual hydrocarbon molecules present in the vacuum chamber, originated from the pump oil, is responsible for the formation of EBCDs.

In this part of the work, it was investigated if polymer grafts can be prepared by the SIPGP of styrene and acrylic monomers onto thin electron beam induced carbon deposits on isolators, semiconductors and conductors. Moreover, the dependence between the applied electron beam dosage and the resulting graft morphology was studied. EBCDs have a composition close to $C_9H_2O_1$ containing diverse functionalities including hydroxyl and aliphatic C-H groups (see chapter 2.5.4.3) which can be activated by hydrogen abstraction during the SIPGP process. It must be noted here that no experimental or theoretical data are available from the actual C-H and O-H bond dissociation energies (BDEs) in EBCDs surface functionalities.

EBCDs have 90% sp^2 and 10 % sp^3 hybridized carbon. In other words, EBCDs can be regarded as polycyclic sp^2 aromatic hydrocarbons with sp^3 defects. The C-H BDEs of sp^3

centers in polycyclic sp^2 aromatic hydrocarbons has been calculated by Ahlrichs and coworkers.²⁶⁰ It was found that the C-H BDEs of sp^3 centers varied between 20 and 72 $\text{kcal}\cdot\text{mol}^{-1}$, depending on the location of the sp^3 center (see Figure 69). These very low BDEs are mainly due to the delocalization of electrons throughout the entire conjugated system.

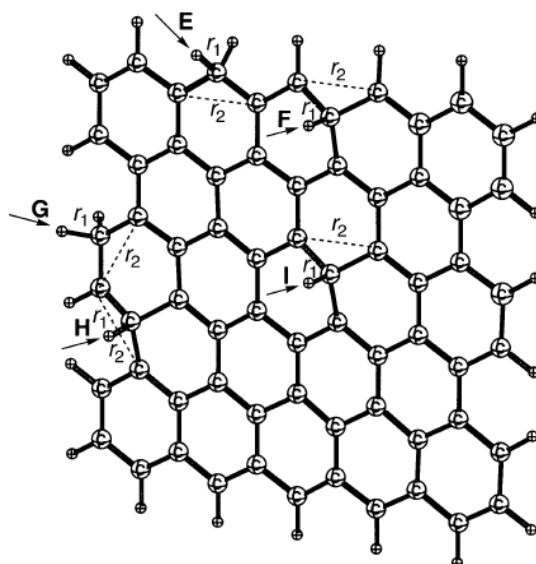


Figure 69. Different sp^3 centers in polycyclic aromatic hydrocarbons.²⁶⁰

The preparation of structured layers by the EBCD has several major advantages:

1. High resolution (analog to electron beam lithography).
2. Substrate independent (EBCDs can be prepared on almost any substrate).
3. No modification of the substrate other than cleaning.
4. Experimentally extremely simple.

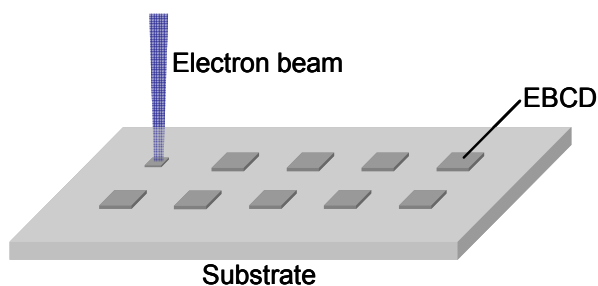


Figure 70. Irradiation of the substrate by an electron beam induces the formation of EBCDs on the irradiated surface areas.

4.4.2 SIPGP on EBCDs on silica

4.4.2.1 SIPGP of styrene on EBCDs on silica

In a first set of experiments, the SIPGP of styrene was tested on structured EBCDs on P-doped Si(100) wafers. A very thin layer (approximately 1-2 nm) of *native oxide* is formed on the surface when silicon is exposed to air under ambient conditions.

The substrates were first cleaned by a piranha solution ($\text{H}_2\text{SO}_4/\text{H}_2\text{O}_2$) and successively irradiated with an electron flood gun (50 eV; $60\text{mC}/\text{cm}^2$) through a stencil mask with circular openings of 1 μm radius. EBCD structures with a thickness of 0.9 ± 0.4 nm were created on the irradiated surface regions (Figure 71a). The substrates were then submerged in bulk monomer and irradiated with UV-light ($\lambda_{\text{max}} = 350$ nm). Approximately 150 nm thick PS grafts were selectively formed on the EBCDs after 23 h of UV irradiation (Figure 71b).

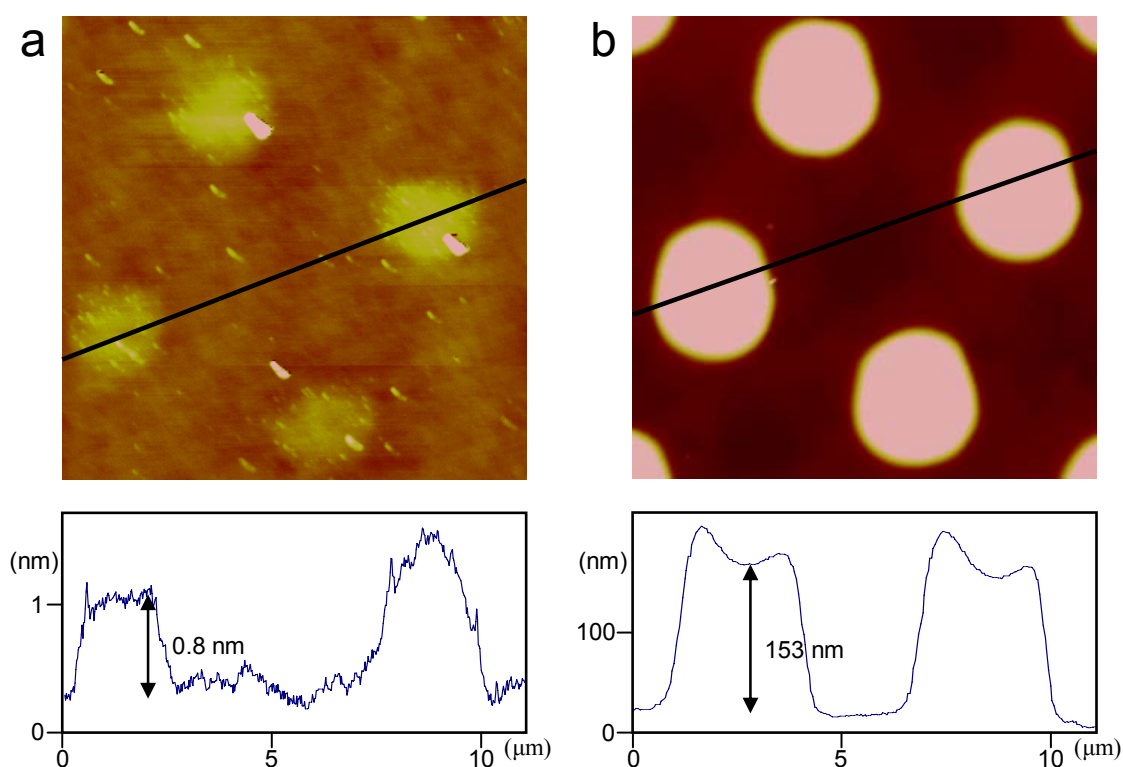


Figure 71. (a) AFM scans of EBCDs on silicon dioxide, created by an electron flood gun in combination with a stencil mask with circular openings of 1 μm radius. (b) Approximately 150 nm thick PS grafts were formed by the SIPGP of styrene (t_p : 23 h) on these EBCD structures.

At first sight, it may be surprising that no polymer grafts were formed on the bare silica. Silica has silanol surface functionalities from which hydrogen could be abstracted by a photoactivated monomer. However, the reactivity difference between the silica and the EBCD surfaces for the SIPGP can be explained easily by comparing the BDEs of both surface functionalities for hydrogen abstraction: the absence of polymer grafts on bare silica substrates is attributed to the very high SiO-H BDE of $119.3 \text{ kcal}\cdot\text{mol}^{-1}$ (in contrast to the C-H BDE between 20 and $72 \text{ kcal}\cdot\text{mol}^{-1}$ for EBCDs).²⁶¹

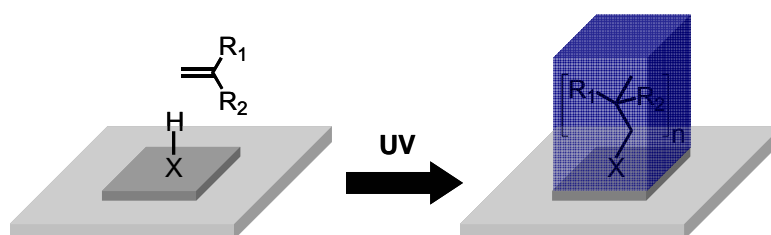


Figure 72. Principle for the formation of structured polymer grafts: a substrate coated with structured EBCDs is immersed into bulk monomer and irradiated with UV. Polymer grafts are selectively formed on the EBCDs by SIPGP (X = C or O).

4.4.2.2 Stability of the polymeric layer and EBCDs on silica

In order to verify that the EBCDs and the polymer grafts were strongly attached to the substrate, the described experiment was repeated with additionally two prolonged ultrasound cleaning steps (typical procedure: sonification in respectively ethyl acetate, toluene, H_2O , toluene, H_2O , acetone and ethanol; each solvent 5 minutes): one after the EBCD step and one after the SIPGP step. These two drastic cleaning steps had no significant effect on the morphology of the polymer structures. The only effect was that significantly cleaner substrates were obtained (unavoidable physisorbed material (polymer, dust, etc.) is removed during the ultrasound treatment). For this reason, these two cleaning steps were applied for all further experiments. The stability of the structures against these prolonged ultrasonic treatments is a strong indication that the EBCDs and the polymer grafts are covalently bonded to the silica substrate.

The thermal stability of the EBCDs and the polymer grafts was investigated by cleaning the substrates by Soxhlet extraction in different high boiling solvents. Successive Soxhlet extractions over night in water and mesitylene (boiling point = 164.7°C), after the EBCD step and the SIPGP step, had no influence on the resulting polymer structures.

This excellent thermal stability of the polymer structures is an additional indication that the polymer grafts are strongly attached to the substrate. The chemical stability of the polymer grafts will be discussed in chapter 4.4.6.

4.4.2.3 SIPGP on EBCDs on silica: *ex situ* kinetic studies

The *ex situ* kinetic studies of the SIPGP of styrene was performed on identical EBCD structures on silica. In Figure 73 the thickness of the dry polymer layer thickness (h_d) and error (θ) are plotted as a function of the polymerization time.

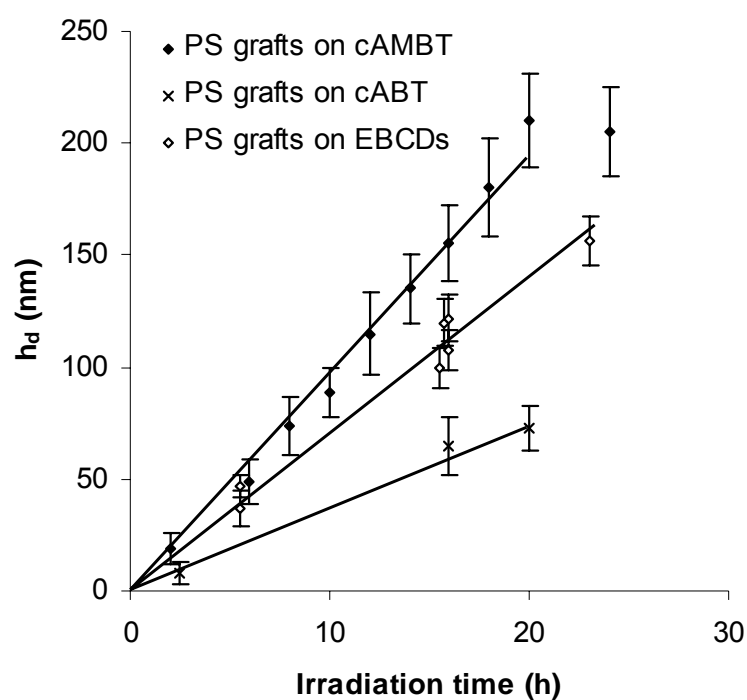


Figure 73. Dry polymer layer thickness, h_d , as a function of the irradiation time as measured by AFM on structured polymer grafts (1 μm radius, EBCD at 50 eV; electron dosage: 60 mC/cm^2).

The average height and error were obtained by AFM measurements as described in chapter 4.1.1. Figure 73 reveals a linear relationship between h_d and the irradiation time and a relatively good experimental reproducibility. It has already been pointed out in chapter 4.1.1 that due to the self-initiated photopolymerization of styrene in solution, experiments over 30 hours could not be performed because of the solidification of the bulk monomer phase.

Figure 73 also reveals that the average thickness growth rate under identical UV-irradiation conditions is significantly smaller on cABT SAMs than on EBCDs. This is probably due to

the low BDEs on EBCDs for hydrogen abstraction. An average thickness growth rate of $dh_d/dt = 6.97 \text{ nm}\cdot\text{h}^{-1}$ was determined by a linear fit of all the data points in Figure 73. The growth rate (k_g) was calculated using Eq. 13 (see Table 9).

The SIPGP of five other monomers (AA, MMA, tBMA, 4-vinylpyridine (4VP), 4-vinylbenzylchloride (4VBC)) was performed in bulk on identical EBCD structures on silica. In all experiments, polymer grafts were selectively formed on the EBCDs. The dry polymer layer thickness (h_d), as determined by AFM, are summarized in Table 9. A systematic kinetic study was not performed for these monomers since the dh_d/dt -values were calculated from only 1 data point. However, comparing the k_g -values to the rate constant for the propagation reaction (k_p) for the free radical polymerization in solution it can be observed that the k_g -values correlate roughly with the k_p -values.

monomer	t_p	h_d (nm)	dh_d/dt [$\text{nm}\cdot\text{h}^{-1}$]	ρ [$\text{g}\cdot\text{cm}^{-3}$]*	k_g [$\text{mol}\cdot\text{cm}^{-2}\cdot\text{h}^{-1}$]	k_p [$\text{mol}\cdot\text{l}^{-1}\cdot\text{s}^{-1}$]
AA	5 min	38 ± 4	460 ± 40	1.15	7.3 ± 8	6.600
MMA	5.5h	117 ± 10	21.3 ± 1.8	1.19	0.25 ± 0.02	143
tBMA	5.5h	120 ± 15	21.8 ± 2.7	1.02	0.16 ± 0.02	121
styrene	see Figure 73		6.97 ± 0.14	1.05	0.070 ± 0.001	44
4VP	17h	310 ± 13	18.2 ± 7.6	1.18	0.20 ± 0.01	12
4VBC	5.5h	15 ± 3	2.7 ± 0.5	1.14	0.020 ± 0.004	-

Table 9. Polymer grafts created by the SIPGP on 0.9 ± 0.4 nm thick EBCDs on silicon dioxide. Comparison between k_g for the SIPGP and k_p for the free radical polymerization in solution at room temperature from literature.¹⁷⁴

(*) from references 174 and 262.

4.4.2.4 Influence of the electron dosage on the polymer layer thickness and preparation of three dimensional polymer architectures

In chapters 4.1 and 4.2, it has been shown that when the electron beam lithography step was performed on ω -functionalized biphenylthiol SAMs on gold, not only the 2D locus of the polymer grafts could be controlled, but also the thickness of the resulting polymer grafts due to the fact that the surface concentration of potential polymer grafting points was determined by the locally applied electron beam dosage.

In this section, it has been investigated if also for the SIPGP on EBCDs, the polymer layer thickness could be controlled by the locally applied electron dosage. The influence of the electron beam dosage on the polymer layer thickness was studied on a naturally oxidized silicon substrate. A $10 \times 50 \mu\text{m}^2$ electron dosage gradient structure was prepared as described in previous chapters. The electron dose was continuously increased from 0 to 57.5 mC/cm^2 . AFM measurements of the EBCD gradient on silica (Figure 74) revealed that the carbon deposition thickness increases with increasing dosage and reaches 0.9 nm at maximum electron beam dosage (57.7 mC/cm^2). This behavior is in agreement with earlier reports.¹⁶⁰ The fluctuations in the height profile (Figure 74b) is due to the fact that the thickness of the EBCDs is similar to the substrate roughness ($\text{rms} = 0.41 \text{ nm}$). Below 10 mC/cm^2 , the EBCDs were too thin to be detected by AFM. This indicates that the EBCDs cover the silica substrate only partially at low electron beam doses.

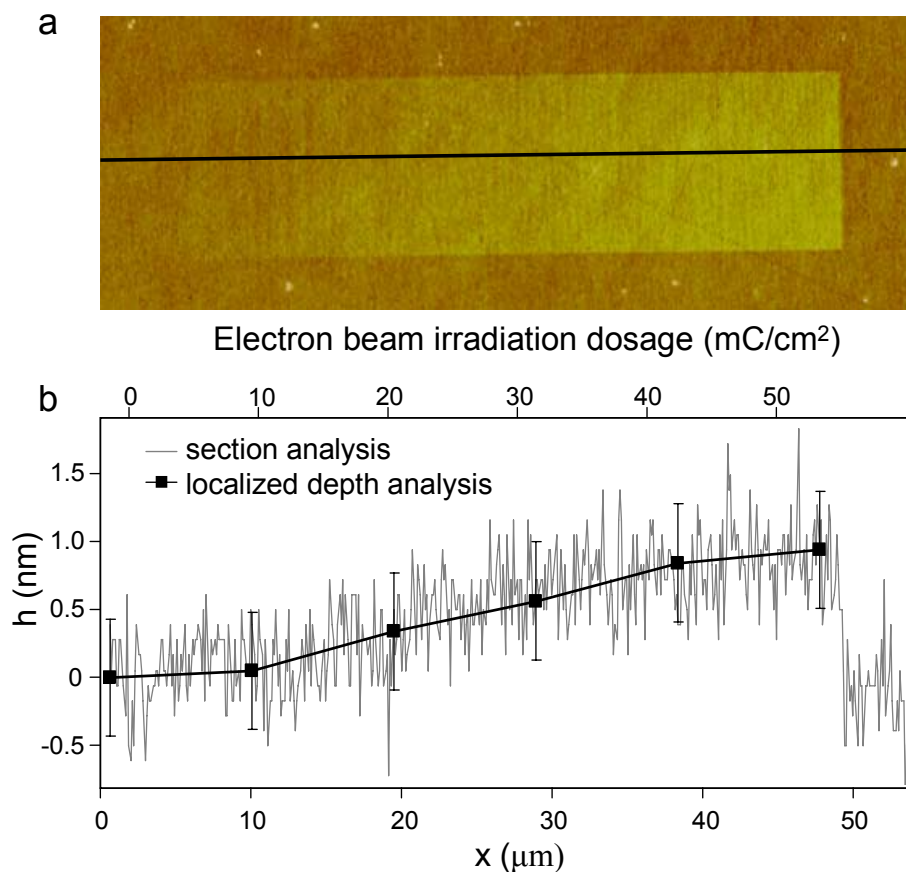


Figure 74. (a) AFM height measurement of an EBCD gradient on a oxidized silicon wafer and (b) height analysis. The average layer thickness at different electron beam doses was determined by localized depth analysis.

The substrate was successively immersed in bulk monomer (styrene or MMA) and irradiated with UV-light. The AFM images of the resulting polymer structures and corresponding height profiles are displayed in Figure 75.

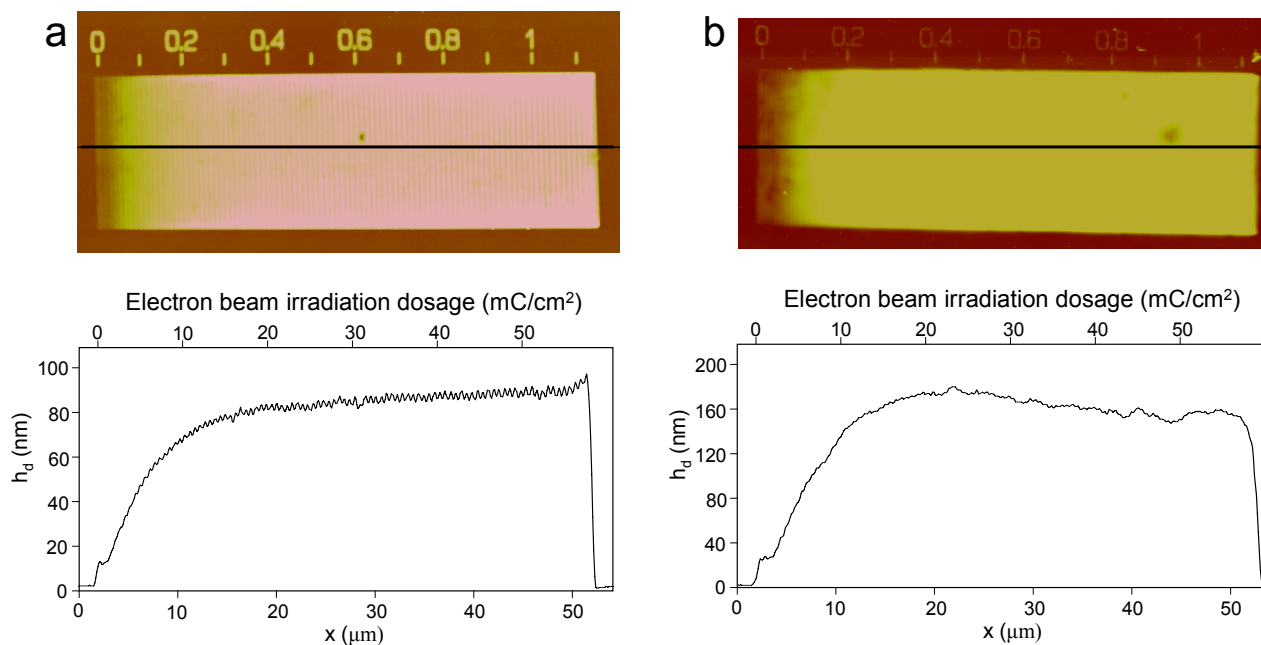


Figure 75. AFM measurements ($55 \times 18 \mu\text{m}^2$) and height profile of polymer graft structures created by the SIPGP of (a) styrene ($t_p = 15$ h) and (b) MMA ($t_p = 8.5$ h) on identical EBCD gradients on silica. The electron beam dosage was linearly increased from 0 to 57.5 mC/cm^2 .

The resulting polymer layer thickness is obviously dependent on the electron beam dosage and thus the amount of carbon deposits. It can also be observed that the influence of the electron beam dosage is similar for both monomers. The polymer layer thickness increases between 0 and 20 mC/cm^2 and remains almost constant above 20 mC/cm^2 (the PS thickness increases slightly above 20 mC/cm^2 while the PMMA thickness decreases).

The polymer layer thickness profiles in Figure 75 can be explained as follow: below 20 mC/cm^2 , the EBCDs cover only partially the silica substrate. An increase of the electron beam dosage increases the EBCD amount and thus the surface concentration of potential grafting points for the SIPGP step. At approx. 20 mC/cm^2 , the substrate is completely covered by carbon deposits. A further increase of the electron beam dosage increases the thickness of the EBCDs, but the surface concentration of potential grafting points for the SIPGP remains constant.

It has been mentioned that the gradient structure consists of hundred parallel $10 \times 0.5 \mu\text{m}^2$ lines with linearly increasing electron dosage. In Figure 75a, these individual lines can clearly

be recognized and are also apparent as fluctuation in the height profile. This is caused by a small lateral spacing between the individual lines, or by a partial overlapping of these lines. However, since above 20 mC/cm^2 , an increase of the electron beam dosage does not result in an increase of the polymer layer thickness, it can be concluded that the individual EBCD lines are slightly separated. This has been observed several times for some other surfaces. A possible explanation is the presence of thermal creep during the lithographic step

The dependence between the polymer layer thickness and the amount of locally deposited carbon allows the preparation of complex 3D polymer architectures on surfaces. The polymer layer thickness can be controlled directly by the EBCD preparation. The shape of the desired polymer architecture can be predicted using the thickness/electron dosage function in Figure 75. This approach has been applied for the preparation of different 3D polymer architectures on the micro- and nanometer scale on silica (Figure 76).

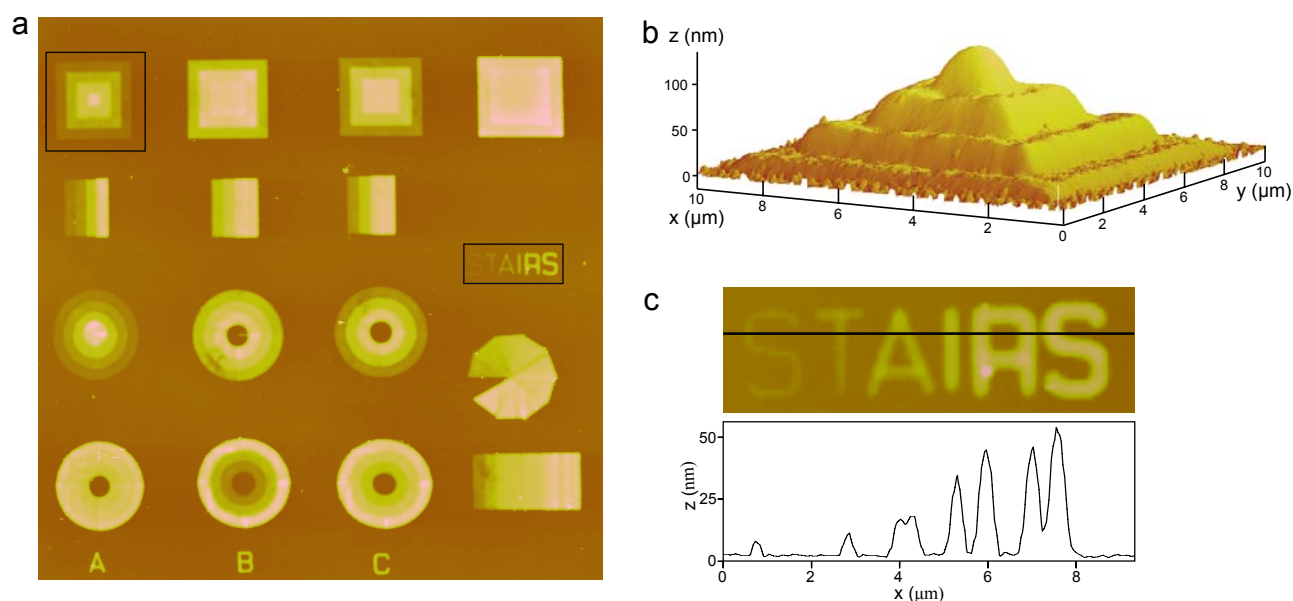


Figure 76. (a) AFM scan ($50 \mu\text{m}^2$) of three dimensional PS grafts on silica (t_p : 15h). (b) Three dimensional representation of a detail AFM scan of a PS ‘micro pyramid’ indicated in the main image (a). The SIPGP of styrene was performed on 7, 5, 3 and $1 \mu\text{m}^2$ concentric EBCD squares created with an electron beam dosage of respectively 1, 3, 7 and 23 mC/cm^2 resulting in 17, 44, 81 and 129 nm thick steps. (c) Detail AFM scan of the word ‘STAIRS’. Each letter of the word ‘STAIRS’ was created with a electron beam dosage of 1, 2, 4, 8, 12 and 16 mC/cm^2 resulting in respectively 6, 10, 16, 35, 44 and 53 nm thick letters. The line width at half maximum height varies between 200 nm and 350 nm.

The 129 nm high *micro step pyramid* in Figure 76b was created by writing 4 concentric squares with increasing electron beam dosage during the EBCD process. This experiment

shows that highly defined 3D polymer architectures can be prepared by a free radical polymerization technique, without surface-bonded initiators and without SAM as resist layer.

4.4.3 Micro- an nanostructured polymer grafts on various substrates

It has already been pointed out that one major advantage of this simple two-step procedure is the preparation of structured polymer grafts on various substrates. There are only two limitations:

1. Stable EBCDs cannot be prepared on all substrates. However, it can already be mentioned that from the different substrates tested by us, gold was the only material where apparently no EBCDs were formed. The reason for this is still unclear. It may be attributed to the inert character of gold surfaces. It is very probable that a thin EBCD layer is formed during the electron beam irradiation, but that this layer may not be bonded strongly to gold.
2. A reactivity contrast between the bare substrate and the EBCDs is required during the SIPGP step.

In order to demonstrate that this technique can be applied to a broad variety of materials, structured polymer grafts were created on isolators, semiconductors and conductors. In all experiments, the substrates were intensively cleaned before and after the polymerization step in various solvents and ultrasound irradiation.

4.4.3.1 Structured polymer grafts on isolators

Structured polymer grafts have been prepared on three different isolators: mica, borosilicate glass and ethylene-*co*-tetrafluoroethylene (ETFE) substrates. At first sight, the EBCD process may not be performed on electrical isolators due to charge accumulation. This problem has been observed when non-conductive substrates were structured by *direct writing* with a focused electron beam. However, defined microstructured polymer grafts could be prepared on isolators if the EBCD process was performed with an electron floodgun in combination with a stencil mask. One possible reason for this is that the electrons can leave via the conductive stencil mask (which is in contact with the non-conductive substrate) and mask holder.

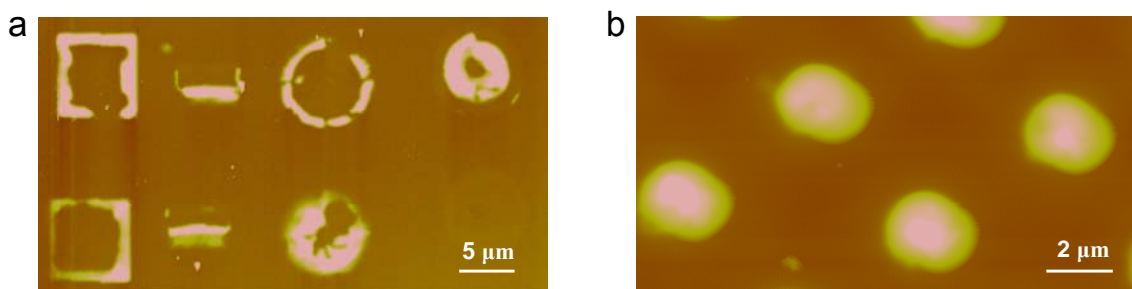


Figure 77. PS grafts by the SIPGP of styrene on mica substrates structured by (a) *direct writing* with a focused electron beam or (b) with an electron floodgun (50 eV; 60 mC/cm²) in combination with a stencil mask with openings of 1 μm radius. The same write field as in Figure 76 was used for the structures in (a).

This problem is clearly visible in Figure 77. In Figure 77a, the SIPGP of styrene was performed on a freshly cleaved muscovite mica substrate, structured with EBCD by *direct writing* using the same electron beam write field applied for the substrate in Figure 76. Obviously, a better control of the 2D locus of the polymer grafts could be achieved with an electron floodgun in combination with a stencil mask (Figure 77b).

In this experiment, 360 ± 50 nm thick PS grafts were selectively formed on the irradiated surface regions after the SIPGP of styrene (t_p : 18.6 h). The reactivity difference between the muscovite mica and the EBCD surfaces for the SIPGP can, also here, be explained directly by comparing the energies required for hydrogen abstractions. Muscovite is a sheet silicate mineral with a chemical composition of $\text{KAl}_2(\text{AlSi}_3\text{O}_{10})(\text{F},\text{OH})_2$. Muscovite has a layered structure of aluminum silicate sheets which can be cleaved easily. Cleaved muscovite is characterized by the presence of surface Al-OH bonds.²⁶³ The absence of polymer grafts on the bare muscovite substrate can be explained by the high AlO-H BDE of 116 kcal·mol⁻¹.²⁶⁴ In general, it is presumable that polymer grafts will not be formed directly onto most (aluminum) silicates during the SIPGP due to the high BDEs of AlO-H and SiO-H.

The same approach has been applied for the preparation of microstructured polymer grafts on borosilicate glass (Borofloat® 33). Borofloat® 33 has a composition of 81% silica, 13% boric oxide, 4% sodium/potassium oxide, and 2% aluminum oxide.²⁶⁵ The SIPGP of styrene (t_p : 16h) and MMA (t_p : 2.7h) on identical EBCD structures (1 μm radius, 50 eV, 60 mC/cm²), resulted in 250 ± 50 nm thick PS and 100 ± 10 nm thick PMMA grafts, respectively.

It was observed that under identical EBCD and SIPGP conditions, approximately two times thicker PS grafts were formed on borosilicate glass than on silica substrates. It has already been mentioned that the EBCD process is strongly influenced by the applied substrate material. This could, at least partially, be the reason for the strong polymer layer thickness

difference. However, the fact that borosilicate glass is almost completely transparent for UV-light with a spectral distribution between 300 and 400 nm (in contrast to silicon wafers) is probably the determining factor (Figure 78). The SIPGP experiments were performed by placing the substrate (immersed in monomer) in the middle of a cylindrical UV chamber with 16 UV lamps. In other words, the effective UV intensity in the surface vicinity is higher for transparent substrates.

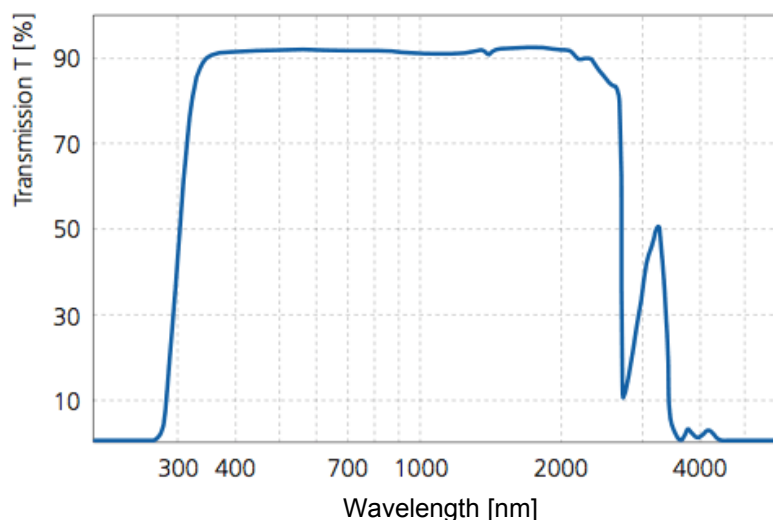


Figure 78. UV-VIS transmission spectrum of Borofloat® 33.²⁶⁵

Finally, the same process was tested on flat ETFE substrates, prepared by Dr. Celestino Padeste from the laboratory for micro- and nanotechnology in the Paul Scherrer Institute in Villigen (Switzerland). AFM measurements revealed that after the SIPGP of styrene (t_p : 16h), the surface regions covered by EBCDs were approximately 230 nm. However, attenuated total reflectance-Fourier transform infrared (ATR-FTIR) measurements showed that polymer grafts were also formed on the bare ETFE substrate (Figure 79).

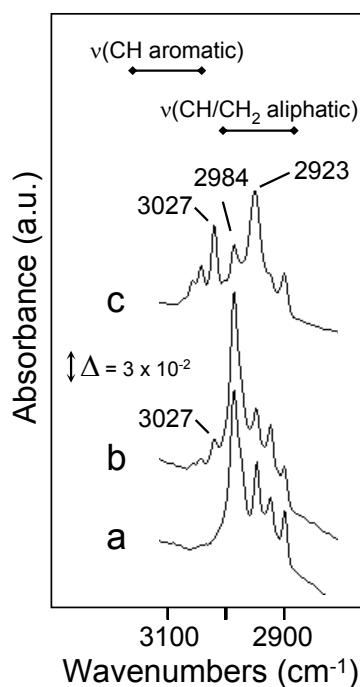


Figure 79. ATR-FTIR spectra between 2900 and 3100 cm^{-1} of: (a) native ETFE substrate, (b) ETFE substrate after the SIPGP of styrene (t_p : 16h), (c) an ETFE substrate covered by EBCDs (50 eV; electron dosage: 60 mC/cm^2) after the SIPGP of styrene, performed under identical polymerization conditions.

In Figure 79, the ATR-FTIR spectrums of a native ETFE substrate (a) is compared to ETFE substrates coated with PS grafts (b and c). The SIPGP of styrene was performed under identical conditions on a bare ETFE substrate (b) and on an ETFE substrate, previously coated with an EBCD layer (c). Besides the aliphatic $\nu_{\text{al}}(\text{CH})$ stretching bands below 3000 cm^{-1} , both spectrums exhibit the characteristic aromatic $\nu_{\text{ar}}(\text{CH})$ stretching vibrational mode for PS at 3027 cm^{-1} . This indicates that a thin PS layer was formed on the bare ETFE surface during the SIPGP process. The presence of polymer grafts on the bare ETFE substrate can be explained by the presence of C-H bonds in the ETFE polymer backbone prone to hydrogen radical abstraction by photoactivated monomers.²⁶⁶

4.4.3.2 Structured PS grafts on semiconductors and conductors

In this section, structured PS grafts were prepared on identical EBCD gradients on different semiconductors and conductors (gallium (III) nitride (GaN), gallium (III) arsenide (GaAs), germanium, silicon nitride (Si_3N_4), silicon (Si) and aluminum (Al)). It has to be mentioned that these experiments were performed with new UV-lamps and that the polymer layer

thicknesses presented in this section cannot directly be compared with previously described experiments. For this reason, the SIPGP on an EBCD gradient on silica was repeated.

To investigate the influence of the substrate on the EBCD and SIPGP process, PS grafts were prepared by the SIPGP of styrene on identical $10 \times 50 \mu\text{m}^2$ EBCD gradients (0 to 57.5 mC/cm^2) on the various substrates.

1. Native oxide layer on Si, Si₃N₄, Ge, Al and GaAs

It is known that Si, Si₃N₄,²⁶⁷ Ge,²⁶⁸ Al and GaAs²⁶⁹ substrates readily oxidize in contact with air, forming a native oxide layer (silica on Si and Si₃N₄, GeO₂ on Ge, Al₂O₃ on Al and Ga₂O₃ on GaAs). This native oxide layer can be removed easily by wet chemical treatment using e.g. HF (aq) or HCl (aq). For the here described experiments, it was difficult to perform the entire process under inert atmosphere (in order to avoid a rapid re-oxidation) since the contact of the substrate with air is inevitable when the substrate was introduced and removed from the electron beam irradiation chamber. Hence, PS gradients were prepared in a first set of experiments on native oxide layers on Si, Si₃N₄, Ge, Al and GaAs. The substrates were cleaned before the EBCD process in a piranha solution, to remove organic contaminations.

Figure 80 shows the AFM scans and height profile analysis of the resulting PS structures on oxidized Si (a), Si₃N₄ (b), Al (c), Ge (d) and GaAs (e) substrates.

First, it can be observed that PS grafts with thicknesses of the same order of magnitude were selectively formed on the carbon deposits on Si, Si₃N₄, Al and Ge substrates. The height profile of the PS gradient structure on oxidized GaAs in Figure 80e reveals that polymer grafts were also formed on the non-irradiated surface regions (the red narrow in Figure 80e). This is probably due to the fact that the O-H bond dissociation energy of hydroxyl surface functionalities is significantly lower in Ga₂O₃ substrates ($98 \text{ kcal}\cdot\text{mol}^{-1}$)²⁷⁰ as compared to silica ($119 \text{ kcal}\cdot\text{mol}^{-1}$)²⁶¹ or Al₂O₃ substrates ($116 \text{ kcal}\cdot\text{mol}^{-1}$).²⁶⁴ However, the GaO-H BDE is higher than the maximum photon energy of the applied UV source ($95.3 \text{ kcal}\cdot\text{mol}^{-1}$).

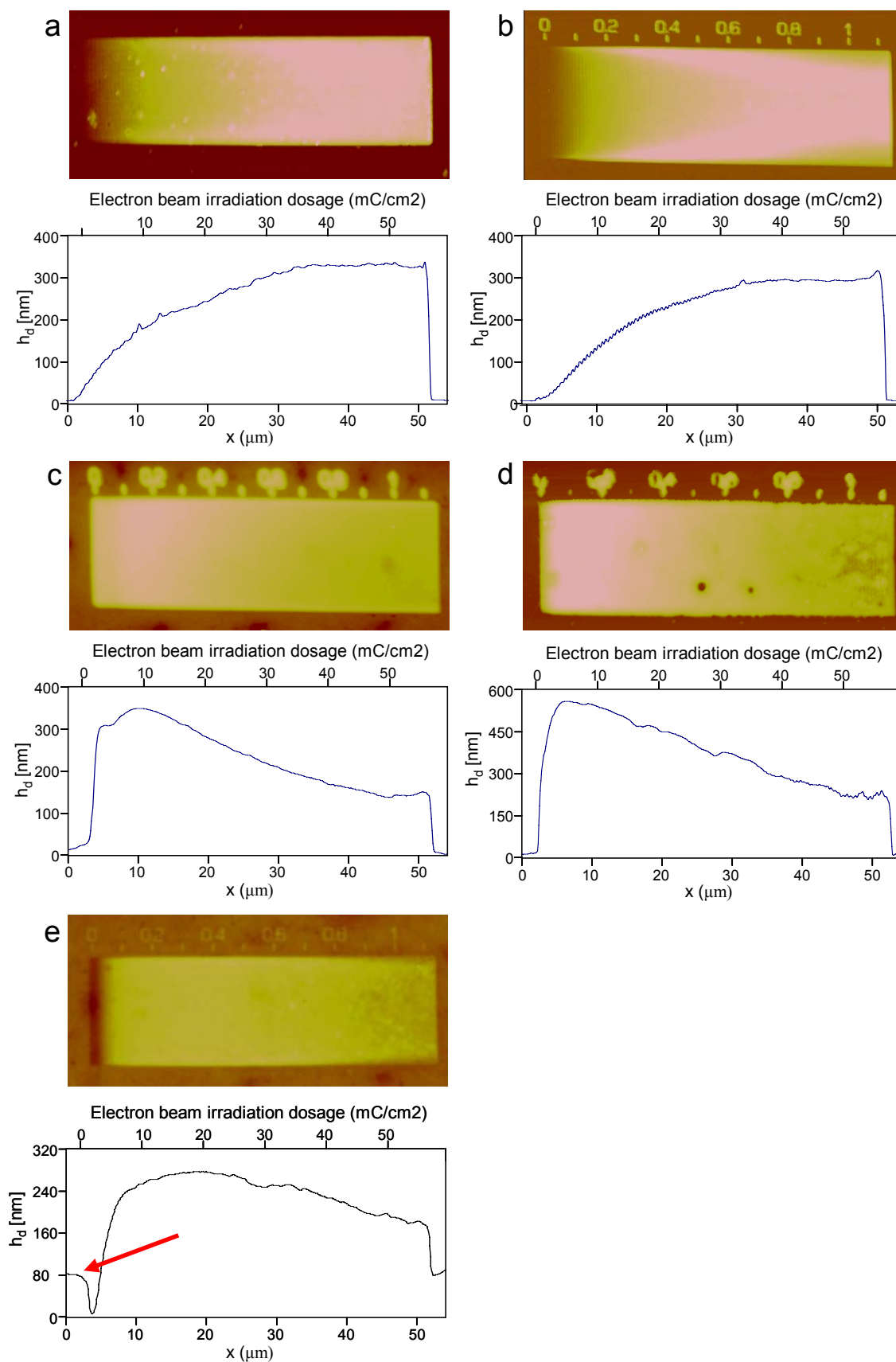


Figure 80. AFM images ($55 \times 20 \mu\text{m}^2$) and height profile of PS grafts by the SIPGP of styrene on identical EBCD gradients on oxidized (a) silicon (t_p : 15.7 h), (b) silicon nitride (t_p : 19 h), (c) aluminum (t_p : 15.5 h), (d) germanium (t_p : 22 h) and (e) gallium arsenide (t_p : 16h).

Hence, the reactivity of surfaces toward SIPGP cannot completely be explained by the required energy to abstract a hydrogen atom from a surface functionality and that probably other factors have to be taken into account. It has been mentioned that specific interactions between the monomer and the surface may have an important influence on the substrate reactivity. Coordination between the π electrons of the vinyl bond and metal ions of the substrate may, for instance, play a role. However, the hydrogen abstraction energy can be used as a rough estimation in order to predict the substrate reactivity toward SIPGP.

Figure 80 a and b show that the PS gradient structures on oxidized Si and Si_3N_4 substrates have a very similar height profile. This can be expected since an identical thin native silica layer covers both substrates. The polymer layer thickness increases with increasing electron beam dosage until it reaches a maximum of approx. 360 nm on the silicon and 305 nm on the silicon nitrate substrate at applied dosage values of approx. 30 mC/cm^2 . This dependency of the electron beam dosage on the polymer layer thickness has been discussed in chapter 4.4.2.4 and can be understood by the increase of the carbon deposition surface coverage with increasing electron dosage.

Various highly defined three dimensional polymer architectures have been prepared on Si_3N_4 substrates (Figure 81). The possibility to create structured polymer grafts directly onto Si_3N_4 cantilevers by this procedure is currently under investigation in an ongoing cooperation with the research group of Dr. Rüdiger Berger at the Max-Planck-Institute for Polymer Research in Mainz. Cantilevers coated with thin polymer grafts are to be applied for the fabrication of specific (bio)-sensors.²⁷¹

A different polymer layer thickness dependency upon the EBCD was observed on oxidized Al, Ge and GaAs substrates (Figure 80 c, d and e). On these substrates, the maximum polymer layer thickness is already reached around 10 mC/cm^2 . This indicates (according to the here above proposed mechanism) that a continuously EBCD layer is reached at a lower electron beam dosage on these substrates than on silica. The EBCD gradient was measured on an oxidized GaAs substrate (Figure 82).

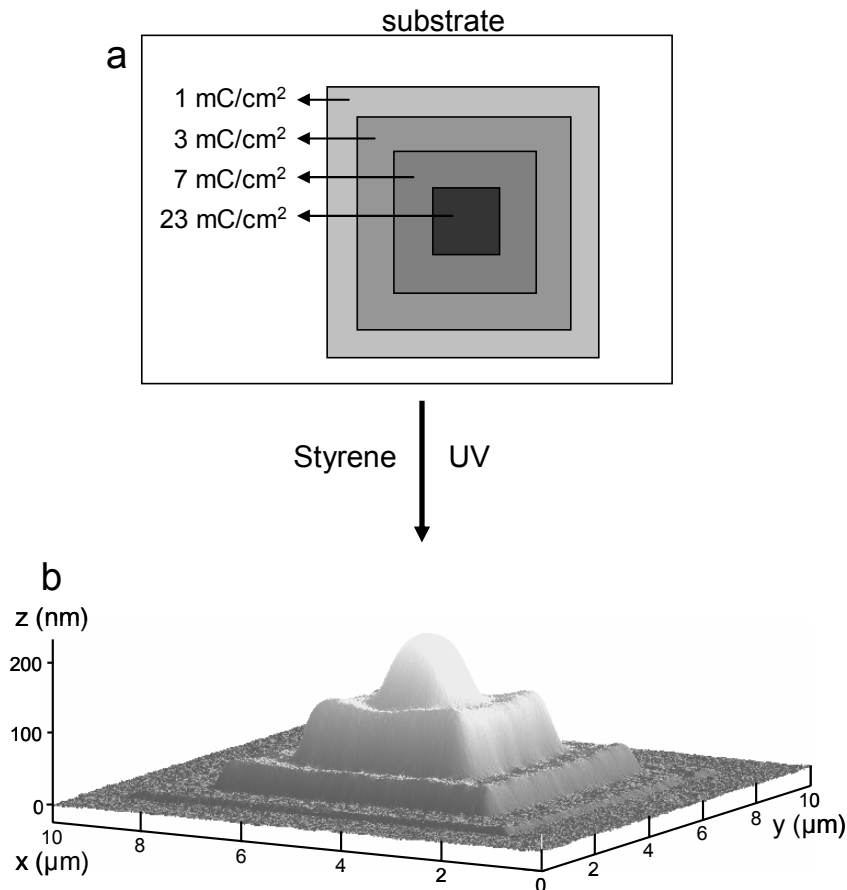


Figure 81. (a) EBCD irradiation scheme: 7, 5, 3 and 1 μm^2 concentric EBCD squares were created on silicon nitride with an electron beam dosage of 1, 3, 7 and 23 mC/cm^2 , respectively. The SIPGP (t_p : 19h) of styrene was performed on these EBCD structures. (b) Three dimensional representation of an AFM scan of the resulting PS micro-pyramid (6, 38, 118 and 207 nm thick steps).

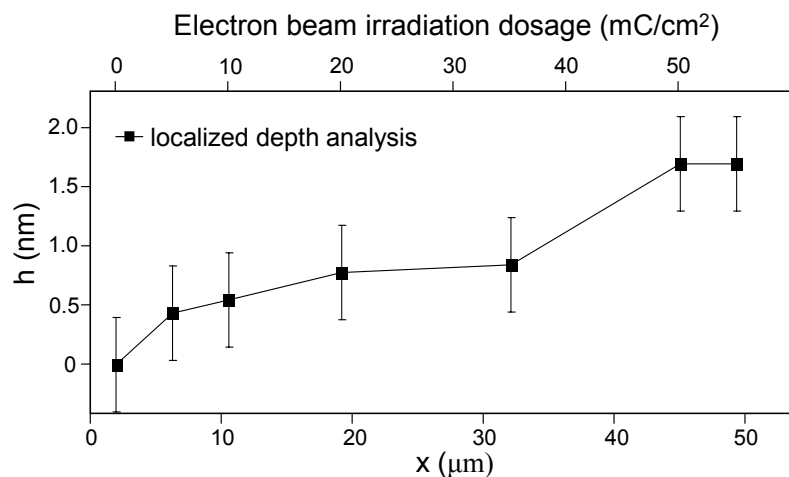


Figure 82. EBCD thickness on an oxidized GaAs substrate as a function of the electron beam dosage gradient measured by AFM.

Also here, the EBCD thickness increases with increasing electron beam dosage and reaches approx. 1.7 nm at 50 mC/cm². Figure 82 confirms the hypothesis that the EBCD thickness increase is approx. two times faster on oxidized GaAs as compared to silica. Thus a continuous EBCD layer is obtained at lower electron beam dosage. It has already been mentioned that the EBCD thickness increase depends on the nature of the used substrate, however, the exact reason for this is unknown.

Figure 80 shows also a polymer layer thickness decrease on oxidized Al, Ge and GaAs substrates between approx. 10 and 50 mC/cm². This could be accounted to an electron beam induced conversion of EBCD surface functionalities. This behavior is very similar to the decrease of the polymer layer thickness on cABT SAMs on gold at high electron beam doses, due to the electron beam induced abstraction of the 4'-amino function. The EBCDs on oxidized GaAs substrates at 15 mC/cm², corresponding to the maximum polymer layer thickness, and 50 mC/cm² were investigated by XPS by Dr. Küller in order to investigate the differences in surface composition. However, no significant differences in the XPS spectra could be observed. Thus, currently, the exact reason for the decrease of the polymer layer thickness above 10 mC/cm² remains unclear.

2. GaAs and GaN

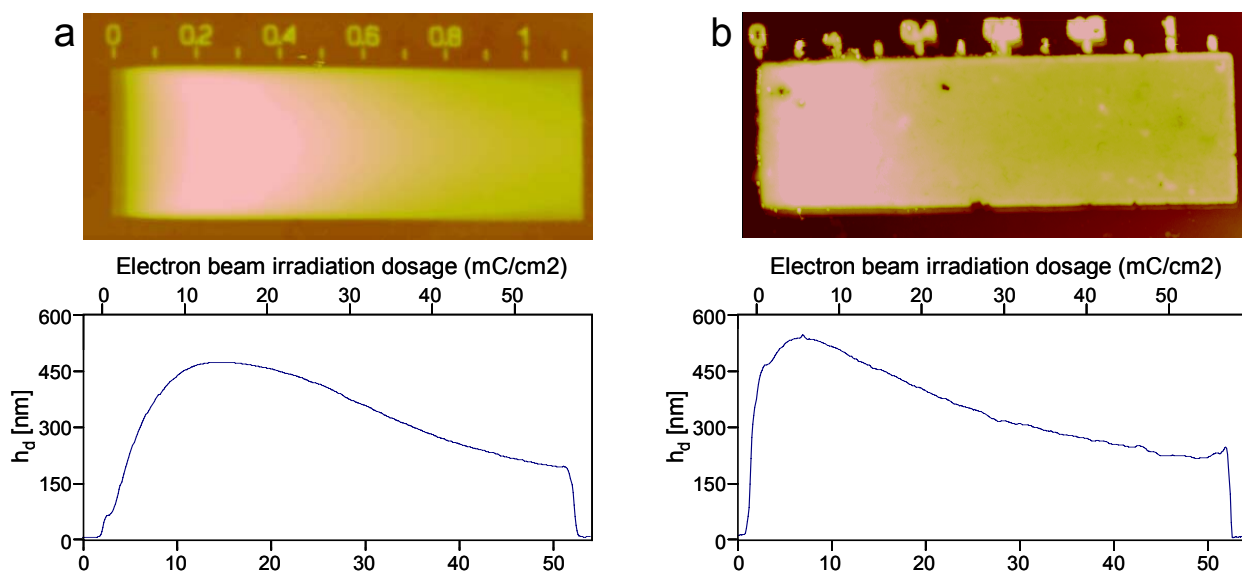


Figure 83. AFM images ($55 \times 20 \mu\text{m}^2$) and height profile of PS grafts by the SIPGP of styrene on identical EBCD gradients on (a) GaAs (t_p : 18h) and GaN (t_p : 21h).

Figure 80 shows that polymer grafts were also formed directly on Ga_2O_3 . For this reason, it was investigated if the EBCD SIPGP process could be applied directly on GaAs and GaN substrates. From naturally oxidized substrates, the oxide layer was stripped by a treatment with concentrated HCl ²⁷² and the substrates were kept under argon atmosphere. However, a partial oxidation of the substrates cannot be completely excluded.

Figure 83 shows that polymer grafts were selectively formed on the previously irradiated surface regions. The maximum layer thickness is approximately 460 nm on the GaAs substrate and 550 nm on GaN substrate. The polymer layer thickness has qualitatively the same electron beam dosage dependence as on oxidized Al, Ge and GaAs substrates. The absence of polymer grafts on unirradiated GaAs and GaN surface regions indicates that the substrates were not oxidize prior to the EBCD SIPGP process.

In conclusion, it can be stated that the SIPGP on EBCDs can be performed for the preparation of stable polymer grafts on various substrates. The gradient structures in Figure 80 and Figure 83 give the polymer layer thickness/electron dosage dependency which allows the fabrication of polymer grafts with predictable 3D architectures.

Preliminary results have shown that structured polymer grafts can also be prepared on Ag surfaces by this approach. 170 ± 30 nm thick PS grafts (t_p : 17 h) were selectively formed on EBCD structures, prepared by the floodgun-mask method (Figure 84).

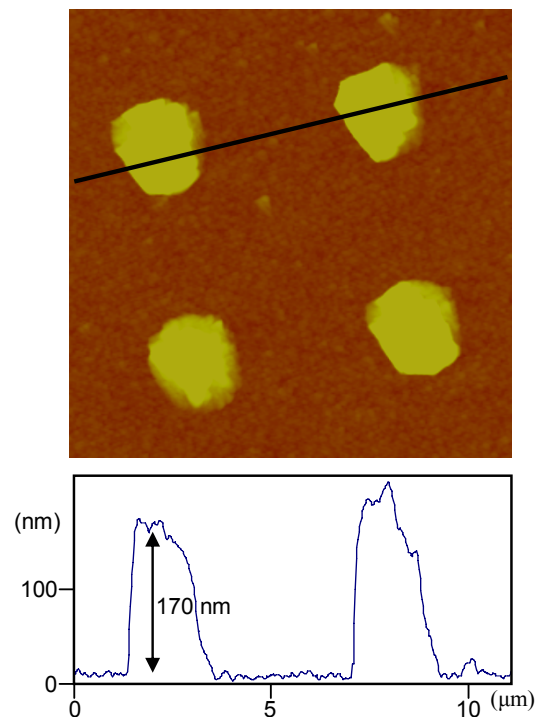


Figure 84. 170 ± 30 nm thick PS grafts were formed by the SIPGP of styrene (t_p : 17 h) on structured EBCDs on Ag ($1\mu\text{m}$ radius; 50 eV; $60\text{ mC}/\text{cm}^2$).

4.4.4 Molecular architecture of polymer grafts prepared by SIPGP

Since hydrogen radicals can be abstracted from diverse surface functionalities, it is very likely that during the SIPGP, hydrogen radicals of previous grafted polymer chains are also abstracted by photoactivated monomer biradicals, resulting in the formation of a grafted macro radical. The polymerization initiated by these macro radicals leads to the formation of a grafted branched polymer chain. In other words, it is likely that polymer grafts prepared by SIPGP have a branched architecture.

The architecture of grafted polymer chains was investigated indirectly by studying the influence of the hydrolyzation of the ester group in structured poly(*tert*-butyl methacrylate), (PtBMA) grafts on the dry polymer layer thickness. The hydrolyzation of (PtBMA) grafts results in poly(methacrylic acid) (PMAA) grafts (Figure 85).

When linear PtBMA grafts are hydrolyzed, the grafting density σ remains constant while the molecular weight of the grafted chains (M_n) decreases by 39.5 %, due to the cleavage of the *tert*-butyl group (Figure 85a). Furthermore, the bulk density, ρ , decreases approximately to 7.5 % when amorphous PtBMA is hydrolyzed to PMAA.¹⁷⁴ When the dry thickness of linear PtBMA grafts (h_{d1}) is known, the expected PMAA thickness (h_{d2}) after hydrolyzation can thus be calculated using Eq. 1:

$$h_{d2} = \frac{h_{d1}\rho_1 M n_2}{M n_1 \rho_2} \quad \text{Eq. 19}$$

According to Eq. 19, the hydrolyzation of linear PtBMA grafts results in a thickness decrease of approximately 33 %.

However, a stronger thickness decrease can be expected for the hydrolyzation of branched PtBMA chains. If the branching occurs partly on the *tert*-butyl group, the hydrolysis of the ester function will lead to the cleavage of entire polymer chains (Figure 85b). In other words, the hydrolysis of branched PtBMA grafts results in the cleavage of more grafted material compared to the hydrolysis of linear PtBMA grafts.

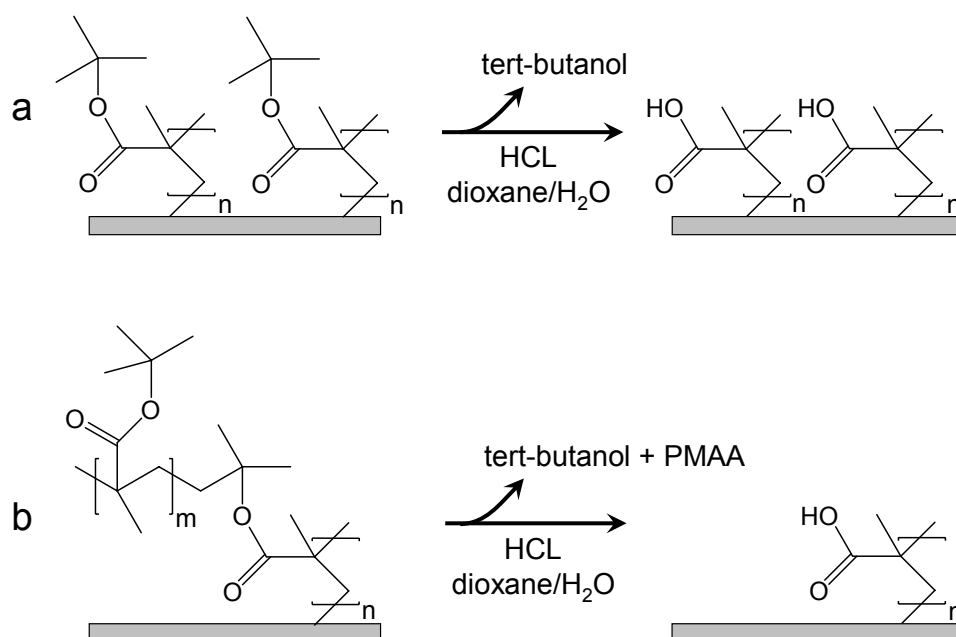


Figure 85. The hydrolysis of PtBMA grafts in a HCl/dioxane/water results in PMAA grafts and t-butanol. The hydrolysis of branched PtBMA grafts (b) results in the cleavage of more grafted material compared to the hydrolysis of linear PtBMA grafts (a).

The following experiment was performed: 116 ± 10 nm thick patterned PtBMA grafts were created by the SIPGP of tBMA on structured EBCDs (t_p : 5h). Successively, the ester group was hydrolyzed by placing the sample in refluxing HCl:dioxane:water (2:3:4 volume ratio) for 3h. After hydrolyzation, the sample was intensively rinsed, dried, and the polymer layer thickness was measured.

The hydrolyzation of 116 nm thick linear poly(tBMA) brushes would result in approximately 77 nm thick PMAA brushes, however here, a thickness of 26 ± 5 nm was measured (corresponding to a thickness decrease of approximately 78 %). The significant thickness decrease, due to hydrolyzation of the ester group, is a strong indication that PtBMA grafts formed by SIPGP have a branched architecture (in order to control the stability of the polymer grafts under these hydrolyzation conditions, a sample with PS grafts on structured EBCDs was placed under identical reaction conditions; no significant thickness decrease was observed).

This approach shows that the chemical composition of polymer grafts can be determined only by measuring the polymer layer thickness. This concept will be used again in next chapters, especially to quantify polymer analogue reactions.

4.4.5 Successive SIPGP

In previous section, it was demonstrated that hydrogen atoms can be abstracted from already grafted polymer chains by photoactivated monomer biradicals, resulting in the formation of a grafted macro radical. These macro radicals can initiate a free radical polymerization. Thus, it is likely that grafted block copolymers can be prepared by successive SIPGP steps.

This straightforward approach has been applied for the preparation of structured PS-PMMA block copolymers on borosilicate glass. The SIPGP ($t_p = 3$ h) of MMA was performed on a Borofloat® 33 sample coated with structured PS grafts (Figure 86). The sample was successively cleaned in different solvents and ultrasound irradiation. Figure 86b shows that the SIPGP of MMA on 250 ± 50 nm thick PS grafts gives 410 ± 50 nm thick PS-PMMA block copolymer grafts. Figure 86b also shows that the SIPGP of MMA results in a significant broadening of the polymer structures. This can be explained by fact that polymer chains at the edges of the structures can extend to polymer free surface regions (chapter 2.6). Thus, the polymer structures do not only grow perpendicularly to the substrate surface, but in all directions.

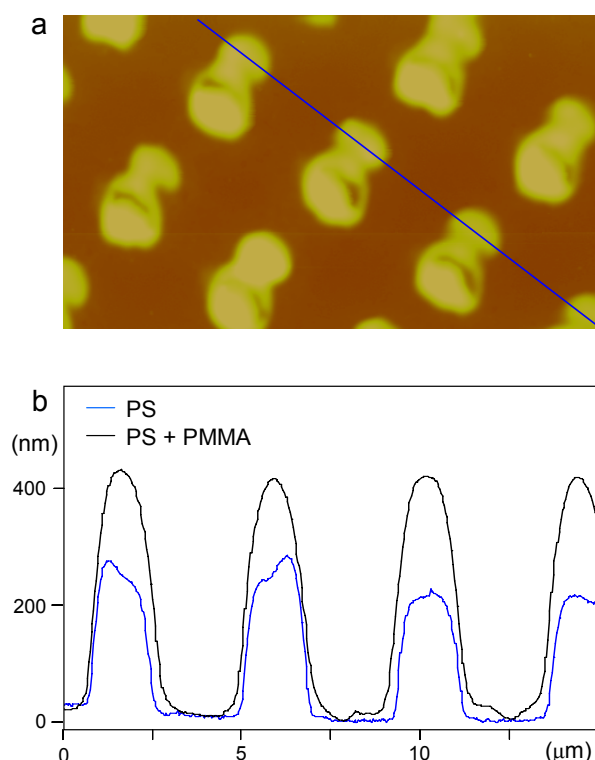


Figure 86. 250 ± 50 nm thick PS grafts were formed by the SIPGP of styrene ($t_p: 19$ h) on structured EBCDs on Borofloat® 33 ($1\mu\text{m}$ radius; 50 eV; 60 mC/cm²). The shape of the polymer dots is caused by small movements of the stencil mask during the EBCD process. The SIPGP of MMA ($t_p: 3$ h) on these PS dots results in 410 ± 50 nm thick PS-PMMA block copolymer grafts.

The same approach has been applied for the formation of a 1450 nm thick PS gradient structure. Four successive SIPGP steps were performed on an EBCD gradient structure. The height profile of the same gradient after each polymerization step is shown in Figure 87a. In Figure 87b, the thickness of the gradient structure at different gradient locations, determined after each polymerization, is plotted as a function of the total irradiation time.

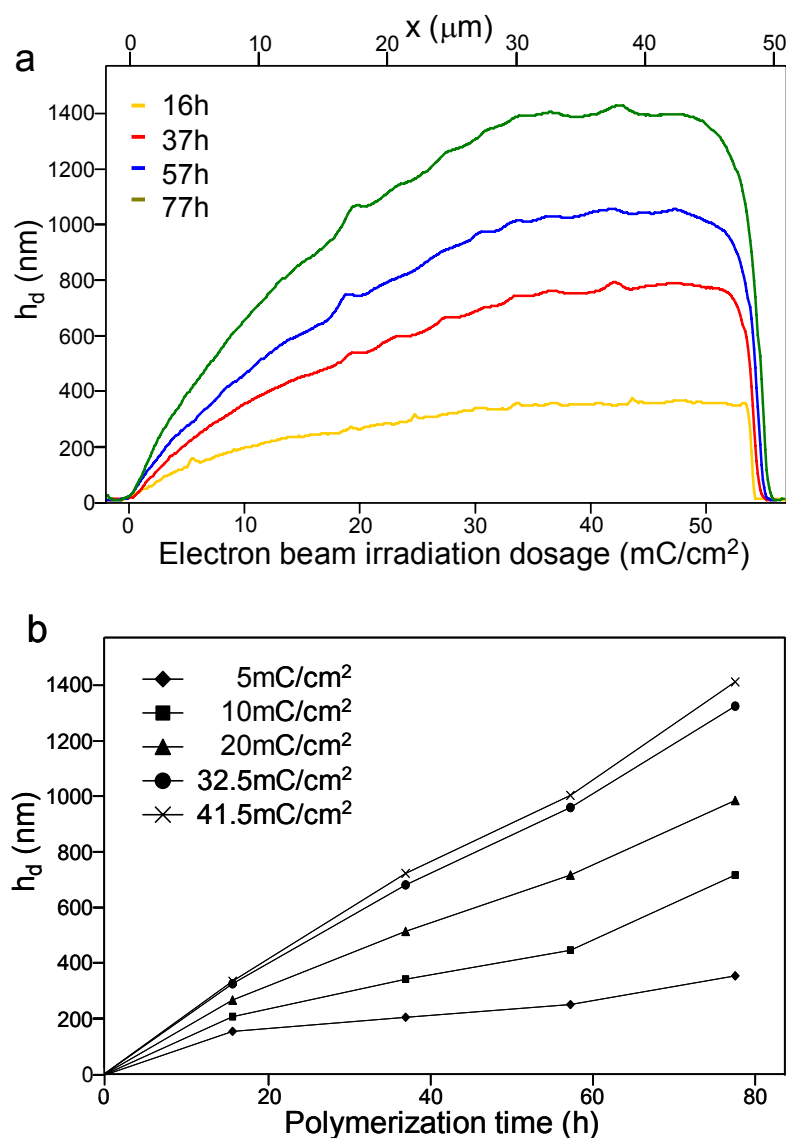


Figure 87. (a) Height profiles as measured by AFM of the same PS gradient structure on an oxidized silicon substrate after successive polymerization steps. (b) The polymer layer thickness of the gradient structure at different electron beam doses in function of the total irradiation time.

Obviously, the polymer layer growth rate depends of the electron beam dosage. The dependency between the polymer layer thickness and the electron beam dosage remains after each polymerization step (Figure 87a). In other words, the polymer layer growth rate is faster

for thicker structures. This can be understood as following: it has already been mentioned in previous chapters that such polymer layer thickness gradient structures are in fact polymer grafting density gradients. Thus, thicker polymer structures (with a higher grafting density) have more potential grafting points for successive SIPGP steps.

Different PS microstructures were prepared on a GaAs substrate (t_p : 18 h). The substrate was then resubmerged in styrene for a second SIPGP step (t_p : 16 h). Figure 88 shows that the structure thickness increases significantly after the second polymerization while the structure shape remains. Also here, a broadening of the PS structures can be observed.

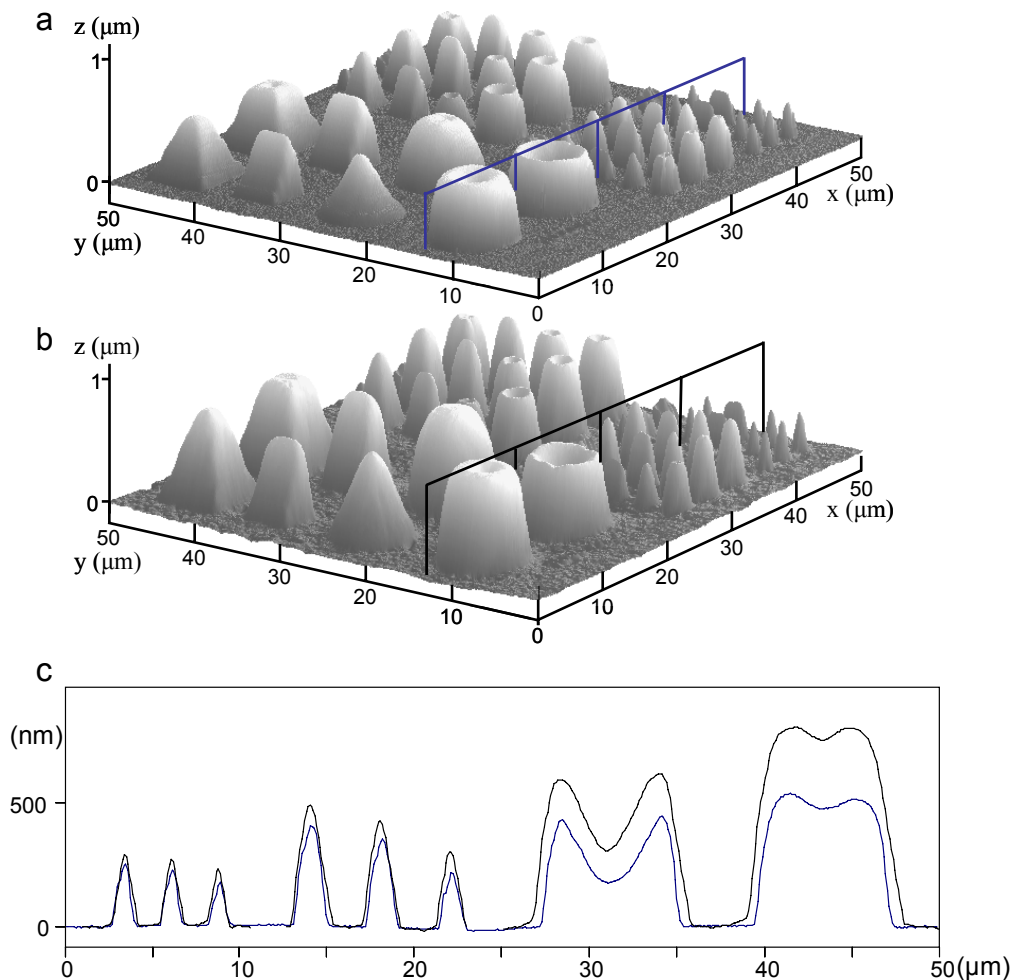


Figure 88. (a) Three dimensional representation of an AFM image of the microstructured PS grafts (t_p : 18h). (b) The same substrate after the polymerization of styrene for 16 more hours. (c) Section analysis as indicated in (a) and (b).

Different section analyses with a 1:1 aspect ratio of PS structures in Figure 88 are depicted in Figure 89. Figure 89 clearly shows that the polymer structures growth uniformly in all directions and that the polymer layer thickness increase is identical to the structure

broadening. The later resolution of the polymer patterns is thus limited by the polymer layer thickness.

It has been previously mentioned that the thickness of the polymer grafts created by SIPGP is limited by the solidification of the bulk monomer due to the photopolymerization. However, it is shown here that the polymer grafts with unlimited thicknesses can be prepared by successive polymerization steps or by refreshing regularly the bulk monomer phase.

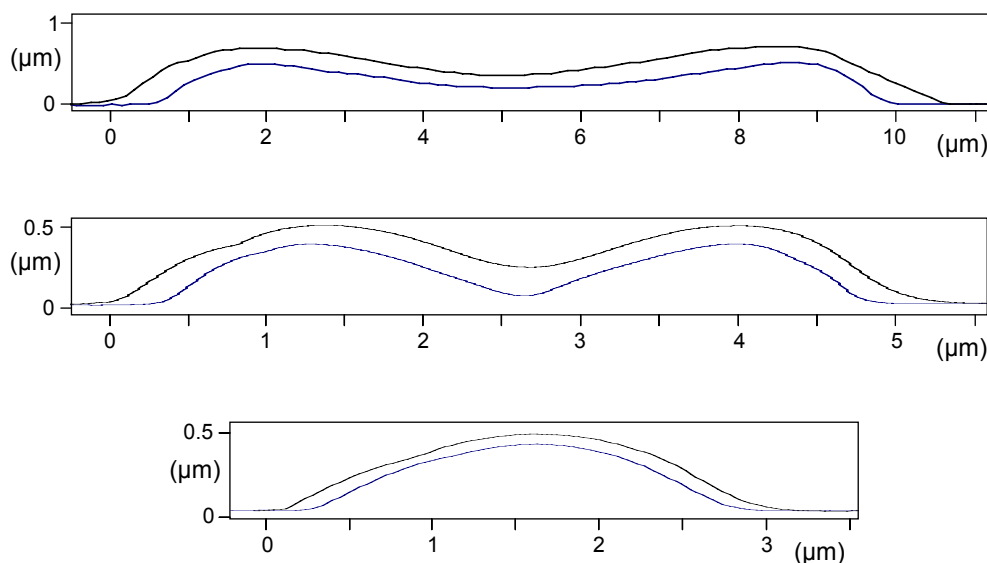


Figure 89. 1:1 aspect ratio section analysis of three different PS structures in Figure 88a (bleu) and Figure 88b (black).

4.4.6 Functionalization of PS grafts on EBCDs

In chapter 4.3.3, different synthetic routes have been investigated for the functionalization of PS grafts on oxidized UNCD substrates, taking advantage of the chemical stability of the polymer layer. In this section, these functionalization reactions were performed under identical reaction conditions on structured PS grafts on oxidized Si and Si₃N₄ substrates.

4.4.6.1 Structured PAMS grafts on silica

The polymer analogue modification of PS grafts on EBCDs on silica into poly((4-aminomethyl)styrene) grafts (PAMS) via the Tscherniac-Einhorn reaction was confirmed by DRIFT measurements. The IR spectra (not shown) after the amidoalkylation and hydrazinolysis are similar to the IR spectra presented in Figure 62.

The structured polymer grafts were measured by AFM after each reaction step and revealed a significant thickness change after each functionalization (Figure 90).

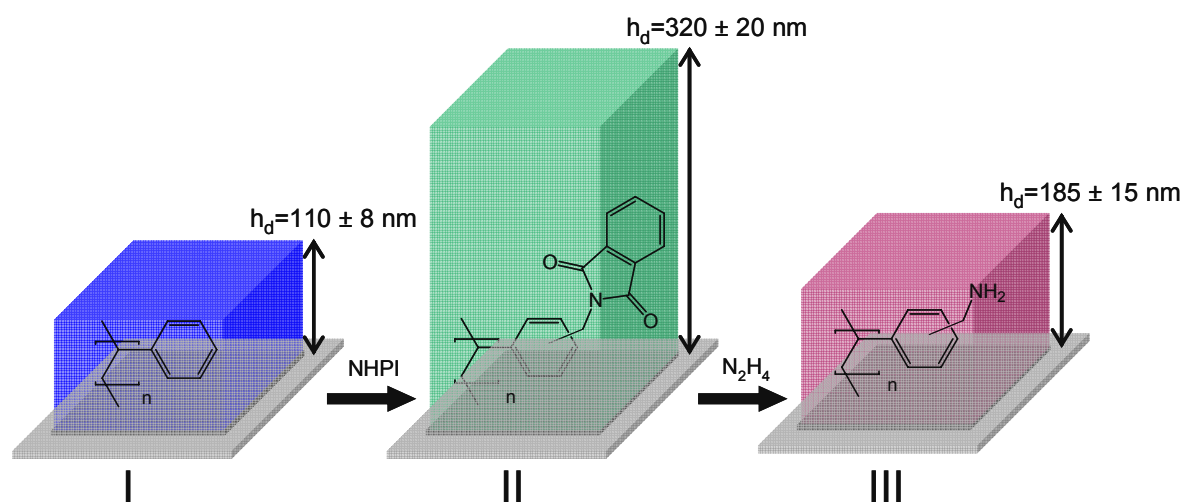


Figure 90. Functionalization of PS grafts (I) with N-(hydroxymethyl)phthalimide (NHPI) and reduction of II (PVBP) with hydrazine in refluxing ethanol results in PAMS grafts (III). h_d was measured by AFM after each functionalization steps. The substrate was intensively washed with ultrasound in different solvents after each reaction steps.

Since the dry polymer layer thickness is given by $h_d = M_n \sigma / \rho N_{Av}$, the change in M_n by the polymer analogue conversion of the polymer side functionalities can be calculated (if the bulk density of the different polymer types is known) by the measurement of h_d before and after the reaction. Assuming that the grafting density remains constant and using the bulk density of the given polymer:

$$\frac{M_{n,1}}{M_{n,2}} = \frac{h_{d,1}}{h_{d,2}} \cdot \frac{\rho_1}{\rho_2} \quad \text{Eq. 20}$$

The bulk density of poly(4-vinylbenzyl)phthalimide (PVBP) and PAMS was calculated by the additive group contribution approach²⁶² since no experimental data for the respective polymers are available in literature.

Using Eq. 20, the average substitution degree (number of aminoalkyl groups per aromatic ring) was calculated for PVBP and PAMS grafts (the average degree of substitution can be directly be calculated from the change in M_n). An average substitution degree of 1.37 ± 0.21 for PVBP grafts and 1.37 ± 0.19 for PAMS grafts was calculated. It is noteworthy that an

identical average substitution degree was calculated independently for PVBP and PAMS grafts by comparing $h_{d,PS}$ with $h_{d,PVBP}$ and $h_{d,PS}$ with $h_{d,PAMS}$, respectively.

The introduction of more than one alkyl group on each aromatic ring when PS is treated with an excess of alkylation reagent is in agreement with earlier reports: while the first substitution occurs in the para position, the second is located in ortho position.²⁷³ The high degree of substitution indicates that the polymer grafts must be functionalized not only at the polymer-solvent interfaces but throughout the entire layer. This experiment shows again that the chemical composition of polymer grafts can be determined only by measuring the polymer layer thickness.

4.4.6.2 Functionalization of structured PAMS grafts

In chapter 4.3.3.5, we showed that the aminomethyl side chain functionality of the PAMS grafts can be further functionalized with rhodamine B isothiocyanate (RBITC). However, the fluorescence image (Figure 63) of the labeled PAMS grafts does not prove that the coupling occurred throughout the entire polymer layer. Restricted diffusion of the steric demanding RBITC would lead to functionalization only at the proximal polymer layer. This might be expected since it was shown that the SIPGP leads to branched polymer grafts. In order to elucidate this, a PAMS gradient was labeled with RBITC. The PAMS thickness gradient was obtained by the chemical modification of the PS gradient structure on Si_3N_4 (Figure 80b).

In Figure 91, the fluorescence intensity of the polymer structure correlates nicely with the polymer layer thickness. If the fluorescence dye was only coupled to amino groups at the polymer-solvent interface, the measured fluorescence intensity would have been constant and independent of the polymer layer thickness. The good correlation between the polymer layer thickness and the fluorescence intensity proves that the PAMS grafts were functionalized throughout the entire polymer layer.

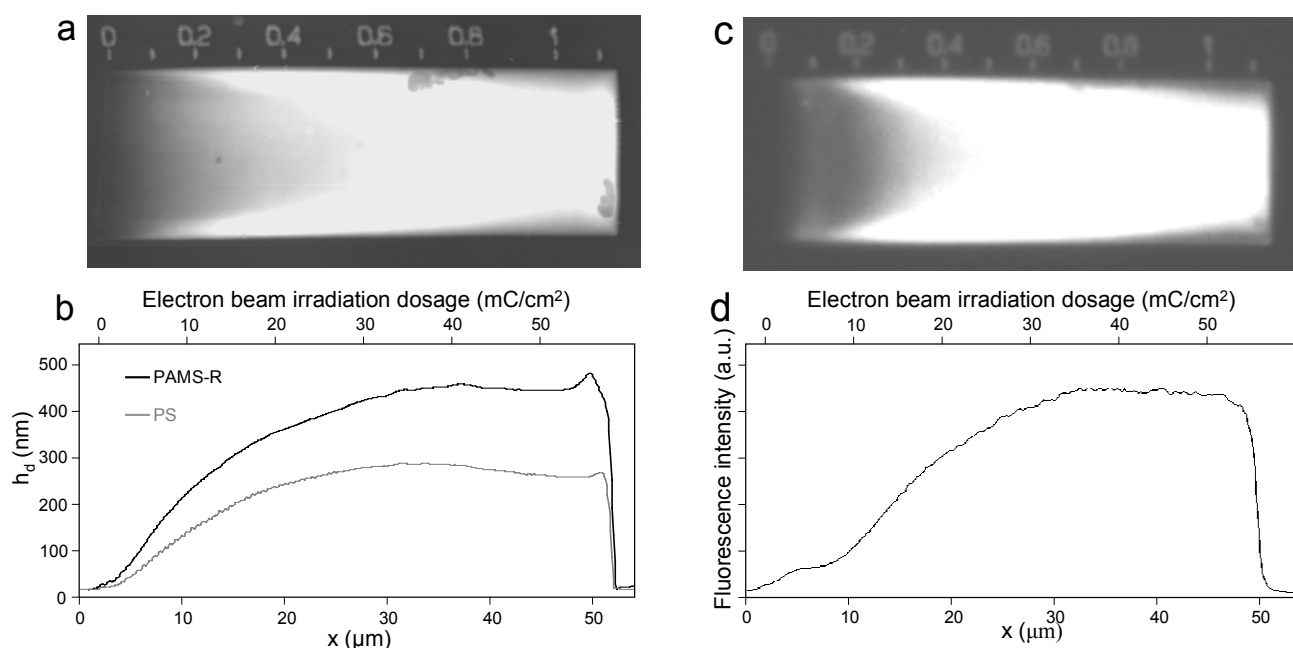


Figure 91. (a) AFM image of a PAMS thickness gradient structure on oxidized silicon nitride, functionalized with RBITC (PAMS-R). (b) Average height profile along the gradient direction from the same structure before and after the PS to PAMS-R conversion. (c,d) Fluorescence image and section analysis of the same PAMS-R structure. The fluorescence intensity in (d) was obtained by a pixel analysis of image (c) along the gradient direction.

This result demonstrates that PAMS grafts can be applied for the preparation of polymer grafts with complex functionalities. The functionalization of PAMS grafts with enzymes is under investigation in the research group of the WSI. The preparation of *enzyme surface concentration gradients* by this approach will be the subject of future research. Such surfaces may be used for fundamental biomedical research for e.g., a better understanding of cell adhesion phenomena.

4.4.6.3 Nitration and sulfonation of structured PS grafts

The nitration and sulfonation of PS grafts on structured EBCDs on silica was performed as outlined in chapter 4.3.3.3. The successful conversion of PS grafts to poly(nitrostyrene) (PNS) and poly(styrenesulfonic acid) (PSSA) was confirmed by DRIFT spectroscopy. AFM measurements of the structured polymer grafts revealed a polymeric layer thickness increase of approximately 140% and 170% upon the introduction of nitro and sulfonic acid groups respectively, which results in an increase of the molecular weight of the grafted polymer chains. This demonstrates that beside the thermal and ultrasound stability, the polymer grafts

created by the on structured EBCDs are chemically stable under various reaction conditions such as strong reduction, oxidation or under acidic conditions.

In contrast to PS, PSSA is hydrophilic and crosslinked PSSA resins are commonly used as hydrogels.²⁷⁴ Water contact angle measurements on unstructured PSSA grafts showed a complete wetting of the substrate whereas unfunctionalized PS grafts display a water contact angle of approx. $\theta = 90^\circ$.

A PSSA thickness gradient on an oxidized silicon wafer was prepared by sulfonation of a PS gradient structure. Observation of the PSSA gradient with an optical microscope revealed an instantaneous color change of the structure by e.g. breathing onto the substrate (Figure 92). The color is typical for thin transparent films having thicknesses comparable to the wavelength of light. The color originates from the interference between light waves reflected at the top surface of the film and at the bottom surface. The color depends on the film thickness. A sudden color change of the structure is thus probably due to a thickness increase caused by the swelling of the hydrophilic PSSA layer under the influence of increasing humidity.

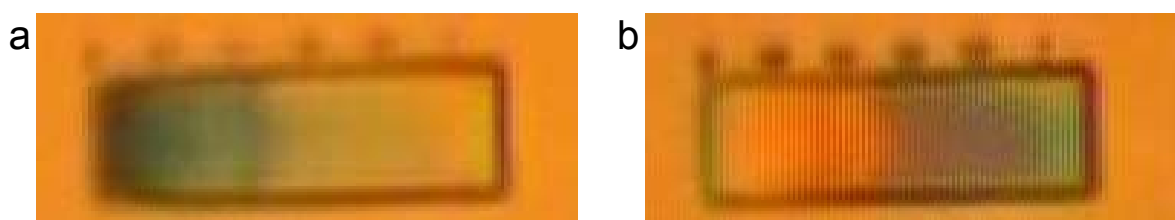


Figure 92. (a) Optical micrograph of a $10 \times 50 \mu\text{m}^2$ PSSA thickness gradient on an oxidized silicon wafer. (b) Photograph of the same structure at higher air humidity.

The humidity induced swelling of the PSSA gradient structure was investigated quantitatively in the research group of Dr. Rüdiger Berger at the Max-Planck-Institute for Polymer Research in Mainz. The PSSA gradient was measured by AFM under different relative humidity (RH) at ambient temperature using an environmental AFM setup.²⁷⁵ Figure 93 shows that for the entire gradient structure, the polymer layer thickness increases with increasing RH. An RH increase of 5 to 97.1% results in a polymer layer thickness increase of approx. 140% or in a swelling degree (Q) of approx. 1.4.

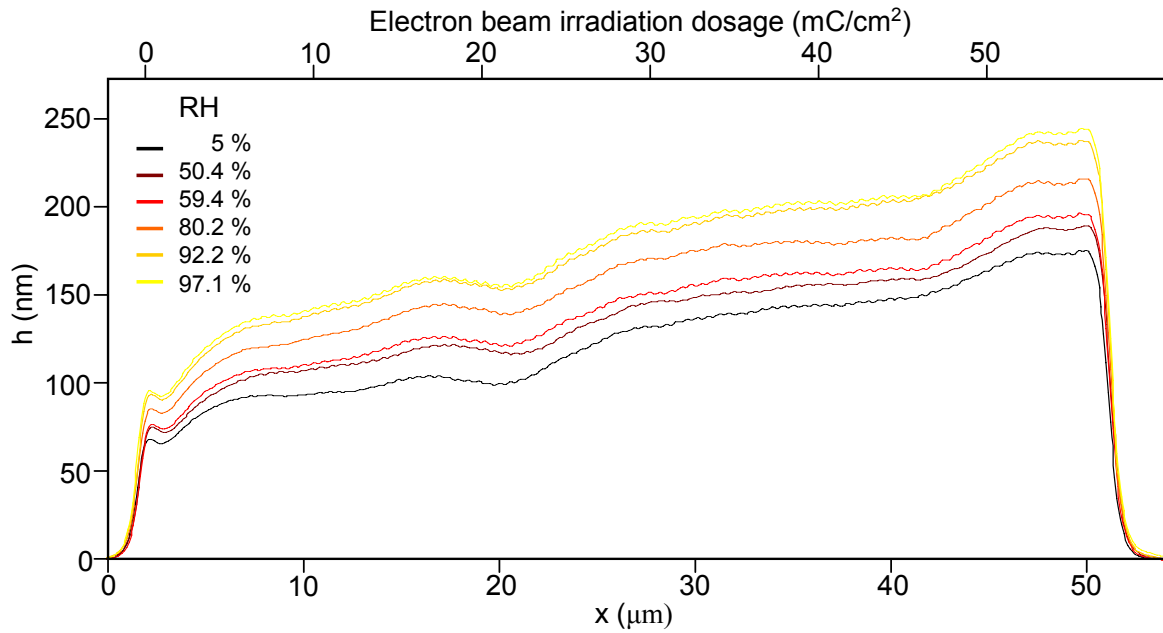


Figure 93. Height profiles (measured by AFM) along the gradient direction from a PSSA thickness gradient on oxidized silicon at different relative humidity (RH). The measurements were performed at room temperature.

The dependency between the degree of swelling (Q) and the relative humidity is shown in Figure 94. The degree of swelling is given by:

$$Q = h_s / h_d \quad \text{Eq. 21}$$

where h_s is the swollen and h_d the dry polymer layer thickness. The experimental data in Figure 94 was obtained by comparing Q for the gradient at 3, 30 and 50 mC/cm^2 . Figure 94 shows that the degree of swelling is independent of the polymer layer thickness.

The sorption behavior of a mobile permeant (humid air in this case) is dependent on the interaction strength between the mobile permeant and the polymer matrix. In the case of very strong interactions between the polymer molecules and the permeant, a Langmuir absorption behavior is observed.²⁷⁶ The permeant is incorporated easily at low vapor pressures, leading to an asymptotic dependence at higher vapor pressures.

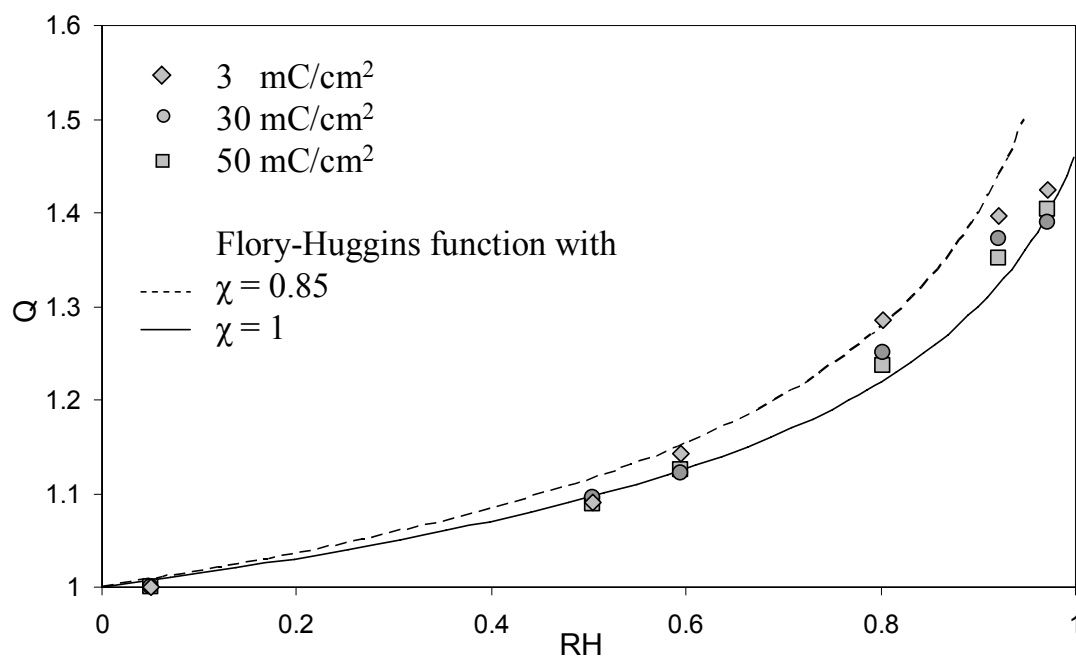


Figure 94. The degree of swelling (Q) of the PSSA graft gradient at 3, 30 and 50 mC/cm^2 (Figure 93) as a function of the relative air humidity. The polymer layer thickness of the gradient at a relative humidity of 5% was taken as the dry polymer layer thickness. This is a good approximation, since the thickness increase of hydrophilic polymer grafts is insignificantly below an HD of 10%.²⁷⁷ The data was fitted via the Flory-Huggins relationship according to Eq. 23, using different χ -values.

If the interactions between mobile molecules are stronger than the polymer-permeant interactions, the amount of absorbed molecules in the polymer matrix increases exponentially with increasing vapor pressure and the sorption behavior can be described by the Flory-Huggins relationship.²⁷⁶

$$\ln(RH) = \ln \phi + (1 - \phi) + \chi(1 - \phi)^2 \quad \text{Eq. 22}$$

with ϕ as the volume fraction of water molecules in the polymer matrix and χ the Flory-Huggins interaction parameter. χ is a measure for the heat of mixing between the mobile phase and the polymer. This sorption dependency is typical for the interaction between water and hydrophobic polymers. Values between 0.5 and 1.0 for χ indicates that the interaction between water molecules is stronger compared to the water-polymer interaction. It has already been pointed out by Rhe *et al.*²⁷⁷ that in principle, a further term should be added in Eq. 22 for the elastic pressure of the polymer due to the stretching of the polymer chains. However, since the degree of swelling is relatively small, the change of the free energy of the system due to chain stretching is considered to be small when compared to other contributions. The

Flory-Huggins relationship in Eq. 22 can also be expressed as a function of the degree of swelling. The volume fraction of water molecules in the polymer matrix can be calculated from the degree of swelling as $\phi = 1 - 1/Q$:

$$\ln(RH) = \ln(1 - 1/Q) + 1/Q + \chi(1/Q)^2 \quad \text{Eq. 23}$$

The data in Figure 94 were fitted via the Flory-Huggins relationship according to Eq. 23 using χ -values of 0.85 and 1. The very good agreement between the observed humidity induced swelling of the PSSA grafts and the fit function shows that the PSSA grafts have a Flory-Huggins-type sorption behavior. This swelling behavior is in good agreement with earlier reports on the swelling behavior of different hydrophilic polymer grafts in humid air.^{277,278} At first sight, this swelling behavior is unexpected for hydrophilic polymers, however, it must be considered that air is a bad solvent for the studied polymers and even at 100% relative humidity, the total amount of water molecules in air is less than 3% at room temperature.

The instantaneous color change of the gradient by breathing onto the substrate proves that the responds of the polymer layer, the swelling, is very fast. In general, the time for swelling of hydrogels is proportional to the square of the hydrogel thickness and reaches several hours for conventional hydrogels.²⁷⁹ The apparent fast thickness increase of the PSSA grafts is attributed to the polymer thickness of $\sim 100\text{nm}$, as compared to several millimeters for conventional hydrogel materials. This fast swelling illustrates the potential of thin polymer grafts for the preparation of stimuli responsive surfaces for e.g. sensor applications.

4.4.7 Functionalization of P4VP grafts with gold

One major advantage of the SIPGP EBCD approach is that this technique allows the fabrication of thermally and chemically stable polymer grafts on very different substrates with precise three dimensional architectures even at the sub-micrometer scale. The fabrication of metal structures with the same architectures may also have interesting scientific and industrial application. Highly defined metallic nanowires on surfaces may, for instance, find applications in quantum electronics.

In this section, it was investigated if the polymer structures can be converted into conductive metal structures. Metallic architectures can be prepared by the incorporation of elemental metal in the structured polymer grafts by a two-step procedure:

1. complexation of the polymer grafts with metal ions,
2. reduction of the metal ions to elemental metal.

The polymer grafts can, i.e., successively be removed by e.g. plasma treatment. In other words, the structured polymer grafts would act as a three dimensional template for the fabrication of the desired metallic structure.

The preparation of complex three dimensional metallic structures by this approach is an ongoing project between the research group of Jordan and Grunze. Here, the first preliminary results are presented. As apparent, this work is still far from a desired one-to-one translation of the three dimensional polymer architectures to conductive metallic structures.

In order to demonstrate the potential of this approach, the replacement of structured poly(4-vinylpyridine) (P4VP) grafts by elemental gold was investigated in a first set of experiments following a well established synthetic route: reaction of the P4VP grafts with HAuCl_4 and reduction of the gold salt to elemental gold. The incorporation of elemental gold in polymer films containing amino groups by this approach has been studied intensively. Various synthetic routes were developed for the reduction of the polymer-attached AuCl_4^- ions including heating,²⁸⁰ UV-light,²⁸¹ hydrogen plasma²⁸² and conventional reducing agents in solution such as hydrazine.²⁸³ Since hydrogen plasma also etches organic polymers, it will not only reduce the gold salt, but also remove the polymeric layer in one single step.^{284,285}

The reaction between PS-P2VP block copolymers and HAuCl_4 and successive reduction of the gold salt with hydrazine has been intensively studied by Spatz and coworkers for the preparation of micelles loaded with gold nanoparticles.²⁸³ The same synthetic route has been used here for the incorporation of elemental gold in structured P4VP grafts (Figure 95).

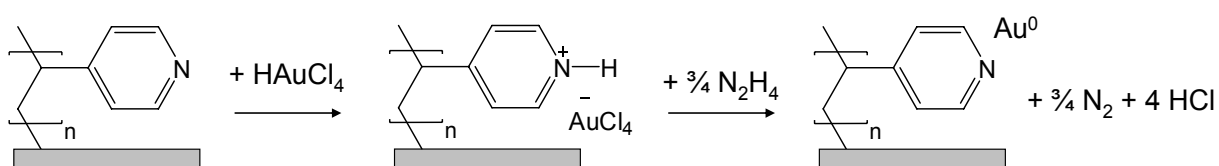


Figure 95. Reaction of P4VP with HAuCl_4 and reduction of the gold salt to elemental gold.

310 ± 13 nm thick P4VP grafts were prepared by the SIPGP of 4VP (t_p : 17h) on structured EBCDs on an oxidized silicon wafer ($1\mu\text{m}$ radius; 50 eV ; 60 mC/cm^2). The substrate was then immersed in a $\text{NaAuCl}_4 \cdot 2\text{H}_2\text{O}$ solution in methanol over night at room temperature. The substrate was rinsed with methanol, dried and characterized. The successful reaction between the gold salt and the P4VP grafts was confirmed by AFM and DRIFT. A polymer layer thickness of 550 ± 30 nm was found (Figure 97). This thickness increase of 177% is probably

not only due to the incorporation of HAuCl_4 groups, but also due to the repulsive Coulomb forces within the created polyelectrolyte graft by quaternization.

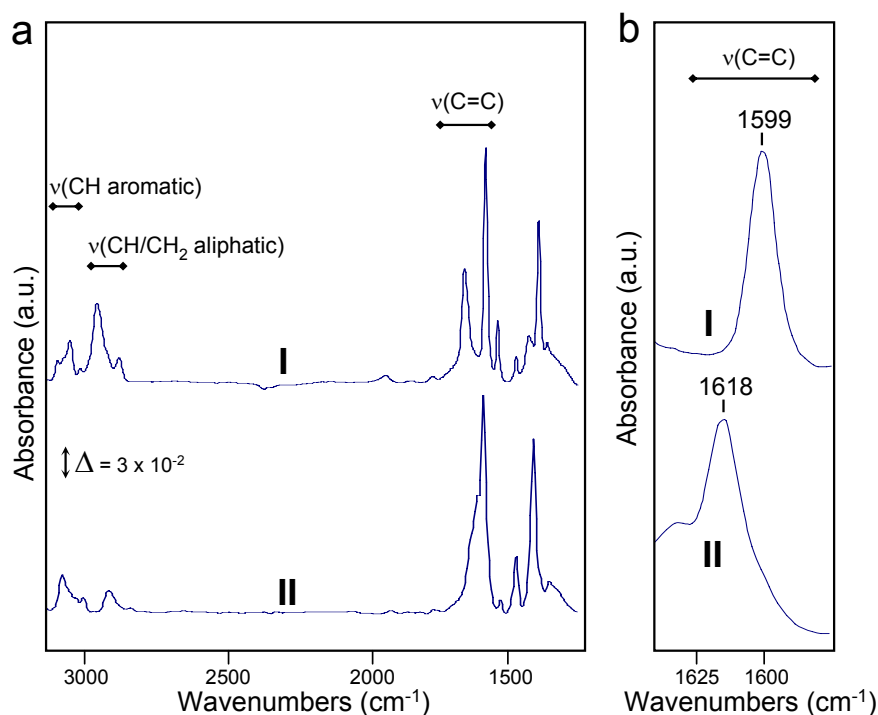


Figure 96. (a) DRIFT spectra of P4VP (I) and P4VP- HAuCl_4 (II) grafts on silica. (b) Detailed view of the spectra between 1635 and 1575 cm^{-1} .

In order to investigate the chemical composition of the polymer grafts, DRIFT measurements were performed before and after the quaternization (Figure 96). The spectrum of the P4VP grafts shows the typical absorption bands of the bulk spectrum of P4VP, such as the aliphatic and aromatic $\nu(\text{C-H})$ stretching vibrations around 3000 cm^{-1} and the vibrational bands from the $\text{C}=\text{C}$ double bonds of the pyridine ring at 1599 cm^{-1} .²⁸⁶ Upon quaternization the P4VP grafts, a new adsorption band can be observed at 1618 cm^{-1} for the aromatic $\nu(\text{C}=\text{C})$ stretching mode. The shift of the $\nu(\text{C}=\text{C})$ stretching band to slightly higher wavenumbers due to the quaternization reaction of the pyridine ring is in agreement with previous reports (Figure 96b).²⁷⁷

The reduction of AuCl_4^- was performed by placing the sample in a N_2H_4 solution (THF) for 72 hours. The samples were rinsed with THF and ethanol. The sample had a brown metallic color after the reduction indicating the presence of elemental gold. AFM measurements showed a significant thickness decrease of the structures from 550 ± 30 nm to 360 ± 30 nm. AFM scans from individual polymer dots revealed a very rough topography of the structures, in contrast to the P4VP and P4VP- HAuCl_4 grafts (Figure 97).

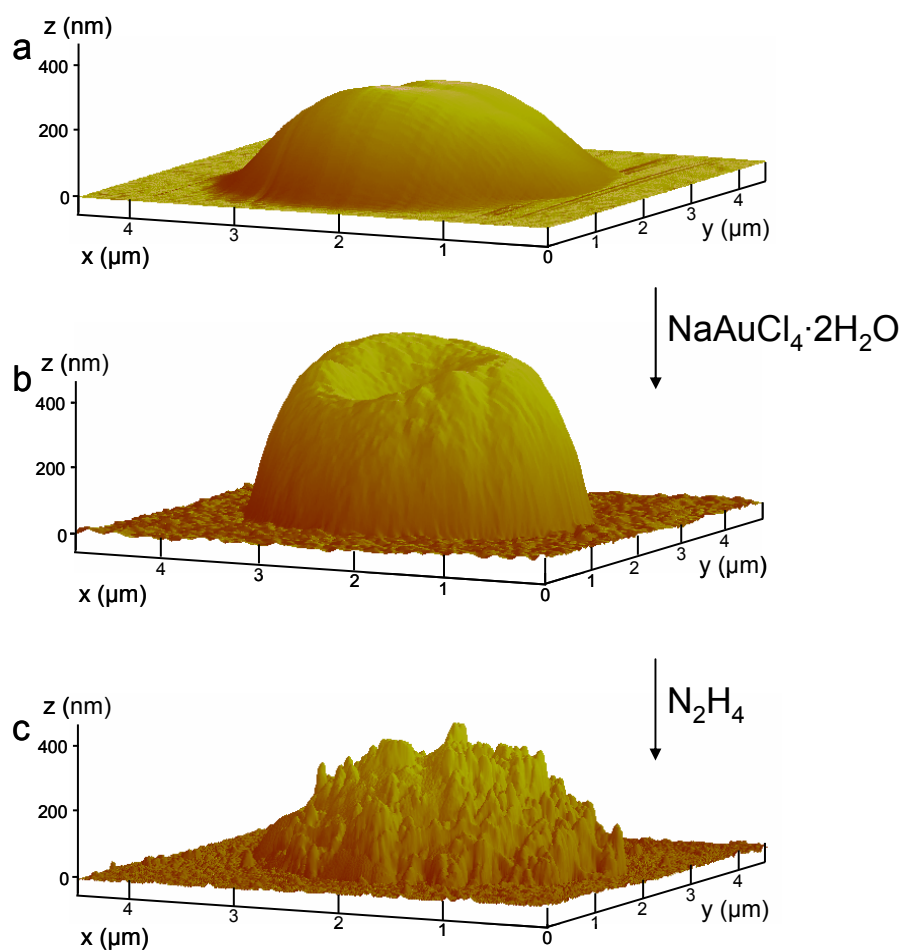


Figure 97. AFM scans of: (a) P4VP dot (EBCL: $1 \mu\text{m}$ radius; 50 eV ; 60 mC/cm^2), (b) P4VP dot after the reaction with $\text{NaAuCl}_4 \cdot 2\text{H}_2\text{O}$, (c) the same dot after reduction with hydrazine.

This indicates that the created gold structures consist of gold particle agglomerates, not of a continuous and homogeneous gold film. The organization of elemental gold created by the reduction of polymer bonded AuCl_4^- salts into nanoparticle agglomerations has been observed in various studies.²⁸⁰⁻²⁸⁷ The improvement of the reduction conditions in order to obtain more homogeneous gold structures (by changing the reaction solvent, reaction temperature, eventual additives, etc.) is currently under investigation.

Alternatively, the reduction of P4VP- HAuCl_4 by hydrogen plasma was investigated. Figure 98 shows a scanning electron microscope (SEM) images from the P4VP- HAuCl_4 grafts before (Figure 98a) and after H_2 -plasma treatment (Figure 98b,c).

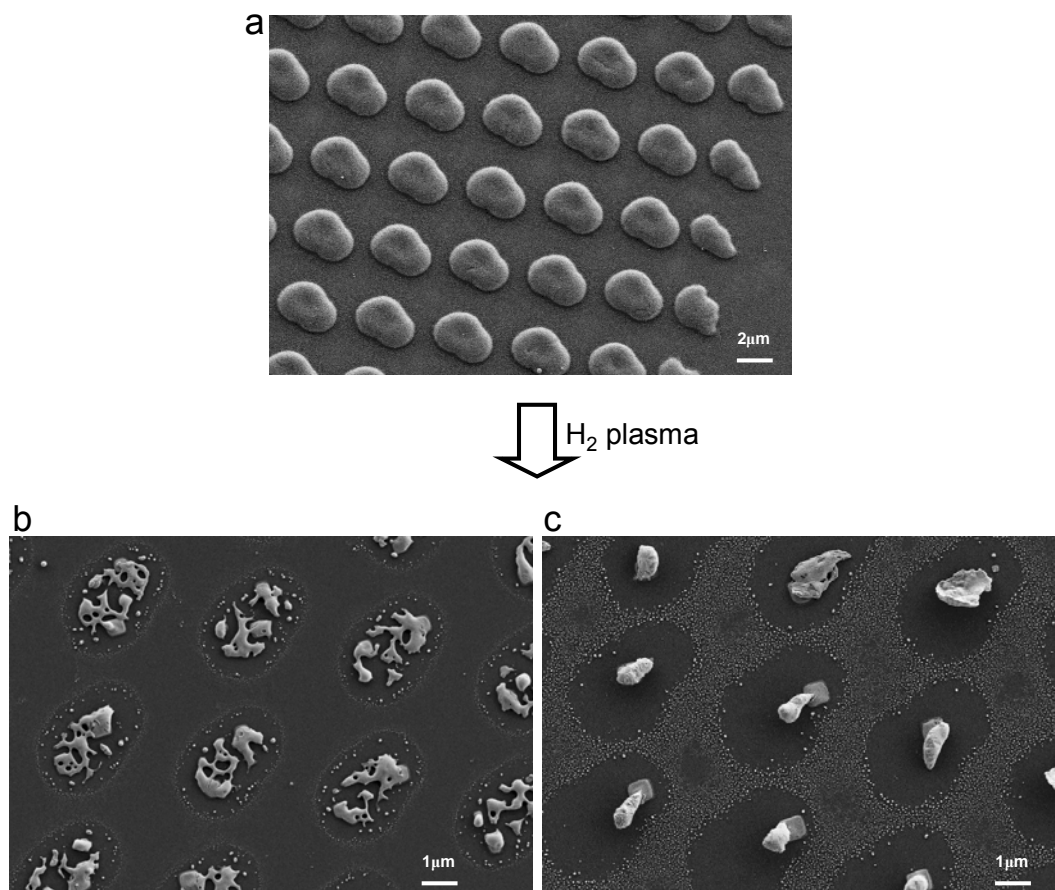


Figure 98. (a) SEM image of P4VP-HAuCl₄ dots (EBCL: 1 μm radius; 50 eV; 60 mC/cm²). (b and c) SEM images of the same sample after hydrogen plasma treatment.

Figure 98 b and c are two electron micrographs taken from the same substrate at different areas. These images indicate the formation of gold clusters at the surface regions that were previously coated with P4VP-HAuCl₄ grafts. All organic material has been etched away by the plasma treatment. However, Figure 98 b and c also show a poor reproducibility of the cluster shape.

It can be concluded from these preliminary results that this approach can potentially be applied for the formation of patterned metal structures. However, significant improvement of the coupling and reduction conditions is needed in order to create homogeneous and reproducible metallic structures.

5 Conclusion

The first aim of this work was to provide answers to some fundamental questions related to the recently developed procedure to fabricate micro- and nanostructured polymer grafts. The procedure as outlined in Figure 99 involves:

1. Modification of a gold substrate with a self-assembled monolayer (SAM) of 4'-nitrophenylthiol (NBT).
2. Structuring of the NBT SAM by electron beam chemical lithography (EBCL).
3. Modification of the amino group to an asymmetric azo-initiator.
4. Surface-initiated photopolymerization (SIPP) in the presence of a bulk vinyl monomer by irradiation with UV-light ($\lambda_{\max} = 350$ nm).

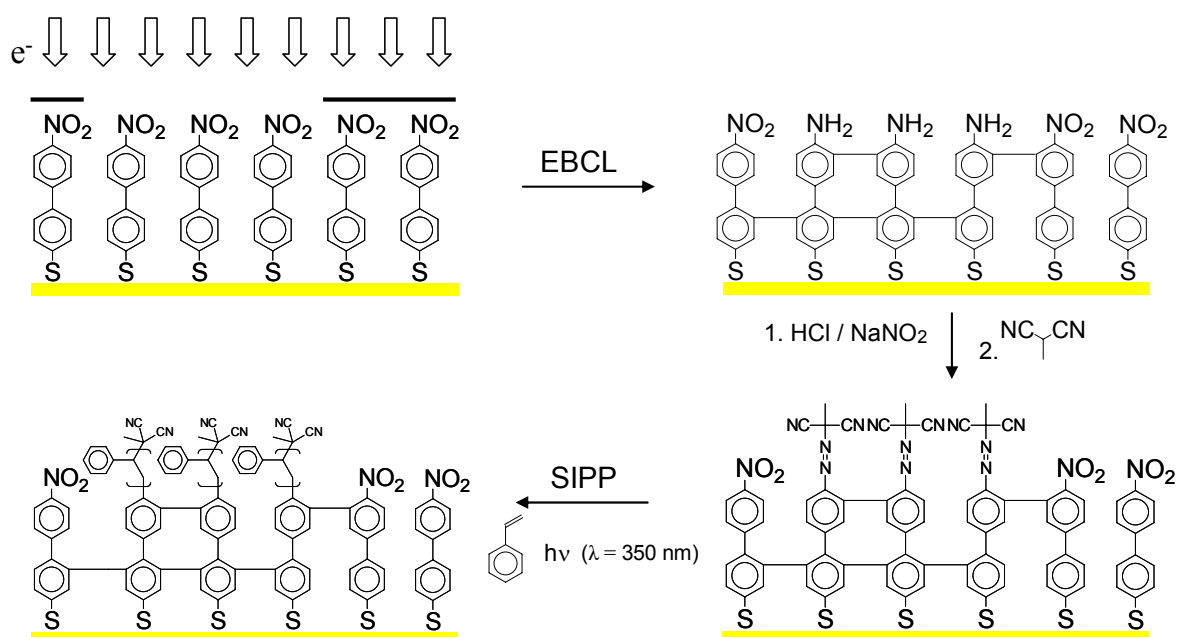


Figure 99. Schematic representation for the preparation of polymer grafts on gold.

This approach allows the preparation of nanostructured polymer grafts down to sub-50 nm resolution.¹⁵¹ The following questions have been investigated during this work: What are the kinetics of the SIPP on nanostructured surfaces? What is the influence of the lateral feature size on the resulting polymer structure? What is the influence of the electron beam dosage and

energy on the resulting polymer grafts? What is the molecular architecture of the grafted polymer chains? How do nanostructured polymer grafts behave in various environments?

First, *ex-situ* kinetic studies revealed an almost linear relationship between the dry polymer layer thickness (h_d) and the polymerization time. It has also been observed that the polymer layer thickness could be controlled by the locally applied electron dosage during the EBCL step (Figure 100). EBCL thus provides a direct tool to control not only the 2D locus of the polymer grafts but also the polymer layer thickness. The gradient structure in Figure 100 gives the polymer layer thickness to electron dosage dependency which allows the fabrication of polymer grafts with controllable three dimensional architectures.

XPS studies have shown that the polymer layer thickness is proportional to the surface concentration of amino groups, created during the EBCL step. The dry polymer layer thickness is given by $h_d = M_n \sigma / \rho N_{Av}$, where M_n , σ , ρ are respectively the number average molecular weight, grafting density and bulk density of the polymer and N_{Av} the Avogadro constant. An increase of the polymer layer thickness at a higher amino group surface concentration was attributed to an increase of the polymer grafting density.

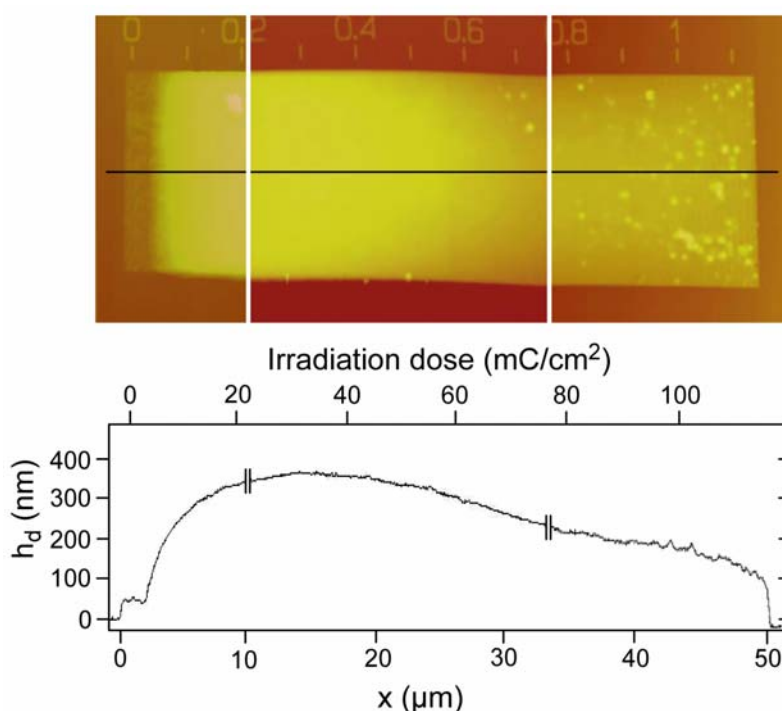


Figure 100. AFM scan and height profile of a polystyrene gradient structure. The electron dosage increases linearly from 0 to 115 mC/cm^2 going from left to right, as indicated by the written scale bar visible at the top of the AFM image ($t_p = 16.5\text{h}$).

Furthermore, it has been observed that the thickness of polymer structures created under identical reaction conditions is strongly influenced by the lateral footprint size (50 - 1000 nm). This can be understood by the fact that the molecular dimension of the grafted polymer chains is in the same dimension as the lateral feature size and that the polymer chains at the edges of the structures can extend to polymer free surface regions. This leads to less chain crowding and thus, less chain stretching in smaller structures.

It was discovered later, that the third step outlined in Figure 99, the modification of the amino group to an azo-initiator, is not necessarily required. Structured polymer grafts with similar thicknesses and lateral resolution were created by UV irradiation of a structured NBT SAM, submerged in bulk vinyl monomer. Here, styrene, methyl methacrylate and tert-butyl methacrylate were successfully tested. In all experiments, polymer grafts were selectively formed on the crosslinked (by electron beam irradiation) SAM areas. The same was also observed in analogue experiments with other monolayers on gold such as biphenylthiol, methyl- and hydroxyl-biphenylthiol SAMs, structured by EBCL. At this point, two questions arose:

1. Which initiator-free mechanism is responsible for the formation of polymer grafts?
2. Why are polymer grafts selectively formed on the crosslinked SAM regions?

A few studies reported on the preparation of polymer grafts directly onto organic substrates by the self-initiated photografting and photopolymerization (SIPGP).^{71,72} The mechanism of the SIPGP is illustrated in Figure 101. By absorbing a photon, the vinyl monomer (here styrene) acts as a photosensitizer and reaches a biradical, $\cdot\text{St}\cdot$ (a). In solution, $\cdot\text{St}\cdot$ can initiate a free radical polymerization of styrene (b). In the meantime, $\cdot\text{St}\cdot$ may also abstract a hydrogen atom from a surface functionality (c). The radical formed on the substrate initiates the free radical grafting polymerization of styrene (d). Also block copolymers can be prepared by this mechanism since hydrogen atoms of polymer grafts can be abstracted during the SIPGP process.

It was found that non-crosslinked SAM molecules desorbed from the surface during the SIPGP process due to the photo-oxidation of the Au-S bond. Crosslinked SAM molecules are more stable due to the multiple adhesion sites of the entire layer. In other words, polymer grafts are selectively formed on the previously irradiated SAM-regions by SIPGP, while not crosslinked SAM molecules desorb from the substrate under the polymerization reaction conditions.

By this, morphologically highly defined polymer grafts with thicknesses up to several hundred nanometers can be formed on various inorganic substrates (Figure 102). Again, the polymer layer thickness can be controlled by the locally applied electron dosage.

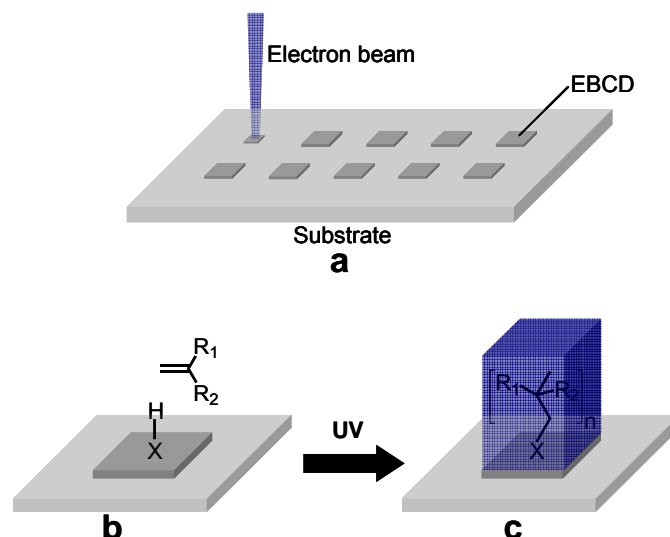


Figure 102. Principle for the formation of structured polymer grafts on various substrates. (a) Irradiation of the substrate by an electron beam induces the formation of EBCDs on the irradiated surface areas. (b) The structured substrate is immersed into bulk monomer and irradiated with UV for the SIPGP. (c) Polymer grafts are selectively formed on the previously irradiated surface regions. (X = C or O).

Upon electron irradiation of a substrate, thin electron beam induced carbon deposits (EBCDs) are formed on the exposed surface area.¹⁵⁴⁻¹⁵⁶ The decomposition of residual hydrocarbon molecules present in the vacuum chamber originated from the pump oil, is responsible for the formation of these EBCDs. EBCDs are very stable, highly crosslinked hydrocarbon deposits with a composition close to $C_9H_2O_1$.

Based on previous results, we assumed that the SIPGP was responsible for the formation of polymer grafts on these EBCDs. EBCDs contain diverse functionalities including hydroxyl, aromatic and aliphatic C-H groups which can be activated by hydrogen abstraction during the SIPGP process.

In a first set of experiments, the SIPGP of different monomers was performed on EBCDs of a few Ångströms thickness. Styrene, methyl methacrylate, tert-butyl methacrylate, 4-vinylpyridine, 4-vinylbenzylchloride and acrylic acid were successfully grafted and the polymer layer thickness growth (dh_d/dt) rate was determined. It was found that the dh_d/dt -values correlate with the monomer polymerization rate of in solution.

One further advantage of this two-step approach is that chemically and thermally stable EBCDs can be prepared on almost any substrate (except gold). Thus, polymer grafts were successfully prepared on different conductors (aluminum and silver), semiconductors (silicon, silicon nitride, germanium, gallium arsenide, gallium nitride) and isolators (mica, borosilicate glass).

AFM measurements revealed that at low electron doses, the created EBCD structures cover the substrate only partially. An increase of the electron beam dosage increases the EBCD surface concentration and thus the surface concentration of potential grafting points for the SIPGP. The dependency between the polymer layer thickness and the locally applied electron dosage allows the preparation of 3D polymer architectures (Figure 103). The shape of the resulting polymer architecture can be predicted using the found thickness to electron dosage dependency.

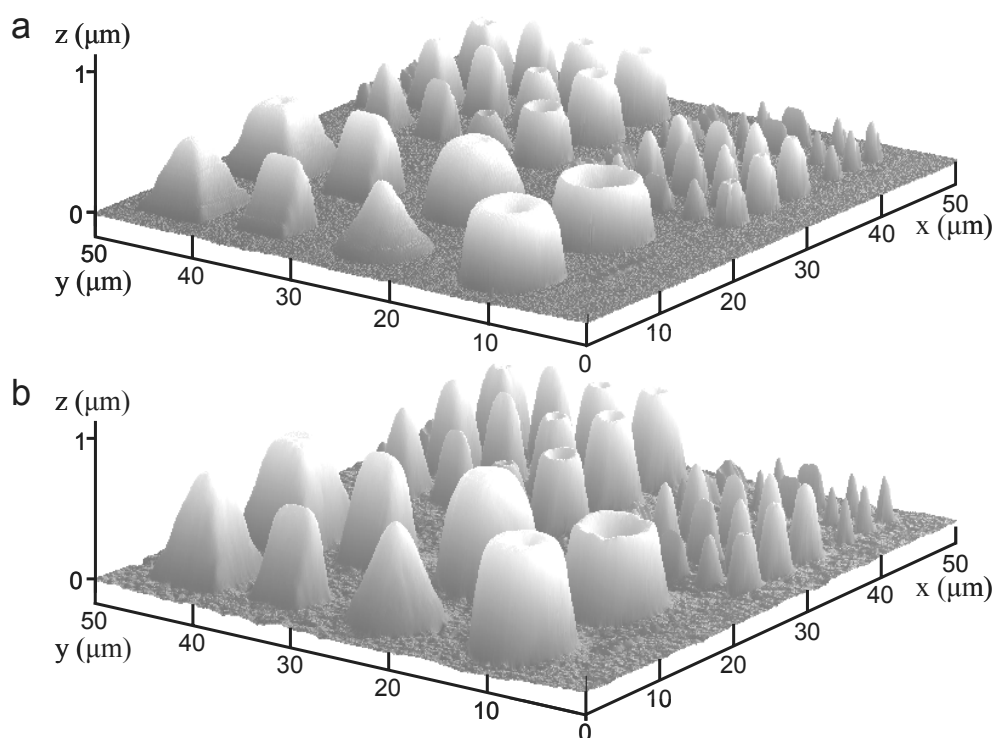


Figure 103. (a) AFM image of 3D microstructured PS grafts on a GaAs substrate by the SIPGP of styrene (t_p : 18h) on structured EBCDs. The EBCD process was performed using a focused electron beam of a scanning electron microscope coupled to a pattern generator. The pattern generator allows the creation of almost any imaginable two dimensional structures and the applied electron dosage can be controlled for each created structure. (b) PS structures after the polymerization of styrene during 34 hours on the same EBCDs.

Prolonged ultrasound treatment in different solvents and Soxhlet extraction in high boiling solvents demonstrated the excellent (thermal) stability of the polymer grafts. Furthermore, it has been found that the polymer grafts are stable under various chemical conditions, even under such drastic conditions as concentrated sulfuric or nitric acid. This allowed polymer analogue functionalizations of polymer grafts without stability constraints. Different synthetic routes have been investigated for the preparation of (3D) structured polymer grafts with all various chemical functionalities on different substrates for the preparation of e.g. stimuli responsive surfaces. Polymer analogue reactions on structured polymer grafts have been studied using conventional analytical methods such as fluorescence microscopy, XPS and infrared spectroscopy. Furthermore, since the dry polymer layer thickness is proportional to the molecular weight of the grafted polymer chains, we could determine in certain cases, the conversion of polymer analogue reactions by measuring the polymer layer thickness before and after the reaction. This concept has also been applied to determine the molecular architecture of polymer grafts.

A common idea in the polymer community is that well defined polymer grafts can only be achieved by living polymerization techniques on highly defined SAMs.³¹ However, it has been demonstrated here that a free radical polymerization technique allows an unmatched control over the polymer layer morphology on the sub-micrometer scale. The here developed EBCD-SIPGP approach has a multitude of advantages compared to existing approaches for the preparation of structured polymer grafts:

- Simple two-step procedure.
- Resist- and SAM-free approach.
- No surface-bonded initiators required.
- Substrate independent.
- The polymer grafts are thermally and chemically extremely stable which is up to now a major drawback for commonly used SAM-based systems. This allows polymer analogue functionalizations of polymer grafts in various reaction conditions and thus the preparation of polymer coatings with a broad variety of chemical functions.
- High resolution: EBCD structures with sub-10 nm resolution can be prepared with modern electron beam optics.
- Electron beam lithography is not restricted to any length scale. While larger surface areas can be structured using an electron flood gun in combination with a stencil mask, much smaller and more complex structuring can be fabricated by *direct writing* with a

focused electron beam. This is a major advantage compared to SPM-based lithography approaches.

- Polymer grafts with three dimensional architectures can be prepared due to the dependency between the electron beam dosage and the polymer layer thickness.
- The preparation of multi block copolymers is possible.

Stable polymer grafts having all kinds of dimensions, architectures and chemical functionalities on various substrates can now be prepared, based on this study. These structures may open new perspectives in various fundamental and applied research areas such as sensor technologies, biomedicine, nanofluidics, nano-optics, biochip technologies and microelectronics.

An additional project which was to couple biological systems (enzyme, cells, etc.) to electric conductive synthetic diamond in order to use this material in amperometric biosensor implants. The unique bulk and surface properties makes diamond an ideal material for biomedical applications.

First, nitrobiphenyl SAMs on diamond surfaces were synthesized and characterized. We have studied the radiation induced conversion of the terminal nitro group into an amino group in order to expand the EBCL of biphenyl SAMs to diamond surfaces. In the second part, the SIPGP of vinyl monomers has been applied for the preparation of polymer grafts directly onto oxidized OH-terminated diamond substrates. Also here, different synthetic routes have been investigated for the functionalization of polymer grafts, in order to prepare polymer coatings with various chemical functions. The functionalization of these polymer grafts with enzymes is currently under investigation.

6 German Abstract

Das erste Ziel dieser Arbeit war, Antworten auf verschiedene fundamentale Fragen bezüglich mikro- und nanostrukturierter Polymerbürsten zu finden. Zu Beginn dieser Studie wurde hierzu eine bestehende Prozedur in vier Stufen angewandt (Abbildung 1):

1. Modifikation einer Goldoberfläche mit einer selbstorganisierten Monolage (SAM) aus Nitrobiphenylthiol (NBT).
2. Strukturierung der NBT SAM durch Elektronenstrahlchemolithographie (*electron beam chemical lithography*, EBCL).
3. Umwandlung der Aminogruppe in einen asymmetrischen Azoinitiator.
4. Oberflächeninitiierte Photopolymerisation (*surface-initiated photopolymerization*, SIPP) in Anwesenheit von Monomer und Bestrahlung mit UV Licht.

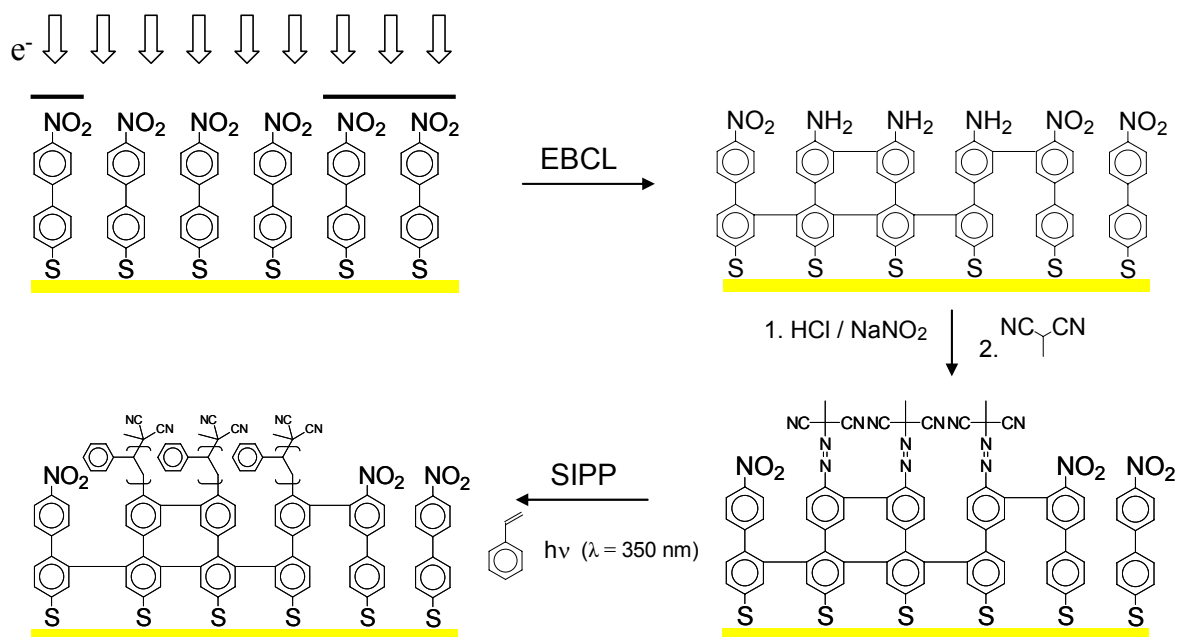


Abbildung 1. Schematische Darstellung der Bildung von Polymerbürsten auf Gold

Dieser Ansatz ermöglicht die Herstellung von nanostrukturierten Polymerbürsten mit einer Auflösung von unter 50 nm.¹⁵¹

Ex-situ Studien der Kinetik zeigten zunächst einen beinahe linearen Zusammenhang zwischen der Dicke der trockenen Polymerschicht (h_d) und der Polymerisationszeit (t_p). Es konnte auch

beobachtet werden, dass die Schichtdicke durch die lokal angewandte Elektronendosis während des EBCL-Schritts bestimmt wird (Abbildung 2). Daher stellt EBCL nicht nur eine Methode zur zweidimensionalen Strukturierung von Polymerbürsten, sondern auch zur Kontrolle der Polymerschichtdicke dar. Der Gradient in Abbildung 2 zeigt die Abhängigkeit der Schichtdicke des Polymeren von der Bestrahlungsdosis. Durch diese Abhängigkeit ist es möglich, Polymerbürsten mit kontrollierbarer 3D Architektur zu erzeugen.

Wie Untersuchungen mit Elektronenspektroskopie zur chemischen Analyse (ESCA) zeigten, ist die Polymerschichtdicke proportional zur Oberflächenkonzentration von Aminogruppen, die während EBCL entstanden sind. Die Schichtdicke des trockenen Polymeren h_d ergibt sich zu $h_d = M_n \sigma / \rho N_{Av}$, mit M_n das Zahlenmittel der Polymermolmasse, σ die Pfropfungsdichte, ρ die Polymerdichte und N_{Av} die Avogadrozahl. Eine Zunahme der Schichtdicke mit höherer Dichte von Aminogruppen auf der Oberfläche wird einer zunehmenden Pfropfungsdichte des Polymeren zugeschrieben. Mit wachsender Pfropfungsdichte kommen sich die Polymermoleküle immer näher, worauf sie sich strecken. Dies führt zu einer Zunahme von h_d .

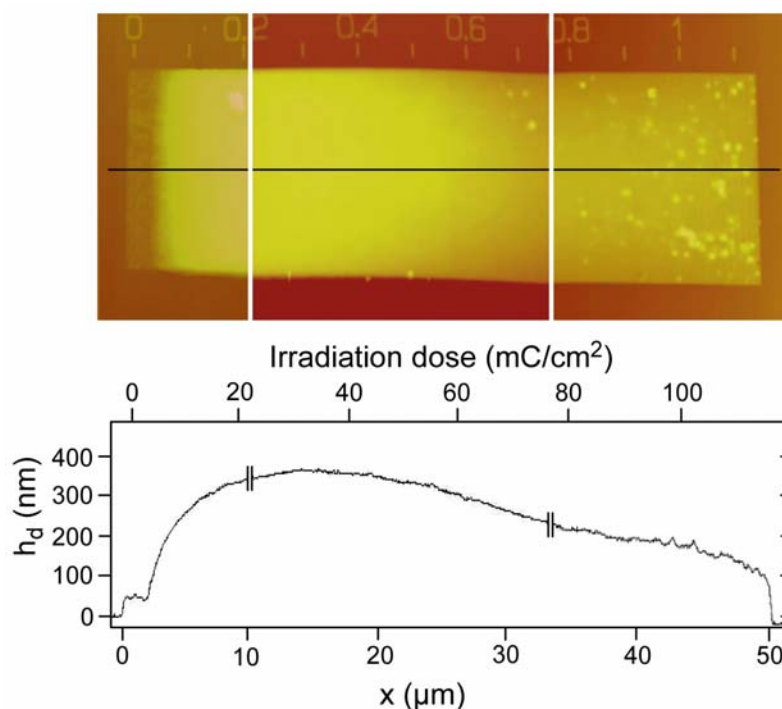


Abbildung 2. AFM Aufnahme und Höhenprofil eines Polystyrol-Höhengradienten. Die Dosis der Elektronenbestrahlung nimmt von 0 bis 115 mC/cm² linear zu.

Darüberhinaus wurde beobachtet, dass die Dicke der Polymerstrukturen bei identischen Reaktionsbedingungen stark von der Fläche der Strukturen abhängt. Dieses Verhalten liegt daran, dass die molekulare Dimension der gepfropften Polymerketten in ihrer Größenordnung

der bestrahlten Fläche entspricht und dass sich die Ketten an den Rändern der der Struktur auch in nicht belegte Bereiche ausdehnen können. Daher stehen auf kleineren Flächen die Ketten weniger dicht gedrängt, wodurch sie sich dort weniger strecken müssen.

Wir entdeckten später, dass der dritte Schritt der der in Abbildung 1 beschrieben ist (Umwandlung der Aminogruppe in einen asymmetrischen Azoinitiator) nicht notwendig ist: strukturierte Polymerbürsten mit vergleichbarer Länge und lateraler Auflösung konnten durch Eintauchen einer unmodifizierten, aber bestrahlte NBT SAM in Vinylmonomer und anschließende UV-Bestrahlung erzeugt werden. Styrol, Methylmethacrylat und Tert-butylmethacrylat wurden erfolgreich getestet. Polymerbürsten wurden in allen Experimenten selektiv auf den vernetzten Stellen der SAMs gebildet. Das gleiche Phänomen zeigte sich auch in analogen Experimenten mit anderen ω -funktionalisierten BPT SAMs auf Gold, die mit EBCL strukturiert worden sind. An dieser Stelle ergaben sich zwei Fragen:

1. Durch welchen initiatorfreien Mechanismus entstehen Polymerbürsten?
2. Wieso bilden sich Polymerbürsten ausschließlich auf den quervernetzten Regionen der SAM?

Einige Studien berichteten über die Darstellung von Polymerbürsten auf verschiedenen organischen Substraten durch Eintauchen der Substrate in Vinylmonomer und Bestrahlung mit UV. Dieses Phänomen wurde *self-initiated photografting and photopolymerization* (SIPGP) genannt. Der Mechanismus von SIPGP ist in Abbildung 3 dargestellt.

- a) Durch Absorption eines Photons agiert das Vinylmonomer (hier: Styrol) als Photosensibilisator und nimmt eine Form, die zwei freie Radikale enthält ein ($\cdot\text{St}\cdot$).
- b) In Lösung kann $\cdot\text{St}\cdot$ eine freie Radikalische Polymerisation von Styrol initiieren.
- c) In der Zwischenzeit kann $\cdot\text{St}\cdot$ auch ein Proton von einer funktionellen Gruppe auf einer Oberfläche abstrahieren.
- d) Das auf der Oberfläche gebildete Radikal initiiert die Freie Radikalische Polymerisation von Styrol.

Auch Blockcopolymerere können so erzeugt werden, da während des SIPGP-Prozesses Wasserstoffatome aus den Polymerbürsten abstrahiert werden können.

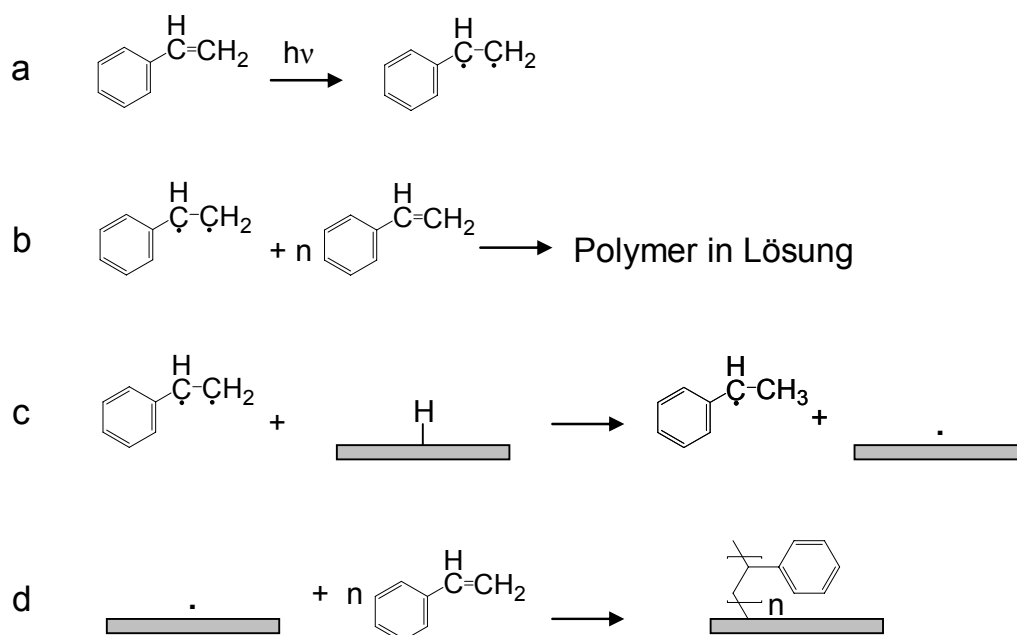


Abbildung 3. Prinzip der SIPGP von Styrol

Wir entdeckten dass durch die Photooxidation der Au-S Bindung während des SIPGP Prozesses nicht quervernetzte SAM Moleküle von der Oberfläche desorbieren, während quervernetzte SAMs aufgrund multipler Adhäsionstellen der gesamten Monolage stabiler sind. In anderen Worten bilden sich durch SIPGP Polymerbürsten selektiv auf vorher bestrahlten Flächen, während nicht vernetzte Teile der SAM von der Oberfläche desorbieren.

Des Weiteren wurde herausgefunden, dass die Stärke der Polymerschichten von der lokal angewandten Elektronendosis abhängt. Dies wird der Tatsache zugeschrieben, dass die Schichtdicke vom Umsatz der Biphenyl- Vernetzungsreaktion abhängt: Ist die Monolage nicht vollständig quervernetzt (bei geringer Elektronendosis), desorbieren während SIPGP SAM Moleküle von der Oberfläche. Dies verringert die Dichte der potentiellen Reaktionsstellen auf der Oberfläche und somit die resultierende Polymerschichtdicke.

Diese einzigartige Kombination von EBCL als lithographischer Technik um lokal die Oberflächenchemie zu steuern und SIPGP um die erzeugten Unterschiede zu verstärken, erlaubt es, Polymerbürsten mit kontrollierbarer Morphologie zu erzeugen. Mit diesem vereinfachten Verfahren in drei Schritten konnten außerordentlich definierte Polymerbürsten mit dreidimensionaler Architektur und einer Höhe von bis zu 450 nm erzeugt werden.

Diese Ergebnisse ermutigten uns, die EBCL-SIPGP Methode für die Darstellung strukturierter Polymerbürsten auf anderen Substraten als Gold zu erproben. Nach einigen erfolglosen Versuchen, diesen Ansatz auch auf Siliziumsubstrate zu übertragen, entdeckten wir, dass der

erste Schritt der Prozedur (die Modifikation eines Substrats mit einer Biphenylmonolage) ebenfalls nicht erforderlich war. Die Prozedur vereinfacht sich folgendermaßen:

1. Elektronenbestrahlung einer blanken Oberfläche.
2. Bestrahlung der Oberfläche mit UV-Licht in Anwesenheit von Monomer.

Morphologisch hochdefinierte, dicke (bis zu einige Hundert Nanometer) Polymerbürsten können selektiv auf den zuvor bestrahlten Regionen der Oberflächen gebildet werden (Abbildung 4). Auch hier kann die Schichtdicke durch die eingesetzte Elektronendosis kontrolliert werden.

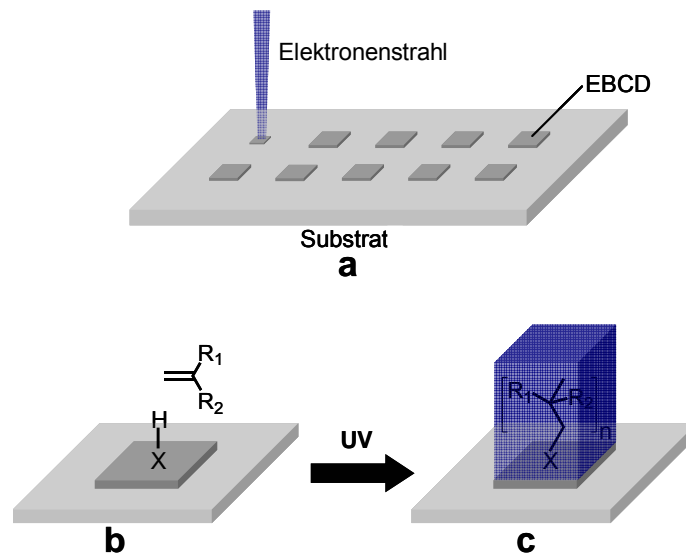


Abbildung 4. Prinzip der Bildung strukturierter Polymerbürsten auf unterschiedlichen Substraten. (a) Bestrahlung des Substrats durch einen Elektronenstrahl induziert EBCD auf den bestrahlten Regionen der Oberfläche. (b) Das Strukturierte Substrat wird für SIPGP in Monomer getaucht und mit UV Licht bestrahlt. (c) Polymerbürsten bilden sich selektiv auf den vorher bestrahlten Flächen.

Wenn ein Substrat mit Elektronen bestrahlt wird, bilden sich dünne Elektronenstrahlinduzierte Kohlenstoffablagerungen (*electron-beam induced carbon deposition*, EBCD) auf den der Strahlung ausgesetzten Oberflächenregionen. Für deren Entstehung ist die Zersetzung von in der Vakuumkammer verbliebenen Kohlenwasserstoffmolekülen aus dem Vakuumpumpenöl verantwortlich. EBCDs sind sehr stabile, stark vernetzte Kohlenwasserstoffablagerungen mit einer Zusammensetzung dicht an C_9H_2O .

Auf der Basis der vorangegangenen Ergebnisse nahmen wir an, dass SIPGP für die Entstehung der Polymerbürsten auf den EBCDs verantwortlich ist. EBCDs enthalten

verschiedene Funktionalitäten wie Hydroxyl und aromatische und aliphatische C-H Gruppen, die durch Wasserstoffabstraktion während des SIPGP Prozesses aktiviert werden können. In einer ersten Reihe von Experimenten wurde die SIPGP verschiedener Monomere auf EBCDs von einigen Angström Dicke durchgeführt. Styrol, Methylmethacrylat, Tert-butylmethacrylat, 4-Vinylpyridin und Acrylsäure wurden erfolgreich gepropft und die Schichtdickenwachstumsrate (dh_a/dt) wurde bestimmt. Es stellte sich heraus, dass die dh_a/dt -Werte mit der Polymerisationsgeschwindigkeit der Monomere in Lösung korrelieren. Ein weiterer Vorteil dieses Zweischnitt-Ansatzes ist, dass chemisch und thermisch stabile EBCDs auf beinahe allen Substraten (außer Gold) erzeugt werden können. Auf diese Weise wurden Polymerbürsten auf verschiedenen Leitern (Aluminium und Silber), Halbleitern (Silizium, Siliziumnitrid, Germanium, Galliumarsenid, Galliumnitrid) und Isolatoren (Glimmern, Borosilikatglas) erzeugt.

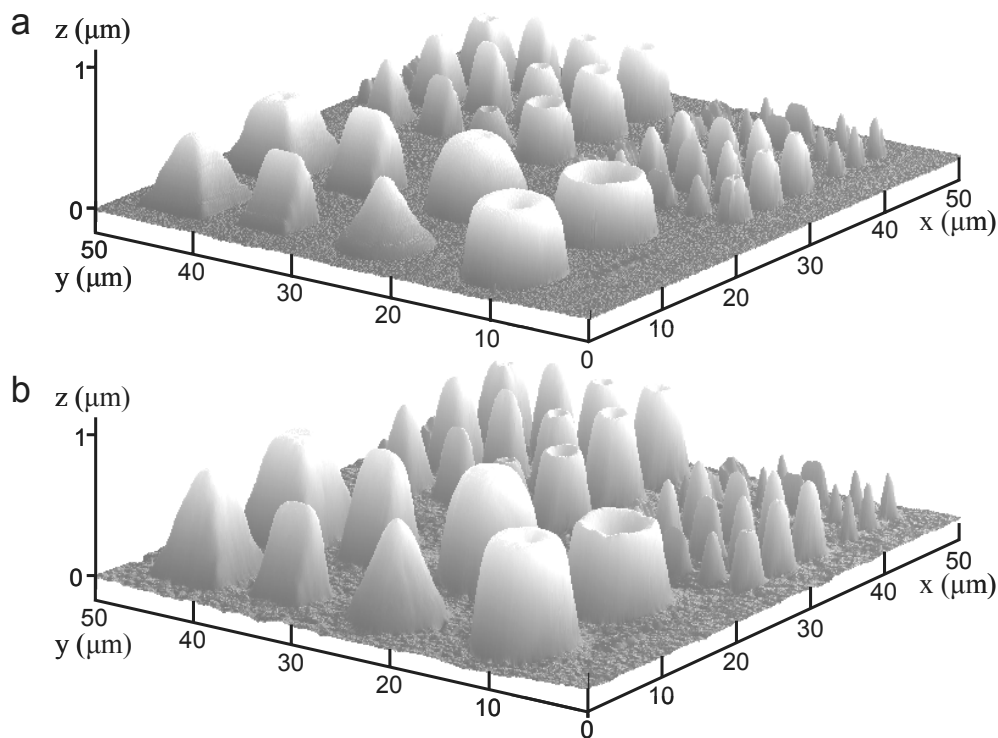


Abbildung 5. (a) AFM Bild von 3D mikrostrukturierten PS Bürsten auf einem GaAs Substrat, erzeugt durch SIPGP von Styrol ($t_p = 18$ h) auf strukturierten EBCD. Der EBCD-Prozess wurde durchgeführt mit Hilfe eines fokussierten Elektronenstrahls aus einem Rasterelektronenmikroskop, das mit einem Mustergenerator gekoppelt ist. Der Mustergenerator ermöglicht die Herstellung beinahe jeder denkbaren zweidimensionalen Struktur, wobei die Elektronendosis für jede einzelne Struktur gewählt werden kann. (b) PS Strukturen nach der Polymerisation von Styrol nach 34 h auf demselben EBCD.

Durch AFM Messungen konnte gezeigt werden, dass bei niedriger Elektronendosis die erzeugten EBCD-Strukturen die Oberfläche nur unvollständig bedecken. Eine Erhöhung der Dosis des Elektronenstrahls erhöht die Oberflächenkonzentration von EBCD und somit auch die Oberflächenkonzentration von Anknüpfungspunkten für SIPGP. Die Abhängigkeit zwischen der Schichtdicke und der örtlich angewandten Elektronendosis ermöglicht den Aufbau dreidimensionaler Polymerarchitekturen (Abbildung 5). Die Form der resultierenden Polymerarchitektur kann mit Hilfe der Abhängigkeit zwischen Schichtdicke und Elektronendosis kontrolliert werden.

Langes Behandeln in Ultraschall in verschiedenen Lösungsmitteln sowie Soxhlet Extraktion in hochsiedenden Lösemitteln demonstrierten die ausgezeichnete (thermische) Stabilität der Polymerbürsten. Darüberhinaus hat sich gezeigt, dass die Polymerbürsten auch unter verschiedenen chemischen Bedingungen stabil sind (selbst unter so drastischen Bedingungen wie konzentrierter Schwefel- oder Salpetersäure). Dies ermöglichte die weitere Funktionalisierung der Polymere ohne Einschränkungen der Stabilität. Verschiedene Synthesewege für die Herstellung 3D strukturierter Polymerbürsten mit allen Arten von funktionellen Gruppen auf unterschiedlichen Substraten wurden untersucht. Hierdurch können z.B. auf äußere Einflüsse reagierende Oberflächen erzeugt werden. Polymeranaloge Reaktionen auf strukturierten Polymerbürsten wurden unter Verwendung konventioneller analytischer Methoden, wie z.B. Fluoreszenzmikroskopie, ESCA und Infrarotspektroskopie. Da die Stärke der trockenen Polymerschicht darüber hinaus proportional zum Molekulargewicht der aufgewachsenen Polymerketten ist, konnten wir in einigen Fällen den Umsatz der polymeranalogen Reaktionen durch Messung der Schichtdicke vor und nach der Reaktion bestimmen. Dieses Konzept wurde auch angewendet, um die molekulare Architektur der Polymerbürsten indirekt zu bestimmen.

Eine unter Polymerchemikern weit verbreitete Ansicht ist, dass gut definierte Polymerbürsten nur durch lebende Polymerisation auf hoch geordneten SAMs entstehen können. Hier wurde jedoch gezeigt, dass eine freie radikalische Polymerisation unerreichbar gute Kontrolle über die Morphologie der Polymerschicht bis in den Sub-Mikrometermaßstab ermöglicht. Dieser EBCD-SIPGP Ansatz hat eine Vielzahl von Vorteilen gegenüber bisher bestehenden Ansätzen zur Herstellung von strukturierten Polymerschichten:

- Einfache Zwei-Schritt-Prozedur.
- SAM freier Ansatz.
- Oberflächengebundene Initiatoren sind nicht nötig.

- Unabhängig vom Substrat.
- Die Polymerbürsten sind thermisch und chemisch extrem stabil.
- Hochaufgelöste Strukturen (EBCDs mit weniger als 10 nm Auflösung) können mit modernen Elektronenstrahloptiken erzeugt werden.
- Elektronenstrahlolithographie ist auf keinen Längenmaßstab beschränkt: während größere Oberfläche mit einer *flood gun* und einer Lochmaske strukturiert werden können, ist es möglich kleinere und komplexere Strukturen durch direktes Schreiben mit einem gebündelten Elektronenstrahl zu erzeugen.
- Aufgewachsene Polymere mit dreidimensionaler Architektur können aufgrund der Abhängigkeit der Polymerschichtdicke von der Elektronendosis aufgebaut werden.
- Die Herstellung von Blockcopolymeren ist möglich.

Stabile Pfropfpolymeren mit allen denkbaren Dimensionen, Architekturen und chemischen Funktionalitäten können nun, basierend auf dieser Studie präpariert werden. Diese Strukturen könnten neue Perspektiven für Grundlagen- und anwendungsorientierte Forschung, wie z.B. Biomedizin, Sensortechnologie, Nanofluidforschung, Nanooptik, Biochiptechnologie und Mikroelektronik eröffnen.

Ein zusätzliches Projekt ist die Kopplung von biologischen Systemen (Enzyme, Zellen, usw.) mit elektrisch leitfähigem Diamant, um dieses Material in amperometrischen Biosensoren zu verwenden. Die einmaligen Bulk- und Oberflächeneigenschaften (inert, hart, biokompatibel, exzellente elektrische Eigenschaften) machen Diamant zu einem sehr vielversprechenden Material für biomedizinische Anwendungen.

Zunächst haben wir Nitrobiphenyl SAMs auf Diamantoberflächen synthetisiert und charakterisiert. Danach haben wir die strahlungsinduzierte Konversion der terminalen Nitrogruppe in eine Aminogruppe untersucht, um EBCL von Biphenyl SAMs auf Diamantoberflächen zu erweitern. Im zweiten Teil dieses Projekts wurde SIPGP von Vinylmonomeren angewendet, um Polymere auf oxidierte OH-terminierte Diamantoberflächen aufzupropfen. Auch hier wurden unterschiedliche Syntheserouten für die Funktionalisierung der Polymerbürsten untersucht, um Polymerbeschichtungen mit verschiedenen gewünschten chemischen Funktionalitäten herzustellen. Die Funktionalisierung dieser Polymerschichten mit Enzymen wird zurzeit untersucht.

7 Experimental part

7.1 Characterization techniques

Atomic force microscopy (AFM):

Fa. Digital Instruments, MMAFM-2

Scanner: 5298 J and 5308 E

AFM tips: Nanodevices, MPP-11100

All AFM measurements were performed in tapping mode. The AFM measurements were analyzed and visualized using the Nanoscope III-software (version 5.12r3, Digital Instruments).

The measurement of the thickness of the NB SAM on H-terminated diamond (chapter 4.3.2.2) was performed following the protocol of McCreery *et al.*²²³ First a $1 \times 1 \mu\text{m}^2$ large section was scratched into the NB modified substrate at a deflection setpoint of 15 V in full contact mode. The same region was then imaged at an area of $3.4 \mu\text{m}^2$ in tapping mode. The scanned data were then analyzed by the section analysis of individual scan lines crossing the trench as well as by the local depth analysis option by choosing larges possible areas within the scratched region an of the intact surface around the trench. The scratching experiment and data analysis were repeated several times to ensure reproducibility and for better statistics.

Infrared measurements

Bruker, IFS 55 with a nitrogen cooled MCT-detector.

Polarization filter

Spectral resolution: 4 cm^{-1}

The infrared measurements of the polymer grafts were recorded using a diffusion reflectance Fourier transformed (DRIFT) setup from Spectra Tech. 550 scans were accumulated. Attenuated total reflection Fourier transformed infrared (ATR-FTIR) measurements were performed with a ZnSe crystal from Spectra Tech.

In chapter 4.3.3, unfunctionalized oxidized UNCD samples was used as background spectrum. In chapter 4.4, the DRIFT measurements were performed on samples, structured

with a stencil mask in combination of an electron flood gun. Figure 104 shows where the background and sample scans were obtained.

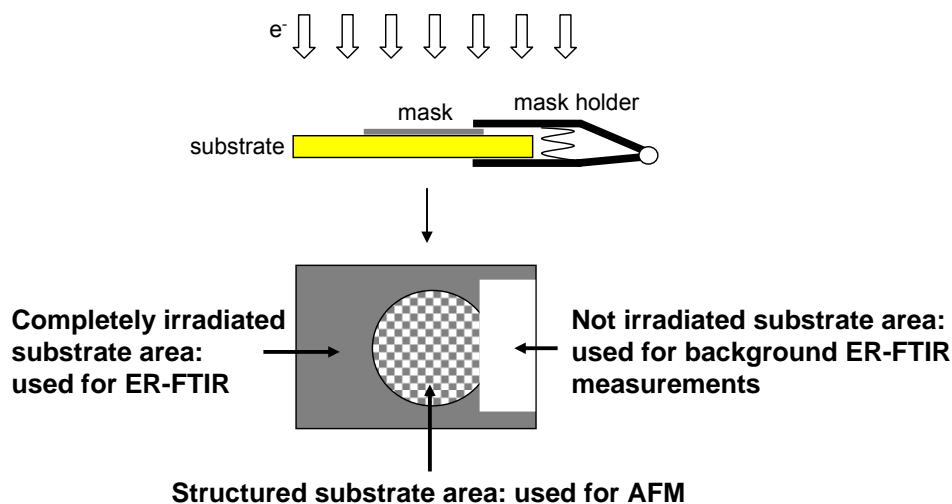


Figure 104. The surface area that has been completely irradiated during the EBCD was used for recording the DRIFT spectra. During electron beam irradiation, part of the substrate was screened by the mask holder. This area was used to record the background.

Nuclear magnetic resonance (NMR) spectroscopy:

Bruker, ARX 300

^1H -NMR: 300.10 MHz

^{13}C -NMR: 75.48 MHz

Standard: solvent signal as intern standard.

Acetonitrile: ^1H -NMR: $\delta = 1.93$ ppm, ^{13}C -NMR: $\delta = 118.2$ ppm

DMSO: ^1H -NMR: $\delta = 2.49$ ppm, ^{13}C -NMR: $\delta = 39.5$ ppm

Fluorescence microscopy:

The fluorescence measurements were performed with an Axiovert 200M AG microscope from Zeiss equipped with an ORCA-ER camera (Hamamatsu Photonics, Japan). The sample was irradiated using a 00 filter set (530-585 nm).

The cross section analysis were obtained by a pixel analysis of the 256 bit black and white fluorescence image using software Image J package.²⁸⁸

Water contact angle measurements:

The water contact angles were determined with a full automated Krüss DSA 10 Mk2 contact angle goniometer. The data were obtained with the aid of the Krüss Drop Shape Analysis v3 software package

***In situ* X-ray photoelectron spectroscopy (XPS) studies (chapter 4.1):**

The *in situ* XPS studies were performed in the research group for Applied Physical Chemistry of Prof. Dr. Michael Grunze at the Universität Heidelberg. For the XPS monitoring of the conversion upon electron irradiation, a freshly prepared SAM of NBT was irradiated with 10 eV electrons. The doses were estimated by multiplication of the exposure time with the current density ($\approx 19 \mu\text{A}/\text{cm}^2$). The electron gun was mounted at a distance of ≈ 15 cm from the sample to ensure uniform illumination. The base pressure in the vacuum chamber during the irradiation was 1×10^{-8} mbar.

The XPS characterization was performed immediately after the irradiation, without exposure of the irradiated films to ambient air. The measurements were performed with an Al $K\alpha$ X-ray source and a LHS 11 analyzer. The spectra acquisition was carried out in normal emission geometry with an energy resolution of ≈ 1.0 eV. The X-ray source was operated at a power of 260 W and positioned ≈ 1.5 cm away from the samples. The energy scale was referenced to the Au $4f_{7/2}$ peak of coated gold at a binding energy (BE) of 84.0 eV.²⁸⁹ For each sample, a wide scan spectrum as well as the C1s, N1s, and Au4f detail spectra were measured. The emphasis was put on the N1s spectra, since they provided direct information on the chemical identity of the SAM composition, which was of main interest for SIP. XPS spectra were fitted by symmetric Voigt functions using a Shirley-type background correction. The fits were performed self-consistently; for identical spectral regions the same fit parameters were used.²⁸⁹

Ex situ XPS measurements in chapter 4.3.3:

The XPS measurements of polymer grafts on UNCD samples were performed in the research group of Dr. José Antonio Garrido at the Walter Schottky Institute, TU München. 12 mm^2 unstructured oxidized UNCD samples were used. XPS was carried out under UHV conditions at 2×10^{-9} mbar base pressure. The XPS system was equipped with a Mg $K\alpha$ X-ray source (1253.6 eV; X-ray current: 10 mA; X-ray Voltage: 10 kV) and a Escalab MK II analyzer. The spectra were recorded with an angle of 49° between the incident X-ray beam and the electron detector. The peak areas for the determination of the surface atom composition were

calculated by the integration of a Voigt fit (80% Gaussian and 20 % Lorentzian) using Origin 7.5 software.

Scanning electron microscopy (SEM):

The SEM measurements were performed in the research group of Prof. Grunze by Dr. Alexander Küller with a LEO 1530 scanning electron microscope. The electron beam energy was set at 3 keV, vacuum pressure $\sim 5 \times 10^{-6}$ mbar. The secondary electrons were detected with an in-lens-detector.

7.2 Solvents, chemicals and substrates

The major experimental difficulty for the modification of surfaces is that extremely clean reaction conditions are required. All used glasswork, tweezers and spatula were previously cleaned in an isopropyl KOH bath, rinsed with distilled water and clean acetone. The substrates were always stored in sealed vessels in order to avoid contamination.

All chemicals were purchased from Aldrich, ABCR or Acros (American chemical society purity or higher). Solvents of lower grade were purified and dried prior to use.

All monomers (styrene, MMA, tBMA, AA, 4VBCl and 4VP) were passed through a basic Al_3O_2 column (Aldrich) to remove the inhibitor. The monomers were dried with CaH_2 and purified by fractionation distillation at reduced pressure. The monomers were stored at $-20\text{ }^\circ\text{C}$ and degassed by at least 4 freeze-thaw cycles before use.

7.2.1 Substrate pretreatment

Aluminum, gold and silver substrates:

Thin aluminum, gold and silver films (around 50 nm thick) on p-doped silicon substrates were obtained from Albert Coatings, Heidelberg.²⁹⁰ Before use, the substrates were cleaned by exposing the surfaces for 2 hours in UV-light (253 nm) under inert atmosphere. The surfaces were then washed with dimethylformamide and ethanol and dried by a jet of nitrogen.

RMS roughness: gold: 1.4 nm; silver: 5.0 nm.

Gallium Arsenide, Gallium Nitride and Germanium substrates:

P-doped GaAs, GaN and Ge substrates were received from the research group of Prof. Dr. Gerhard Abstreiter and Dr. Martin Eickhoff at the Walter Schottky Institute of the TU München.

For the EBCD on the native oxide layer, the substrates were cleaned by a piranha solution (concentrated H₂SO₄/H₂O₂ 2/1 volume ratio), rinsed with water and dried before use.

For the EBCD process on the bare substrate, the substrates were placed for 30 minutes in a 1 M HCl solution, in order to remove the native oxide layer, rinsed with water and dried by a jet of nitrogen. The substrates were kept under an inert and dry argon atmosphere before and after the EBCD process.

Glass substrates:

Mechanically polished borosilicate glass (Borofloat® 33) was obtained from Schott GmbH, Mainz. Before use, the samples were cleaned by ultrasound in ethyl acetate and ethanol, 5 min each and dried by a jet of nitrogen. RMS roughness: 0.32 nm

Glassy carbon substrates:

Mechanically polished glassy carbon substrates (Sigradur®) were purchased from HTW Hochtemperatur-Werkstoffe GmbH, Thierhaupten. Before use, the samples were cleaned by ultrasound in ethyl acetate and ethanol, 5 min each and dried by a jet of nitrogen.

Graphite substrates:

Mechanically polished graphite substrates were purchased from CP-Graphite GmbH, Wachtberg. The samples were used as received.

Mica substrates:

Mica sheets (muscovite) were obtained from Alfa Aesar GmbH, Ward Hill, USA. The mica substrates were freshly cleaved before use.

Poly(ethylene-alt-tetrafluoroethylene) (ETFE) substrates:

ETFE substrates were a gift by Dr. Celestino Padeste from the laboratory for micro- and nanotechnology in the Paul Scherrer Institut in Villigen (Switzerland). Samples were prepared as followed:

*Extruded Nowoflon ET-6235 films having thicknesses of 100 nm were purchased from Nowoflon GmbH, Siegsdorf, Germany. The average molar weight of the Dyneon ET-6235 copolymer used to make these films is approximately 400 000 Dalton. [...] To obtain a flat test surface, a piece of ETFE film was placed between two polished 49 silicon wafers. In a hot press which is optimized for nano-imprint lithography, this sandwich was heated for 5 min at 230 °C under a pressure of 200 N/cm². The procedure results in a reduction of film thickness of about 5% - 10%, and a drastic reduction in surface roughness. No evidence of thermal degradation of the polymer was observed due to this treatment.*²⁹¹

Silicon substrates:

P-doped Si(100) wafers were obtained from Crystech Inc., Qingdao, China.

Before use, the samples were sonificated for 5 minutes in ethyl acetate and ethanol, dried by a jet of nitrogen and cleaned in a piranha solution, rinsed with water and dried again. RMS roughness: 0.41 nm.

Silicon nitride:

p-doped Si₃N₄ wafers were obtained from Crystech Inc., Qingdao, China.

The samples were sonificated for 5 minutes in ethyl acetate and ethanol and dried by a jet of nitrogen before use.

Ultrananocrystalline diamond (UNCD) substrates:

The UNCD samples were obtained from the Walter Schottky Institute, TU München. The employed samples were about 1 µm thick UNCD layers grown by microwave-assisted chemical vapor deposition on 600 µm thick p-doped silicon (100) substrates. Conductive UNCD films were grown from a N₂/Ar/CH₄ gas mixture with 20% nitrogen in the gas phase.²⁰⁸

The surfaces were cleaned by sequential rinsing in acetone, 2-propanol, and water prior to insertion into an oxygen plasma system (Giga-Etch 100-E, TePla AG, Germany), where they were treated for 300 s with an oxygen plasma (300 W load coil power; pressure of 1.5 mbar). For subsequent hydrogenation (to obtain H-terminated diamond), samples were transferred into a vacuum chamber, for hydrogenation by atomic hydrogen generated by a hydrogen gas flow of 150 standard cm³ over a hot (2000 °C) tungsten filament, placed at a distance of 4 cm from the substrate. During the process, the sample temperature (700 °C) was determined with a thermocouple.

The structuring of the hydrogenated UNCD samples was performed using a S1805 Shipley photo resist that was spin coated at 6000 rpm onto the substrate. Structuring was then performed using a MJB3 mask aligner (SUSS MicroTec). The samples were then oxidized using the same procedure as described above, with the photoresist. The photo resist was removed after the oxidation step by sonification in acetone and 2-propanol.

Under these oxidation conditions, the diamond surface has hydroxyl surface groups.²¹⁹ The quality of the oxidation process was controlled by static water contact angle measurements ($\theta \leq 10^\circ$).

7.2.2 Preparation of ω -functionalized biphenylthiol SAMs on gold

The synthesis of 4-mercapto-1,1'-biphenyl (BT), 4'-methyl-1,1'-biphenyl-4-thiol (MBT), 4'-hydroxy-1,1'-biphenyl-4-thiol (HBT) and 4'-nitro-1,1'-biphenyl-4-thiol (NBT) and the preparation of the SAMs was performed in the research group of Prof. Grunze.^{156,252} The SAMs were prepared by immersing the gold substrate in a 15 mmol solution of the respective ω -functionalized biphenylthiols in ethanol for three days. The substrates were cleaned by sonification for 5 minutes in air and dried.

7.2.3 Micro- and nanostructuring of the substrates by electron beam lithography

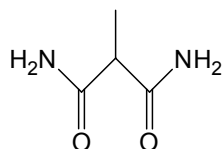
The electron beam lithography was performed in the research group of Prof. Grunze. The electron beam lithography of the ω -functionalized biphenylthiol SAMs and the preparation of the electron beam induced carbon deposits (EBCDs) were performed under identical irradiation conditions. No precursor molecules were introduced into the vacuum chamber during the EBCD process.

A flood gun (Specs Flood Gun 15/40, electron energy: 50 eV) was used to irradiate the samples through a stencil mask (Quantifoil Micro Tools, Jena, hole radius: 1 μm , center-to-center distance: 4 μm).

Direct writing with a focused e-beam was performed with a LEO 1530 scanning electron microscope with a Raith Elphy Plus Pattern Generator System (REPGS) software. The electron beam energy was set at 3 keV, vacuum pressure $\sim 5 \times 10^{-6}$ mbar.

7.3 Synthesis and characterization of chemical compounds

Methylmalonodiamide:

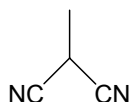


A mixture of 100 g (0.57 mol) methylmalonic acid diethyl ester and 300 ml 25 % NH₃ aqueous solution was stirred during 2 days at room temperature. The precipitation was filtered and recrystallized from water to give 30 g (0.26 mol) white crystals.

Yield: 45 %

¹H-NMR: (in d₆-DMSO): δ (ppm) = 7.10 (d, 2H, NH₂); 3.05 (q, 1H, CH); 1.15 (d, 3H, CH₃)

Methylmalonodinitrile:



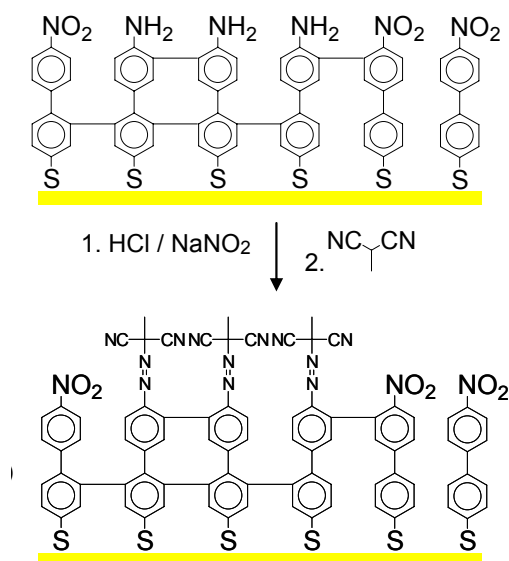
5 g (43.1 mmol) of methylmalonodiamide was mixed with 20 g P₂O₅ and heated at 190 °C in fine vacuum. The product (2 g, 25 mmol, white crystals) was collected in a flask, cooled in an ice bath, over a bended glass tube.

Yield: 58 %

¹H-NMR: (in d₆-DMSO): δ (ppm) = 4.73 (q, 1H, CH); 1.63 (d, 3H, CH₃)

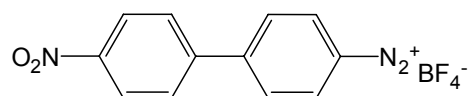
Crosslinked 4'-azomethylmalonodinitrile-1,1'-biphenyl-4-thiol (cAMBT) SAMs:

The synthesis of cAMBT SAMs was performed according to the procedure by Schmelmer *et al.*¹⁵⁴



The irradiated substrates bearing SAMs of cross-linked cABT were diazotized at 0 °C by treatment with an aqueous solution of HCl (0.5 mL concentrated HCl in 2 mL water) and subsequent treatment with sodium nitrite (1 mmol) in water (2 mL). Finally, the azo-initiator was prepared by the reaction of the substrate with methylmalonodinitrile and sodium acetate (1 g) in water/ethanol (2.5 mL:1.5 mL) for 45 min. The substrate was rinsed with water and dried.

4'-nitro-1,1-biphenyl-4-diazonium tetrafluoroborate (NBD):



Approximately 0.5 g (2.3 mmol) of 4-amino-4'-nitrobiphenyl was weighed into a round-bottom flask; then 10 mL of 50% fluoroboric acid was added and the resulting mixture stirred. A 3/1 molar ratio of NaNO₂ was weighed into a separate vial, just enough water was added to dissolve the NaNO₂ at room temperature, and the solution was cooled to 0 °C in an ice bath along with the precursor solution. The cold NaNO₂ solution was added dropwise, and the temperature was always kept below 4 °C. Following the complete addition of NaNO₂, the mixture was stirred for ~30 min at 0 °C. The insoluble diazonium salt was filtered and washed with anhydrous ether. The product (5.2 g, 1.7 mmol, white crystal) was recrystallized from

acetonitrile (at 0 °C) and stored at -20 °C. Directly before further use, NBD was reprecipitated from dry ether.

Yield: 72%

¹H-NMR: (in d₃-acetonitrile): δ (ppm) = 8.61 (d, 2H); 8.43 (d, 2H); 8.25 (d, 2H); 8.04 (d, 2H)

7.3.1 Nitrobiphenyl SAMs on H-terminated diamond

A freshly hydrogenated diamond surface was immersed into a degassed and saturated solution of NBD in approximately 0.5 mL of acetonitrile and stirred for 72 h. During the reaction, a gradual color change of the originally clear and colorless reaction solution to a bright yellow and finally to a deep orange color was observed. In some cases the reaction time was varied by some hours but without effect of the reported spectroscopic results. Finally, the surface was cleaned by sonification for several minutes in acetonitrile, ethyl acetate and ethanol successively.

7.3.2 Surface-initiated polymerization (SIPP and SIPGP)

The surface-initiated photopolymerization (SIPP) on cAMBT SAMs, the self-initiated photografting and photopolymerization (SIPGP) on cBT, cMBT, cHBT, cABT on gold substrates, on electron beam induced carbon deposition on various substrates, on oxidized UNCD, on glassy carbon and on graphite were performed in an identical way.

The substrates were added to approx. 2 mL of freshly distilled and degassed monomer (styrene, methyl methacrylate (MMA), tert-butyl methacrylate (tBMA), acrylic acid (AA), 4-vinylpyridine (4VP) or 4-vinylbenzylchloride (4VBC)) in a glass photoreaction vial. Polymerization was performed for different time periods under irradiation with UV-light ($\lambda_{\text{max}} = 350 \text{ nm}$ or 300 nm , 9.2 mW/cm^2) in a Rayonet Photochemical Reaction Chamber (Branford, Connecticut) at room temperature. After the polymerization, the samples were removed from the reaction solution and immediately washed with a good solvent for the respective polymer (PS and P4VBC in toluene; PMMA and poly(tBMA) in acetone, PAA and P4VP in DMF). To ensure that only chemically grafted polymers remained on the surface, all substrates were additionally cleaned under ultrasound irradiation for 5 minutes in the same good solvents. The

samples were additionally sonificated in ethyl acetate and ethanol for 5 minutes each. This washing procedure were sometimes repeated to remove all contaminations.

7.3.3 Polymer analogue reactions

The chemical modifications of polymer grafts were performed identically on the different substrates.

Hydrolyzation of poly(tBMA) grafts

A substrate with poly(tBMA) grafts was placed in a refluxing HCl solution (2 mL concentrated HCl in 3 ml dioxane and 4 ml water) for 3h. The substrate was rinsed with water, dioxane, ethyl acetate and ethanol.

Sulfonation of PS grafts

A substrate coated with PS grafts was submerged in a solution of 1 ml acetic anhydride (Ac₂O) in 5 ml 1,2-dichloroethane. The solution was cooled by an ice bath and 0.36 ml of concentrated H₂SO₄ was added slowly. The solution was heated at 60°C for 3h. During the reaction, a phase separation of the solution was observed. The sulfonation of the PS grafts was only successful when the substrate was totally submerged in the lower phase. The substrate was then removed from the reaction solution and intensively rinsed with 1,2-dichloroethane and water and dried.

Nitration of PS grafts

A substrate coated with PS grafts was submerged in a mixture of 1 ml HNO₃ and 2.5 ml H₂SO₄. The mixture was heated at 60°C for 1h. The substrate was removed from the reaction mixture and intensively washed with water and dried.

Poly((4-aminomethyl)styrene) (PAMS) grafts

The conversion of the PS to the PAMS grafts was performed following a procedure by Mitchell *et al.*²⁵⁵ for the functionalization of crosslinked PS resins. A substrate coated with PS grafts was submerged in a solution of 40 mg N-(hydroxymethyl)phthalimide (NHPI) in 5 ml dichloromethane (DCM) and 5 ml trifluoroacetic acid (TFA). 0.09 ml trifluoromethanesulfonate (CF₃SO₃H) was added slowly under N₂ atmosphere. The reaction

was allowed to proceed over night at room temperature. The substrate was removed from the solution and washed by sonification in $\text{CF}_3\text{SO}_3\text{H}$ -DCM (1:1), DCM, ethyl acetate and ethanol to obtain poly(4-vinylbenzyl)phthalimide (PVBP) grafts. PAMS grafts were obtained by refluxing the PVBP grafts in ethanol (5ml) containing 5% hydrazine dihydrate for 16h. The substrate was cleaned by sonification in ethanol.

Fluorescent labeling of PAMS grafts

PAMS grafts were submerged in a 10 mM rhodamine B isothiocyanate solution in ethanol for 3 days at room temperature under absence of light. The surface was washed by sonification in ethanol.

Modification of P4VP grafts with gold aurate and reduction

P4VP grafts were submerged in a 3 mM sodium chloroaurate solution in methanol over night at room temperature. The surface was washed without sonification in methanol.

The polymer bonded gold salts were reduced by placing the substrate for 72 h in a 1M N_2H_4 solution in THF. The substrate was successively rinsed with THF and ethanol.

The reduction with hydrogen plasma was performed in the research group of Prof. Grunze by Dr. Alexander Küller using a TePla 100-E Plasma system at 150 W for 1 hour with a hydrogen pressure of 0.4 Torr.

8 References

- ¹ Stoye, D. *Paints, Coatings and Solvents*, VCH, Weinheim, **1993**.
- ² Pearson, R. *Bull. Intern. Jomon Cult. Conf.* **2004**, 1.
- ³ Marrion, A. R. *The Chemistry and Physics of coatings*, 2nd Ed. RSC, **2004**.
- ⁴ Woodson, M.; Liu, J. *Phys. Chem. Chem. Phys.* **2007**, 9, 207.
- ⁵ Rhe, J.; Novotny, V.; Clarke, T.; Street, G. B. *J. Tribol. Trans. ASME* **1996**, 118, 663.
- ⁶ Padeste, C.; Farquet, P.; Potzner, C.; Solak, H. H. *J. Biomater. Sci. Polymer Edn.* **2006**, 17, 1285.
- ⁷ Peyman, G. A.; Koziol, J. E.; Yasuda, H. *US Patent/4312575*, **1981**.
- ⁸ LaPorte, R. J. *Hydrophilic Polymer Coatings for Medical Devices: Structure/Properties, Development, Manufacture and Applications*, CRC, New York, **1997**.
- ⁹ Akkerman, H. B.; Blom, P. W. M.; de Leeuw, D. M.; de Boer, B. *Nature* **2006**, 441, 69.
- ¹⁰ Chen, K. S.; Lin, I. K.; Ko, F. H. *J. Micromech. Microeng.* **2005**, 15, 1894.
- ¹¹ Craighead, H. G. *Science* **2000**, 290, 1532.
- ¹² Bretagnol, F.; Valsesia, A.; Ceccone, G.; Colpo, P.; Gilliland, D.; Ceriotti, L.; Hasiwa, M.; Rossi, F. *Plasma Processes and Polymers* **2006**, 3, 443.
- ¹³ Agheli, H.; Malmstrom, J.; Larsson, M.; Textor, M.; Sutherland, D. S. *Nano Lett.* **2006**, 6, 1165.
- ¹⁴ Bailey, R. C.; Hupp, J. T. *Anal. Chem.* **2003**, 75, 2392.
- ¹⁵ Stoykovich, M. P.; Cao, H. B.; Yoshimoto, K.; Ocola, L. E.; Nealey, P. F. *Adv. Mater.* **2003**, 15, 1180.
- ¹⁶ Nath, N.; Chilkoti, A. *Adv. Mater.* **2002**, 14, 1243.
- ¹⁷ Beebe, D. J.; Moore, J. S.; Yu, Q.; Liu, R. H.; Kraft, M. L.; Jo, B. H.; Devadoss, C. *Proc. Natl. Acad. Sci. U.S.A.* **2000**, 97, 13488.
- ¹⁸ Douglas, J. F.; Kent, M. S.; Satija, S. K.; Karim, A. *Polymer Brushes: Structure and Dynamics*. In: Buschow, K. H. J. (ed) *Encyclopedia of Materials: Science and Technology*, Elsevier, Amsterdam, **2001**.
- ¹⁹ Bhat, R. R.; Tomlinson, M. R.; Wu, T.; Genzer, J. *Adv. Polym. Sci.* **2006**, 198, 51.
- ²⁰ Alexander, S. *J. Phys. France* **1977**, 38, 983.
- ²¹ Potemkin, I.; Khokhlov, A. R.; Reineker, P. *Eur. Phys. J. E: Soft Matter.* **2001**, 4, 93.
- ²² Kizhakkedathu, J. N.; Brooks, D. E. *Macromolecules* **2003**, 36, 591.

- ²³ Steenackers, M.; Küller, A.; Stoycheva, S.; Grunze, M.; Jordan, R. Submitted.
- ²⁴ Advincula, R. C.; Brittain, W. J.; Caster, K. C.; Rühle, J. *Polymer Brushes*, VCH, Weinheim, **2004**.
- ²⁵ *Surface-Initiated Polymerization I & II* Ed.: Jordan, R., Adv. Polym. Sci. **2006**, 197.
- ²⁶ Laible, R.; Hamann, K. *Adv. Coll. Interface Sci.* **1980**, *13*, 65.
- ²⁷ Zhao, B.; Brittain, W. J. *J. Am. Chem. Soc.* **1999**, *121*, 3557. b) Matyjaszewski, K.; Miller, P. J.; Shukla, N.; Immaraporn, B.; Gelman, A.; Luokala, B. B.; Siclvan, T. M.; Kickelbick, G.; Vallant, T.; Hoffmann, H.; Pakula, T. *Macromolecules* **1999**, *32*, 8716.
- ²⁸ Jordan, R.; Ulman, A.; Kang, J. F.; Rafailovich, M.; Sokolov, J. *J. Am. Chem. Soc.* **1999**, *121*, 1016.
- ²⁹ Jordan, R.; Ulman, A. *J. Am. Chem. Soc.* **1998**, *120*, 243. b) Jordan, R.; West, N.; Ulman, A.; Chou, Y. M.; Nuyken, O. *Macromolecules* **2001**, *34*, 1606.
- ³⁰ Kim, N. Y.; Jeon, N. L.; Choi, I. S.; Takami, S.; Harada, Y.; Finnie, K. R.; Girolami, G. S.; Nuzzo, R. G.; Whitesides, G. M.; Laibinis P. E. *Macromolecules* **2000**, *33*, 2793.
- ³¹ Edmondson, S.; Osborne, V. L.; Huck, W. T. S. *Chem. Soc. Rev.* **2004**, *1*, 14.
- ³² Ulman, A. *Chem. Rev.* **1996**, *96*, 1533.
- ³³ Sagiv, J. *J. Am. Chem. Soc.* **1980**, *102*, 92.
- ³⁴ Gun, J.; Iscovici, R.; Sagiv, J. *J. Colloid Interface Sci.* **1984**, *101*, 201.
- ³⁵ Gun, J.; Sagiv, J. *J. Colloid Interface Sci.* **1986**, *112*, 457.
- ³⁶ Carson, G.; Granick, S. *J. Appl. Polym. Sci.* **1989**, *37*, 2767.
- ³⁷ Finklea, H. O.; Robinson, L. R.; Blackburn, A.; Richter, B.; Allara, D. L.; Bright, T. *Langmuir* **1986**, *2*, 239.
- ³⁸ Actis P.; Manesse M.; Nunes-Kirchner C.; Wittstock G.; Coffinier Y.; Boukherroub R.; Szunerits S. *Phys. Chem. Chem. Phys.* **2006**, *8*, 4924.
- ³⁹ Ulman, A. *J. Mater. Educ.* **1989**, *11*, 205.
- ⁴⁰ Walczak, M. W.; Chung, C.; Stole, S. M.; Widrig, C. A.; Porter, M. D. *J. Am. Chem. Soc.* **1991**, *113*, 2370.
- ⁴¹ Shimazu, K.; Sato, Y.; Yagi, I.; Uosaki, K. *Bull. Chem. Soc. Jpn.* **1994**, *67*, 863.
- ⁴² Demoz, A.; Harrison, D. J. *Langmuir* **1993**, *9*, 1046.
- ⁴³ Stratmann, M. *Adv. Mater.* **1990**, *2*, 191.
- ⁴⁴ Sheen, C. W.; Shi, J. X.; Martensson, J.; Parikh, A. N.; Allara, D. L. *J. Am. Chem. Soc.* **1992**, *114*, 1514.
- ⁴⁵ Gu, Y.; Lin, B.; Smentkowski, V. S.; Waldeck, D. H. *Langmuir* **1995**, *11*, 1849.

- ⁴⁶ Pinson, J.; Podvorica, F. *Chem. Soc. Rev.* **2005**, *34*, 429.
- ⁴⁷ Strother, T.; Knickerbocker, T.; Russell, J. N. Jr.; Butler, J. E.; Smith, L. M.; Hamers, R. J. *Langmuir* **2002**, *18*, 968.
- ⁴⁸ Yu, S. S. C.; Downard, A. J. *Langmuir* **2007**, asap.
- ⁴⁹ Kooi, S. E.; Baker, L. A.; Sheehan, P. E.; Whitman, L. J. *Adv. Mater.* **2004**, *16*, 1013.
- ⁵⁰ Besson, E.; Gue, A. M.; Sudor, J.; Korri-Youssoufi, H.; Jaffrezic, N.; Tardy, J. *Langmuir*, **2006**, *22*, 8346.
- ⁵¹ Teare, D. O. H.; Barwick, D. C.; Schofield, W. C. E. Garrod, R. P. Ward, L. J. Badval, J. P. *S. Langmuir* **2005**, *21*, 11425.
- ⁵² Husseman, M.; Malmstroem, E. E.; McNamara, M.; Mate, M.; Mecerreyes, D.; Benoit, D. G.; Hedrick, J. L.; Mansky, P.; Huang, E.; Russell, T. P.; Hawker, C. J. *Macromolecules* **1999**, *32*, 1424.
- ⁵³ Kim, J. B.; Brüning, M. L.; Baker, G. L. *J. Am. Chem. Soc.* **2000**, *122*, 7616.
- ⁵⁴ Zhang, H.; Rühle, J. *Macromolecules* **2005**, *38*, 4855.
- ⁵⁵ Jordan, R.; Ulman, A.; Kang, J. F.; Rafailovich, M. H.; Sokolov, J. *J. Am. Chem. Soc.* **1999**, *121*, 1016.
- ⁵⁶ Matrab, T.; Chancolon, J.; L'hermite, M. M.; Rouzaud, J. N.; Deniau, G.; Boudou, J. P.; Chehimi, M. M.; Delamar, M. *Coll. Surf. A* **2006**, *287*, 217.
- ⁵⁷ Devaux, C.; Chapel, J. P. Beyou, E. Chaumont, P. *Eur. Phys J. E.* **2002**, *7*, 345.
- ⁵⁸ Radhakrishnan, B.; Ranjan, R.; Brittain, W. *J. Soft Matter.* **2006**, *2*, 386.
- ⁵⁹ Von Werne, T.; Patten, T. E. *J. Am. Chem. Soc.* **1999**, *121*, 7409.
- ⁶⁰ Pyunm J.; Jia, S. J.; Kowalewski, T.; Patterson, G. D.; Matyjaszewski, K. *Macromolecules* **2003**, *63*, 5094.
- ⁶¹ Blomberg, S.; Ostberg, S.; Harth, E.; Nosman, A. W.; Van Horn, B.; Hawker, C. J. *J. Polym. Sci. Part A Polym. Chem.* **2002**, *40*, 1309.
- ⁶² Tsujii, Y.; Ohno, K.; Yamamoto, S.; Goto, A.; Fukuda, T. *Adv. Polym. Sci.* **2006**, *197*, 1.
- ⁶³ Odian, G. *Principles of polymerization*, Third Edition, Wiley Interscience, New York, **1993**.
- ⁶⁴ Full, J. Dissertation, Freie Universität Berlin, **2002**. (online-address: <http://www.diss.fu-berlin.de/2002/215/index.html>, accessed on April 12th, **2007**).
- ⁶⁵ Albright, T. A.; Hoffman P.; Hoffmann. R. *J. Am. Chem. Soc.* **1977**, *99*, 7546.
- ⁶⁶ <http://www.roempp.com/prod/index1.html>, accessed on April 13th, **2007**.

- ⁶⁷ Li, S. J.; Li, C. G.; Li, T.; Cheng, J. J.; “*Polymer Photochemistry Principles and Applications*”, 1st edition, Fudan University Press, Shanghai. **1993**, 110.
- ⁶⁸ Yang, W.; Rånby, B. *J. Appl. Polym. Sci.* **1996**, 62, 533.
- ⁶⁹ Yang, W. T.; Rånby, B. *Polym. Bull.* **1996**, 37, 89.
- ⁷⁰ Yang, W.; Rånby, B. *J. Appl. Polym. Sci.* **1996**, 62, 545.
- ⁷¹ Deng, J.-P.; Yang, W.-T.; Rånby, B. *Macromol. Rapid Commun.* **2001**, 22, 535.
- ⁷² Wang, H.; Brown, H. R. *Macromol. Rapid Commun.* **2004**, 25, 1095.
- ⁷³ Fang, W. H.; Liu, R. Z. *J. Am. Chem. Soc.* **2000**, 122, 10886.
- ⁷⁴ Hollas, J. M.; Ridley, T. J. *Mol. Spectrosc.* **1981**, 89, 232.
- ⁷⁵ Wan, J.; Nakatsuji, H.; *Chem. Phys.* **2004**, 302, 125.
- ⁷⁶ Smith, R. K.; Lewis, P. A.; Weis, P. S. *Prog. Surf. Sci.* **2004**, 75, 1.
- ⁷⁷ Akkerman, H. B.; Blom, P. W. M.; de Leeuw, D. M.; de Boer, B. *Nature* **2006**, 441, 69.
- ⁷⁸ Weibel, D. B.; DiLuzio, W. R.; Whitesides, G. M. *Nat. Rev. Microbiol.* **2007**, 5, 209.
- ⁷⁹ Kumar, A.; Whitesides, G. M. *Appl. Phys. Lett.* **1993**, 63, 2002.
- ⁸⁰ Li, H. W.; Muir, B. V. O.; Fichet G.; Huck, W. T. S. *Langmuir* **2003**, 19, 1963.
- ⁸¹ Xia, Y.; Whitesides, G. M. *Annu. Rev. Mater. Sci.* **1998**, 28, 153.
- ⁸² Mrksich, M.; Whitesides, G. M. *TIBTECH* **1995**, 13, 228.
- ⁸³ Xia, Y. N.; Mrksich, M.; Kim, E.; Whitesides, G. M. *J. Am. Chem. Soc.* **1995**, 117, 9576.
- ⁸⁴ Kane, R. S.; Takayama, S.; Ostuni, E.; Ingber, D. E.; Whitesides, G. M.; *Biomaterials* **1999**, 20, 2363.
- ⁸⁵ Shin, H. S.; Yang, H. J.; Jung, Y. M.; Bin Kim, S. *Vib. Spectrosc.* **2002**, 29, 79.
- ⁸⁶ Huang, J. X.; Tao, A. R.; Connor, S.; He, R. R.; Yang, P. D. *Nano Lett.* **2006**, 6, 524.
- ⁸⁷ Farhan, T.; Huck, W. T. S. *Eur. Polym. J.* **2004**, 40, 1599.
- ⁸⁸ Shah, R. R.; Merreceyes, D.; Husemann, M.; Rees, I.; Abbott, N. L.; Hawker, C. J.; Hedrick, J. L. *Macromolecules* **2000**, 33, 597.
- ⁸⁹ Husemann, M.; Mecerreyes, D.; Hawker, C. J.; Hedrick, J. L.; Shah, R.; Abbott, N. L. *Angew. Chem., Int. Ed.* **1999**, 38, 647.
- ⁹⁰ Zhou, F.; Zheng, Z.; Yu, B.; Liu, W.; Huck, W. T. S. *J. Am. Chem. Soc.* **2006**, 128, 16253.
- ⁹¹ <http://www.mobot.org/jwccross/spm/spm-text.htm>, accessed on March 28th, **2007**.
- ⁹² Eigler, D. M.; Schweizer, E. I. *Nature*, **1991**, 344, 524.
- ⁹³ Sohn, L. L.; Willett, R. L. *Appl. Phys. Lett.* **1995**, 67, 1552.
- ⁹⁴ Majurndar, A.; Oden, P. L.; Carrejo, J. P.; Nagahara, L. A.; Graham, J. J.; Alexander, J. *Appl. Phys. Lett.* **1992**, 61, 2293.

- ⁹⁵ Okada, Y.; Amano, S.; Kawabe, M.; Shimbo, B. N.; Harris, J. S. Jr. *J. Appl. Phys.* **1998**, *83*, 1844.
- ⁹⁶ Hong, S.; Mirkin, C. A. *Science*, **2000**, *288*, 1808.
- ⁹⁷ Kaholek, M.; Lee, W. K.; LaMattina, B.; Caster, K. C.; Zauscher, S. *Polymer Brushes* **2004**, *381*.
- ⁹⁸ Ahn, S. J.; Lee, W. K.; Zauscher, S. *Mater. Res. Soc. Symp. Proc.* **2003**, *735*, 111.
- ⁹⁹ Liu, X.; Guo, S.; Mirkin, C. A. *Angew. Chem., Int. Ed.* **2003**, *42*, 4785.
- ¹⁰⁰ Kaholek, M.; Lee, W. K.; LaMattina, B.; Caster, K. C.; Zauscher, S. *Nano Lett.* **2004**, *4*, 373.
- ¹⁰¹ Piner, R. D.; Zhu, J.; Xu, F.; Hong, S. H.; Mirkin, C. A. *Science*, **1999**, *283*, 661.
- ¹⁰² Ginger, D. S.; Zhang, H.; Mirkin, C. A. *Angew. Chem., Int. Ed.* **2004**, *43*, 30.
- ¹⁰³ Garcia, R.; Martinez, R. V.; Martinez, J. *Chem. Soc. Rev.* **2006**, *35*, 29.
- ¹⁰⁴ Xu, S.; Liu, G.-Y. *Langmuir* **1997**, *12*, 127.
- ¹⁰⁵ Lewis, M. S.; Gorman, C. B. *J. Phys. Chem. B* **2004**, *108*, 8581.
- ¹⁰⁶ Gorman, C. B.; Carroll, R. L.; He, Y.; Tian, F.; Fuierer, R. *Langmuir* **2000**, *16*, 6312.
- ¹⁰⁷ Yang, L.; Lua, Y. Y.; Lee, M. V.; Linford, M. R. *Acc. Chem. Res.* **2005**, *38*, 933.
- ¹⁰⁸ Liu, G. Y.; Xu, S.; Qian, Y. *Acc. Chem. Res.* **2000**, *33*, 457.
- ¹⁰⁹ Fresco, Z. M.; Fréchet, J. M. J. *J. Am. Chem. Soc.* **2005**, *127*, 8302.
- ¹¹⁰ Maoz, R.; Cohen, S. R.; Sagiv, J. *Adv. Mater.* **1999**, *11*, 55.
- ¹¹¹ Höppener, S.; Schubert, U. S. *Small* **2005**, *1*, 628.
- ¹¹² Snow, E. S.; Campbell, P. M.; Perkins, F. K. *Proc. IEEE* **1997**, *85*, 601.
- ¹¹³ Dagata, J. A.; Scneir, J.; Harary, H. H.; Evans, C. J.; Postek, M. T.; Bennett, J. *Appl. Phys. Lett.* **1990**, *56*, 2001.
- ¹¹⁴ Balgar, T.; Franzka, S.; Hartmann, N.; Hasselbrink E. *Langmuir* **2004**, *20*, 3525.
- ¹¹⁵ Blackledge, C.; Engebretson, D. A.; McDonald J. D. *Langmuir* **2000**, *16*, 8317.
- ¹¹⁶ Peter, M.; Li, X. M.; Huskens, J.; Reinhoudt, D. N. *J. Am. Chem. Soc.* **2004**, *126*, 11684.
- ¹¹⁷ Davis, J. J.; Coleman, K. S.; Busuttil, K. L.; Bagshaw, C. B. *J. Am. Chem. Soc.* **2005**, *127*, 13082.
- ¹¹⁸ Blasdel, L. K.; Banerjee, S.; Wong, S. S. *Langmuir* **2002**, *18*, 5055.
- ¹¹⁹ *Introduction to microlithography*, 2. Ed.: Thompson, L. F.; Willson, C. G.; Bowden, M. J. Am. Chem. Soc., Washington DC, **1994**.
- ¹²⁰ Solak, H. H. *J. Phys. D: Appl. Phys.* **2006**, *39*, R171.

- ¹²¹ Wollman, E. W.; Kang, D.; Frisbie, C. D.; Lorkovic, I. M.; Wrighton, M. S. *J. Am. Chem. Soc.* **1994**, *116*, 4395.
- ¹²² Tarlov, M. J.; Burgess, D. R. F.; Gillen, G. *J. Am. Chem. Soc.* **1993**, *115*, 5305.
- ¹²³ Huang, J. Y.; Dahlgren, D. A.; Hemminger, J. C. *Langmuir* **1994**, *10*, 626.
- ¹²⁴ Bratton, D.; Yang, D.; Dai, J.; Ober, C. K. *Polym. Adv. Technol.* **2006**, *17*, 94.
- ¹²⁵ Smith, K. C. A.; Oatley, C. W. *J. Appl. Phys.* **1995**, *6*, 391.
- ¹²⁶ Buck, D. A.; Shoulders, K.; *Proceeding Eastern Joint Computer Conference*, ATEE, New York, **1957**.
- ¹²⁷ Broers, A. N.; Molzen, W. W.; Cuomo, J. J.; Wittels, N. D. *Appl. Phys. Lett.* **1976**, *29*, 596.
- ¹²⁸ Alice, D. R.; Broers, A. *Appl. Phys. Lett.* **1990**, *57*, 2271.
- ¹²⁹ Craighead, H. G.; Howard, R. E.; Jackel, L. D.; Mankiewich, P. M. *Appl. Phys. Lett.* **1983**, *42*, 38.
- ¹³⁰ Matsui, S.; Ichihashi, T.; Mito, M. *J. Vac. Sci. Technol. B* **1989**, *7*, 1182.
- ¹³¹ Djenizian, T.; Schmuki, P. *J. Electroceram.* **2006**, *16*, 9.
- ¹³² Rai-Choudhury, P. *SPIE Handbook of Microlithography, Micromachining and Microfabrication, Volume I*. CNF, New York, **2000**.
- ¹³³ Umbach, C. P.; Washburn, S.; Laibowitz, R. B.; Webb, R. A. *Phys. Rev. B* **1984**, *30*, 4048.
- ¹³⁴ Broers, A. N.; Hoole, A. C. F.; Ryan, J. M. *Microelectron. Eng.* **1996**, *31*, 131.
- ¹³⁵ Liddle, A.; Gallatin, G. M.; Ocola, L. E. *Mat. Res. Soc. Symp. Proc.* **2003**, *739*, 19.
- ¹³⁶ Chen, W.; Ahmed, H. *Appl. Phys. Lett.* **1993**, *62*, 1499.
- ¹³⁷ Craighead, H. G.; Howard, R. E.; Jackel, L. D.; Mankiewich, P. M. *Appl. Phys. Lett.* **1983**, *42*, 38.
- ¹³⁸ Murray, M.; Scheinfein, M.; Isaacson, M.; Adesida, I. *J. Vac. Sci. Technol. B* **1985**, *3*, 367.
- ¹³⁹ Lercel, M. J.; Craighead, H. G.; Parikh, A. N.; Seshadri, K.; Allara, D. L. *Appl. Phys. Lett.* **1996**, *68*, 1504.
- ¹⁴⁰ Kaholek, M.; Lee, W.-K.; Ahn, S.-J.; Ma, H.; Caster, K.C.; LaMattina, B.; Zauscher, S. *Chem. Mater.* **2004**, *16*, 3688.
- ¹⁴¹ Kaholek, M.; Lee, W.-K.; LaMattina, B.; Caster, K.C.; Zauscher, S. *Nano Lett.* **2004**, *4*, 373.
- ¹⁴² Ahn, S.-J.; Kaholek, M.; Lee, W.-K.; LaMattina, B.; LaBean, T.H.; Zauscher, S. *Adv. Mater.* **2004**, *16*, 2141.

- ¹⁴³ Götzhäuser, A.; Geyer, W.; Stadler, V.; Eck, W.; Grunze M.; Edingler, K.; Weimann, Th.; Hinze, P. *J. Vac. Sci. Technol. B* **2000**, *18*, 3414.
- ¹⁴⁴ (a) Geyer, W.; Stadler, V.; Eck, W.; Zharnikov, M.; Götzhäuser, A.; Grunze M. *Appl. Phys. Lett.* **1999**, *75*, 2401.
- ¹⁴⁵ Eck, W.; Götzhäuser, A.; Zharnikov, M.; Stadler, V.; Geyer, W.; Grunze M. *PCT/DE00/03264*, **1999**.
- ¹⁴⁶ Eck, W.; Küller, A.; Grunze, M.; Völkel, B.; Götzhäuser, A. *Adv. Mater.* **2005**, *17*, 2583.
- ¹⁴⁷ Cyganic, P.; Vandeweert, E.; Postawa, Z.; Bastiaansen, J.; Vervaecke, F.; Lievens, P.; Silverans, R. E.; Winograd, N. *J. Phys. Chem B* **2005**, *109*, 5085.
- ¹⁴⁸ Korniaikov, A.; Küller, A.; Gupta, P.; Loos, K.; Spagnoli, C.; Ulman, A.; Eck, W.; Grunze, M. Unpublished results.
- ¹⁴⁹ Götzhäuser, A.; Eck, W.; Geyer, W.; Stadler, V.; Weimann, Th.; Hinze, P.; Grunze M. *Adv. Mater.* **2001**, *13*, 806.
- ¹⁵⁰ Geyer, W.; Stadler, V.; Eck, W.; Götzhäuser, A.; Grunze, M.; Sauer, M.; Weimann, Th.; Hinze, P. *J. Vac. Sci. Technol. B* **2001**, *19*, 2732.
- ¹⁵¹ Schmelmer, U.; Paul, A.; Küller, A.; Steenackers, M.; Ulman, A.; Grunze, M.; Götzhäuser, A.; Jordan, R. *Small* **2007**, *3*, 459.
- ¹⁵² Nuyken, O.; Weidner, R. *Adv. Polym. Sci.* **1986**, *73-74*, 147.
- ¹⁵³ Prucker, O.; Habicht, J.; Park, I. J.; Rühle, J. *Mater. Sci. Eng. C* **1999**, *8-9*, 291.
- ¹⁵⁴ Schmelmer, U.; Jordan, R.; Geyer, W.; Eck, W.; Götzhäuser, A.; Grunze, M.; Ulman, A. *Angew. Chem. Int. Ed.* **2003**, *42*, 559.
- ¹⁵⁵ Schmelmer, U.; Paul, A.; Küller, A.; Jordan, R.; Götzhäuser, A.; Grunze, M.; Ulman, A. *Macromol. Symp.* **2004**, *217*, 223.
- ¹⁵⁶ Kang, J. F.; Ulman, A.; Liao, S.; Jordan, R.; Yang, G.; Liu, G. Y. *Langmuir* **2001**, *17*, 95.
b) Kang, J. F.; Ulman, A.; Liao, S.; Jordan, R. *Langmuir* **1999**, *15*, 2095.
- ¹⁵⁷ Wang, A.; Tang, H.; Cao, T.; Salley, S. O.; Simon Ng, K. Y. *J. Coll. Interf. Sci.* **2005**, *291*, 438.
- ¹⁵⁸ Schlenoff, J. B.; Li, M.; Ly, H. *J. Am. Chem. Soc.* **1995**, *117*, 12528.
- ¹⁵⁹ Broers, A. N.; Molzen W. W.; Cuomo, J. J. Wittels, N. D. *Appl. Phys. Lett.* **1976**, *29*, 596.
- ¹⁶⁰ Bret, T.; Mauron, S.; Utke, I.; Hoffmann, P. *Microelec. Eng.* **2005**, *78*, 300.
- ¹⁶¹ Djenizian, T.; Balaur, E.; Schmuki, P. *Nanotech.* **2006**, *17*, 2004.
- ¹⁶² Djenizian, T.; Santinacci, L.; Schmuki, P. *Appl. Phys. Lett.* **2001**, *78*, 2940.
- ¹⁶³ Patra, M.; Linse, P.; *Nano Lett.* **2006**, *6*, 133.

- ¹⁶⁴ W.-K. Lee, M. Patra, P. Linse, S. Zauscher, *Small* **2007**, *1*, 63.
- ¹⁶⁵ Wilder, K.; Quate, C. F.; Singh, B.; Alvis, R.; Arnold, W. H. *J. Vac. Sci. Technol. B* **1996**, *14*, 4004.
- ¹⁶⁶ Cappella, B.; Dietler, G. *Surf. Sci. Rep.* **1999**, *34*, 1.
- ¹⁶⁷ Patra, M.; Linse, P.; *Macromolecules* **2006**, *39*, 4540.
- ¹⁶⁸ Kidoaki, S.; Ohya, S.; Nakayama, Y.; Matsuda, T. *Langmuir* **2001**, *17*, 2402.
- ¹⁶⁹ Steenackers, M.; Küller, A.; Ballav, N.; Zharnikov, M.; Grunze, M.; Jordan, R. *Small* **2007**, in print.
- ¹⁷⁰ Dyer, D. J.; Feng, J.; Schmidt, R.; Wong, V. N.; Thao, T.; Yagci, Y. *Macromolecules* **2004**, *37*, 7072.
- ¹⁷¹ Dyer, D. J.; Feng, J.; Fivelson, C.; Paul, R.; Schmidt, R.; Zhao, T. *Polymer Brushes* **2004**, 129.
- ¹⁷² Prucker, O.; Habicht, J.; Park, I.J.; Rühle, J. *Mater. Sci. Eng. C* **1999**, 8-9, 291.
- ¹⁷³ Dyer, D. J. *Adv. Polym. Sci.* **2006**, *197*, 47.
- ¹⁷⁴ Bandrup, J.; Immergut, E. H. *Polymer handbook*, 3rd edition, Wiley, New York, **1989**.
- ¹⁷⁵ M. Zharnikov, A. Shaporenko, A. Paul, A. Götzhäuser, A. Scholl, *J. Phys. Chem. B* **2005**, *109*, 5168.
- ¹⁷⁶ Eck, W.; Stadler, V.; Geyer, W.; Zharnikov, M.; Götzhäuser, A.; Grunze, M. *Adv. Mater.* **2000**, *12*, 805.
- ¹⁷⁷ Y. Tai, A. Shaporenko, M. Grunze, M. Zharnikov, *J. Phys. Chem. B* **2005**, *109*, 19411.
- ¹⁷⁸ R. R. Baht, M. R. Tomlinson, T. Wu, J. Genzer, *Adv. Polym. Sci.* **2006**, *198*, 51.
- ¹⁷⁹ Z. Bao, M. L. Brüning, G. L. Baker, *Macromolecules* **2006**, *39*, 5251.
- ¹⁸⁰ Mitsuishi, K.; Shimojo, M.; Takeguchi, M.; Tanaka, M.; Furuya, K. *Jap. J. Appl. Phys.* **2006**, *45*, 5517.
- ¹⁸¹ Paul, R.; Schmidt, R.; Feng, J.; Dyer, D. J. *J. Polym. Sci.; Part A: Polym Chem* **2002**, *40*, 3284.
- ¹⁸² Schmidt, R.; Zhao, T.; Green, J.-B.; Dyer, D. J. *Langmuir* **2002**, *18*, 1281.
- ¹⁸³ Feng, J.; Dyer, D. J. *Polymer Preprints* **2005**, *46*, 102.
- ¹⁸⁴ Feng, J.; Haasch, R. T.; Dyer, D. J. *Macromolecules* **2004**, *37*, 9525.
- ¹⁸⁵ Chen, X.; Tolbert, L. M.; Henderson, C. L.; Hess, D. W.; Rühle, J. *J. Vac. Sci. Technol. B* **2001**, *19*, 2013.
- ¹⁸⁶ Prucker, O.; Rühle, J. *Macromolecules* **1998**, *31*, 592.
- ¹⁸⁷ Niwa, M.; Date, M.; Higashi, N. *Macromolecules* **1996**, *29*, 3681.

- ¹⁸⁸ Brewer, N. J.; Janusz, S.; Critchley, K.; Evans, S. D.; Leggett, G. J. *J. Phys. Chem. B* **2005**, *109*, 11247.
- ¹⁸⁹ Brewer, N. J.; Rawsterne, R. E.; Kothari, S.; Leggett, G. J. *J. Am. Chem. Soc.* **2001**, *123*, 4089.
- ¹⁹⁰ Fouassier, J. P. *Photoinitiation, Photopolymerization and Photocuring*, Hanser Verlag, München, **1995**.
- ¹⁹¹ Taylor, H. S.; Vernon, A. A. *J. Am. Chem. Soc.* **1931**, *53*, 2527.
- ¹⁹² *Ultra violet locator* Sadtler Research Laboratories, Philadelphia, Pa. **1967**.
- ¹⁹³ Ambartzumian, K. V.; Letokhov, V. S. *In Chemical and Biochemical Applications of Lasers, Vol III*. Academic, New York, **1977**.
- ¹⁹⁴ Jonsson, M.; Lind, J.; Eriksen T. E.; Merényi, G. *J. Am. Chem. Soc.* **1994**, *116*, 1423.
- ¹⁹⁵ Wright, J. S.; Carpenter, D. J.; McKay, D. J.; Ingold, K. U. *J. Am. Chem. Soc.* **1997**, *119*, 4245.
- ¹⁹⁶ Li, Z.; Cheng, J. P. *J. Org. Chem.* **2003**, *68*, 7350.
- ¹⁹⁷ Klein, E.; Lukes, V. *THEOCHEM* **2006**, *767*, 43.
- ¹⁹⁸ Stein, S. E.; Brown, R. L. *J. Am. Chem. Soc.* **1991**, *113*, 787.
- ¹⁹⁹ Aihara, J. I.; Fujiwara, K.; Harada, A.; Ichikawa, H.; Fukushima, K.; Hirota, F.; Ishida, T. *THEOCHEM* **1996**, *366*, 219.
- ²⁰⁰ Bakowicz, K.; Mitura, S. *J. Wide Bandgap Mater.* **2002**, *9*, 261.
- ²⁰¹ Hupert, M.; Muck, A.; Wang, R.; Stotter, J.; Cvackova, Z.; Haymond, S.; Show Y.; Swain, G. M. *Diam. Relat. Mater.* **2003**, *12*, 1940.
- ²⁰² Carlisle, J. A.; *Nat. Mater.* **2004**, *3*, 668.
- ²⁰³ Yarnell, A. *Chem. Eng. News* **2004**, *82*, 26.
- ²⁰⁴ Shih, H. C.; Sung, C. P.; Fan, W. L.; Hsu, W. L. *Thin Solid Films* **1993**, *232*, 41.
- ²⁰⁵ Grün, D. M. *Annu. Rev. Mater. Sci.* **1999**, *29*, 211.
- ²⁰⁶ Williams, O. A.; Nesládek, M.; *Phys. Stat. Sol.* **2006**, *13*, 3375.
- ²⁰⁷ Schrantz, G.; Linn, J.; Belcher, R. *US Patent/5683939* **1997**.
- ²⁰⁸ Bhattacharyya, S.; Auciello, O.; Birrell, J.; Carlisle, J. A.; Curtiss, L. A.; Goyette, A. N.; Grün, D. M.; Krauss, A. R.; Schlüter, J.; Sumant A. V.; Zapol, P. *Appl. Phys. Lett.* **2001**, *79*, 1441.
- ²⁰⁹ Strother, T.; Knickerbocker, T.; Russell, J. N. Jr.; Butler, J. E.; Smith, L. M.; Hamers, R. J. *Langmuir* **2002**, *18*, 968.
- ²¹⁰ Freedman, A.; Stinespring, C. D.. *Appl. Phys. Lett.* **1990**, *57*, 1194.

- ²¹¹ Sappok, R.; Boehm, H. P. *Carbon* **1968**, *6*, 283.
- ²¹² Miller, J. B.; Brown, D. W. *Langmuir* **1996**, *12*, 5809.
- ²¹³ Szunerits, S.; Jama, C.; Coffinier, Y.; Marcus, B.; Delabouglise, D.; Boukherroub R. *Electrochem. Commun.* **2006**, *8*, 1185.
- ²¹⁴ Zhang, G. J.; Song, K. S.; Nakamura, Y.; Funatsu, T.; Ohdomari, I.; Kawarada, H. *Langmuir* **2006**, *22*, 3728.
- ²¹⁵ Notsu, H.; Fukazawa, T.; Tatsuma, T.; Tryk, D. A.; Fujishima, A. *Electrochem. Solid-State Lett.* **2001**, *4*, H1.
- ²¹⁶ Härtl, A.; Schmich, E.; Garrido, J. A.; Hernando, J.; Catharino, S.C.R.; Walter, S.; Feulner, P.; Kromka, A.; Steinmüller, D.; and Stutzmann, M. *Nat. Mater.* **2004**, *3*, 736.
- ²¹⁷ Boukherroub, R.; Wallart, X.; Szunerits, S.; Marcus, B.; Bouvier, P.; Mermoux, M. *Electrochem. Commun.* **2005**, *7*, 937.
- ²¹⁸ Actis P.; Manesse M.; Nunes-Kirchner C.; Wittstock G.; Coffinier Y.; Boukherroub R.; Szunerits S. *Phys. Chem. Chem. Phys.* **2006**, *8*, 4924.
- ²¹⁹ Hernando, J.; Pourrostami, T.; Garrido, J. A.; Williams, O. A.; Gruen, D. M.; Kromka, A.; Steinmuller, D.; Stutzmann, M. *Diamond Relat. Mater.* **2007**, *16*, 138.
- ²²⁰ Matrab, T.; Chehimi, M. M.; Boudou, J. O.; Bendic, F.; Wang, J.; Naguib, N. N.; Carlisle, J. A. *Diamond Relat. Mater.* **2006**, *15*, 639.
- ²²¹ Wang, J.; Firestone, M. A.; Auciello, O.; Carlisle, J. A. *Langmuir* **2004**, *20*, 11450.
- ²²² Kariuki, J. K.; McDermott, M. T. *Langmuir* **2001**, *17*, 5947.
- ²²³ Anariba, F.; DuVall, S. H.; McCreery, R. L. *Anal. Chem.* **2003**, *75*, 3837.
- ²²⁴ Allongue, P.; Henry de Villeneuve, C.; Cherouvrier, G.; Corte's, R. Bernard, M.-C. *J. Electroanal. Chem.* **2003**, *550-551*, 162.
- ²²⁵ Pinson, J.; Podvorica, F. *Chem. Soc. Rev.* **2005**, *34*, 429.
- ²²⁶ Chen, B.; Flatt, A. K.; Jian, H.; Hudson, J. L.; Tour, J. M. *Chem. Mater.* **2005**, *17*, 4832.
- ²²⁷ Stewart, M. P.; Maya, F.; Kosynkin, D. V.; Dirk, S. M.; Stapleton, J. J.; McGuinness, C. L.; Allara, D. L.; Tour, J. M. *J. Am. Chem. Soc.* **2004**, *126*, 370.
- ²²⁸ Laforgue, A.; Addou, T.; Belanger, D. *Langmuir* **2005**, *21*, 6855.
- ²²⁹ Hurley, B. L.; McCreery, R. L. *J. Electrochem. Soc.* **2004**, *151*, B252.
- ²³⁰ Chausse', A.; Chehimi, M. M.; Karsi, N.; Pinson, J.; Podvorica, F.; Vautrin-UI, C. *Chem. Mater.* **2002**, *14*, 392.
- ²³¹ Lud, S. Q.; Steenackers, M.; Jordan, R.; Bruno, P.; Grün, M. D.; Feulner, P.; Garrido, J. A.; Stutzmann, M. *J. Am. Chem. Soc.* **2006**, *128*, 16884.

- ²³² Solak, A. O.; Eichorst, L. R.; Clark, W. J.; McCreery, R. L. *Anal. Chem.* **2003**, *75*, 296.
- ²³³ <http://www.uksaf.org/data/sfactors.html>, accessed on May 6th, **2007**.
- ²³⁴ Zapol, P.; Sternberg, M.; Curtiss, L. A.; Frauenheim, Th.; Gruen, D. M. *Phys. Rev. B* **2002**, *65*, 045403.
- ²³⁵ Volkov, A.; Wu, G.; Coppens, P. *J. Synchrotron Radiat.* **1999**, *6*, 1007.
- ²³⁶ Xu, T.; Yang, S.; Lu, J.; Xue, Q.; Li, J.; Guo, W. M.; Sun, Y. *Diamond Relat. Mater.* **2001**, *10*, 1441.
- ²³⁷ Wilson, J. I. B.; Walton, J. S.; Beamson, G., *J. Electron Spectrosc. Relat. Phenom.* **2001**, *121*, 183.
- ²³⁸ Carlisle, J. A.; Auciello, O. *The Electrochemical Society Interface* **2003**, *12*, 28.
- ²³⁹ Popov, C.; Kulisch, W.; Boycheva, S.; Yamamoto, K.; Cecone, G.; Koga, Y. *Diamond Relat. Mater.* **2004**, *13*, 2071.
- ²⁴⁰ Mendes, P.; Belloni, M.; Ashworth, M.; Hardy, C.; Nikitin, K.; Fitzmaurice, D.; Critchley, K.; Evans, S.; Preece, J. *ChemPhysChem.* **2003**, *4*, 884.
- ²⁴¹ Vase, K. H.; Holm, A. H.; Pedersen, S. U.; Daasbjerg, K. *Langmuir* **2005**, *21*, 8085.
- ²⁴² Allongue, P.; Delamar, M.; Desbat, B.; Fagebaume, O.; Hitmi, R.; Pinson, J.; Savéant, J. *M. J. Am. Chem. Soc.* **1997**, *119*, 201.
- ²⁴³ Delamar, M.; Desarmot, G.; Fagebaume, O.; Hitmi, R.; Pinson, J.; Saveant, J. M. *Carbon* **1997**, *35*, 801.
- ²⁴⁴ Brooksby, P. A.; Downard, A. J. *L Langmuir* **2004**, *20*, 5038.
- ²⁴⁵ Richter, G. Diploma thesis, TU München, **2007**.
- ²⁴⁶ Li, L.; Davidson, J. L.; Lukehart, C. M. *Carbon* **2006**, *44*, 2308.
- ²⁴⁷ Petrini, D.; Larsson, K. *J. Phys. Chem. C* **2007**, *111*, 795.
- ²⁴⁸ Dörwald, F. Z. *Organic Synthesis on Solid Phase* **2002**, Wiley-VCH Verlag GmbH, Weinheim.
- ²⁴⁹ Tran, Y.; Auroy, P. *J. Am. Chem. Soc.* **2001**, *123*, 3664.
- ²⁵⁰ Hesse, M.; Meier, H.; Zeeh, B. *Spektroskopische Methoden in der organischen Chemie* Georg Thieme Verlag, Stuttgart, **1995**.
- ²⁵¹ Hart, R.; Janssen, R. *Makromol. Chem.* **1961**, *43*, 242.
- ²⁵² Porter, M. D.; Bright, T. B.; Allara, D. L. *Anal. Chem.* **1986**, *58*, 2461.
- ²⁵³ Nase, M. M.; Saidi, H. *Appl. Surf. Sci.* **2006**, *252*, 3073.
- ²⁵⁴ Zenftman, H. *J. Chem. Soc.* **1950**, 982.

- ²⁵⁵ Mitchell, A. R.; Kent, S. B. H; Engelhard, M.; Merrifield, R. B. *J. Org. Chem.* **1978**, *43*, 2845.
- ²⁵⁶ Gravano, S. M.; Borden, M.; von Werne, T.; Doerffler, E. M.; Salazar, G.; Chen, A.; Kiskak, E.; Zasadzinski, J. A.; Patten, T. E.; Longo, M. L. *Langmuir* **2002**, *18*, 1938.
- ²⁵⁷ Tsukanova, V.; Lavoie, H.; Harata, A.; Ogawa, T.; Salesse, C. *J. Phys. Chem. B* **2002**, *106*, 4203.
- ²⁵⁸ Harris, P. J. F. *Phil. Mag.* **2003**, *84*, 3159.
- ²⁵⁹ Klein, C.; Cornelius, S. H. Jr. *Manual of Mineralogy 20th ed.* Wiley, New York, **1985**.
- ²⁶⁰ May, K.; Unterreiner, B. V.; Dapprich, S.; Ahlrichs, R. *Phys. Chem. Chem. Phys.* **2000**, *2*, 5089.
- ²⁶¹ Allendorf, M. D.; Melius, C. F.; Ho, P., Zachariah, M. R. *J. Phys. Chem.* **1995**, *99*, 15285.
- ²⁶² Van Krevelen, D. W. *Properties of Polymers*, Elsevier Science Publishers B. V. **1990**.
- ²⁶³ Maslova, M. V.; Gerasimova, L. G.; Forsling, W. *Coll. J.* **2004**, *66*, 322.
- ²⁶⁴ Børve, K. J.; Pettersson L. G. M. *J. Phys. Chem.* **1991**, *95*, 3214.
- ²⁶⁵ <http://www.schott.com>, accessed on May 15th, **2007**.
- ²⁶⁶ Park, Y. W.; Inagaki, N. *J. Appl. Polym. Sci.* **2004**, *93*, 1012.
- ²⁶⁷ Kazinczi, R.; Mollinger, J. R.; Bossche, A. *MEMS 2000: proceedings. 13th Annual International Conference on Micro Electro Mechanical Systems*, **2000**, 229. online access: <http://ieeexplore.ieee.org/iel5/6757/18063/00838521.pdf>, accessed on May 1st, **2007**.
- ²⁶⁸ Peksheva, N. P.; Strukov, V. M. *Russ. Chem. Rev.* **1979**, *48*, 1092.
- ²⁶⁹ Reinhardt, F.; Dwir, B.; Kapon, E. *Appl. Phys. Lett.* **1996**, *68*, 3168.
- ²⁷⁰ Collins, S. E.; Baltanas, M. A.; Bonivardi, A. L. *Langmuir* **2005**, *21*, 962.
- ²⁷¹ Toda, M.; Itakura, A. N.; Büscher, K.; Graf K.; Berger, R. *e-J. Surf. Sci. Nanotechnol.* **2004**, *4*, 96.
- ²⁷² Janzen, O.; Hahn, C.; Mönch, W.; *Euro Phys. J. B* **1999**, *9*, 315.
- ²⁷³ Gaylord, N. G.; Hoffenberg, D. S.; Matyska, B.; Mach, K. *J. Pol. Sci. Pol. Chem. Ed.* **1968**, *6*, 269.
- ²⁷⁴ Xu, L.; Li, X; Zhai, M.; Huang, L.; Peng, J.; Li, J.; Wei, G. *J. Phys. Chem. B*, **2007**, *111*, 3391.
- ²⁷⁵ http://www.veeco.com/products/Metrology_and_Instrumentation, accessed on May 21st, **2007**.
- ²⁷⁶ Naylor, T. *Permeation Properties*, Pergamon Press, New York, **1989**.
- ²⁷⁷ Biesalski, M.; Rühle, J. *Langmuir* **2000**, *16*, 1943.

- ²⁷⁸ K ugler, R.; Schmitt, J.; Knoll, W. *Macromol. Chem. Phys.* **2002**, *203*, 413.
- ²⁷⁹ Yui, N.; Mrsny, R.; Park, K. *Reflexive Polymers and Hydrogels: Understanding and Designing Fast Responsive Polymeric Systems*. Boca Raton, FL, CRC Press, **2004**.
- ²⁸⁰ Chen, H.; Dong, S. *Talanta* **2007**, *71*, 1752.
- ²⁸¹ Kumaran, A. U. S.; Miyawaki, T.; Ichimura, M. *Jpn. J. Appl. Phys., Part 2* **2006**, *45*, L1283.
- ²⁸² Zou, J.-J.; Zhang, Y.-p.; Liu, C.-J. *Langmuir* **2006**, *22*, 11388.
- ²⁸³ M ossmer, S.; Spatz, J. P.; M oller, M.; Aberle, T.; Schmidt, J.; Burchard, W. *Macromolecules* **2000**, *33*, 4791.
- ²⁸⁴ Glass, R.; M oller, M.; Spatz, J. P. *Nanotechnol.* **2003**, *14*, 1153.
- ²⁸⁵ Glass, R.; Arnold, M.; Bl ummel, J.; K uller, A.; M oller, M.; Spatz, J. P. *Adv. Funct. Mater.* **2003**, *13*, 569.
- ²⁸⁶ Hummel, D. O. *Atlas of Polymer and Plastics Analysis*, 3rd ed.; VCH, Weinheim, **1991**.
- ²⁸⁷ Lala, N. L.; Deivaraj, T. C.; Lee, J. Y. *Coll. Surf. A* **2005**, *269*, 119.
- ²⁸⁸ <http://rsb.info.nih.gov/ij/index.html>, accessed on April 30th, **2007**.
- ²⁸⁹ J. F. Moulder, W. E. Stickle, P. E. Sobol, K. D. Bomben, *Handbook of X-ray Photoelectron Spectroscopy*, Ed.: Chastian, J., Perkin-Elmer Corp.: Eden Prairie, MN, **1992**.
- ²⁹⁰ Georg Albert PVD-Coatings, Heidelberg, Germany (GeorgAlbert@web.de).
- ²⁹¹ Padeste, C.; Solak, H. H.; Brack, H. P.; Slaski, M.; G ursel S. A.; Scherer G. G. *J. Vac. Sci. Technol. B* **2004**, *22*, 3191.